

USING THE ENVIRONMENTS OF TYPE II_n SUPERNOVAE
AND CLASSICAL NOVAE TO CONSTRAIN PROGENITOR
PROPERTIES

by
Conor L. Ransome

A thesis submitted in partial fulfilment of the requirements of
Liverpool John Moores University
for the degree of
Doctor of Philosophy.
July 2022

Declaration

The work presented in this thesis was carried out at the Astrophysics Research Institute, Liverpool John Moores University. Unless otherwise stated, it is the original work of the author in its entirety

While registered as a candidate for the degree of Doctor of Philosophy, for which submission is now made, the author has not been registered as a candidate for any other award. This thesis has not been submitted in whole, or in part, for any other degree.

Conor L. Ransome
Astrophysics Research Institute
Liverpool John Moores University
IC2, Liverpool Science Park
146 Brownlow Hill
Liverpool
L3 5RF
UK

JANUARY 2023

Abstract

Supernovae are the explosive death of stars. Massive stars ($M > 8 M_{\odot}$) end their lives as core-collapse supernovae. A white dwarf that gains mass and reaches the Chandrasekhar mass ($\sim 1.4 M_{\odot}$) explodes as a thermonuclear supernova. Supernovae can be broadly split into two classes based on whether hydrogen is present in the spectrum. Type I supernovae lack hydrogen and type II supernovae exhibit hydrogen.

Type IIn supernovae are a mysterious subclass, they are highly inhomogeneous and are characterised by complex Balmer line profiles with a narrow component which is interpreted as interaction between the SN ejecta and a dense, pre-existing hydrogen-rich circumstellar medium. The progenitor paths for type IIn supernovae are unclear, at least one transient, SN 2005gl has pre-explosion imaging revealing the progenitor to be a luminous blue variable. These luminous blue variables are massive evolved stars that undergo episodic mass loss which may form the required circumstellar material for the type IIn phenomenon. However recent studies on the environments of type IIn supernovae reveal that these transients are not strongly associated with regions of ongoing star formation.

These environmental studies are a powerful indirect method to constrain progenitor paths. In the first part of this thesis, I set out a classification scheme for type IIn supernovae and apply it to archival spectral data. Then using this sample with robust classifications, I observe the hosts of type IIn supernovae with the Liverpool Telescope, the Isaac Newton Telescope and the Las Cumbres Observatory Global Telescope Network 2m. Using these data, I create continuum subtracted $H\alpha$ images and apply the novel pixel statistics technique, normalised cumulative ranking. This method is used to gauge the association of a SN position with the $H\alpha$ emission in the host. There is a mass ladder in terms of this association, the more massive the progenitor, the better the supernovae follow the emission. I present the results of these pixel statistics as well as the radial distributions of type IIn supernovae in order to investigate possible progenitor routes.

In the second part of this thesis, I investigate the environments of classical novae in the Andromeda galaxy, M31. Classical novae are a subset of cataclysmic variable where a

white dwarf accretes hydrogen-rich material from a companion via Roche-lobe overflow, Once sufficient material has been accreted, a thermonuclear runaway occurs on the surface of the white dwarf and a portion of the accreted material is ejected. Generally, classical novae can be split into two spectral classes, Fe II and He/N, based on their characteristic non-Balmer lines.

Previous work has suggested the existence of different populations of classical novae in terms of their radial distribution, or association to the bulge or disc of M31. I investigate the possibility that the spectral classes of classical novae can be separated based on their radial distributions. The progenitor systems of He/N classical novae may have a higher mass white dwarf and may be expected to be associate with the younger populations in the disc of M31. Firstly I present the largest spectroscopically confirmed M31 classical nova sample. Then as well as a radial analysis, for the first time, I will implement the normalised cumulative ranking method on classical novae. In this case with *GALEX* NUV and FUV. I compare the spectral classes to each other in terms of both their radial distributions and association to the UV emission.

Contents

Declaration	ii
Abstract	iii
Contents	v
List of Figures	ix
List of Figures	ix
List of Tables	xvi
List of Tables	xvi
Publications	xviii
0.1 Refereed publications	xviii
0.2 Unrefereed articles	xviii
0.3 Notices	xix
Acknowledgements	xxi
1 Introduction to transient astronomy	1
1.1 Things that go bump in the night: a brief history of transient astronomy	1
1.2 Transient diversity	3
1.2.1 The diversity in exploding transients	3
1.2.1.1 Luminous Red Novae (LRNe)	5
1.2.1.2 Calcium Rich Transients	5
1.2.1.3 Faint type Ia supernova	7
1.2.2 Fast Blue Optical Transients (FBOTs)	7
1.3 Facilities used in this thesis	8
1.3.1 Liverpool Telescope	8
1.3.2 Isaac Newton Telescope	9
1.3.3 Las Cumbres Observatory 2m	10
1.3.4 GALEX	11
1.4 Thesis outline	12
2 Introduction: Type II_n supernovae	13
2.1 Supernovae	13
2.1.1 The deaths of massive stars: core-collapse supernovae	13
2.1.2 Thermonuclear supernovae	16
2.1.3 Observations	17

2.1.4	Supernova classification	18
2.1.4.1	Spectroscopic classification	18
2.1.4.2	Photometric classification	20
2.2	Type II _n supernovae	20
2.2.1	Supernova impostors	23
2.3	The progenitors of supernovae	23
2.3.1	Type IIP and type IIL supernovae	24
2.3.1.1	The progenitor of the type II-pec SN 1987A	25
2.3.2	Stripped envelope supernovae	26
2.3.2.1	Type II _b supernovae	26
2.3.2.2	Type Ib/c supernovae	26
2.3.3	Type II _n supernovae	27
2.4	Studies of the environments of transients	29
3	Creating a spectral classification scheme for type II_n supernovae	32
3.1	The spectra of type II _n supernovae	32
3.2	The motivation for a spectral reclassification	35
3.3	The initial sample	36
3.3.1	The Open Supernova Catalogue	36
3.3.2	The Transient Name Server	37
3.4	Collecting the spectral data	38
3.5	Making a robust classification scheme	38
3.5.1	Our classification algorithm	42
3.6	Our reclassifications	43
3.6.1	The gold sample	43
3.6.2	The silver sample	50
3.6.3	Previously misclassified type II _n supernovae	54
3.6.4	Comparing classifications from databases	63
3.6.5	Comparing to results from SNID	63
3.7	The spectral diversity of SNe II _n	63
3.7.1	SN 1978K and other caveats	64
3.7.2	Supernova impostors	65
3.7.3	Circumstellar Medium Geometry	66
3.7.4	Flash ionisation supernovae and type Ia-CSM supernovae	67
3.7.5	H II region contamination leading to erroneous classifications	68
3.8	Conclusions	69
4	The Hα environments of type II_n supernovae	72
4.1	Environmental studies of supernovae	72
4.1.1	Environmental tracers of underlying stellar population	74
4.1.2	Sample for environmental analysis	75
4.2	Observations	76
4.2.1	Data reduction	77
4.3	Pixel statistics: normalised cumulative ranking	81
4.4	Radial analysis	83
4.5	Results from the pixel statistics analysis	87
4.5.1	Examples of the SN II _n hosts	91

4.5.2	NCR analysis results	92
4.5.3	Comparisons between subsamples	94
4.6	Results from the radial analysis	94
4.7	Using the environments of type IIIn supernovae to constrain possible progenitor systems	97
4.7.1	High mass progenitors	97
4.7.1.1	Luminous blue variables	97
4.7.1.2	Yellow hypergiants	101
4.7.2	Intermediate mass progenitors	102
4.7.2.1	Electron capture supernovae	102
4.7.3	Red supergiants	104
4.7.4	Low mass progenitors	105
4.7.4.1	Type Ia-CSM supernovae	105
4.7.5	Luminous blue variables outside of their parent star forming region	106
4.7.6	SN2005ip and the long-lasting type IIIn supernovae	107
4.7.7	SN2009ip and precursor eruptions	110
4.7.8	Supernova impostors	112
4.7.9	The possible progenitor routes and explosion mechanisms that produce the type IIIn phenomenon	115
4.8	Possible biases	116
4.9	Conclusions and summary	119
5	Introduction: Classical Novae	121
5.1	Classical novae	121
5.1.1	The eruption	121
5.1.2	Nova light-curves	122
5.1.2.1	Light-curve morphology	122
5.1.3	Speed classes	125
5.1.4	Maximum-Magnitude Rate of Decline (MMRD) relation	125
5.1.5	Spectral classes	126
5.1.6	Ejecta velocity	130
5.2	The significance of classical novae	130
5.2.1	Type Ia Supernova progenitors	130
5.2.2	${}^7\text{Li}$ production	131
5.2.3	Recurrent novae (RNe)	131
5.3	Extragalactic nova studies	132
5.3.1	Extragalactic classical nova populations	133
6	The spectral classification of classical novae in the Andromeda galaxy (M31)	137
6.1	The spectral classes of classical novae	137
6.2	Motivation for the classification of classical novae	137
6.3	M31 classical nova catalogue	138
6.3.1	The database	138
6.4	Data analysis	139
6.4.1	The spectra	140
6.4.1.1	Fe II novae	141

6.4.1.2	Fe IIb novae	142
6.4.1.3	He/N novae and He/Nn nova	144
6.4.1.4	The H α profiles of classical novae	146
6.5	Conclusions and summary	157
6.5.1	Distribution of the different spectral classes	158
6.5.2	Summary	159
7	The environments of classical novae in the Andromeda galaxy (M31)	160
7.1	Multiple populations of classical novae	160
7.1.1	Spatial populations	160
7.2	Methods	161
7.2.1	The spectroscopically confirmed sample	161
7.3	<i>GALEX</i> map of the Andromeda galaxy	161
7.4	Methods	162
7.4.1	Pixel statistics: normalised cumulative ranking	162
7.4.1.1	NCR map of Andromeda	163
7.4.2	Radial analysis	164
7.4.3	Modelling CN spatial distributions	167
7.5	Results and discussion	168
7.5.1	Radial analysis results	168
7.5.2	Pixel statistics results from the UV data	173
7.6	Conclusions and Summary	191
8	Conclusions	192
8.1	Chapter 3: Type IIIn supernovae spectral classifications	192
8.2	Chapter 4: The environments of type IIIn supernova	193
8.3	Chapter 6: The spectral classification of M31 classical novae with SPRAT	194
8.4	Chapter 7: The environments of classical novae in the Andromeda galaxy	195
9	Future work	196
9.1	Metallicity of the environments of type IIIn supernovae with the New Technology Telescope	196
9.1.1	The New Technology Telescope	197
9.1.2	Other possible projects	198
A	Appendix	201
A.1	Anderson-Darling test	201
A.2	Isophotal radius code in Python	201
A.3	The SN IIIn hosts	204
A.3.1	Gold	204
A.4	Classical nova spectra	216
	Bibliography	224

List of Figures

1.1	Statue of Polish astronomer Jan Hevelius in Gdansk, Poland. Photograph taken by author.	2
1.2	A schematic diagram of the timescale-luminosity phase space of exploding transients. We see the variety of transients that have been discovered in recent times, filling the luminosity “gap” between classical novae and supernovae. From Kasliwal (2011)	4
1.3	The Liverpool Telescope at sunset at the Observatorio de Roche de los Muchachos, La Palma, Canary Islands. This photograph was taken by the author from the terrace of the Isaac Newton Telescope. The clamshell of the LT is open for evening calibrations, the dome on the right is the Mercator Telescope.	8
1.4	The Isaac Newton Telescope from the secondary mirror access platform (used to change filters on the WFC). The WFC is the instrument placed at the prime focus and can be seen in this image. Here, the mirror petals are closed. This photograph was taken by the author.	9
1.5	The LCO GT2m robotic LT-class telescope located in Siding Springs, Australia. In this image, the clamshell enclosure is open and the telescope is observing. Image credit: LCO.	10
1.6	The <i>GALEX</i> UV space telescope being prepared for its launch on a Pegasus rocket. Image credit: NASA.	11
2.1	A schematic of the layers of a pre-supernova star. In this schematic, the position of each layer represents which element is being fused at the base of that layer. In this example, there is a hydrogen envelope. Figure made by the author.	15
2.2	Example spectra of the spectroscopic sub-classifications of SNe. The main features in each spectrum are highlighted. Figure from Modjaz et al. (2019)	19
2.3	Example light curves of various SN classes. Figure from Wheeler & Harkness (1990) . © IOP Publishing. Reproduced with permission. All rights reserved.	20
2.4	A HST image of η Carinae and the aspherical CSM that makes up the Homunculus nebula. Image: Jon Morse (University of Colorado) NASA Hubble Space Telescope.	28
3.1	An example SN II in $H\alpha$ profile with the narrow, intermediate-width, and broad components shown. This is an example of the classic SN II in “Eiffel Tower” shape which is the product of three model Gaussian components.	33
3.2	An example transient data displayed on the OSC. In this example, the transient is SN 2009ip, a very well studied object so the spectroscopic and photometric data fields are well populated.	37

3.3	An example claimed classification section for SN 2009ip. Note that all previous classifications are included with references.	37
3.4	A decision tree describing my spectral/meta-data classification scheme for SNe IIn.	42
3.5	(<i>Left</i>) Time-series spectra of an exemplar SN IIn – SN 2008J. I show optical spectra at 12 epochs over the range 4000–7500 Å that exhibit strong CSM interaction features. Each spectrum is shifted to the rest frame and plotted with a vertical offset, and the Balmer lines from H α through H δ are indicated with tick marks. The numbers are the days after maximum brightness (2008 Feb. 02) in the <i>i</i> band. (<i>Right</i>) I plot the corresponding H α profiles in velocity space with a vertical offset for clarity.	45
3.6	H α profile and the multi-Gaussian fits for the first spectral epoch (15 days before <i>i</i> band maximum) of SN 2008J. I fit a broad and a narrow component to the data centred around rest-frame H α . The thick black line is the data, the grey lines are the Gaussian components, and the shaded orange area is the total fit along with its 3σ uncertainty region.	45
3.7	Time-series spectra of an exemplar SN IIn – SN 2009ip in NGC 7259. (<i>Left</i>) Spectra spanning 38 epochs over 755 days. The dashed lines mark the Balmer series and there is a vertical offset between each spectrum for clarity. The numbers are the days from maximum brightness (2012 Jul. 24) in the <i>UVM2</i> band. (<i>Right</i>) H α profiles of each epoch in velocity space with a vertical offset.	46
3.8	Multicomponent Gaussian fits to epoch seven (7 days before <i>UVM2</i> -band maximum) of SN 2009ip. I was able to fit three components to the data: a broad feature, an intermediate-width component, and a narrower component. The thick black line is the data, the grey lines are the Gaussian components, and the shaded orange area is the total fit along with its 3σ uncertainty region.	47
3.9	(<i>Left</i>) Spectrum of an exemplar silver class SN IIn – SN 2017gas. I show a single-epoch optical spectrum (15.7 days before maximum brightness in the <i>R</i> band on 2017 Aug. 10) over the range 4000–7500 Å that shows strong CSM interaction features. The spectrum is shifted to the rest frame and the Balmer lines are indicated with tick marks. (<i>Right</i>) The corresponding H α profile in velocity space.	51
3.10	Multicomponent Gaussian fit to the only available spectrum of SN 2017gas. I was able to fit two Gaussian components, one broad and the other narrower. The thick black line is the data, the grey lines are the Gaussian components, and the shaded orange area is the total fit along with its 3σ uncertainty region.	51

3.11	Temporal series of spectra of an example non-SN IIn classification – SN 2009kr. I display optical spectra over the range 4000–7500 Å at nine epochs, showing that the previously claimed CSM interaction features are likely due to the spectra being polluted by emission lines from the underlying H II region; the [N II] lines on either side of H α and the [S II] lines redward of H α are clearly visible at all epochs. This object therefore may be a standard SN II rather than an SN IIn. Each spectrum is shifted to the rest frame, a vertical offset is added for clarity, and the Balmer series from H α through H δ is indicated with tick marks. The numbers on the right of the spectra denote the days from maximum brightness (2009 Nov. 6) in the <i>K</i> band. (<i>Right</i>) Corresponding H α profiles in velocity space, with vertical offsets.	56
3.12	Multicomponent Gaussian fits to the fourth epoch of SN 2009kr just over 12 days past maximum brightness in the <i>K</i> band. I was able to fit a broad component to the H α profile along with three narrow components at H α and [N II] $\lambda\lambda$ 6548, 6584. The [S II] $\lambda\lambda$ 6717, 6731 lines are also visible. The presence of these lines indicates that the narrow features seen in this H α profile probably originate from the underlying H II region. The thick black line is the data, the grey lines are the Gaussian components, and the shaded orange area is the total fit along with its 3σ uncertainty region.	57
3.13	Time-series spectra of an example of a negative SN IIn classification - SN 2002kg. I show optical spectra from 4000-7500 Å over four epochs that are mostly featureless apart from Balmer emission and [N II]. The H α line is strong and narrow and the H β line is also apparent in these spectra. Each epoch is shifted to the rest-frame, an offset is added for clarity and the Balmer series from H δ -H α is marked with a tick. The numbers are the days from maximum (2002 Oct. 26) in the Clear band. (<i>Right</i>) Corresponding H α profiles in velocity space with offsets.	58
3.14	Multicomponent Gaussian fits to the H α profile of the third epoch (778 days post maximum brightness in the Clear band) of SN 2002kg. I fit a narrow H α profile with FWHM ≈ 300 km s $^{-1}$. The thick black line is the data, the grey lines are the Gaussian components, and the shaded orange area is the total fit along with its 3σ uncertainty region.	58
3.15	Time series of spectra of an exemplar silver-class SN IIn – SN 2001fa. I display optical spectra over the range 4000–7500 Å at nine epochs that show CSM interaction features at earlier times, followed by more-standard SN II characteristics with broad H α emission and possible P Cygni features in several lines. Each spectrum is shifted to the rest frame, a vertical offset is added for clarity, and the Balmer series from H α through H δ is indicated with tick marks. The numbers are the days from maximum (2001 Nov. 17) in the Clear band. (<i>Right</i>) Corresponding H α profiles in velocity space, with vertical offsets.	59
3.16	Multicomponent Gaussian fits to the fourth epoch (25.7 days before maximum brightness in the Clear band) of SN 2001fa. I were able to fit two Gaussian components to the data, one intermediate-broad and the other narrow. The thick black line is the data, the grey lines are the Gaussian components, and the shaded orange area is the total fit along with its 3σ uncertainty region.	59

4.1	Filter transmission plots for the LT H α filters (<i>left</i>) and the single LCOGT 2m, rest frame H α filter (<i>right</i>).	76
4.2	An example of the 6634 Å H α (<i>left</i>) and r' -band images (<i>right</i>) from the LT, in this case the host is NGC 151, the host of PTF 11iqb.	78
4.3	An example of matched, non-saturated stars as detected by the IRAF routine, <code>xyxymatch</code> . The stars are circled in red, in this case the image is the host of PTF 11iqb, NGC 151.	79
4.4	An example of a cropped continuum subtracted H α image (without masking), in this case it is NGC 151, the host of PTF 11iqb.	80
4.5	The radial light profile of the host of PTF 11iqb, NGC 151 in the r' -band. The y-axis is the difference in the contained flux between two ellipses. This profile flattens out when the sky level is reached. The x-axis is the number of iterations (i.e, number of expanding ellipses used).	84
4.6	The radial light profile of the host of PTF 11iqb, NGC 151 in H α . The y-axis is the difference in the contained flux between two ellipses. This profile flattens out when the sky level is reached. The x-axis is the number of iterations (i.e. number of expanding ellipses used) and this number of iterations is from the r' -band radial profile	85
4.7	An example of the radial analysis employed in this chapter. Shown is the r' -band image of the host of PTF 11iqb, NGC 151. The transparent red ellipse just intercepts the SN II _n site (red circle). The black ellipse encloses the galaxy r' -band flux. These ellipses are also used in the continuum subtracted H α image. In order to measure the emission from the host, foreground stars were masked.	86
4.8	The continuum-subtracted H α (<i>left</i>) and r' -band (<i>right</i>) environments of PTF 11iqb in NGC 151 ($z=0.0126$). The position of PTF 11iqb is marked with the red circle. PTF 11iqb is an example of a SN II _n associated with star-formation as traced by the H α emission, resulting in an NCR value of 0.845. The foreground star at the top of the image has been masked out in the H α image as the continuum subtraction leaves artefacts which may interfere with the NCR value calculation.	91
4.9	The continuum-subtracted H α (<i>left</i>) and r' -band (<i>right</i>) environments of SN 2003lo in NGC 1376 ($z=0.0139$). The position of SN 2003lo is marked with the red circle. SN 2003lo is an example of a SN II _n that is not associated with star-formation as traced by the H α emission (NCR value of zero). In the case of SN 2003lo, the transient resides in an apparent inter-arm gap.	91
4.10	Cumulative distribution of the NCR values of the subsamples of the SNe II _n environments. The solid blue line is the full sample, the orange dashed line is the gold sample, the solid green line is the silver sample and the red dashed line is the non-zero NCR value sample. Also plotted is the 1:1 relationship (purple dashed line) which represents a population of progenitors which are strongly associated with star formation as traced by H α emission.	93
4.11	Fraction of H α , Fr(H α) flux contained within an ellipse that just encloses the SN pixel.	95
4.12	Fraction of r' -band flux, Fr(R) contained within the ellipse that just enclosed the SN pixel.	96

4.13	Fraction of $H\alpha$, $\text{Fr}(H\alpha)$ flux contained within the ellipse that just enclosed the SN pixel. This is the subsample of SNe IIn with a zero NCR value.	97
4.14	Fraction of r' -band flux contained within the ellipse that just enclosed the SN pixel. This is the subsample of SNe IIn with a zero NCR value.	98
4.15	Fraction of $H\alpha$ flux contained within the ellipse that just enclosed the SN pixel. This is the subsample of SNe IIn with a non-zero NCR value.	99
4.16	Fraction of r' -band flux contained within the ellipse that just enclosed the SN pixel. This is the subsample of SNe IIn with a non-zero NCR value.	100
4.17	Cumulative frequency plot showing the $\text{Fr}(H\alpha)$ and $\text{Fr}(R)$ distributions compared with the 1:1 relation which would be a hypothetical SN IIn population that is evenly distributed in the host in terms of $H\alpha$ or r' -band emission.	101
4.18	The host of SN 2005ip, NGC 2906. The continuum subtracted $H\alpha$ image is on the left and the right panel is the r' -band image of the host. The location of SN 2005ip is marked by the red circle.	109
4.19	The host of SN 2015da, NGC 5337. The continuum subtracted $H\alpha$ image is on the left and the right panel is the r' -band image of the host. The location of SN 2015da is marked by the red circle. Note that SN 2015da is in one of the strongest star formation regions in NGC 5337 and the observed excess may be (at least in part) due to the ongoing CSM interaction.	109
4.20	The host of SN 2010jl, NGC 5189A. The continuum subtracted $H\alpha$ image is on the left and the right panel is the r' -band image of the host. The location of SN 2010jl is marked by the red circle. Note that SN 2010jl is in a disturbed host.	110
4.21	The host of SN 2009ip, NGC 7259. The continuum subtracted $H\alpha$ image is on the left and the right panel is the r' -band image of the host. The location of SN 2009ip is marked by the red circle. Note that SN 2009ip is isolated from the main disc of the host and has an NCR value of zero.	111
4.22	The routes that a SN IIn can take in terms of the different possible explosion mechanism (i.e. thermonuclear vs core collapse) and the photometric properties. Within these types there may be further subdivisions in terms of the progenitor types.	116
4.23	NCR distributions of the SNe IIn in this work split into the full sample and the non-zero NCR SNe IIn and also the NCR distribution of the SNe IIP from Anderson et al. (2012) , with both the full SN IIP and non-zero NCR distributions plotted. The 1:1 relation is marked with a dashed blue line.	117
5.1	The anatomy of a nova light-curve. Courtesy of Prof. Matthew Darnley (PhD thesis), originally from McLaughlin (1960)	123
5.2	The distribution of the novae spectral classes in relation to their ejecta velocity as inferred from the widths of the $H\alpha$ emission line. It is clear that the Fe II novae in red have slower ejecta than He/N in the blue cross-hatch. The filled black region represents the He/Nn hybrid class. Taken from Shafter et al. (2011a) © AAS. Reproduced with permission	127
5.3	Template spectra for the Fe II class, taken from Williams (1992) . © AAS. Reproduced with permission	129
5.4	Template spectra of the He/N class, taken from Williams (1992) . © AAS. Reproduced with permission	129

5.5	Histogram of the maximum apparent magnitude of M31 CNe showing the bimodal CN population proposed by Arp 1956a © AAS. Reproduced with permission	133
5.6	Histogram of the maximum apparent magnitude of M31 CNe using updated observations. The initial bimodal distribution found by Arp 1956a is no longer present when new observations are used. Plot from Prof. Matthew Darnley with data from the catalogue of Pietsch (2010)	134
6.1	Spectra is presented for the first five of our chronologically ordered Fe II class CNe. Over-plotted are the more common Fe II characteristic lines. Note that the top spectra had a single SPRAT exposure so cosmic rays must be manually removed. M31N 2015-08c has numerous P-Cygni features that are easily visible.	142
6.2	Spectra for the second group of five chronologically ordered Fe II class novae. M31N 2017-06e is a classic Fe II nova, exhibiting many of the Fe lines and the Balmer series extends to H δ	143
6.3	Spectra of four of the Fe IIb class novae. AT2018lcl shows strong Balmer profiles with the H α profile having a FWHM of $\sim 3600 \text{ km s}^{-1}$	144
6.4	The first four chronologically ordered novae of the He/N class. Note that the first three spectra have the classic He/N feature of double peaked, or saddle shaped Balmer series lines. M31N 2017-12d has a fairly noisy spectra with an atypical H α profile but enough information was contained in the other lines to make a classification.	146
6.5	The final two of the chronologically ordered He/N class novae and our only He/Nn nova M31N 2016-04b. M31N 2016-04b has a very flat spectra apart from the blamer lines however the few lines that do appear on this spectra along with the very narrow H α profile allows us to make the tentative classification of He/Nn.	147
6.6	The isolated H α lines of nine of the Fe II CNe in the sample of CNe that have LT SPRAT data. The red line is the Gaussian fit used to measure the FWHM of the H α profile in order to estimate the ejecta velocity. . .	148
6.7	The H α FWHM of the LT SPRAT CNe. The sample is split into the spectral classes.	149
6.8	Overlay of the positions of our catalogue (the ‘new’ CNe combined with the 44 Shafter et al. (2011a) novae) of M31 novae over an image from the Palomar 48-inch telescope. The catalogue novae have been split into their spectral classes and also RNe are featured.	158
7.1	Transmittance plot of the <i>GALEX</i> NUV and FUV filters. The transmittance is in terms of the fraction of transmission and the wavelength axis is in \AA	162
7.2	A cropped <i>GALEX</i> NUV mosaic that has had the normalised cumulative rank processing applied. This image is the entire galaxy, unmasked. . . .	164
7.3	A cropped <i>GALEX</i> NUV mosaic which has had the normalised cumulative rank processing applied. In this image, the inner region of M31 is masked as to discount high NCR values contained within the bulge and therefore biasing any attempt to associate UV emission with regions of recent star-formation.	165

7.4	A cropped GALEX NUV mosaic which has had the normalised cumulative rank processing applied. This image is just the inner region of M31.	166
7.5	(<i>Left:</i>) The isophotal radial distributions of the modelled radial CN distribution with $\theta = 0.18$ and the spectroscopically confirmed CNe from Chapter 6. When compared, these distributions have an AD p-value of ~ 0.00 . (<i>Right:</i>) the radial distribution the the spectroscopically confirmed CNe and the full M31 CN catalogue from Pietsch (2010) . Comparing these distributions, I find an AD p-value of 0.022.	168
7.6	(<i>Left:</i>) the isophotal radial distributions of the spectroscopically confirmed CN sample from Chapter 6 and the sample in Shafter et al. (2011a) . (<i>Right:</i>) the isophotal radial distribution of the combined, full sample (i.e the Chapter 6 sample and the Shafter et al. (2011a) sample) and the combined Fe II spectral class CNe.	169
7.7	(<i>Left:</i>) the isophotal radial distributions of the combined full sample and the combined He/N spectral class CNe. (<i>Right:</i>) the isophotal radial distribution of the combined He/N spectral class CNe and the combined Fe II spectral class CNe.	170
7.8	(<i>Left:</i>) The NUV NCR distributions of the full sample and the Fe II spectral class CNe. (<i>Right:</i>) The NUV NCR distributions of the decomposition of the full sample when it is broken down into a central region and an outer region that has the central region masked.	173
7.9	(<i>Left:</i> the FUV NCR distributions of the He/N and Fe II spectral classes. (<i>Right:</i>) The NUV NCR distributions of the Fe II and He/N spectral classes of CNe.	174
7.10	(<i>Left:</i> the centre of M31 in the NUV NCR colourmap with the colourbar starting at an NCR value of 0.9, here the maximum value is 0.962. (<i>Right:</i>) The NUV NCR image of one of the star forming regions in the spiral arms of M31, here the NCR values reach 0.975.	175
7.11	A cropped GALEX NUV mosaic which has had the normalised cumulative rank processing applied. Overlaid are the CNe classified previously and the CNe from the Pietsch et al. (2007) catalogue.	177
7.12	A cropped GALEX NUV mosaic which has had the normalised cumulative rank processing applied. Overlaid are the CNe in increasing NCR value. Note that the highest NCR value is near a spiral arm.	178
9.1	The New Technology Telescope	197
9.2	Classical novae in M33	199

List of Tables

3.1	The sample of SNe IIn that were reclassified into the “gold” spectral category. From the sample of 115 transients within $z < 0.02$ with data, 37 SNe are classified as “gold” SNe IIn where the CSM interaction is visible throughout multiple epochs. The table gives the common SN name, the discovery date, the common host name, the J2000 coordinates, and the redshift.	48
3.2	The sample of SNe IIn that were reclassified into the “silver” spectral category. From this sample of 115 transients within $z < 0.02$ with data, 50 SNe are classified as “silver” SNe IIn where the CSM interaction is apparent in some epochs but may be short-lived, or there is only one spectrum for the object. The table gives the common SN name, the discovery date, the common host name, the J2000 coordinates, and the redshift.	52
3.3	Objects that are not SNe IIn and the reasons for classifications.	60
3.4	The sample of SNe IIn that were reclassified as not being SNe IIn. From my sample of 115 transients within $z < 0.02$ with data, 28 SNe are not SNe IIn. The CSM interaction may be confused with pollution from H II regions, or the data are noisy, or the object is a gap transient with a spectrum that resembles that of SNe IIn. The table gives the common SN name, the discovery date, the common host name, the J2000 coordinates, and the redshift.	61
3.5	Breakdown of the number of objects in the OSC and TNS having non-SN IIn primary classifications (out of 115) and the number of occurrences where the OSC and TNS disagree on the primary classification.	63
3.6	Results of using SNID to match the spectral data to templates. In total, SNID matched 32 of the 115 targets to SN IIn templates.	63
4.1	The available H α filters on the LT and LCOGT 2m with their central wavelengths and corresponding redshift.	77
4.2	The sample of 79 SNe IIn and their hosts with the discovery date, coordinates, NCR value, Fr(H α) values, Fr(R) value, the telescope I used for the observation and the classification from Chapter 3.	88
4.3	The multi-sample Anderson-Darling test results comparing the NCR values of the sub-samples of SNe IIn. These tests probe whether or not the sub-samples are drawn from the same parent population.	94
4.4	The Hartigan’s dip test and bimodality coefficients for this sub-samples of SNe IIn and the flux fractions.	96
4.5	The sample of eight SN impostors observed. All but one of these transients is unassociated with star forming regions as traced by H α emission. . .	115

5.1	The five nova speed classes from very fast to very slow as defined by Payne-Gaposchkin (1964) with the corresponding t_2 time in days and the magnitude rate of decline, \dot{m}_V in magnitudes per day.	125
6.1	The number of CN spectra from our full sample of 180 observed by different facilities.	139
6.2	The number of each class of nova determined from the 60 CNe with spectra available on the LT database which were able to be used for our classification purposes.	141
6.3	Table 6.3 *: LT SPRAT data †: New classification \diamond Reclassification (continued)	151
6.3	Table 6.3 *: LT SPRAT data †: New classification \diamond Reclassification (continued)	152
6.3	Table 6.3 *: LT SPRAT data †: New classification \diamond Reclassification (continued)	153
6.3	Table 6.3 *: LT SPRAT data †: New classification \diamond Reclassification (continued)	154
6.3	Table 6.3 *: LT SPRAT data †: New classification \diamond Reclassification (continued)	155
6.3	Table 6.3 *: LT SPRAT data †: New classification \diamond Reclassification (continued)	156
7.1	The spectral classes in the full sample of 222 M31 CNe from the Pietsch (2010) catalogue and the Shafter et al. (2011a) survey.	161
7.2	The Anderson-Darling test results for the radial distributions.	171
7.3	The CN sample presented in Shafter et al. (2011a)	179
7.4	Grid presenting the Anderson-Darling test results for the subsamples of M31 CNe NCR values. The values shown are the AD p-values. The lower triangle are the FUV AD p-values and the upper triangle shows the AD p-values for the NUV NCR distributions.	180
7.5	The M31 CNe and their NCR values in FUV and NUV. These distributions are also split into the contributions from within and outside of the masked region. The CNe presented in Shafter et al. (2011a) are towards the end of this table and are separated with a horizontal line after M31N-2018-02a.190	

Publications

0.1 Refereed publications

During the course of the preparation of this thesis, the contents of Chapters 3 and 4 have been published in refereed journals:

- A systematic reclassification of type II_n supernovae
C. L. Ransome, S. M. Habergham-Mawson, M.J. Darnley, P.A. James, A.V. Filippenko, E.M. Schlegel, 2021, Monthly Notices of the Royal Astronomical Society Volume 506, Issue 4, pp.4715-4734, <https://arxiv.org/pdf/2107.02179.pdf>
- An H α survey of the host environments of 77 type II_n supernovae within $z < 0.02$
C. L. Ransome, S. M. Habergham-Mawson, M.J. Darnley, P. A. James, 2022, Monthly Notices of the Royal Astronomical Society, Volume 513, Issue 3, pp.3564-3576, <https://arxiv.org/pdf/2204.09706.pdf>
- Optical spectra of near-Earth asteroids (381906) 2010 CL19 and (453778) 2011 JK
H. Kucakova, O. Mikhalchenko, M. Popescu, **C. L. Ransome**, A. Sharma, 2019, Contributions of the Astronomical Observatory Skalnaté Pleso, vol. 49, no. 3, p. 532-538. <https://ui.adsabs.harvard.edu/abs/2019CoSka...49..532K/abstract>

0.2 Unrefereed articles

- The Spectral Reclassification of Nearby ($z < 0.02$) Type II_n Supernovae
C. L. Ransome, S. M. Habergham-Mawson, M.J. Darnley, P.A. James, A.V. Filippenko, E.M. Schlegel, 2021 Research Notes of the AAS, Volume 5, Issue 5, id.121, 0 pp.

0.3 Notices

- Transient Classification Report for 2021-08-24
C. L. Ransome, 2021, Transient Name Server Classification Report, No. 2021-2919 <https://ui.adsabs.harvard.edu/abs/2021TNSCR2919...1R/abstract>
- Transient Classification Report for 2021-08-19
C. L. Ransome, 2021, Transient Name Server Classification Report, No. 2021-2863 <https://ui.adsabs.harvard.edu/abs/2021TNSCR2863...1R/abstract>
- Transient Classification Report for 2021-08-16
C. L. Ransome, 2021, Transient Name Server Classification Report, No. 2021-2830 <https://ui.adsabs.harvard.edu/abs/2021TNSCR2830...1R/abstract>
- Transient Classification Report for 2021-08-13
C. L. Ransome, 2021, Transient Name Server Classification Report, No. 2021-2798 <https://ui.adsabs.harvard.edu/abs/2021TNSCR2798...1R/abstract>
- Spectroscopic confirmation of the 2020 eruption of recurrent nova M31N 1963-09c
Williams, S. C., Darnley, M. J., Healy, M. W., Murphy-Glaysher, F. J., **C. L. Ransome**, 2020, The Astronomer's Telegram, No. 14145 <https://ui.adsabs.harvard.edu/abs/2020ATel14145...1W/abstract>
- Spectroscopic classification of three M31 novae with the Liverpool Telescope
Williams, S. C., Darnley, M. J., Healy, M. W., Murphy-Glaysher, F. J., **C. L. Ransome**, 2020, The Astronomer's Telegram, No. 14121 <https://ui.adsabs.harvard.edu/abs/2020ATel14121...1W/abstract>
- Spectroscopic classification of AT 2020ubx as a nova in M31
Williams, S. C., Darnley, M. J., Healy, M. W., Murphy-Glaysher, F. J., **C. L. Ransome**, 2020, The Astronomer's Telegram, No. 14053 <https://ui.adsabs.harvard.edu/abs/2020ATel14053...1W/abstract>
- Spectroscopic classification of AT 2020lye as a nova in M31
Williams, S. C., Darnley, M. J., Healy, M. W., Murphy-Glaysher, F. J., **C. L. Ransome**, 2020, The Astronomer's Telegram, No. 13795 <https://ui.adsabs.harvard.edu/abs/2020ATel14145...1W/abstract>
- Classification of AT 2019wlo and AT 2019wvf as M31 novae
Williams, S. C., Darnley, M. J., Healy, M. W., Murphy-Glaysher, F. J., **C. L. Ransome**, 2020, The Astronomer's Telegram, No. 13384 <https://ui.adsabs.harvard.edu/abs/2020ATel13384...1W/abstract>

- Recurrent Nova M31N 2008-12a: spectroscopic confirmation of the 2019 eruption
Williams, S. C., Darnley, M. J., Healy, M. W., Murphy-Glaysher, F. J., **C. L. Ransome**, 2019, The Astronomer’s Telegram, No. 13273 <https://ui.adsabs.harvard.edu/abs/2019ATel13273....1D/abstract>
- Spectroscopic Classification of AT 2019tpb/ASASSN-19aad as a Galactic Nova
Williams, S. C., Darnley, M. J., Healy, M. W., Murphy-Glaysher, F. J., **C. L. Ransome**, 2019, The Astronomer’s Telegram, No. 13241 <https://ui.adsabs.harvard.edu/abs/2019ATel13241....1W/abstract>
- Spectroscopic classification of AT 2019sxc as a nova in M31
Williams, S. C., Darnley, M. J., Healy, M. W., Murphy-Glaysher, F. J., **C. L. Ransome**, 2019, The Astronomer’s Telegram, No. 13228 <https://ui.adsabs.harvard.edu/abs/2019ATel13228....1W/abstract>
- Spectroscopic Classification of AT 2019pjh and M31N 2019-09a as novae in M31
Williams, S. C., Darnley, M. J., Healy, M. W., Murphy-Glaysher, F. J., **C. L. Ransome**, 2019, The Astronomer’s Telegram, No. 13078 <https://ui.adsabs.harvard.edu/abs/2019ATel13078....1W/abstract>
- Spectroscopic classification of M31N 2019-08a as a nova in M31
Williams, S. C., Darnley, M. J., Healy, M. W., Murphy-Glaysher, F. J., **C. L. Ransome**, 2019, The Astronomer’s Telegram, No. 12999 <https://ui.adsabs.harvard.edu/abs/2019ATel12999....1W/abstract>
- Spectroscopic classification of AT 2019lqg as a nova in M31
Williams, S. C., Darnley, M. J., Healy, M. W., Murphy-Glaysher, F. J., **C. L. Ransome**, 2019, The Astronomer’s Telegram, No. 12953 <https://ui.adsabs.harvard.edu/abs/2019ATel12953....1W/abstract>

Acknowledgements

As I sit in an empty auditorium writing this during a break at EAS in Valencia, it is clear that I can only start these acknowledgements by recognising the incredible guidance and support from my supervisors; Stacey Habergham-Mawson, Matt Darnley and Phil James. I came to Liverpool in 2018 as a bit of a blank slate - I remember Phil asking me what the difference between a type I and type II supernova was and he was met with an ‘umm’. Despite this, you all (very patiently...) offered me the freedom to explore and become an independent researcher. Your combined, encyclopedic knowledge of astronomy was invaluable along the way.

You helped me gain the confidence I needed to try new things, whether this be scientifically, or professionally. For example applying for competitive telescope time (and getting it) or encouraging me to apply to be a support astronomer at the Isaac Newton Telescope - something I’d essentially written off for myself, but ended up getting the place. You’ve allowed me the space and opportunity to foster and develop my own ideas and incorporate them into my work.

For all of this I am truly grateful and I would not be where I am now, and would not have had the fantastic experiences I have had without your supervision and unwavering support.

My time in Liverpool has been a formative part of my life and I would like to thank the entire ARI for their kitchen chats, pandemic zooms, pub trips and friendship. The atmosphere at the ARI is inclusive, friendly and a superb place to work that is always abuzz with new ideas and discussion. It has been a privilege to be part of the ARI. There are many amazing people at the ARI I would like to thank; Anna Hodgkinson for all her help organising travel to conferences and for brightening everyone’s day; Marie Martig for being a brilliant mentor; Shaun Brown for making sure the post-pandemic office wasn’t completely empty and always being up for a chat and a pint; Tom Sedgwick for being the only other person who understands the masterpiece that is Kingdom Come and also having an impeccable taste in dogs (hi Ziggy); Saz McDonald for always being up for a coffee or a pub trip (and also for providing access to the aforementioned Ziggy);

Fiona Murphy-Glaysheer for her kindness and discussion on all thing novae; Mike Healy, who gathered a crowd of Germans at the Hofbrauhaus in Munich who were disappointed when they realised you were watching the Liverpool match on your laptop rather than Dortmund. I also thank Andrew Mason who took over the pub tsardom when I was away in La Palma; Sam Stafford for patiently dealing with my coding queries and for looking after Sgt. Spicy and the Pepper Platoon; Danny Horta for his seemingly limitless energy and enthusiasm; the ING-NOT crew for making my time in La Palma so memorable. I also thank the Durham crew, Peter Galea who is always up for putting the world to rights in the Vic and is also an impressive druid in World of Warcraft; Sam and Jake, who as well as being great friends, are also brilliant raid team members; Jonny and Alex who I ended up following to Liverpool.

My family has been a source of strength and love since long before Liverpool and to them I owe everything. Mum and Dad, you have supported me in everything I have done and my achievements are as much yours as they are mine. You made sure I got my education, and instilled in me my stubbornness and sense of ambition that has served me well. You nurtured my early interest in science and helped feed my curiosity, taking me to places like Kennedy Space Center, where the scale of a Saturn V rocket is very apparent when having to wheel along its length in my wheelchair. I would not be here without you, I love you both - you said I could do whatever I put my mind to, and it turns out you weren't wrong. I thank my brother, Finlay and sister, Niamh, my best friends; my grandparents, Anne and Raymond who have been a constant in my life. I also thank my aunties and uncles. I am forever grateful that my Nan and uncle Andy got to see me finish my PhD. I can not leave out my whippets; Winston, Clementine and Merlin, whose companionship has provided me with great joy. Lastly, Al who made sure I rested and played video games. Your love and support has helped kept me going - and also Richard the gecko, who despite having ~one brain cell, is the best boy.

The funding for this PhD was provided by an STFC doctoral studentship, jointly supported by the Faculty of Engineering and Technology at LJMU.

This thesis project has made use of data from the following facilities and resources:

- The LIVERPOOL TELESCOPE. The Liverpool Telescope is operated on the island of La Palma by Liverpool John Moores University in the Spanish Observatorio del Roque de los Muchachos of the Instituto de Astrofísica de Canarias with financial support from the UK Science and Technology Facilities Council. <https://telescope.livjm.ac.uk/>
- The ISAAC NEWTON TELESCOPE. The ISAAC NEWTON TELESCOPE is operated on the island of La Palma by the Isaac Newton Group of Telescopes in the Spanish Observatorio del Roque de los Muchachos of the Instituto de Astrofísica de Canarias.
- The LAS CUMBRES OBSERVATORY GLOBAL TELESCOPE NETWORK, 2M. This work makes use of observations from the Las Cumbres Observatory global telescope network. <https://lco.global/observatory/>
- GALAXY EVOLUTION EXPLORER This research is based on observations made with the GALAXY EVOLUTION EXPLORER, obtained from the MAST data archive at the Space Telescope Science Institute, which is operated by the Association of Universities for Research in Astronomy, Inc., under NASA contract NAS 5-26555.

Unless otherwise stated and reproduced with permission, all results and plots presented in this thesis were produced by myself using the `Python` language, apart from Figure 5.6, which was produced by Prof. Matthew Darnley.

`Python` packages most notably utilised for this work include `numpy`, `scipy`, `matplotlib`, and `astropy` and associated packages within. `IRAF` was also widely utilised for data reduction.

There is a way out of every box, a solution to every puzzle; it's just a matter of finding it.

- Capt. Jean-Luc Picard

Don't listen to anyone who tells you that you can't do this or that. That's nonsense. Make up your mind, you'll never use crutches or a stick, then have a go at everything. Go to school, join in all the games you can. Go anywhere you want to. But never, never let them persuade you that things are too difficult or impossible.

- Grp. Capt. Douglas Bader

This my friend, is a pint.

- Meriadoc Brandybuck

It comes in pints?!

- Peregrin Took

For Deborah and Sheldon

Chapter 1

Introduction to transient astronomy

1.1 Things that go bump in the night: a brief history of transient astronomy

What is a transient when talking about astronomy? Broadly speaking, an astronomical transient is an event that changes with time, with the event having a beginning and an end point. The time over which the event evolves could be a fleeting fraction of a second, or many years (however, still fleeting on astronomical timescales). A transient can be a distant cosmic explosion observed with the biggest, most advanced facilities available, or a comet seen with a pair of binoculars. In this thesis, I concentrate on exploding transients.

Time-domain astronomy in the context of cosmic explosions has a long and varied history. First documented by ancient astronomers in China, Japan and Korea who called newly appearing stars in the sky ‘guest stars’ and have records of these objects dating back to 1500 BCE. These ancient observations are reviewed in [Stephenson & Yau \(1986\)](#). In Latin, the guest stars were known as ‘nova stella’, translating to *new star*. The objects these ancient astronomers observed were most likely either classical novae (CNe) within the Milky Way or supernovae (SNe). In 185 CE the supernova SN 185 occurred (probably a Type Ia; [Zhao et al., 2006](#)) and was the first recorded SN observed by both Chinese and possibly Roman astronomers. The first reliably reported transient, CK Vul, was discovered in 1670 by French astronomer, Anthelme Voituret (see [Shara & Moffat, 1982](#); [Shara et al., 1985](#); [Evans et al., 2002](#)). Previously this was thought to be a CN and then a luminous, red, nova-like transient, but [Evans et al. \(2002\)](#) found that CK Vul was not a nova which is also the conclusion of [Eyres et al. \(2018\)](#) where they suggest a merger between a white dwarf and a brown dwarf. However, more recently, [Banerjee et al. \(2020\)](#) found that CK Vul may be an intermediate luminosity optical transient

(ILOT, transients with luminosities between that of SNe and CNe that evolve to be red and dusty, [Berger et al. 2009a](#)) but the origin of the more luminous ILOTs (such as CK Vul) is not known. [Shara et al. \(2017a\)](#) recovered the binary system of Nova Scorpius 1437 using proper-motion ageing of the shell making this the oldest recovered nova. Nova Orionis 1678 (V529 Ori) is another old classical nova discovered, first observed by Polish astronomer Johannes Hevelius (a statue of Johannes Hevelius, in Gdansk, can be seen in Fig. 1.1). Followup studies of V529 Ori by [Robertson et al. \(2000\)](#) recovered a possible remnant from the nova.



FIGURE 1.1: Statue of Polish astronomer Jan Hevelius in Gdansk, Poland. Photograph taken by author.

In antiquity all astronomy was performed with the naked eye hence only the brightest and longest lasting transient events were likely to be observed. While there were many naked-eye novae occurring pre-telescope, curiously few were reported, with the exception of Galactic supernovae which can be seen in daylight. Novae can be indirectly discovered by looking at star catalogues such as Atlas Coelestis by 17th century English astronomer and first Astronomer Royal, John Flamsteed, and then finding which stars are missing. CK Vul was noted as one of Flamsteed's lost stars (see [Baily, 1845](#)). The peculiar lack of naked-eye nova discoveries is described in [Warner \(2006\)](#) who concludes that the early astronomers were simply not as meticulous as they are often regarded to have been

(see also: [Shara & Moffat, 1982](#); [Shara & Drissen, 1995](#); [Schaefer, 2013](#); [Shafter, 2017](#); [Schaefer, 2018a, 2021](#), for discussions on historical CN observations).

1.2 Transient diversity

Using their peak luminosities and characteristic timescales, transients can be plotted on a timescale-luminosity plot (shown in Fig. 1.2) where clusters of transient classes are shown. Timescale in this case is defined as the time taken for the transient to dim below peak by some magnitude (for example, time to decrease by one magnitude from peak, t_1 , e.g. [Villar et al., 2017](#)). Historically, there was a gap in the timescale-luminosity plot between supernovae and classical novae. However, since the mid-2000s, there has been an explosion in the number of new classifications of exploding transients with the advent of transient surveys such as the Palomar Transient Factory (PTF, [Law et al., 2009](#)). These new transients fill a large six magnitude gap between the realm of classical novae and supernovae. This landscape of exploding transients shown in Fig. 1.2 provides us with a a breadth of new transients to explore.

The plot in Fig. 1.2 continues to be populated, with transients ranging from the faint and fast CNe ([Kasliwal et al., 2011b](#)) to the superluminous supernovae with new surveys such as the Zwicky Transient Facility (ZTF, [Bellm et al., 2019](#)) contributing large numbers of transient alerts ($\sim 10^6$ per night [Graham et al., 2019](#)) leading to thousands of spectroscopically confirmed SN discoveries per year (e.g. the Bright Supernova Survey [Fremling et al., 2020](#); [Perley et al., 2020](#)). Future surveys such as the Legacy Survey of Space and Time (LSST) at the Vera Rubin Observatory ([LSST Science Collaboration et al., 2009](#)) promise huge numbers of transient alerts ($\sim 10^7$ a night). There are several other transient surveys operating as of October 2022 such as the All-Sky Automated Survey for Supernovae (ASAS-SN [Kochanek et al., 2017](#)) and the Young Supernova Experiment (YSE; [Jones et al., 2021](#)).

1.2.1 The diversity in exploding transients

The two extremes (in terms of peak luminosity) of the plot in Fig. 1.2 are superluminous SNe and CNe, with CNe being discussed in Chapter 5. A zoo of transients populate the phase space in Fig. 1.2 such as: Luminous Red Novae ([Munari et al., 2002](#); [Pastorello et al., 2019b](#); [Blagorodnova et al., 2020](#)); Calcium Rich Transients ([Kasliwal et al., 2012b](#); [De et al., 2020](#)); Intermediate Luminosity Red Transients ([Berger et al., 2009b](#); [Kasliwal](#)

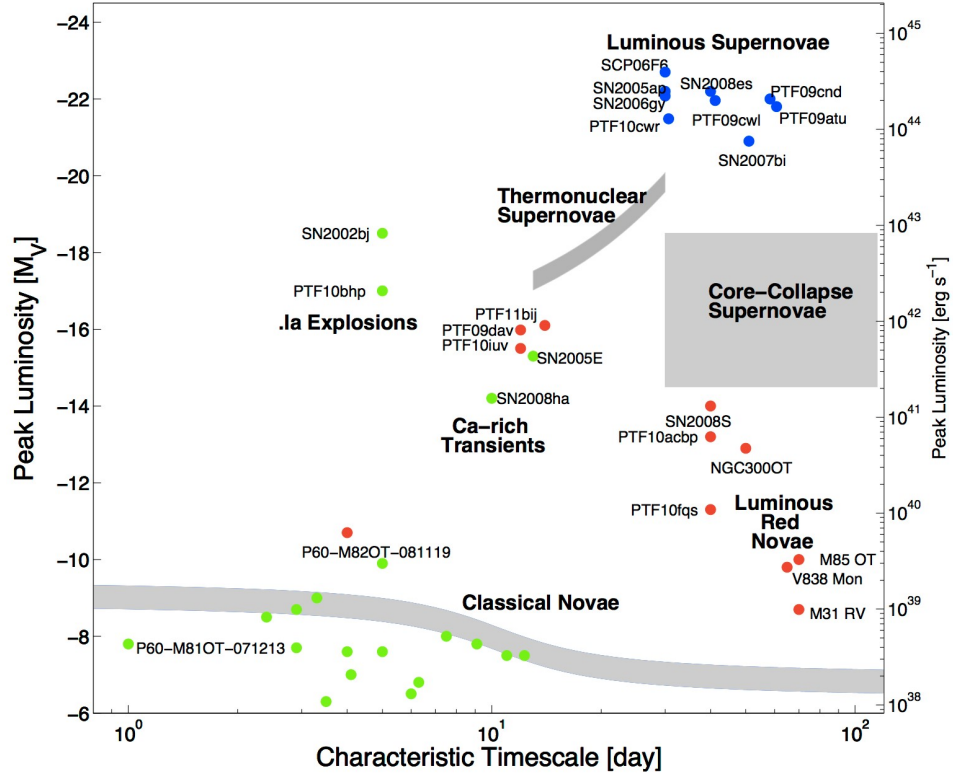


FIGURE 1.2: A schematic diagram of the timescale-luminosity phase space of exploding transients. We see the variety of transients that have been discovered in recent times, filling the luminosity “gap” between classical novae and supernovae. From Kasliwal (2011).

et al., 2017); Kilonovae (Tanvir et al., 2013; Abbott et al., 2017; Smartt et al., 2017), SN Impostors (Van Dyk et al., 2000; Maund et al., 2006; Smith et al., 2011; Kochanek et al., 2012; Pastorello et al., 2019b), .Ia SNe (Bildsten et al., 2007; Shen & Bildsten, 2009; Kasliwal et al., 2011a) and Fast Blue Optical Transients (Inserra, 2019; Perley et al., 2019; Ho et al., 2020). Perley et al. (2020) present a recent study of SN types across the timescale-luminosity phase space using the Bright Transient Survey with ZTF. Those authors construct the timescale-luminosity plot for various transients including thermonuclear SNe, H rich and H poor CCSNe, gap transients and interacting transients. Villar et al. (2017) populate the gaps in timescale-luminosity phase space by utilising theoretical models that incorporate various mechanisms such as radioactive decay, CSM interaction and magnetar central engines. Those authors predict that there will be few physical transient types that will populate the voids where there are short duration (durations below 10 days) and the intermediate luminosity gap between CNe and SNe, some of transients that fill the transient gap (very much a non-exhaustive list) are:

1.2.1.1 Luminous Red Novae (LRNe)

Luminous Red Novae (LRNe) are an intermediate class of transient with a mysterious origin and are characterised by being very red and showing a brightening in the infra-red. [Pastorello et al. \(2019b\)](#) explores the possible origins of LRNe. They demonstrate, based on three examples of LRNe, that one route is a common envelope ejection of a close-binary system and other possibilities include mergers, major instabilities in single massive stars or as discussed in [Shara et al. \(2010\)](#) a slowly evolving classical nova with low M_{WD} and mass accretion rate. An example of an LRN is PTF10fq described in [Kasliwal et al. \(2011a\)](#) which was discovered by the Palomar Transient Facility (PTF) in the spiral galaxy M99. It is noted as the fourth member in a new class with seemingly two groups populating the disc and the bulge of a galaxy which raises questions as to whether the progenitor route is the same for all LRNe. Other proposed possible channels to a LRN may be a helium flash in an asymptotic giant branch (AGB) star ([Munari et al., 2002](#)), or a gas giant planet falling into an ageing parent star ([Kasliwal et al., 2012a](#)). LRNe are of intermediate luminosity being between classical novae and supernovae in Fig. 1.2. PTF 10fq exhibits a broad feature on the Ca II triplet with a FWHM of $10,000 \text{ km s}^{-1}$ which may point towards LRNe having faster ejecta at the poles and slower outflow around the equatorial regions with the slower ejecta having higher mass.

An example of a LRN with uncertain origin is V838 Monocerotis, which was observed in 2002 (see [Williams et al., 2015a](#)). The ejecta expanded rapidly and at its maximum, V838 Mon was one of the most luminous stars in the galaxy, peaking at an absolute magnitude of -9.8. [Williams et al. 2015a](#) describes the discovery of the extra-galactic LRN in M31, M31LRN 2015. Those authors found, using *Hubble Space Telescope* archival data that the probable progenitor source of this event was luminous and red. They conclude that the mechanisms which produce LRN all produce similar outbursts (in terms of the peak luminosity and timescale of the outbursts) and suggest that a stellar merger scenario is likely if there is a single progenitor mechanism. The stellar merger scenario has been suggested for LRNe such as M31-LRN-2015 ([MacLeod et al., 2017](#); [Blagorodnova et al., 2020](#)).

1.2.1.2 Calcium Rich Transients

CRTs are a newer class characterised by a low intermediate (hence ‘gap’ transient) peak luminosity (with examples of CRTs having peak absolute magnitudes of $M > -17$ [De](#)

et al., 2020) and fast photometric evolution compared to other supernovae along with a calcium-rich ejecta, in particular [Ca II] in the nebular phase. CRTs are often classified as some class of core-collapse supernova before the spectroscopic evolution reveals the characteristic strong calcium features (see Kasliwal et al., 2011b).

One of the most peculiar traits of CRTs is that they tend to be found far from the centre of their apparent parent galaxies, up to 40kpc from the nucleus (Kasliwal et al., 2012b) and also tend to have elliptical hosts (however, not all, for example SN 2019ehk which lies within a star forming region in a spiral host Nakaoka et al., 2021). A number of explanations have been put forward to explain this extreme isolation such as: dying hyper-velocity stars kicked out of their parent galaxy via some interaction; stars which have been involved in a tidal interaction at some point during a galaxy merger; the presence of massive stars being accounted for small amounts of star-formation at the high radii; tidal detonation of a He-rich WD in a binary with a neutron star or a black hole or the progenitor system being a white-dwarf and helium-rich star binary. De et al. (2020) present CRTs from ZTF and report that there are three spectroscopic subclasses of CRTs observed in a sample of eight CRTs. These classes include the Ca-Ia which exhibit SN Ia like features, and CRTs showing features similar to SNe Ib/c (Ca-Ib/c). Those authors suggest that the CRTs may originate from helium shell detonation on WDs. However, SN 2019ehk was found in a star forming region within its host. De et al. (2021) derived the synthesised oxygen abundances from the nebular spectrum and suggest that the progenitor had a mass of $9 - 9.5 M_{\odot}$. Those authors suggest SN 2019ehk was a SN IIB-like stripped envelope transient suggesting there may be thermonuclear and core-collapse routes to CRTs.

The first example of a CRT was SN 2005E in the halo of NGC 1032 reported as a new class of transient in Perets et al. (2010). SN 2005E was first classified as a Type Ib supernova, however its photometric evolution, low luminosity, low ejecta mass and the lack of any star-formation in its vicinity rules it out as any known classification of supernova and therefore it was concluded to represent a new type of transient.

The properties of the currently confirmed CRTs are consistent with each other however Kasliwal et al. (2012a) find the spectroscopic evolution of some of these explosions show diversity while their light-curves are all fairly uniform. This may suggest a non-homogenous progenitor channel for these sources however most studies suggest a WD-He rich binary system (see Neunteufel et al., 2019; Galbany et al., 2019). Another proposed origin of CRTs is the tidal disruption of a WD by a stellar mass black hole (providing an explanation to the observed isolation of CRTs Sell et al., 2015).

1.2.1.3 Faint type Ia supernova

In an accreting WD binary system where a carbon-oxygen WD accretes helium (AM Canum Venaticorum binaries), one may expect helium flashes, a helium analogue to classical novae (Bildsten et al., 2007). When the accretion rate is low (under $10^{-6} M_{\odot} \text{ yr}^{-1}$) and the donor mass decreases in models, the ignition mass required for the helium flashes increases until the ignition mass is greater than the donor mass. This leads to a final flash which can produce a thermonuclear SN that peaks at a typical magnitude of -16 powered by the decay of ^{48}Cr , ^{52}Fe and ^{56}Ni (Bildsten et al., 2007; Shen & Bildsten, 2009). These objects also tend to have faster decline times than normal SNe Ia (see also Foley et al., 2013; Dong et al., 2022). An example of a possible observed faint SN Ia is SN 2010X (Kasliwal et al., 2010) having a decay time of around 5 days. This rapid evolution makes the discovery and observation of faint SNe Ia difficult but surveys such as iPTF and ZTF with high cadences are more likely to detect these transients.

1.2.2 Fast Blue Optical Transients (FBOTs)

Recent transient surveys have allowed for the discovery of increasing numbers of rapidly evolving transients. One such group are the FBOTs, a heterogeneous group of transients. FBOTs reach their peak quickly, typically in less than ten days and fade exponentially within a month post peak (Drout et al., 2014; Inserra, 2019). FBOTs have wide magnitude range from faint core-collapse range to the superluminous (Inserra, 2019). Due to the heterogeneity of FBOTs, there are a range of possible explanations for the observed properties. One route may be recombination in an envelope due to a dense but low mass circumstellar wind around a CCSN (Drout et al., 2014). However the well-studied FBOT, AT 2018cow, with a peak of $M_g = -20.4$ (Perley et al., 2019; Prentice et al., 2018) may offer other scenarios such as a tidal disruption event, a failed supernova that collapsed into a black hole or the transient being powered by a central engine such as a magnetar (Perley et al., 2019; Margutti et al., 2019; Inserra, 2019).

The study of cosmic explosions is entering an exciting time with more objects being discovered than ever before with strange and diverse properties. This trend will continue with surveys such as the Zwicky Transient Facility (ZTF) and future facilities such as the Large Synoptic Survey Telescope (LSST) and the New Robotic Telescope (NRT or LT2).

In this thesis, I will focus on two very different ends of the timescale-luminosity phase-space; classical novae (CNe) and type IIIn supernovae (SNe IIIn).

1.3 Facilities used in this thesis

The work in this thesis has made extensive use of various observatories and facilities. Telescopes used in this thesis are the Liverpool Telescope (LT), Isaac Newton Telescope (INT) and the Los Cumbres Observatory 2m (LCOGT 2m). The New Technology Telescope (NTT) was used also but the data will be used in future work described in Chapter 9. I have also used archival data from many sources. I describe some of these facilities below.

1.3.1 Liverpool Telescope



FIGURE 1.3: The Liverpool Telescope at sunset at the Observatorio de Roche de los Muchachos, La Palma, Canary Islands. This photograph was taken by the author from the terrace of the Isaac Newton Telescope. The clamshell of the LT is open for evening calibrations, the dome on the right is the Mercator Telescope.

The Liverpool Telescope¹ (LT; [Steele, 2004](#)) is one of the world's largest completely autonomous telescopes. The LT is a 2m, Ritchey-Chrétien design telescope on an alt-az mount located at the Observatorio de Roche de los Muchachos (ORM), La Palma, Canary Islands, Spain.

The LT has a clamshell type enclosure rather than a traditional dome. This allows the LT to respond to events that require a rapid follow-up which is one of the four main scientific goals for the LT. The other three goals are: small surveys and serendipitous

¹<https://telescope.livjm.ac.uk/>

source follow-up, monitoring of variable objects with timescales from seconds to years and coordinated, simultaneous observations in conjunction with other facilities. Therefore, the LT is perfectly suited for the study of transient sources such as CNe and SNe.

The LT has a number of instruments available. I use the wide field optical imaging camera, IO:O (Smith & Steele, 2017)² in the work presented in this thesis. Other instruments include the SPectrograph for the Rapid Acquisition of Transients (SPRAT; Piascik et al., 2014), a low resolution ($R \approx 350$), high throughput, long-slit spectrograph, and the Multicolor OPTimised Optical Polarimeter (MOPTOP³), a polarimeter designed with time-domain astronomy in mind. Archival SPRAT data is used in this thesis.

1.3.2 Isaac Newton Telescope



FIGURE 1.4: The Isaac Newton Telescope from the secondary mirror access platform (used to change filters on the WFC). The WFC is the instrument placed at the prime focus and can be seen in this image. Here, the mirror petals are closed. This photograph was taken by the author.

The Isaac Newton Telescope (INT⁴) is a 2.54 m optical telescope operated by the Isaac Newton Group of Telescopes and is located at the ORM, La Palma, Canary Islands, Spain, located close to the LT. Originally located at Herstmonceux, UK, the INT was relocated to La Palma in 1981 to take advantage of the superb observing conditions on

²<https://telescope.livjm.ac.uk/TelInst/Inst/IOO/>

³<https://telescope.livjm.ac.uk/TelInst/Inst/MOPTOP/>

⁴<https://www.ing.iac.es//Astronomy/telescopes/int/>

the island. The INT was given a new mirror in 1982 and had first light (with the new mirror in 1984).

Currently, the INT has two instruments at its disposal. At the prime focus, the Wide Field Camera (WFC⁵), a 33' field of view camera with an assortment of broad and narrowband filters. At the Cassegrain focus there is the Intermediate Dispersion Spectrograph (IDS⁶), with gratings covering dispersions of $0.24\text{\AA} - 4.00\text{\AA}$, used with either a red sensitive detector, RED+2 or a blue sensitive detector, EEV10. In this thesis, the imaging camera, WFC is used.

1.3.3 Las Cumbres Observatory 2m



FIGURE 1.5: The LCOGT 2m robotic LT-class telescope located in Siding Springs, Australia. In this image, the clamshell enclosure is open and the telescope is observing.
Image credit: LCO.

The Las Cumbres Observatory 2m telescope (LCOGT 2m⁷, formerly the Faulkes Telescope South) at the Siding Springs Observatory, New South Wales, Australia, is a 2m LT-class autonomous telescope operated by LCO⁸ (Brown et al., 2013). The LCOGT 2m at Siding Springs Observatory offers two instruments. Firstly, the Spectral⁹ camera with a 10.5' field of view and a range of broad and narrowband filters. The LCOGT 2m also

⁵<https://www.ing.iac.es//Astronomy/instruments/wfc/>

⁶<https://www.ing.iac.es//Astronomy/instruments/ids/>

⁷<https://lco.global/observatory/telescopes/2m0/>

⁸<https://lco.global/>

⁹<https://lco.global/observatory/instruments/spectral/>

has the FLOYDS¹⁰ cross-dispersed, low resolution spectrograph with resolving power $R \approx 400 - 700$.

The Spectral camera was used for our Southern hemisphere observations.

1.3.4 GALEX



FIGURE 1.6: The *GALEX* UV space telescope being prepared for its launch on a Pegasus rocket. Image credit: NASA.

The Galaxy Evolution Explorer (*GALEX*, [Martin et al., 2003](#)) is a space telescope was launched via a Pegasus-XL rocket on the underside of a Boeing 747 in 2003. After 2006 its mission was extended and it was decommissioned on the 28th June 2013. *GALEX* optics are a 50cm Ritchey-Chrétien with near-UV (NUV), 1770-2370 Å and far-UV (FUV), 1350-1780 Å channels.

The data are publicly available at the Mikulski Archive for Space Telescopes (MAST) website, in this work (see Chapter 7), M31 mosaics taken in 2006 in both NUV and FUV are used.

¹⁰<https://lco.global/observatory/instruments/floyds/>

1.4 Thesis outline

This thesis will focus on using robust spectral classifications of SNe IIn and CNe in order to produce robust samples. Then I will use these samples in environmental analysis on their host galaxies. The aim of this environmental analysis is to constrain the progenitor properties of these transients.

The thesis will be set out as described below.

Chapter 2 - Introduction: type IIn supernovae: I describe supernovae, their progenitors and environments with a focus on type IIn supernovae.

Chapter 3 -The systematic reclassification of type IIn supernovae: I describe the classification scheme for SNe IIn based on their $H\alpha$ profiles and reclassify nearby ($z < 0.02$) SNe IIn using the new scheme. This work has been published in [Ransome et al. \(2021\)](#).

Chapter 4 - The $H\alpha$ environments of nearby ($z < 0.02$) SNe IIn: In this chapter I will present the results from the largest SN IIn environmental study to date. Using the robust classifications from Chapter 3 to inform the sample selection. I then discuss the implications in term of the progenitor paths for SNe IIn and also compare the spectral categories of SNe IIn. This work was published in [Ransome et al. \(2022\)](#).

Chapter 5 - Introduction: classical novae: I describe classical novae, the eruption mechanisms, extragalactic novae and their possible populations in terms of radial positions and association to different underlying stellar populations.

Chapter 6 - The classification of classical novae in Andromeda (M31): In order to build a solid spectroscopically confirmed sample of M31 CNe, I collect spectral data from archives and classify each spectrum.

Chapter 7 -The environments of classical novae in M31: In this chapter, I present the results for the first environmental analysis for M31 CNe utilising techniques previously used in SN environmental studies. I will also look at the radial distribution of the CNe and relate this to the spectral classes and investigate any difference in possible progenitors.

Chapter 8 - Conclusions: Here I will summarise the conclusions from each chapter.

Chapter 9 - Future work: Finally I will discuss extensions to the work in this thesis.

Chapter 2

Introduction: Type II_n supernovae

2.1 Supernovae

SNe are the violent, explosive deaths of stars and are some of the largest, most energetic explosions observed in the Universe. SNe are extremely important in terms of the material ejected chemically enriching their environments and hosts. Many of the heavy elements needed for rocky planets to form, and indeed for life to evolve, were formed in SN explosions (along with AGB stars and kilonovae which also produce heavy elements). In this section, I will summarise the SN phenomenon and how we categorise these dramatic events.

2.1.1 The deaths of massive stars: core-collapse supernovae

Stars with zero age masses (ZAMS) $\sim 8\text{--}10 M_{\odot}$ and above end their lives when they exhaust their nuclear fuel and their cores collapse, and are therefore known as core-collapse supernovae (CCSNe, [Woosley et al., 2002](#)). Throughout the majority of the life of the star, it is in the main sequence (MS), with a balance between radiation pressure from fusion reactions in the core and gravity. During the MS, hydrogen fusion reactions result in helium production. Most of the energy production in stars over $\sim 1.5 M_{\odot}$ is from fusion reactions in the carbon, nitrogen, oxygen (CNO) cycle. The CNO cycle is a series of reactions that fuses hydrogen to helium, using carbon, nitrogen and oxygen as catalysts. This process releases energy as the mass of the four hydrogen nuclei that are used to make a helium nucleus in the CNO cycle have a higher mass than the resultant helium, and therefore energy is released. This energy then helps maintain hydrostatic equilibrium. The luminosity (rate of energy production) is related to the mass of a star

through the mass-luminosity relation, $L \propto M^{3.5}$. Using the mass-luminosity relation, the time a star spends in the main sequence is proportional to its mass with the timescale $\tau_{MS} \sim M^{-2.5}$ (Hansen & Kawaler, 1994). Massive stars spend the majority of their lives burning their hydrogen fuel. Therefore, the more massive the star, the shorter its lifetime.

When the hydrogen fuel in the core is exhausted, the hydrogen fusion ceases. When this energy production is halted, the stellar core contracts. This contraction increases the core density and pressure and allows for hydrogen burning in a shell outside the core. This hydrogen is then used up and the next phase in the evolution off the MS of our star depends on its initial mass. A star with an initial mass $\sim 8\text{-}25 M_{\odot}$ will evolve into a red supergiant (RSG) and more massive stars may shed their hydrogen atmospheres rapidly via winds and evolve into Wolf-Rayet stars with no hydrogen atmosphere (Woosley et al., 1994). The hydrogen atmospheres can also be stripped by binary interactions. At this point, helium burning commences where carbon and oxygen is produced. When the helium fuel in the core runs out, then the ashes from the helium burning are used as fuel in carbon burning, where magnesium, neon and sodium are produced. This sequence of burning and forming heavier elements continues until the pre-supernova star has an iron core. Iron fusion is endothermic so no further fusion reactions occur in the core.

At this point, our star has an iron core with burning in progressively lighter element shells as one moves away from the core. As there is no longer any outward pressure from the reactions in the core, the contraction due to gravity causes the core to become degenerate and held up by electron degeneracy pressure. However, there is a limit to how much electron degeneracy pressure can hold the stellar core from collapse. This limit is the Chandrasekhar mass, around $1.4 M_{\odot}$ (Chandrasekhar, 1931; Mazzali et al., 2007). The core gains mass as a result of nuclear shell burning depositing material onto the core. Once the core of our dying star exceeds the Chandrasekhar mass, the degeneracy pressure can no longer fight self gravity and core-collapse begins. In the extreme core environments, photodisintegration of the iron in the core takes place where a photon breaks up an iron nucleus into helium and neutrons and can then form protons and neutrons from the helium previously formed (Arnould, 1976). Then at the centre of the core, the densities are so high that protons and electrons form neutrons and neutrinos in a process called neutronisation. Photodisintegration is an endothermic reaction so takes energy from the core and energy is transported from the core in the neutronisation reactions in the form of the weakly interacting neutrinos (Burrows, 1990). This energy loss accelerates collapse until the core material reaches nuclear densities ($10^{14}\text{-}10^{15} \text{ g cm}^{-3}$). At this point neutron degeneracy pressure combined with the strong

nuclear force halts further collapse. The material collapsing on this impassable barrier then rebounds and moves outwards through the other infalling material creating a shock wave. Neutrino transport and this shockwave carry energy from the core-collapse and this is the death of our star in a SN explosion. The SN explosion is further powered by neutrino heating which increases the pressure and helps the shock move through the rest of the iron core. A schematic of the layers in a pre-supernova star is shown in Fig. 2.1.

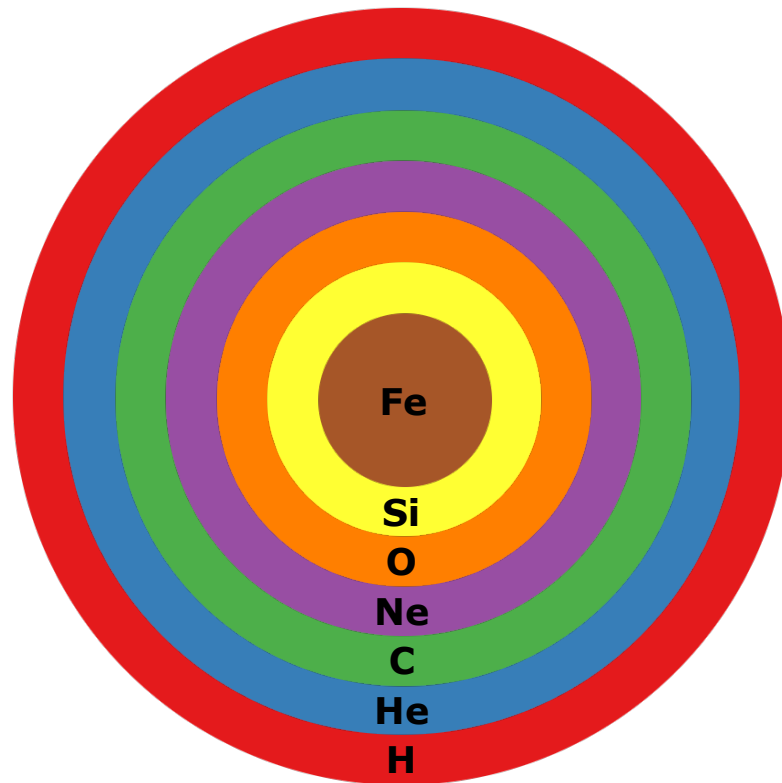


FIGURE 2.1: A schematic of the layers of a pre-supernova star. In this schematic, the position of each layer represents which element is being fused at the base of that layer. In this example, there is a hydrogen envelope. Figure made by the author.

If the mass of the neutron core exceeds $\sim 2M_{\odot}$, then neutron degeneracy pressure can no longer resist the contraction due to gravity. This is the Tolman-Oppenheimer-Volkoff limit, beyond which, our star will collapse into a black hole (Oppenheimer & Volkoff, 1939; Woosley & Weaver, 1995). A black hole is a gravitational singularity (infinitesimal radius and infinite density) and nothing can escape its gravity, not even photons. These remnants, whether they are a neutron star or a black hole can form a central engine that may pump energy into the SN ejecta/remnant whether this be beamed emission from a pulsar or from an accreting black hole.

Described above is the single star route to a SN explosion. However the evolution of stars in binary systems is also important. The importance of binary evolution in thermonuclear SNe is described in Section 2.1.2. For CCSNe, binary interactions have other roles to play, indeed, most massive stars form in binary systems (e.g. [Sana et al., 2012](#)). Binary interactions can help strip the atmospheres of the progenitors of stripped-envelope SNe, as described in Section 2.3.2. Furthermore, in a binary system, the SN progenitor may be a mass gainer, for example, in the case of SNe IIIn that occur in regions unassociated with an O-star cluster, [Smith & Tombleson \(2015\)](#) suggest that the LBV progenitor is a mass gainer in a binary system with a WR donor.

2.1.2 Thermonuclear supernovae

Thermonuclear SNe, or type Ia SNe (SNe Ia) have low mass progenitors in contrast to CCSNe and are the most common SN observed (around 70 per cent; [Fremming et al., 2020](#)). SNe Ia occur in binary systems where at least one of the stars is a carbon-oxygen white dwarf (CO WD) that gains mass. Once the WD gains enough mass such that it exceeds the aforementioned Chandrasekhar mass, carbon fusion is ignited and there is a runaway, terminal explosion. There are two possible scenarios for a WD to gain mass and exceed the Chandrasekhar limit and explode as a SN Ia:

1. **Single degenerate:** in this “classic” mode of WD mass gain, the WD is in a binary system with an evolved, non-degenerate star e.g. a red giant. Hydrogen rich matter is transferred to the surface of the WD via Roche-lobe overflow ([Whelan & Iben, 1973](#); [Leung, 2018](#)). This is a similar model to classical novae which I will discuss in a later section.
2. **Double degenerate:** in this scenario, the binary system is composed of two WDs. The WDs spiral in and eventually merge. This merger results in the product exceeding the Chandrasekhar mass and a SN Ia explosion. [Santander-García et al. \(2015\)](#) report the discovery of a possible double degenerate SN Ia progenitor at the centre of the planetary nebula, Henize 2-428 that they predict will merge in 700 Myr.

There is some discussion as to whether sub-Chandrasekhar mass WDs can explode as a SN Ia in the single degenerate channel. [Taubenberger et al. \(2008\)](#) reports that the sub-luminous SN Ia, SN 2005bl (an example of the SN 1991bg-like SNe Ia) had a low radioactive nickel yield, along with a fast light-curve decay and spectroscopic evolution.

Those authors found that modelled spectra were found to be consistent with other SN 1991bg-like SNe Ia such as SN 1999by. [Blondin et al. \(2018\)](#) modelled the spectrum of SN 1999by and found that a sub-Chandrasekhar WD progenitor produced the best match. Those authors suggest that all of these low-luminosity SN 1991bg-like SNe Ia may have a sub-Chandrasekhar mass progenitor.

Due to SNe Ia exploding at a similar mass, they have constrained properties, e.g. their light curves. This makes them valuable as relative distance indicators, or “standardisable candles” where the light-curves of SNe Ia can be "stretched" to scale as the peak luminosity is proportional to the timescale, or how broad the light-curve is (the Phillips relation [Pskovskii, 1977](#); [Rust, 1974](#); [Phillips, 1993](#)). This makes SNe Ia invaluable in cosmology where SNe Ia can be used to measure the acceleration of the expansion of the Universe and therefore probe dark energy ([Riess et al., 2004](#)).

2.1.3 Observations

As discussed in Section 1.1, there is a long history of pre-telescopic SN observations with the first SN observed being SN 185 ([Zhao et al., 2006](#)), however, there is an older observation of a possible SN observed in India in 4600 BCE ([Joglekar et al., 2011](#)). Other Galactic SNe include SN 1054, with the remnant being the Crab Pulsar ([Collins et al., 1999](#); [Smith, 2013](#)) and Kepler’s supernova, SN 1604 ([Baade, 1943](#)). However, SN 1604 was the last Galactic SN observed. The diligence of pre-telescopic astronomers is sometimes overstated ([Warner, 2006](#)) - no one seemed to notice the SN that made Cassiopeia A (but it may be one of Flamsteed’s lost stars [Hughes, 1980](#)). This is still surprising as the estimated SN rate for the Milky Way is one SN per 50 years. Either we are well overdue a cosmic lightshow, or we miss Galactic SNe as they are concentrated in the disc of the Milky Way and therefore may be obscured by dust ([van den Bergh & Tammann, 1991](#)). However, it should be noted that studies of historical astronomy tend to focus on the Northern Hemisphere so there may be further historical SN observations in the Global South ([Murphey et al., 2021](#)).

With the advent of telescopes, observations of extragalactic SNe were possible. The first extragalactic SN to be observed was S Andromedae, or SN 1885A, a SN I ([de Vaucouleurs & Corwin, 1985](#); [Chevalier & Plait, 1988](#)) which may have first been seen during a public astronomy event but was first reported by [Hartwig \(1885\)](#). After the introduction of modern astronomical CCDs ([Boyle & Smith, 1970](#)), the discovery of SNe accelerated greatly. Now modern surveys such as the Zwicky Transient Facility (ZTF; [Bellm et al., 2019](#)) are finding vast numbers of transient sources (5932 SNe discovered as of 20 Aug

2022¹) and future surveys such as the Legacy Survey of Space and Time at the Vera Rubin Observatory are promising millions of transient detections every year (LSST Science Collaboration et al., 2009).

2.1.4 Supernova classification

The observational properties of SNe can be utilised to categorise these transients into classifications. I will now briefly describe the two primary classification parameters for SNe, the SN spectrum and its light-curve.

2.1.4.1 Spectroscopic classification

A possible “first filter” when classifying SNe is by analysing their spectra (Popper, 1937; Minkowski, 1941; Wheeler & Harkness, 1990; Filippenko, 1997). From here we can classify a SN based on whether hydrogen is present. If there is no hydrogen, the SN is a type I SN (SN I) and if there is hydrogen, it is a type II SN (SN II). With the exception of SNe Ia which are thermonuclear explosions, the other SN classes are CCSNe and these SNe can be further categorised based on their spectra. SNe Ia are characterised by prominent silicon features in their spectra, from a silicon layer that forms when the WD is close to the Chandrasekhar limit (Kato et al., 2018). There are eight spectroscopic sub-classifications of CCSNe; SN II, SN IIb, SN IIn, SN Ib, SN Ic, SN Ic-bl (“bl” standing for broad-lined), SN Ibn and SNe Icn. SN II show prominent, broad, hydrogen Balmer series lines with associated P-Cygni profiles. SNe IIb have prominent helium features but weaker (but still present) hydrogen features. SNe IIb are sometimes considered transitional objects between normal SNe II and SNe Ib (see Section 2.3). SNe IIn show prominent Balmer series lines with superimposed, narrow ($\sim 10^2 \text{ km s}^{-1}$) features that originate from interaction with circumstellar material and also tend to lack P-Cygni features unlike regular SNe II. However, it should be noted that SNe IIn are a heterogeneous class and the CSM geometry effects the photometric and spectral behaviour and evolution of the transient. SNe Ib lack any hydrogen features but have characteristic helium lines, SNe Ibn show narrow features on these helium lines indicating SN ejecta interacting with helium rich material. SNe IIb, SNe Ib and SNe Ibn are known as the helium rich supernovae. Comparatively, SNe Ic are helium poor and show weak silicon absorption, a small number of SNe Ic show very broad absorption features and are termed SNe Ic-bl. The newest spectroscopic SN class are the SNe Icn

¹<https://www.ztf.caltech.edu/>

that show narrow carbon and oxygen emission features, indicating interaction of the SN ejecta with carbon and oxygen rich circumstellar matter (Gal-Yam et al., 2021; Perley et al., 2022). Reviews on the spectral classification of SNe include Filippenko (1997) and Modjaz et al. (2019). An outline of the spectral classes of SNe is shown in Fig. 2.2.

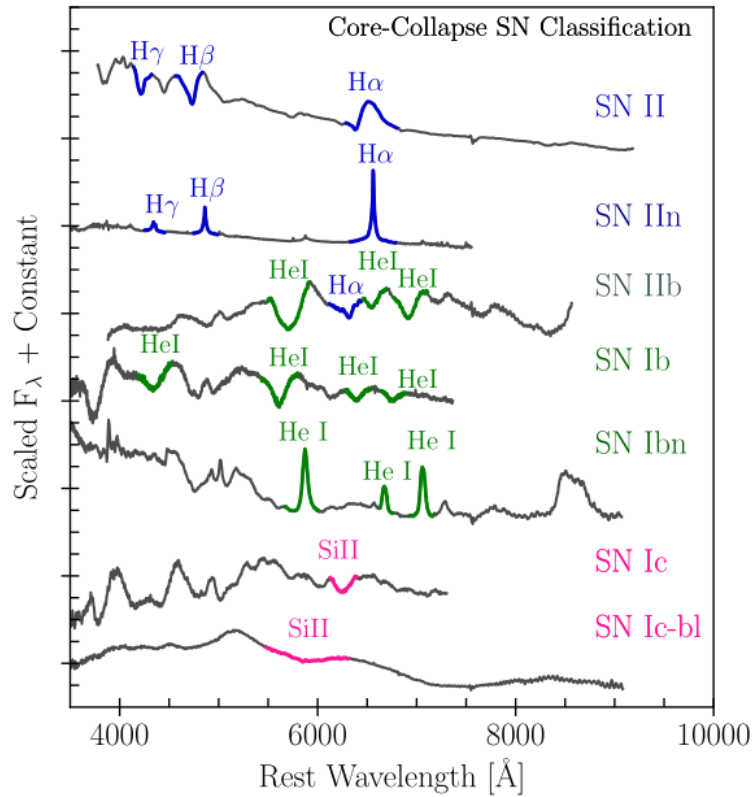


FIGURE 2.2: Example spectra of the spectroscopic sub-classifications of SNe. The main features in each spectrum are highlighted. Figure from Modjaz et al. (2019).

With the large number of transients being detected by transient surveys, the classification of SNe benefits greatly from automated classifiers. One automated classifier is SuperNova IDentification (SNID; Blondin & Tonry, 2007) that correlates a spectrum with sets of templates at different spectral epochs to find the best match. Advances in machine learning allow for classifiers to improve over time and also not rely on template libraries (which in themselves may be limited and biased). An example of such a classifier is Deep learning for the Automated Spectral classification of supernovae and their Hosts (DASH; Muthukrishna et al., 2019).

2.1.4.2 Photometric classification

Additionally to the spectral features of SNe, we can also categorise SNe based on their light curves. Regular SNe II can be split into two photometric classes, SNe II-plateau (SNe IIP) and SNe II-linear (SNe IIL) based on the post-peak light curve shape. SNe IIP have a stalled decay after maximum light due to the progenitor having a massive hydrogen envelope resulting in a recombination wave that lasts for around 100 days. SNe IIL have a linear decay after peak brightness. The progenitors of SNe IIL have a smaller hydrogen envelope than that of the SNe IIP progenitors (Barbon et al., 1979; Doggett & Branch, 1985). Some SNe IIIn have very slow light curve decays, possibly due to ongoing interaction with circumstellar medium and these may be subclassified as SNe IIIn-E (Branch & Wheeler, 2017). Some SNe are extremely luminous and those with an absolute magnitude of ~ -21 may be considered as superluminous SNe (SLSNe) which can also be spectroscopically split similarly to what is described in Section 2.1.4.1 into SLSNe-I and SLSNe-II. Example SN light curves are shown in Fig. 2.3.

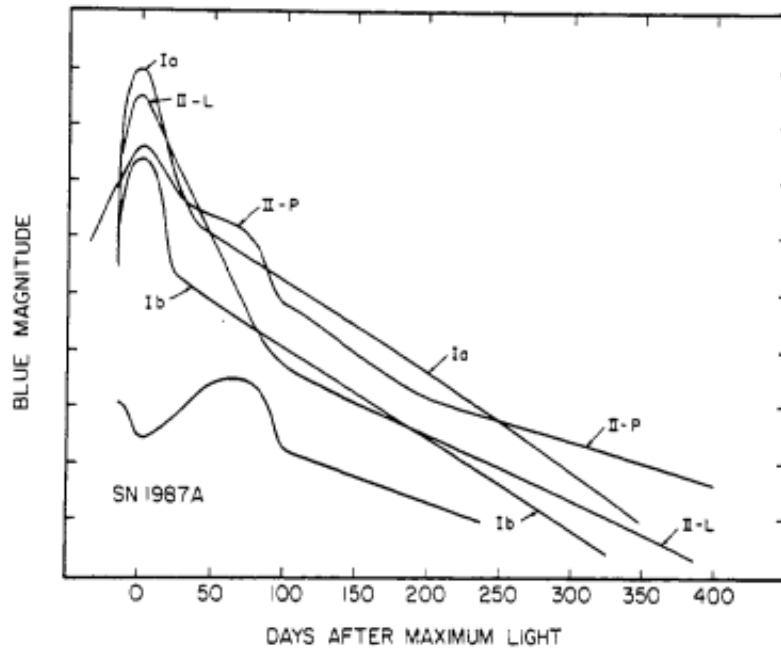


FIGURE 2.3: Example light curves of various SN classes. Figure from Wheeler & Harkness (1990). © IOP Publishing. Reproduced with permission. All rights reserved.

2.2 Type IIIn supernovae

Type IIIn supernovae (SNe IIIn) were first characterised as “Seyfert I” SNe due to the resemblance in the spectra to active galactic nuclei (Filippenko, 1989). SNe IIIn are

uncommon transients that account for around 7% of the observed CCSNe population (Li et al., 2011). Schlegel (1990) coined the classification name of SN II_n with the “n” standing for “narrow” based on the characteristic narrow emission features in the Balmer lines, most obvious on the H α line profile. This was based on the observations of three prototypical SNe II_n (SN 1987F, SN 1988Z and SN 1989C). This narrow feature has a full width half maximum (FWHM) of a few hundred km s⁻¹ and is superimposed on broader components, an intermediate component with a FWHM of a few thousand km s⁻¹ and/or a broad component that may have a FWHM of tens of thousands km s⁻¹ (Filippenko, 1997).

The narrow Balmer line profile feature originates from recombination after the SN ejecta has shocked and subsequently ionised a pre-existing shell of cold, dense and slow moving hydrogen-rich circumstellar medium (CSM; Chugai, 1991; Chugai & Danziger, 1994). The CSM has densities in the range $\sim 10^{-11}$ – 10^{-15} g cm⁻³ (Dessart et al., 2009; Chatzopoulos et al., 2012; Yaron et al., 2017). The intermediate feature may be formed via the interaction of the SN ejecta with a dense, clumpy wind and then further broadened via Thomson scattering (Chugai, 2001; Chugai et al., 2004; Dessart et al., 2009; Humphreys et al., 2012; Huang & Chevalier, 2018). The broad component originates from the expansion of the fast SN ejecta. Perhaps due to this CSM interaction, SNe II_n are generally luminous compared to other classes of SNe, with absolute magnitudes ranging from $M_R \sim -17$ (e.g. SN 1994aj, Benetti et al., 1998) to the superluminous with $M_R \sim -21$ (e.g. the most luminous SN at the time of discovery, SN 2006gy Smith et al., 2007). This is a large range in luminosity which is not seen elsewhere in the time-scale luminosity phase of exploding transients. SNe II_n have an average peak luminosity of $M_B = -18.7$ (Kiewe et al., 2012). However some possible SNe II_n are subluminous such as SN 2008S that peaked at $M_V \sim -14$ (Botticella et al., 2009). Unlike other SNe II, SNe II_n lack the broad P-Cygni absorption features observed on the Balmer lines. The lack of P-Cygni features is perhaps due to the optically thick ionised CSM creating a photosphere when it starts to recombine. However, there are some exceptions such as SN 2012ab where the CSM geometry may have allowed for the observation of the P-Cygni features (Gangopadhyay et al., 2020). SNe II_n also have a blue continuum (particularly at pre-maximum, similar to other SNe at this point in its evolution, but in SNe II_n, the blue continuum lasts longer than in other SNe Schlegel 1990) which may originate from the strong CSM interaction with some showing a pseudo-continuum formed by neighbouring, broadened lines (possibly mostly Fe lines) that blend together (Schlegel, 1990; Stathakis & Sadler, 1991; Turatto et al., 1993).

SNe II_n are a highly heterogeneous class of SNe. As previously discussed, SNe II_n have

large range of peak luminosities, but they also have different light curve shapes and durations. In other words, SNe II_n inhabit a large region in the timescale-luminosity phase-space seen in Fig. 1.2. One may expect SNe II_n to be more long lived than other SN classes due to the CSM interaction but some SNe II_n exhibit ongoing interaction for years post explosion, leading to a very long lived light curve. SN 1988Z, one of the prototype SNe II_n, was found to be long lived SN II_n with the slow decay possibly being due to ongoing CSM interaction, or a pulsar injecting energy into the CSM and ejecta (Stathakis & Sadler, 1991). These long lived SNe II_n are sometimes known as SN 1988Z-like SNe II_n or SN II_n-E (Branch & Wheeler, 2017). SN 2005ip is another example of a SN II_n with a very slow decline. Stritzinger et al. (2012) found that there was ongoing CSM interaction six and a half years post explosion and the light curve was still declining slowly. Haberman et al. (2014) found that SN 2005ip was still the strongest H α source in NGC 2906 three years post explosion and it was still bright in the observations of Stritzinger et al. (2012). Fox et al. (2020) found that the light curve of SN 2005ip only appreciably started to decline around 5000 days post explosion. They note that this decline was accompanied by a change in the spectrum where some high ionisation lines had weakened, as was seen at a similar epoch in SN 1988Z. Similarly to regular SNe II, SNe II_n can be separated into different photometric classes, the SNe II_n-P (e.g. SN 2011ht and PTF 11iqb; Mauerhan et al., 2013; Smith et al., 2015) and SN II_n-L (e.g. SN 1999el and SN 1998S; Di Carlo et al., 2002; Taddia et al., 2015).

SNe II_n show an infra-red (IR) excess a few months post explosion which is interpreted as pre-existing and new dust in the CSM (Gerardy et al., 2002). Those authors suggest that the initial IR luminosity, around 130 days post-explosion was due to pre-existing dust in the CSM due to how soon after the explosion the IR peak was seen. Observations have shown evidence of pre-existing dust from a number of SNe II_n such as SN 1998S (Fassia et al., 2000), SN 2005ip (Fox et al., 2010) and SN 2009kn (Kankare et al., 2012). Furthermore, SNe II_n create dust, for example, SNe 2005ip was found to have formed dust in the shocked region of the CSM (Fox et al., 2010). Smith et al. (2009b) found that there was dust in the SN ejecta of SN 2005ip. Fox et al. (2011) used *Spitzer* data of 68 SNe II_n to probe their dust behaviour. Those authors found that while there was some new dust being formed by the SNe II_n as indicated by optical spectra, the later time IR excesses observed were consistent with pre-existing dust in the CSM.

2.2.1 Supernova impostors

Some transients are initially classified as SNe IIn because they exhibit the multicomponent and narrow $H\alpha$ emission features. However, it later becomes apparent, when the progenitor star is reobserved after the brightening phase, that they originate from nonterminal explosions within a dense CSM. These transients typically lie within gaps in the timescale-luminosity phase space of exploding transients (Kasliwal, 2011). With absolute magnitudes ranging from -10 to -14 (between novae and SNe), they may be generally termed “gap transients.” A subset of them are sometimes named SN “impostors”; they have spectra similar to those of SNe IIn, but they are subluminous, typically $M_V \approx -11$ to -14 (Kochanek et al., 2012). Such events may be due to mass-loss episodes from LBVs, similar to the great eruption of η Car (Smith et al., 2011). After this initial eruption, the progenitor may be obscured by dust that forms after the initial eruption (Kochanek et al., 2012) however some objects such as SN 2002kg do not much produce dust (Kochanek et al. 2012; Humphreys et al. 2014, 2017). Other examples include SN 1997bs, SN 1999bw, SN 2000ch, SN 2001ac and SN 2002kg (Kochanek et al., 2012). These outbursts can sometimes occur just a few months before a full SN explosion — for example, SN 2006jc (an SN Ibn rather than an SN IIn; Pastorello et al., 2007; Smith et al., 2013), SN 2009ip (Foley et al., 2011; Mauerhan et al., 2013; Pastorello et al., 2013), and SN 2015bh (Boian & Groh, 2018; Thöne et al., 2017).

2.3 The progenitors of supernovae

The most direct way to determine the progenitor of a SN is via deep pre-explosion imaging that shows the progenitor star. To resolve underlying stellar populations (supergiant populations, not individual stars, can be detected at distances of up to 100 Mpc; Benvenuti et al., 1996) and to therefore recover a progenitor, facilities such as the *Hubble Space Telescope* (HST) or large ground based telescopes with adaptive optics are best suited to the task. Post-explosion imaging is then used to investigate whether the progenitor survived. Not all SN classes have such direct detections of progenitors so the determination of a possible progenitor, or constraining progenitor properties, is reliant on observations and theory. Furthermore, where there is pre-explosion imagery, it is sometimes unclear if the observed progenitor is a singular star or a cluster. Moreover, pre-explosion imagery may be in a limited set of filters, making the determination of where the progenitor may fall on the Hertzsprung-Russell diagram difficult. Therefore,

indirect methods of constraining SN progenitor properties are invaluable. I will now briefly discuss the possible progenitor systems of some SN classes.

2.3.1 Type IIP and type IIL supernovae

SNe IIP are the most common CCSN class, making up 70 per cent of all SN II (Li et al., 2011). SNe IIP have progenitors that have retained a large hydrogen layer. The recombination front propagating through the thick hydrogen layer in the ejecta creates the characteristic plateau in the light curve of a SN IIP. Red supergiants (RSGs) are SNe IIP progenitors with zero age masses $\approx 8-30 M_{\odot}$ and radii of a few hundred, to over $1000 R_{\odot}$ (Smartt et al., 2009; Arnett, 1980).

Theoretical predictions were consistent with observations, a number of SNe IIP have directly detected RSG progenitors. For example, SN 2003gd in NGC 628 (Hendry et al., 2005) was found to have a progenitor $\approx 8 M_{\odot}$ based on observations of the SN host in the months preceding the explosion with HST and the 8.1m Gemini North Telescope in Hawaii (Van Dyk et al., 2003). Another example of a SN IIP with a direct progenitor detection is SN 2013ej in NGC 628 (Fraser et al., 2013b). A source coincident with SN 2013ej was detected in pre-explosion HST imaging with the *F814W* filter. Fraser et al. suggest that the progenitor mass was $8-15.5 M_{\odot}$.

SNe IIL are less common compared to SNe IIP, accounting for $\sim 6\%$ of observed CCSNe (Smith et al., 2011). SNe IIL have a quicker photometric decline, indicating there was a smaller hydrogen envelope in the progenitor when compared to SNe IIP. This indicates that the progenitors of SNe IIL undergo more mass-loss preceding explosion than the progenitors of SNe IIP. However there is debate as to whether the progenitors of SNe IIL and SNe IIP are distinct or if there is a continuum of progenitors that produces the IIP or IIL phenomenon. The aforementioned SN 2013ej has been classified as both a SN IIP and SN IIL as it has a decline time shorter than is typical for SNe IIP (Fraser et al., 2013b; Utrobin & Chugai, 2017; Yuan et al., 2016; Mauerhan et al., 2017a). Anderson et al. (2014) analyse the *V*-band light-curves of 116 hydrogen rich SNe and found that the SNe IIP and SNe IIL in their sample were not clearly delineated from one another so the behaviour in these SN classes may be considered a continuum. Hiramatsu et al. (2021b) propose a transitional SN class between SNe IIP and SNe IIL, the SNe II short plateau based on the observations of three examples of such transients, SN 2006Y, SN 2006ai and SN 2016egz. Hiramatsu et al. suggest the progenitors of these transitional SNe are high mass RSGs with an initial mass of $\sim 18-22 M_{\odot}$. This proposed class of transitional SN between SNe IIP and SNe IIL is perhaps an indication that the distinction between the

two classes is getting weaker as more SNe are discovered. This may suggest a ‘continuum’ of mass loss in the SN progenitors.

Both SNe IIP and SNe IIL show signatures of CSM interaction at early times due to mass loss from their progenitors shortly prior to the SN explosion (Morozova et al., 2018). The amount, and distribution of CSM surrounding the progenitor star may differentiate SN IIP and SN IIL since the latter are more likely to be surrounded by a dense CSM (Morozova et al., 2017). Nagao et al. (2021) looked at spectropolarimetry data of SN 2013ej and SN 2017ahn with the assumption that both are SNe IIL. Those authors found that at early times, SN 2013ej was highly polarised, interpreted as aspherical interaction with CSM while SN 2017ahn had low polarisation, indicating an almost spherical explosion. Nagao et al. conclude that SNe IIL may have progenitors similar to SNe IIP in the case of SN 2013ej-like transients and a separate progenitor type for SN 2017ahn-like transients.

2.3.1.1 The progenitor of the type II-pec SN 1987A

The closest (~ 50 kpc Pietrzyński et al., 2019) SN in the modern, telescopic age was SN 1987A in the Large Magellanic Cloud (LMC) which also helped confirm the core-collapse scenario with the detection of neutrinos (White & Malin, 1987; Arnett et al., 1989). SN 1987A was unusual in that it was subluminal compared to similar SN classes such as SNe IIP, with a peak absolute magnitude of ~ -15.5 , and it was classified as a SN II-pec.

The progenitor of SN 1987A was SK-69-202 and was found in pre-explosion photographic plates shortly after the SN explosion (Walborn et al., 1989). Interestingly, the progenitor was found to be a blue supergiant rather than an RSG with a mass of $16-22 M_{\odot}$ (McCray, 2016). The compact progenitor of SN 1987A suggests the star underwent mass loss at some point prior to explosion and evolved to a blue supergiant from an RSG. Indeed, in 1989, the SN ejecta had started to shock a circumstellar ring of material that had been ejected from SK-69-202 20,000 years prior to the SN explosion (Crotts et al., 1989; Burrows et al., 1995; McCray, 2016; Kangas et al., 2022).

2.3.2 Stripped envelope supernovae

2.3.2.1 Type IIb supernovae

SNe IIb initially evolve similarly to regular SNe II but the hydrogen features quickly dissipate and helium features become prominent. In other words, a SN IIb initially looks like a SN II and then evolves to appear like a SN Ib. The progenitors of SNe IIb suffer from a greater degree of mass loss prior to explosion than the progenitors of SNe IIL.

One of the most extensively studied SN IIb is SN 1993J in M81 ([Ripero et al., 1993](#)). Early observations of SN 1993J found that this transient initially evolved as a SN II with hydrogen features but these features disappeared within around 90 days of the explosion with helium features starting to appear at this time. This behaviour confirmed this transient as a SN IIb ([Nomoto et al., 1993](#); [Filippenko et al., 1993](#); [Wheeler et al., 1993](#); [Woosley et al., 1994](#)). The evolution of SN 1993J was consistent with a progenitor with an initial mass of $\sim 13 - 16 M_{\odot}$ but the small hydrogen envelope may suggest mass loss due to a binary interaction with a bound companion. [Aldering et al. \(1994\)](#) investigates the progenitor of SN 1993J which was recovered in pre-explosion imaging. They report that the UBVRI photometry of the progenitor was inconsistent with spectral energy distributions of single stars. They find models of a red and blue star (or a red star with an OB association) fit the observations well. With this binary scenario, the authors suggest that an RSG may evolve towards the blue via mass stripping from a companion. [Maund et al. \(2004\)](#) present observations of the location of SN 1993J ten years post-explosion. [Maund et al.](#) report the discovery of the companion of SN 1993J to be a massive star (possibly a B spectral class star) that may end its life as a blue supergiant due to its binary interaction and explode as a SN 1987A-like SN.

2.3.2.2 Type Ib/c supernovae

SNe Ib/c (the general group of SNe Ib and Ic) progenitors suffer from even greater pre-explosion mass loss than the progenitors of SNe IIb as (generally) there is no hydrogen present in the spectra of these transients. However, similarly to the discussion in the previous sections, there may be a continuum of mass loss between the progenitors of SNe IIb and SNe Ib ([Branch et al., 2002](#); [Elmhamdi et al., 2006](#); [Gilkis & Arcavi, 2022](#)).

The expected progenitors of SNe Ib/c may be: Wolf Rayet (WR) stars, massive stars that have lost their hydrogen layer ([Crowther, 2007](#); [Dessart et al., 2012](#)); stars that have had their hydrogen atmospheres stripped through binary interactions ([Podsiadlowski](#)

et al., 1992), or stars that evolved in a binary but the SN explosion of a one of the stars blows the atmosphere off the other (Hirai et al., 2020).

There are a small number of SNe Ib/c with recently identified possible progenitor stars or systems. The first of these was iPTF 13bvn in NGC 5806 and initially, it was thought this transient had a WR progenitor (Cao et al., 2013a). Further observations, however, suggest a helium giant star in an interacting binary system, based on spectral energy density fitting (Eldridge et al., 2014). SN 2019yvr in NGC 4666 had a progenitor detection in pre-explosion imaging taken 2.6 yr prior to the SN explosion. This progenitor was found to have an initial mass $9.1 - 11.9 M_{\odot}$ and spectral energy density fitting of the pre-explosion imaging may indicate a yellow hypergiant (YHG) progenitor (Kilpatrick et al., 2021; Sun et al., 2022). SN 2017ein in NGC 3938 is the first SNe Ic with a possible progenitor detection in pre-explosion HST imaging (Kilpatrick et al., 2021). Kilpatrick et al. report the progenitor may have been a single WR-like star of mass $\sim 55 M_{\odot}$ but the photometry better fits a model with a close, interacting binary system where an $80 M_{\odot}$ progenitor is stripped by a $48 M_{\odot}$ companion. Late time imaging of the SNe Ib/c, SN 2013ge may have revealed a companion to the progenitor of SN 2013ge which was consistent with a B supergiant star; this is the first possible detection of a progenitor companion in post-explosion imaging (Fox et al., 2022).

Some SNe Ib have been observed to interact with hydrogen-rich CSM at later times indicating that the progenitors undergo enhanced mass-loss pre-explosion. This interaction would result in the spectra resembling that of a SNe IIn (e.g. SN 2014C; Milisavljevic et al. 2015, and SN 2019yvr; Sun et al. 2022).

2.3.3 Type IIn supernovae

The CSM interaction characteristic of SNe IIn requires that the progenitors suffer considerable mass loss prior to the SN explosion. Proposed progenitors of SNe IIn are luminous blue variables (LBVs), evolved stars that undergo violent episodic mass loss and may in some cases represent an evolutionary phase between an O-type star and a WR (Humphreys & Davidson, 1994; Weis & Bomans, 2020). Using light-curve modelling analysis on the bolometric light-curves of a sample of eleven SNe IIn, Moriya et al. (2014) found that the mass loss rate of many SNe IIn progenitors is above $10^{-3} M_{\odot} \text{ yr}^{-1}$. Mass loss may also come from more violent episodes (Ofek et al., 2014). Some SNe IIn undergo significant mass loss episodes in the years preceding the SN explosion. SN2009ip for example was initially a SN impostor at its 2009 eruption and then in 2012 it ended its life as a (possible) SNe IIn after a period of eruptive mass loss from a possible luminous blue

variable progenitor (Ofek et al., 2014; Pastorello et al., 2017). This mode of mass-loss is also observed in SN2015bh (Boian & Groh, 2018), SN2016bdu (Pastorello et al., 2017) and SN2018cnf (Pastorello et al., 2019b). One example of a Galactic LBV that may end its life as a SN II_n is η Carinae (see Fig. 2.4), surrounded by the Homunculus nebula with its lobes and equatorial bands (Smith et al., 2003; Smith, 2006; Akashi & Kashi, 2020; Millour et al., 2020; Kurfürst et al., 2020).

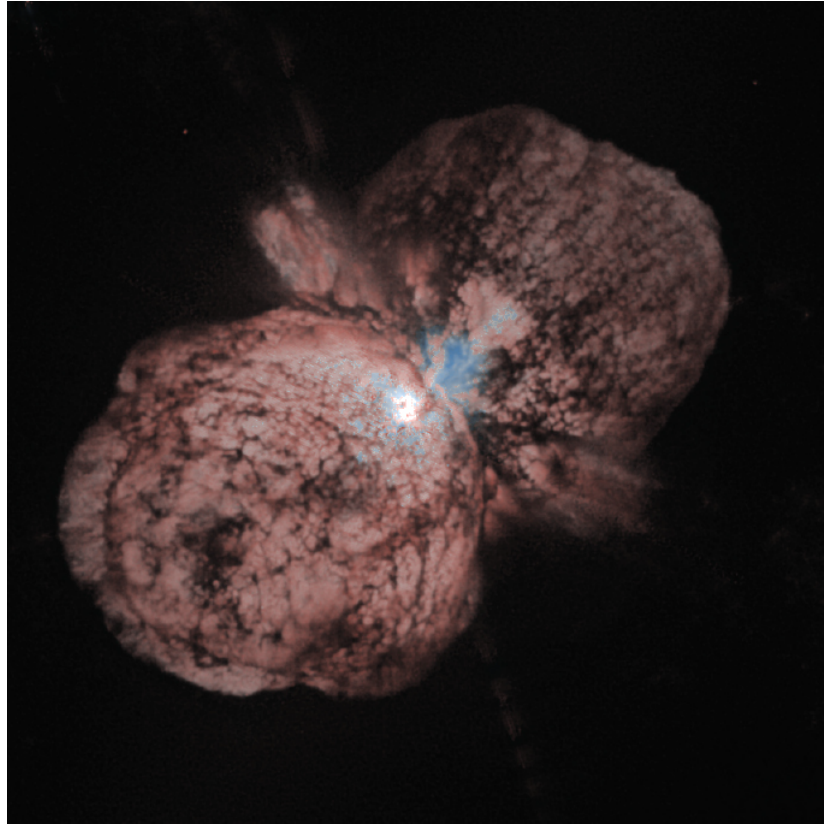


FIGURE 2.4: A HST image of η Carinae and the aspherical CSM that makes up the Homunculus nebula. Image: Jon Morse (University of Colorado) NASA Hubble Space Telescope.

There has been one solid progenitor detection for SNe II_n. SN 2005gl in NGC 266 was discovered on 2005 Oct 05 by Puckett et al. (2005a) and the classification spectrum was taken by Blanc et al. (2005b) that identified SN 2005gl as a SN II_n. Gal-Yam et al. (2007) used archival HST imaging of NGC 266 taken in 1997 as part of a campaign studying active galactic nuclei. Gal-Yam et al. found that there is a source at the location of SN 2005gl in the $F547M$ filter with $M_V \sim -10.3$. They suggest that if the recovered progenitor was a single star, then it would most likely be an LBV (the first suggestion of LBVs as direct SN progenitors was by Kotak & Vink, 2006). Gal-Yam & Leonard (2009) found that the progenitor, NGC 266_LBV 1, may have been a very massive LBV with a mass in excess of $50 M_{\odot}$. As mentioned previously, some SNe II_n have precursor

events that can give clues to the possible nature of the progenitor. SN 2009ip had two precursor eruptions before the final 2012 explosion that was possibly a terminal SN explosion. [Smith et al. \(2014\)](#) suggest that the final 2012 eruption of SN 2009ip had a blue supergiant progenitor that then interacted with the dense CSM from the previous mass loss eruptions.

The progenitor paths of SNe IIn are unclear and the progenitors of SNe IIn do not seem to be solely massive blue stars. For example, environmental analysis has shown that where SNe IIn are found in their hosts is inconsistent with all the progenitors being high mass LBVs ([Haberman et al., 2014](#)).

In this thesis, I will concentrate on constraining the progenitor properties of SNe IIn based on environmental analysis.

2.4 Studies of the environments of transients

Properties of SNe can be constrained via the study of their host environment. These observations involve data taken either before the SN explosion or after the SN has faded to quiescent levels such that the environmental data is not contaminated by the SN flux.

The earliest note of the environments of SNe come from [Baade & Zwicky \(1934\)](#) where it was recognised that SNe occur in both the centres and the spiral arms of galaxies. Early specific environmental studies uncovered the difference between SNe I (SNe Ia but this distinction was not made at the time) and SNe II in that SNe I tend to occur in elliptical galaxies (however SNe Ia are now known to also occur in spiral hosts) while SNe II tend to occur in star forming spiral galaxies ([Reaves, 1953](#)). Later studies discovered that SNe II were concentrated around spiral arms, indicating SNe II are associated with star formation ([Maza & van den Bergh, 1976](#)). Furthermore, SNe are observed in irregular and dwarf hosts (e.g. SN 2008ha in UGC 12682; [Foley et al. 2009](#), and dwarf galaxies have been discovered using SNe; [Park et al. 2019](#); [Sedgwick et al. 2019](#)) as well as in intergalactic regions ([Filipović et al., 2022](#)).

Unresolved stellar populations in the environment around a SN position within its host galaxy can also be correlated to SNe in order to constrain the progenitor properties. One method of associating SNe to a stellar population is to measure the distance between a SN and its closest H II region. Early studies investigating the association of SNe to nearby H II regions did not find any difference in association to the H II regions between the SN classes considered (SN II and SN Ib/c, e.g. [van Dyk, 1992](#); [Bartunov et al., 1994](#)).

However later studies show that SN Ib/c are more centrally concentrated in their hosts ([van den Bergh, 1997](#); [Wang et al., 1997](#)) which is interpreted as a metallicity effect due to a metallicity gradient in the host galaxy ([Henry & Worthey, 1999](#)).

More recent studies have utilised a number of techniques to study the environments of SNe which I summarise below.

- 1. Star formation tracers and pixel statistics:** The pixel statistics technique, normalised cumulative ranking (NCR) was developed by [James & Anderson \(2006\)](#). This method uses the cumulative sum of the pixel values in an image, normalised by the cumulative total to associate a pixel with whatever emission is being investigated. This technique directly associates the pixel containing the SN with emission, unlike earlier methods of associating SNe locations to H α emission where the distance to the nearest H II is used ([van den Bergh, 1997](#)). This method has been used with H α emission in order to associate the SNe with regions of ongoing star formation that is traced by H α emission ([Anderson & James, 2008](#); [Habergham et al., 2014](#)). [Kangas et al. \(2017\)](#) used NCR in order to determine the association of SN progenitor stars (e.g. RSGs and LBVs) with H α emission in the LMC and M33. [Hosseinzadeh et al. \(2019\)](#) investigated the UV association of the SN Ibn, PS1-12sk using deep observations from HST. Those authors did not detect UV emission within 1 kpc of PS1-12sk and conclude that this may suggest that not all SNe Ibn have massive progenitors.
- 2. Radial analysis:** The radial distribution of SNe in a host galaxy is a proxy for metallicity where the centres of galaxies are generally older and have higher in metallicity than further out in the disc ([Henry & Worthey, 1999](#)). This method was used to show SNe Ic were more centrally located than SNe Ib in undisturbed galaxies ([Habergham et al., 2012](#)).
- 3. Local metallicities:** Rather than using a proxy for metallicity like above, local metallicities can be directly measured. Local metallicities are calculated using line ratio diagnostics such as the O3 N2 method of [Pettini & Pagel \(2004\)](#). This method has been used by [Habergham et al. \(2014\)](#) where it was found that SNe IIn have environments with higher metallicity than that of SNe IIP and that SN impostors resided in regions of lower metallicity than the SN classes in the study (see also [Prieto et al., 2008](#); [Taddia et al., 2015](#)). [Lunnan et al. \(2014\)](#) present a study of 31 SLSNe-I from the Pan-STARRS survey. Those authors found that the host metallicities of these hydrogen poor SLSNe were similar to the host metallicities

of Long Gamma Ray Bursts and find that lower metallicity environments form more SLSNe-I (see also [Perley et al., 2016](#)).

4. **Integrated field unit observations:** The age of a particular stellar population (e.g. an H II region) can be studied using multi object spectroscopy, or integrated field units (IFUs). For example, [Galbany et al. \(2018\)](#) studied 232 host galaxies of 272 SNe, looking at the characteristic ages of the underlying stellar populations. [Galbany et al.](#) found that SNe II_n had two populations, one in an old stellar population and the other in a young stellar population. [Galbany et al. \(2016\)](#) used IFU data of 115 SNe from the CALIFA survey and found that the metallicity of the local SN environment is in a sequence depending on the SN class. Starting from lowest metallicity to highest, this sequence is SN Ia → SN Ic → SN II. The utility of these IFU studies on single objects is shown by [Izzo et al. \(2018\)](#). Those authors found that the environment of SN 2017egm (a SLSN-I) was not in the standard host for SLSNe-I (dwarf galaxies with bursty star formation). However, the environment of this SN within its spiral host held a young stellar population and the bursty star formation may have been prompted by interactions with a companion galaxy.
5. **Spectral energy distribution fitting:** Spectral energy distribution (SED) fitting can be used in order to measure parameters such as the star formation rate and stellar mass of SN host galaxies (e.g. [Taggart & Perley, 2021](#); [Schulze et al., 2021](#)). [Schulze et al. \(2021\)](#) present a study of 888 SNe from PTF and found that the SNe Ib/c in their sample were in hosts with a higher star formation rate. [Taggart & Perley \(2021\)](#) constructed SED models for 150 nearby CCSNe from the All-Sky Automatic Search for Supernovae and found that SLSNe occurred more often compared to CCSNe in lower mass galaxies with high (specific) star formation rates (see also [Angus et al., 2016](#)).

I will implement and discuss some of the environmental analysis methods described above in this thesis in order to attempt to constrain progenitor systems.

Chapter 3

Creating a spectral classification scheme for type IIIn supernovae

3.1 The spectra of type IIIn supernovae

As discussed in Chapter 2, SNe IIIn are characterised by the narrow features superimposed on broader hydrogen Balmer line profiles and the general lack of broad P-Cygni features.

The formation of the narrow hydrogen Balmer features is due to the SN ejecta shocking a pre-existing, cold, slow, and dense circumstellar medium (CSM). Emission from the initial interaction then ionises the surrounding unshocked CSM resulting in an $H\alpha$ excess (Chugai, 1991; Chugai & Danziger, 1994). The broad components of the lines originate from the expansion of the fast-moving SN ejecta. The interaction of the SN ejecta with a clumpy, dense wind may contribute to the formation of the intermediate width components (Chugai & Danziger, 1994). There may also be broadening via the scattering of a photon from a thermal electron or from the dense, shocked shell (Chugai, 2001; Dessart et al., 2009; Humphreys et al., 2012; Huang & Chevalier, 2018; Kiewe et al., 2012). These features can constitute the classic SN IIIn $H\alpha$ profile shape, reminiscent of the Eiffel Tower, shown in Fig. 3.1 where the example model $H\alpha$ profile shown is constructed from three Gaussian components (with illustrative FWHM ≈ 200 , 1100, and 2700 km s^{-1}).

The CSM has number of possible origins. Mass-loss is required in SN IIIn progenitors to build up the CSM required for the SN IIIn phenomenon and the progenitors may suffer from episodic mass loss preceding the terminal SN explosion (Smith, 2014). Using light-curve modelling analysis on the bolometric light curves of a sample of SNe IIIn,

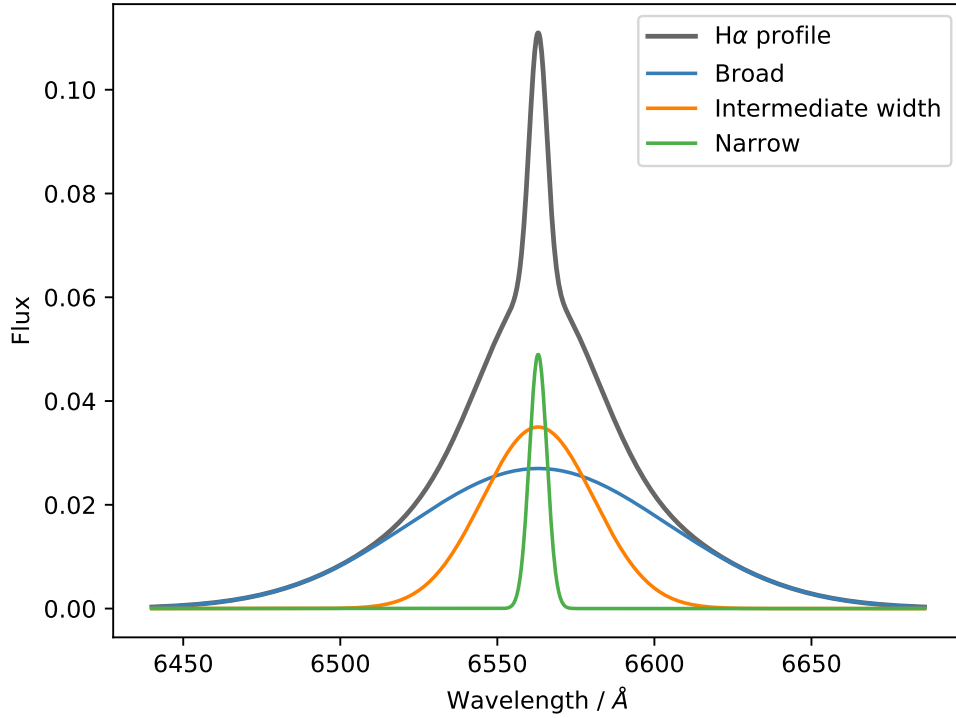


FIGURE 3.1: An example SN IIIn $H\alpha$ profile with the narrow, intermediate-width, and broad components shown. This is an example of the classic SN IIIn “Eiffel Tower” shape which is the product of three model Gaussian components.

Moriya et al. (2014) found that the required mass-loss rate of many SN IIIn progenitors exceeds $10^{-3} M_{\odot} \text{ yr}^{-1}$. Some SNe IIIn suffer significant precursor mass-loss events in the years preceding the SN explosion (Ofek et al., 2014). SN 2009ip was initially recognised as a SN impostor, at its 2009 eruption, and then in 2012 it evolved into a probable SN IIIn (but see also Fraser et al., 2013a) following its terminal explosion or a period of eruptive mass loss from its luminous blue variable (LBV) progenitor (Mauerhan et al., 2013; Ofek et al., 2014; Pastorello et al., 2017). Other examples of this mode of mass-loss include SN 2015bh (Boian & Groh, 2018), SN 2016bdu (Pastorello et al., 2017), and SN 2018cnf (Pastorello et al., 2019b).

There is great diversity in the spectra of SNe IIIn. Generally speaking, one may expect to see lines of O I, He I, Ca II, and Fe II along with H I emission. However, the common defining traits are the multicomponent $H\alpha$ lines with the signature narrow features shown in Fig. 3.1, and a blue continuum. However, even these $H\alpha$ profiles can be diverse in strength, duration, and shape. Some SNe IIIn exhibit their narrow features and multicomponent $H\alpha$ (and other Balmer line) profiles throughout their evolution. Other

transients classified as SNe II_n seem to show narrow features only in the early stages of their evolution, with these features lasting just a few days or even hours (i.e. flash ionisation SNe). Other SNe II_n may show longer term (longer than the flash ionisation timescale but shorter than most other SNe II_n) or late time CSM interaction. Ofek et al. (2014) term such transients with short-lived SN II_n phases as “weak” SNe II_n, with an example being PTF11iqb (Smith et al., 2015). These “weak” SNe II_n may suggest that lower-mass SN progenitors experience the mass loss required for the CSM interaction as seen in some SNe IIP and SNe IIL (for example, ASASSN-15oz, Bostroem et al., 2019; SN 2013fs and SN 2013fr, Bullivant et al., 2018). While SNe II_n do not typically show the broad P Cygni features one observes in other SNe II, there are sometimes narrow P Cygni absorption associated with the narrow H α features. Moreover, asymmetry in both the SN ejecta and the surrounding CSM can profoundly affect the shape of the H α profile. In some cases one may see asymmetric redshifted or blueshifted components in the H α profiles (for example, there may be blueshifted wings in the later epochs of the spectra of SN 2008J; see Fig. 3.5). One interpretation is a SN II_n within an aspherical and/or clumpy CSM. In the case of a SN II_n having an LBV progenitor, it can easily be inferred how this asymmetry and complex structure (e.g., SN 1998S Mauerhan & Smith, 2012; Shivvers et al., 2015) can arise by observing the Homunculus nebula around the LBV η Carinae with its asymmetric lobes (Smith et al., 2003; Smith, 2006; Akashi & Kashi, 2020; Millour et al., 2020; Kurfürst et al., 2020). When one considers the viewing angle to the observer, it is clear that CSM geometry is important to these observations as the results of this asymmetry are a deviation from the classic SN II_n H α profile shape.

Given that there is such a variety in the progenitor paths and possible origins of the CSM, it may be expected that the spectra of SNe II_n are quite varied. SNe II_n are as a whole, heterogeneous and pinning down a classification can be challenging. With this complication in mind, in this chapter, I set out a systematic classification system based on common SN II_n spectral features, the complex hydrogen Balmer profiles (with a concentration on the H α profiles) combined with meta-data such as if there has been a post-explosion detection of a progenitor that indicates the transient is a SN impostor. I set out the motivation for this reclassification in Section 3.2. I describe the sources of these data in Section 3.3.1 — Section 3.4. In Section 3.5 I will describe the classification scheme itself. My results are outlined in Section 3.6 where I present tables of the spectral reclassifications. I will compare my classifications with those of online databases in Section 3.6.4 and to the classifications from SNID in Section 3.6. I will discuss my results and their implications in Section 3.7 and summarise my conclusions in Section 3.8.

3.2 The motivation for a spectral reclassification

It became apparent that it was necessary to systematically reclassify SNe IIn when constructing the SN IIn sample for this thesis. Online databases held numerous classifications for each object and some primary classifications were incorrect.

With the great diversity of SNe IIn in mind, it is worth noting that spectral classification software packages such as SuperNova IDentification (SNID; [Blondin & Tonry, 2007](#)) use template libraries for SN spectral classification. The SNID SN IIn template selection is limited to three objects: SN 1996L, SN 1997cy, and SN 1998S. Furthermore, SNID has templates over a number of epochs; however, some objects can be classified as a SN IIn at a particular epoch when it may be a SN impostor or a SN Ia-CSM (a SN Ia exploding in a dense CSM), or vice versa. This issue may be worsened if the target only has a single spectrum available.

Spectral contamination from the interstellar medium (ISM) or the underlying H II region can hamper classification efforts if the data reduction did not remove the ISM signal sufficiently. As there is a strong and narrow H α emission feature in the ISM and H II regions, it can often appear that the narrow features superimposed on the broader components may be the H α feature seen in SNe IIn due to CSM interaction. This is challenging to distinguish from the SN spectra if the spectrum has low resolution and the nearby [N II] lines that lie to the blue and red side of the H α line are blended together with the H α emission. Online databases may retain the SN IIn classification for some of these objects that have no strong evidence of CSM interaction.

The literature holds various studies with differing methods of classifying SNe IIn. [Ofek et al. \(2014\)](#) call SNe IIn with CSM interaction for a short period of time (e.g. PTF 11iqb) “weak” SNe IIn. Typically, a “classic” SN IIn will have enduring CSM interaction features which may last years post-explosion. There are sub-categories of SNe IIn that have been described such as SN IIn-P and IIn-L, and SN IId where the narrow H α line has a (also narrow) P Cygni profile, with an example being SN 2013gc ([Benetti, 2000](#); [Reguitti et al., 2019](#)). Furthermore, at later epochs an object may evolve out of a SN IIn classification and be subsequently reclassified (for example, as a standard SN II such as SN 2001fa). Online resources register the object with the new classification despite the previous evidence of CSM interaction and therefore previous evidence of the transient being a SN IIn. The SN IIn subclass was coined by [Schlegel \(1990\)](#). There are pre-1990 SNe that have subsequently been identified as possible SNe IIn (for example, SN 1978K, SN 1987C, and SN 1989R). However, public databases may retain the original classification, so when

one searches for SNe IIn, the pre-1990 SNe may be omitted.

3.3 The initial sample

In order to construct the initial sample of SNe IIn, I use online databases. I use the Open Supernova Catalogue (OSC) described in Section 3.3.1 to find transients that have had a SN IIn classification at some point. When this filter is applied, I also set a redshift (upper) limit of 0.02 as this is the limit used in the environmental analysis in Chapter 4. The initial sample (before any spectral data was collected) comprised 144 objects that had held a SN IIn classification at some point on the online databases. The cutoff for this sample was January 2019.

3.3.1 The Open Supernova Catalogue

The OSC¹ is an online database of SNe and SN candidates and associated transients such as LBVs (Guillochon et al., 2017). OSC aggregates transient data from a variety of sources such as literature SN discoveries and other online databases.

Various filters can be applied to find transients. Each SN has an individual page that contains its meta-data including spectra, light curves, host galaxy information, references (discovery telegrams, papers on the object etc) and also spectral classifications. The spectral classifications section includes the current and previous classifications, including the relevant reference for each classification. Fig. 3.3.1 shows the data displayed on an OSC page (in this example is for SN 2009ip where there is a good amount of data). Fig. 3.3 shows the claimed classification section of the page for SN 2009ip. The photometric and spectroscopic data (and radio/X-ray data when available) can be downloaded as either a .csv or JSON file. OSC was the main source of spectral data for this reclassification work. The spectral data is reduced but assumed not to be flux calibrated. On 8th March 2022, the OSC became irreparably corrupted and is no longer operating online. However the open source material, along with the OSC database can be accessed on GitHub².

¹<https://sne.space/>

²<https://github.com/astrocatalogs>

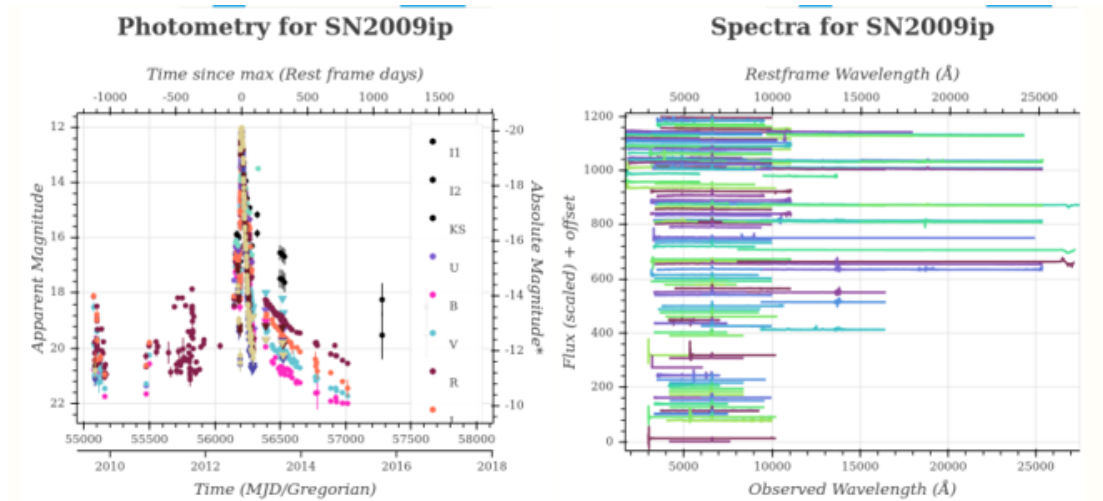


FIGURE 3.2: An example transient data displayed on the OSC. In this example, the transient is SN 2009ip, a very well studied object so the spectroscopic and photometric data fields are well populated.

Claimed Type	IIn ^{1,6,21}
	LBV to IIn ²
	LBV ^{17,18}
	IIn? ²³

FIGURE 3.3: An example claimed classification section for SN 2009ip. Note that all previous classifications are included with references.

3.3.2 The Transient Name Server

The Transient Name Server (TNS³) the other public data source I used for spectral data and is the official International Astronomical Union transient reporting database. Unlike the OSC, TNS is a repository for transient events in general and the astronomical community adds to the database rather than an aggregate site collecting data from many sources. Similarly to OSC, the TNS displays the available spectra and light curves as well as some meta data such as the discovery details and classification reports. Due to astronomers needing to submit data/classifications to TNS, it may lack data for transients that occurred before TNS went online.

³<https://www.wis-tns.org/>

3.4 Collecting the spectral data

The spectra available on OSC and TNS were downloaded in their csv format. The primary spectral classification of each SN on both databases was also noted. A literature search aimed to find the remaining data for SNe that had no publicly available data on these databases. When the data was located, either on some other, non-public database, paper or discovery/classification report, I contacted the original observers/classifiers for data.

After this literature search, spectral data for 115 of the original 144 were recovered. These data can now be used for the reclassification of SNe IIn.

3.5 Making a robust classification scheme

I present the spectra collected from archival sources in Section 3.6. Where available, these are ordered in a time-series plot using `pyplot` (v3.3.3; [Hunter, 2007](#)) and placed into their rest frame using redshifts from the OSC entries.

As the main defining features of SNe IIn spectra are the multicomponent Balmer emission lines, I focus on the strongest line, $H\alpha$. The Python package `pyspeckit` (v0.1.22 [Ginsburg & Mirocha, 2011](#)) is used for the fitting of Gaussian profiles to a multicomponent $H\alpha$ profile, with the coordinates shifted to velocity space in the rest frame of the host (and the flux being in arbitrary units).

I start the $H\alpha$ profile fitting by fitting a baseline to the continuum. Fitting is restricted to the region around $H\alpha$ (6400 Å–6800 Å). I use the `specfit` package in `pyspeckit` to fit Gaussian profiles to each spectrum. FWHM guesses for fits for the relatively narrow ($<1000 \text{ km s}^{-1}$), intermediate ($\sim 1000\text{--}2000 \text{ km s}^{-1}$), and broad ($>5000 \text{ km s}^{-1}$) components are trialled. A reduced χ^2 (calculated, along with uncertainties in the parameters of the fit, by `specfit`) test is used to determine the goodness of fit, which informs whether a two- or three-component fit is most appropriate by favouring the number of components with the lowest reduced χ^2 value. Errors are propagated in the Gaussian component parameters to calculate the total fit uncertainty. Erroneous “IIn” classifications that are present in the literature arise from the background H II region of the host, contaminating the spectrum, presenting the illusion of narrow lines upon a broad feature that originates from the SN itself. To disentangle these features, I fit for the nebular [N II] (6584 Å and 6548 Å) doublet either side of the narrow $H\alpha$ to determine whether any narrow features seen can simply be attributed to H II region pollution rather

than to CSM interaction. As mentioned in Section 3.7.5, the 6584 Å line is stronger than the the 6548 Å line and therefore makes an asymmetric profile when the resolution is low enough such that the [N II] lines appear to blend with the H α line. The flux ratio of the two nitrogen lines is ~ 2.96 (Osterbrock & Ferland, 2006) and should remain constant throughout the evolution of the spectrum in the case of H II region contamination.

I also include possible flash-spectroscopy SNe in this analysis. Flash-spectroscopy SNe show narrow (often unresolved) lines from CSM ionisation for a brief period post explosion (<10 days) before the SN ejecta sweep up the CSM and the broad lines dominate the Balmer line profiles (Khazov et al., 2016). There are a number of SNe IIn that show this brief CSM interaction with examples including SN 1998S (Leonard et al., 2000; Shivvers et al., 2015) and PTF 11iqb (Smith et al., 2015). In these cases CSM interaction reappeared at later spectral epochs, so these flash-ionisation events cannot be eliminated from my reclassification efforts. However, if a spectrum evolves as a standard SN II at later spectral epochs, then I do not classify it as a possible SN IIn.

The SN Ia-CSM subtype is included as part of the SN IIn class. This subtype is included as the CSM interaction features that are characteristic of the SN IIn phenomenon are present in SNe Ia-CSM. While they are not CCSNe, SNe Ia-CSM may be difficult to disentangle from the core-collapse SNe IIn as the SN Ia-like features may be hidden behind the CSM interaction. Some SNe IIn are recognised as possibly having a thermonuclear origin long after discovery so possible unknown SNe Ia-CSM ‘contamination’ can not be ruled out in the sample. Furthermore, the inclusion of SNe Ia-CSM is consistent with previous studies (e.g. Habbergham et al., 2014).

The FWHM of each Gaussian component allows the estimation of the velocities of the narrow component from the CSM interaction and the broader components from electron scattering and the SN ejecta/interaction with a clumpy wind. In order for a transient to be awarded a SN IIn classification, the H α profile must contain at least a narrow component and either an intermediate-width or broad component. Some transients will have all three, a narrow, intermediate, and broad components. The FWHM of the Gaussian components is given by $2\sqrt{2\ln 2}\sigma$, where σ is the standard deviation of the Gaussian profile. The spectral resolution of the spectrum used in the classification of SNe IIn should have high enough spectral resolution such that the H α and [N II] lines are not blended together as this would hinder a clear classification.

The spectra of SN impostors can be very similar to those of SNe IIn. I make a peak magnitude cut (impostors typically have a peak $\gtrsim -14$ mag and this is the limit I use as a cut) and search the literature to see if there is a surviving progenitor or the object is

otherwise a gap transient rather than a fully-fledged SN. It should, however, be noted that a small number of SN impostors may exceed this limit, for example, the (possible) SN impostor, SN 1961V, peaked at an absolute magnitude ~ -18 however whether this transient was a SN impostor or a bona fide SN is debated (Filippenko et al., 1995; Kochanek, 2011; Van Dyk & Matheson, 2012; Patton et al., 2019; Woosley & Smith, 2022). Furthermore, the $H\alpha$ profiles of active galactic nuclei (AGNs) are similar to those of SNe IIn with broad lines from the AGN and narrow galaxy lines (Filippenko, 1989; Osterbrock & Ferland, 2006). Potential AGNs can be ruled out of the sample by regarding the proximity of the transient to the nucleus of the host; Ward et al. (2021) find that very few AGNs are offset significantly from the nucleus. If a SN is central, we can look for the nebular [O III] $\lambda\lambda 4959, 5007$ lines which are found in AGNs; if absent, the object is likely a true SN rather than an AGN. I also check the literature for any AGN identification or if the transient appeared in a paper as a SN. The decision tree for the SNe IIn classification scheme is shown in Fig. 3.4.

The now systematically reclassified spectra can be distributed into three categories as follows.

Gold sample: SNe IIn that maintain their relatively narrow components throughout their evolution. Gold SNe IIn must have multiple spectral epochs that span more than ~ 10 days, which rules out flash-spectroscopy SNe as it is longer than the characteristic timescale of flash-spectroscopy SNe. Gold SNe IIn may have the classic ‘‘Eiffel Tower’’ $H\alpha$ profile or a more complex structure. Gold SNe IIn may be assigned a further sub-category such as SN 1988Z-like or SN 1998S-like. Gold SNe IIn are surrounded by dense CSM for there to be sufficient material to maintain ongoing interaction in order to exhibit the narrow features throughout their spectral evolution.

Silver sample: Silver SNe IIn exhibit spectra with some unambiguous narrow $H\alpha$ features that are consistent with CSM interaction. This interaction may not be long-lived compared to gold-sample objects, and may be a feature in a younger transient that has not been monitored spectroscopically. Silver SNe IIn may not exhibit the narrow interaction features throughout their evolution. An example of a silver SNe IIn that doesn’t show prolonged CSM interaction is PTF11iqb. Smith et al. (2015) remark that PTF11iqb is an SNe IIn that transitions into an SNe IIP (an SNe IIn-P) and may have had a RSG progenitor similar to those of ‘‘normal’’ SNe IIP. PTF11iqb shows renewed CSM interaction at later times that Smith et al. (2015) interpret to be the CSM disc re-emerging as the SN photosphere recedes. I classify transients with a single spectrum available to us as silver SNe IIn owing to the lack of information regarding the spectral

evolution. A silver SN IIn can be promoted to gold with more data. Many of the silver SNe IIn in the sample are in this category owing to there being only a single spectrum on public databases. Possible flash-spectroscopy SNe with a single spectrum are counted as silver SNe IIn as there is not enough information to rule them out. Silver category objects can be demoted to not being an SN IIn if the evolution of the CSM interaction shows that it fades away and the spectrum resembles a “standard” SN II.

Not a SN IIn: The spectral data do not show a SN IIn. The spectrum may be of low quality and noisy, thus unusable for classification. Some of the spectral data do not appear to show a SN spectrum at all, or lack any SN IIn features. For example, the spectrum may be contaminated by narrow lines from the underlying H II region and the narrow H α feature may be misinterpreted as CSM interaction signatures. In the case of contamination from the host H II region, there may be a narrow H α profile with no other structure with [N II] either side of the H α line, there may also be [S II] lines redward of the H α line.

To highlight the ambiguities in SN IIn classification I compare the classifications stated in TNS and OSC to my own reclassifications and also to the results of the template-matching software, SuperNova IDentification (SNID). I do not utilise SNID to aid in the reclassification of SN IIn candidates, I just compare my reclassifications to the SNID outputs. SNID calculates a parameter, *rlap*, which gives a goodness of fit to the template spectra (a full description is given by [Blondin & Tonry, 2007](#)). The higher the *rlap* value, the better the match. SNID has an *rlap* critical limit of 5, where a template match with an *rlap* value < 5 is a poor match. SNID matches the spectrum to a template spectrum, not to the underlying event so other factors may overturn a SNID classification.

3.5.1 Our classification algorithm

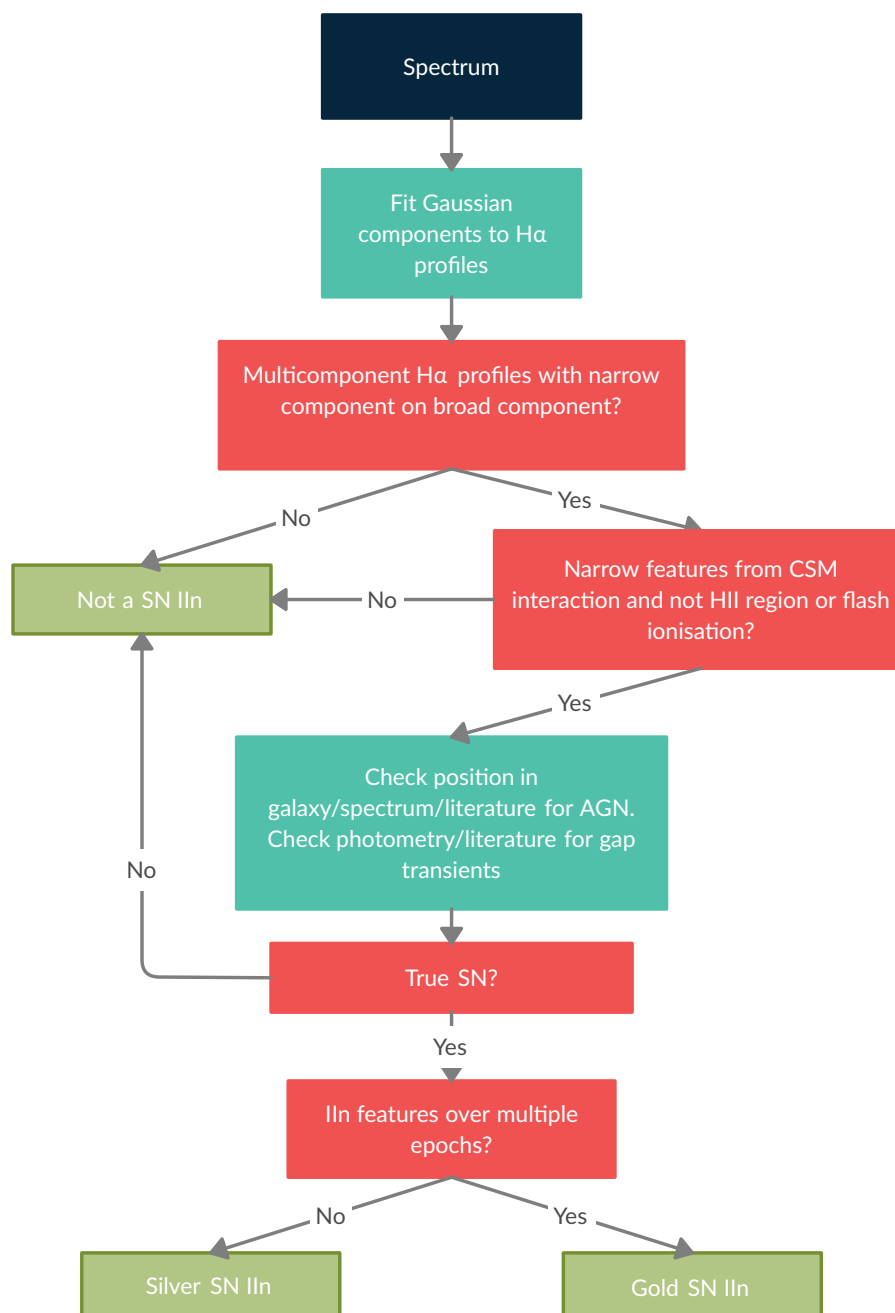


FIGURE 3.4: A decision tree describing my spectral/meta-data classification scheme for SNe IIn.

3.6 Our reclassifications

From the initial sample, I was able to obtain spectral data for 115 SNe IIn candidates.

3.6.1 The gold sample

From the sample of 115 SNe IIn candidates with available spectral data, I classify 37 as “gold.” These gold SNe IIn exhibit unambiguous CSM interaction signatures throughout their spectral evolution, spanning numerous spectral epochs.

One such gold SN IIn is SN 2008J in MCG -02-7-33, discovered on 2008 Jan. 15 (UT date) with the 0.76 m Katzman Automatic Imaging Telescope (KAIT) during the Lick Observatory Supernova Search (LOSS; Filippenko et al., 2001b) at a clear-filter magnitude of 15.4 (Thrasher et al., 2008). Using the Spitzer Space Telescope, Fox et al. (2010) detected late-time near-IR emission at $3.6 \mu\text{m}$ and $4.5 \mu\text{m}$, which they interpret as emission from warm dust. Fox et al. (2013) did not find late-time CSM interaction in optical spectra obtained with the LRIS and DEIMOS instruments on the Keck 10 m telescopes so SN 2008J is not a long-lasting SN IIn.

Taddia et al. (2012) present evidence that SN 2008J may be a reddened thermonuclear SN IIn (thus, a SN Ia-CSM) with $A_V \approx 1.9$ mag. They find that the near-IR light curves and optical spectra of SN 2008J are similar to those of the thermonuclear SN IIn (or SNe Ia-CSM) SN 2002ic (Hamuy et al., 2003) and SN 2005gj (Prieto et al., 2005). Early-time high-resolution spectra show Na I D $\lambda 5891$ absorption features and blueshifted Si II $\lambda 6355$ absorption.

There are twelve epochs of spectral data for SN 2008J shown in Fig. 3.5. These data cover 311 days throughout which the $H\alpha$ profile retains strong CSM interaction signatures. The first four spectra show Na I D and some Si II absorption (Taddia et al., 2012) and later spectra become noisy. All epochs are fairly featureless or noisy apart from the Balmer lines and the Na I D absorption. Fig. 3.6 displays the $H\alpha$ profile for the first epoch of SN 2008J. I obtain a good fit to the data from a pair of Gaussian profiles. The broader component has a FWHM of $\sim 2200 \text{ km s}^{-1}$ and the narrow component has FWHM $\approx 400 \text{ km s}^{-1}$. The profile has the classic “Eiffel Tower” shape. SNID classifies SN 2008J as a SN IIn. As previously mentioned, I include SNe Ia-CSM as SNe IIn due to the SN IIn phenomenon being an environmental effect rather than necessarily being intrinsic to the progenitor.

The second example of a gold-class SN IIn is SN 2009ip in NGC 7259, which was discovered on 2009 Aug. 26 at mag 17.9 by Maza et al. (2009) using the 0.41 m PROMPT-3 telescope at Cerro Tololo Inter-American Observatory. SN 2009ip is notable for being recognised as a SN “impostor” with a peak of about -13.7 mag (Berger et al., 2009b; Smith et al., 2010). Following this initial eruptive phase there were phases of rebrightening before a final eruption in 2012 which has been interpreted as a genuine SN IIn (e.g., Mauerhan & Smith, 2012; Prieto et al., 2012; Pastorello et al., 2013; Margutti et al., 2014; Ofek et al., 2014; Smith, 2014) with a peak around -18.3 mag. However, scenarios where the 2012 eruption was nonterminal are discussed in Section 3.7.2.

During the eruptions in the initial “impostor” phase, it was reported that SN 2009ip may be the result of LBV outbursts (Miller et al., 2009; Li et al., 2009a). Those authors and Nugent (2007) note that archival data from the *HST* and the Palomar Oschin Schmidt telescope reveal a transient coincident with SN 2009ip. This may support the conclusion of Ofek et al. (2014) that there are precursor eruptions to some SNe IIn. Foley et al. (2011) found that there was a possible progenitor identified in archival *HST* data from 1999. Thoene et al. (2015) reported that SN 2009ip had become dimmer than its proposed progenitor by 2015 Nov. 29, which suggests that the 2012 eruption was terminal and SN 2009ip had exploded as a genuine SN. These precursor eruptions may be consistent with an LBV progenitor, if LBVs are a predominant progenitor path for SNe IIn then perhaps these precursor eruptions are common.

I present the time-series spectra of SN 2009ip in Fig. 3.7. 38 spectral epochs spanning 755 days were collected. All epochs show prominent $H\alpha$ emission with the classic SN IIn profile shape. $H\beta$ is also visible at many of the epochs, and $H\gamma$ and $H\delta$ are seen at earlier epochs along with possible He I $\lambda 5876$ emission. Apart from these lines the spectra are featureless. I show the example $H\alpha$ profile at epoch seven of SN 2009ip in Fig. 3.8. I fit three Gaussian components to this line, with the broader component having $\text{FWHM} \approx 5400 \text{ km s}^{-1}$, an intermediate component with $\text{FWHM} \approx 1300 \text{ km s}^{-1}$, and the narrow component having $\text{FWHM} \approx 300 \text{ km s}^{-1}$. SNID classifies SN 2009ip as either an SN IIP or an AGN (although it most certainly is *not* an AGN as it is far from the nucleus of the host).

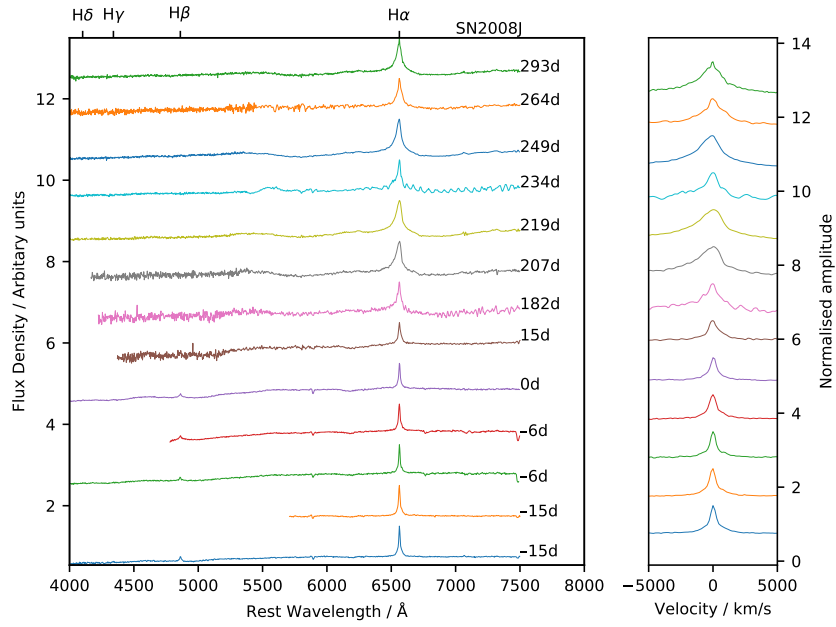


FIGURE 3.5: (*Left*) Time-series spectra of an exemplar SN II_n – SN 2008J. I show optical spectra at 12 epochs over the range 4000–7500 Å that exhibit strong CSM interaction features. Each spectrum is shifted to the rest frame and plotted with a vertical offset, and the Balmer lines from H α through H δ are indicated with tick marks. The numbers are the days after maximum brightness (2008 Feb. 02) in the *i* band. (*Right*) I plot the corresponding H α profiles in velocity space with a vertical offset for clarity.

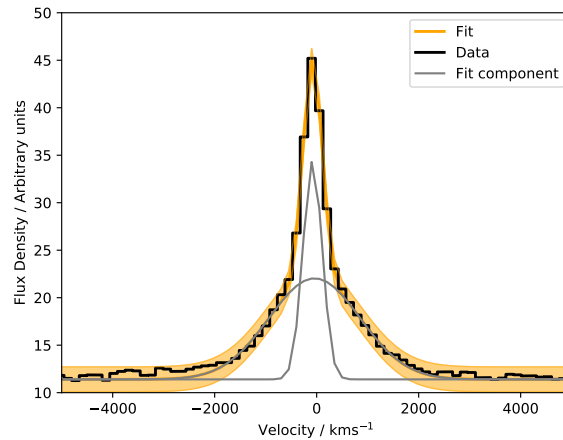


FIGURE 3.6: H α profile and the multi-Gaussian fits for the first spectral epoch (15 days before *i* band maximum) of SN 2008J. I fit a broad and a narrow component to the data centred around rest-frame H α . The thick black line is the data, the grey lines are the Gaussian components, and the shaded orange area is the total fit along with its 3 σ uncertainty region.

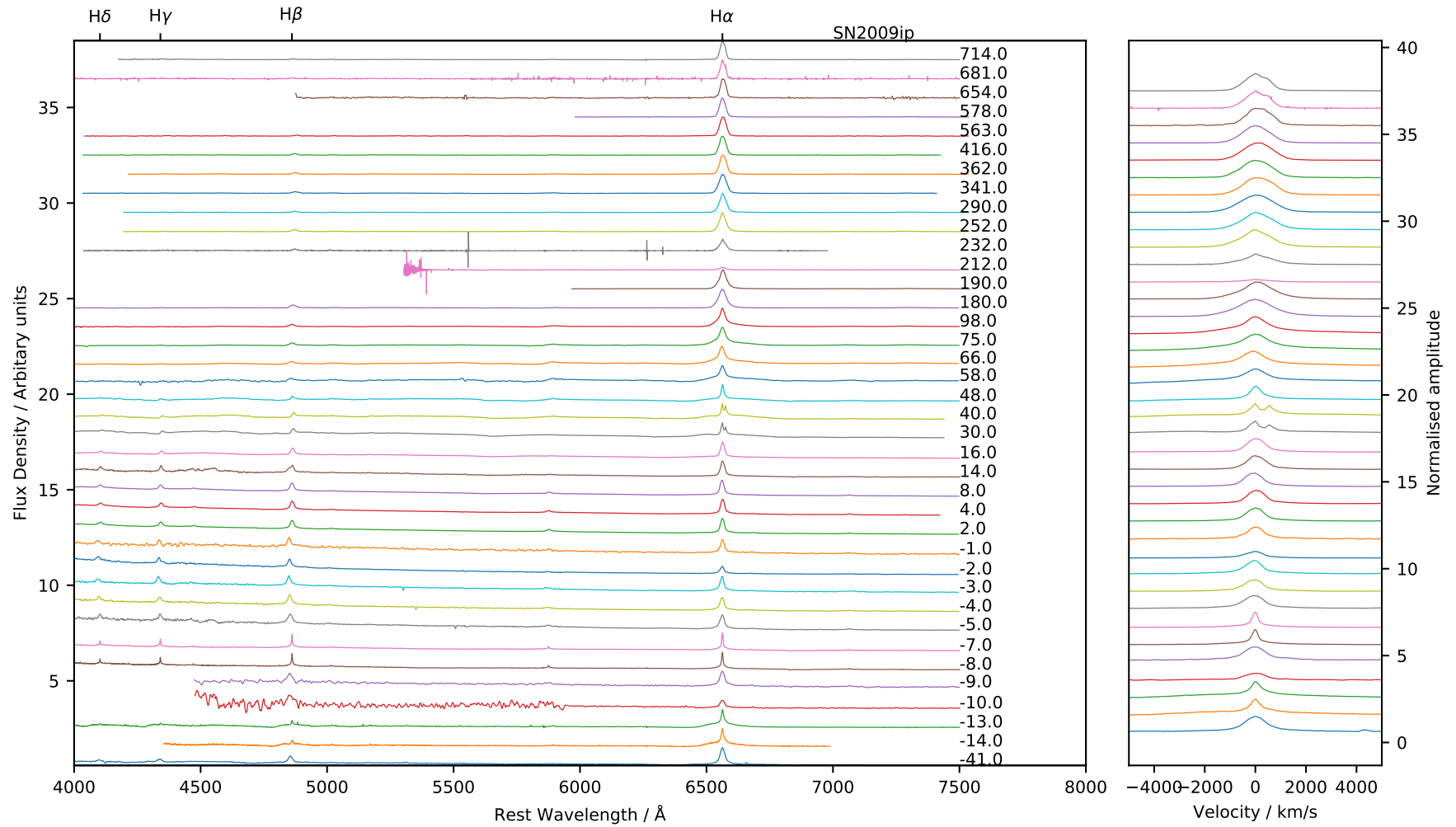


FIGURE 3.7: Time-series spectra of an exemplar SN IIn – SN 2009ip in NGC 7259. (*Left*) Spectra spanning 38 epochs over 755 days. The dashed lines mark the Balmer series and there is a vertical offset between each spectrum for clarity. The numbers are the days from maximum brightness (2012 Jul. 24) in the *UVM2* band. (*Right*) H α profiles of each epoch in velocity space with a vertical offset.

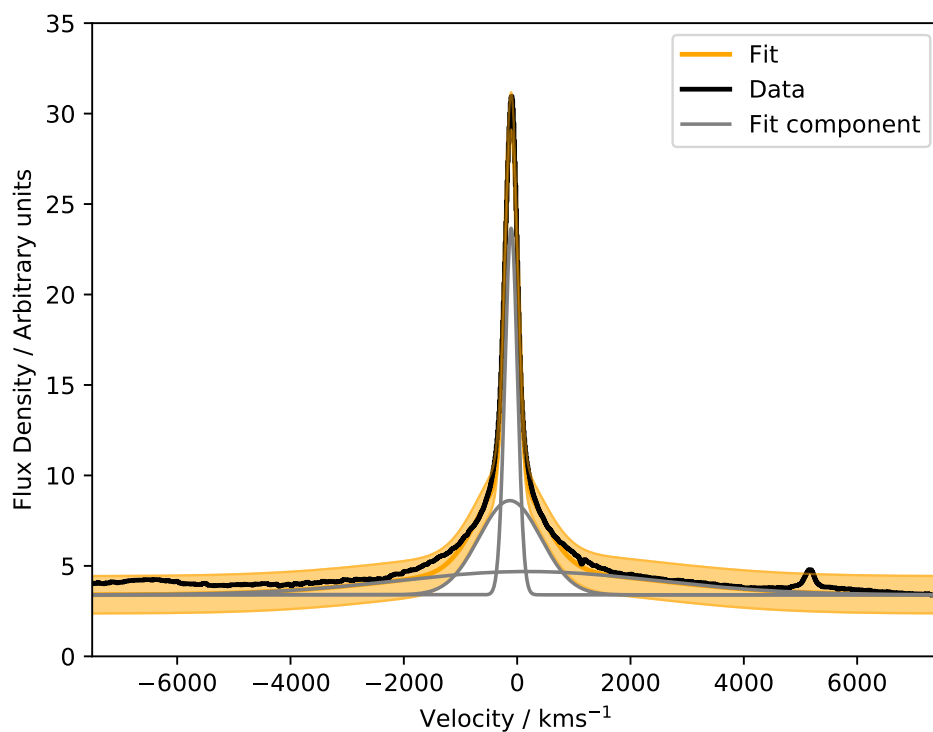


FIGURE 3.8: Multicomponent Gaussian fits to epoch seven (7 days before *UVM2*-band maximum) of SN 2009ip. I was able to fit three components to the data: a broad feature, an intermediate-width component, and a narrower component. The thick black line is the data, the grey lines are the Gaussian components, and the shaded orange area is the total fit along with its 3σ uncertainty region.

TABLE 3.1: The sample of SNe IIn that were reclassified into the “gold” spectral category. From the sample of 115 transients within $z < 0.02$ with data, 37 SNe are classified as “gold” SNe IIn where the CSM interaction is visible throughout multiple epochs. The table gives the common SN name, the discovery date, the common host name, the J2000 coordinates, and the redshift.

Name	Disc. Date	Host Name	R.A.	Dec.	z	OSC	TNS	SNID	Class	Source
SN2005db	2005/07/19	NGC 214	00:41:26.79	25:29:51.60	0.0151	IIn	IIn	Gal	Gold IIn	Blanc et al. (2005a)
SN2005gl	2005/10/05	NGC 266	00:49:50.02	32:16:56.80	0.0155	IIn	IIn	IIn	Gold IIn	Blanc et al. (2005c)
SN1999eb	1999/10/02	NGC 664	01:43:45.45	04:13:25.90	0.0180	II	IIn	AGN	Gold IIn	Modjaz et al. (1999)
SN2003G	2003/01/08	IC 208	02:08:28.13	06:23:51.90	0.0120	IIn	IIn	AGN	Gold IIn	Hamuy & Maza (2003)
SN2008J	2008/01/15	MCG -02-07-33	02:34:24.20	-10:50:38.50	0.0159	Ia	IIn	IIn	Gold IIn	Stritzinger et al. (2008)
SN2013fc	2013/08/20	ESO 154-G10	02:45:08.95	-55:44:27.30	0.0186	IIn	IIn	Ia	Gold IIn	Kankare et al. (2013)
SN2000eo	2000/11/16	MCG -02-09-03	03:09:08.17	-10:17:55.30	0.0100	IIn	IIn	IIP	Gold IIn	Strolger et al. (2000)
SN2006gy	2006/09/18	NGC 1260	03:17:27.06	41:24:19.51	0.0192	II	IIn	IIP	Gold IIn	Foley et al. (2006)
SN1989R	1989/10/04	UGC 2912	03:59:32.56	42:37:09.20	0.0180	II	IIn	IIP	Gold IIn	P. Challis
SN1995G	1995/02/23	NGC 1643	04:43:44.26	-05:18:53.70	0.0160	II	IIP	Gal/IIn	Gold IIn	Filippenko & Schlegel (1995)
SN2010jp	2010/11/11	A061630-2124	06:16:30.63	-21:24:36.30	0.0092	IIn	IIn	AGN	Gold IIn	Challis et al. (2010)
SN2006jd	2006/10/12	UGC 4179	08:02:07.43	00:48:31.50	0.0186	IIn	I Ib	II-pec	Gold IIn	Blondin et al. (2006c)
SN2013gc	2013/11/07	ESO 430-G20	08:07:11.88	-28:03:26.30	0.0034	IIn	IIn	IIn/IIP	Gold IIn	A. Reguitti
SN2009kn	2009/10/26	MCG-03-21-06	08:09:43.04	-17:44:51.30	0.0143	IIn	IIn	AGN	Gold IIn	Steele et al. (2009a)
SN2005kj	2005/11/17	A084009-0536	08:40:09.18	-05:36:02.20	0.0160	IIn	IIn	LBV/IIn/IIP	Gold IIn	Bonnaud et al. (2005)
SN1994ak	1994/12/24	NGC 2782	09:14:01.47	40:06:21.50	0.0085	II	IIn	AGN	Gold IIn	Garnavich et al. (1995)
SN2005ip	2005/11/05	NGC 2906	09:32:06.42	08:26:44.40	0.00718	IIn	II	IIn	Gold IIn	Modjaz et al. (2005b)
SN2010jl	2010/11/03	UGC 5189A	09:42:53.33	09:29:41.80	0.0107	IIn	IIn	AGN	Gold IIn	Yamanaka et al. (2010)
SN1989C	1989/02/03	MCG+01-25-25	09:47:45.49	02:37:36.10	0.0063	II	IIP	IIP	Gold IIn	P. Challis
SN2011ht	2011/09/29	UGC 5460	10:08:10.56	51:50:57.12	0.0036	IIn	IIn	LBV/IIP	Gold IIn	Pastorello et al. (2011)
SN1993N	1993/04/15	UGC 5695	10:29:46.33	13:01:14.00	0.0098	II	IIP	LBV	Gold IIn	This work
SN1998S	1998/03/02	NGC 3877	11:46:06.13	47:28:55.40	0.0030	IIn	IIn	IIn	Gold IIn	Schaefer & Roscherr (1998)
SN1994W	1994/07/29	NGC 4041	12:02:10.92	62:08:32.70	0.00403	II	IIP	LBV/IIn	Gold IIn	This work
SN2011A	2011/01/02	NGC 4902	13:01:01.19	-14:31:34.80	0.0089	IIn	IIn	AGN	Gold IIn	Stritzinger et al. (2011)
SN2000P	2000/03/08	NGC 4965	13:07:10.53	-28:14:02.50	0.0075	II	IIn	IIP/IIn	Gold IIn	Jha et al. (2000)
SN2016bdu	2016/02/28	-	13:10:13.95	32:31:14.07	0.0170	IIn	IIn	AGN	Gold IIn	N. Elias-Rosa
SN1997eg	1997/12/04	NGC 5012	13:11:36.73	22:55:29.40	0.0087	II	-	II-pec→IIn	Gold IIn	Filippenko & Barth (1997)

SN2015da	2015/01/09	NGC 5337	13:52:24.11	39:41:28.60	0.0072	II _n	-	AGN	Gold II _n	J. Zhang
SN1994Y	1994/08/19	NGC 5371	13:55:36.90	40:27:53.40	0.0085	II	II _n	AGN	Gold II _n	Clocchiatti et al. (1994)
SN1995N	1995/05/05	MCG-02-38-17	14:49:28.29	-10:10:14.40	0.0062	II	II _n	AGN/II-pec	Gold II _n	Pollas et al. (1995)
SN2008B	2008/01/02	NGC 5829	15:02:43.65	23:20:07.80	0.0188	II	II _n	II _n	Gold II _n	Blondin et al. (2008)
SN1987B	1987/02/24	NGC 5850	15:07:02.92	01:30:13.20	0.0085	II	-	IIL/II _n	Gold II _n	Schlegel et al. (1996)
SN2012ca	2012/04/25	ESO 336-G9	18:41:07.25	-41:47:38.40	0.0190	Ia-CSM	II _n	II _n	Gold II _n	Inserra et al. (2012)
SN2008S	2008/02/01	NGC 6946	20:34:45.35	60:05:57.80	0.0002	II _n	II _n	IIP/II _n	Gold II _n	Steele et al. (2008)
SN1999el	1999/10/20	NGC 6951	20:37:18.03	66:06:11.90	0.0047	II _n	II _n	Gal/II _n	Gold II _n	Cao et al. (1999)
SN2010bt	2010/04/17	NGC 7130	21:48:20.22	-34:57:16.50	0.0162	II	II _n	Gal	Gold II _n	N. Elias-Rosa
SN2009ip	2012/07/24	NGC 7259	22:23:08.30	-28:56:52.40	0.0059	II _n	-	IIP/AGN	Gold II _n	Li et al. (2009b)

3.6.2 The silver sample

This dataset contains 50 SNe IIn in the silver category. This category is for objects having spectra that are consistent with SNe IIn but where there is only a single spectrum available, or for those where the CSM interaction is short lived such as in the case of “weak” SNe IIn.

In Fig. 3.9 I display the spectrum of the silver SN 2017gas. It was discovered in 2MASX J20171114+5812094 on 2017 Aug. 17 at a V -band magnitude of ~ 16 as part of the All-Sky Automated Survey for SuperNovae (ASAS-SN) with 14 cm telescopes in Chile and Hawaii (Stanek, 2017). I classify SN 2017gas in the silver category because there was only a single spectrum available publicly. It shows very strong CSM interaction features with the “Eiffel Tower” profile being very apparent in the $H\alpha$, $H\beta$, and $H\gamma$ emission lines. Furthermore, some non-Balmer lines seem to exhibit the narrow features expected from CSM interaction; there may be narrow features in Fe II $\lambda 5750$ and Fe II $\lambda 5872$.

SN 2017gas appears to be close to the centre of 2MASX J20171114+5812094, so we must distinguish this object from an AGN. The host offset of SN 2017gas is $1.97''$ (according to PS1; Flewelling et al., 2020), the host has a semimajor axis of $8.80''$, and Skrutskie et al. (2006) report an uncertainty of $0.23''$ in the centre of the host right ascension and declination. Discovery images show the transient being off-centre⁴. The spectrum of SN 2017gas does not show the strong [O III] $\lambda\lambda 4959, 5007$ emission lines that may be associated with AGNs. Furthermore, Ward et al. (2021) found that out of a sample of 5493 AGNs, only nine were offset from the galaxy centre, and the maximum observed offset was $1.649'' \pm 0.004''$. This suggests that the transient is likely an SN rather than an AGN.

The fit to the $H\alpha$ profile of SN 2017gas is shown in Fig. 3.10. I was able to fit two Gaussians with the FWHM of the broad component being $\sim 1900 \text{ km s}^{-1}$ and FWHM $\approx 400 \text{ km s}^{-1}$ for the narrow component. SNID matches the spectrum of SN 2017gas to a galaxy template spectrum.

⁴<https://star.pst.qub.ac.uk/ps1threepi/psdb/candidate/1201711351581208000/>

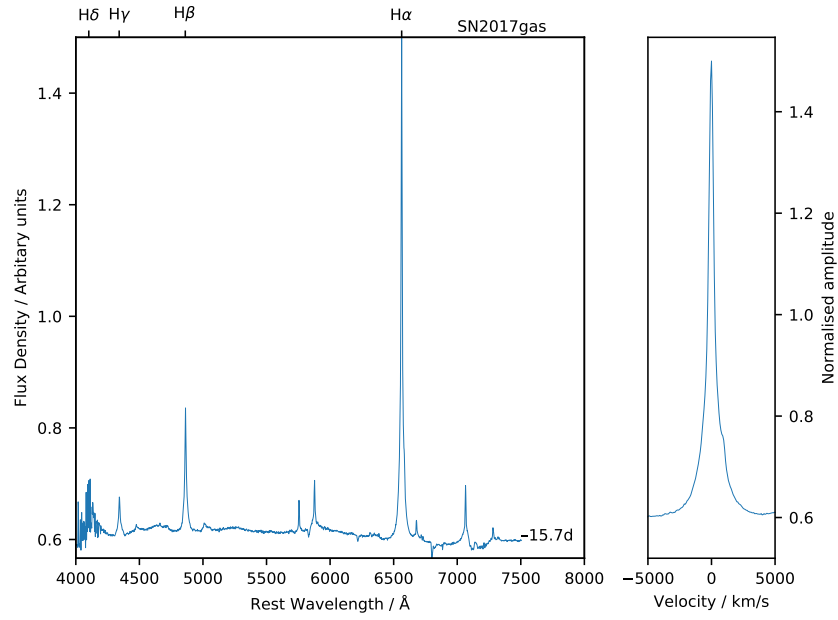


FIGURE 3.9: (*Left*) Spectrum of an exemplar silver class SNIIn – SN 2017gas. I show a single-epoch optical spectrum (15.7 days before maximum brightness in the R band on 2017 Aug. 10) over the range 4000–7500 Å that shows strong CSM interaction features. The spectrum is shifted to the rest frame and the Balmer lines are indicated with tick marks. (*Right*) The corresponding $H\alpha$ profile in velocity space.

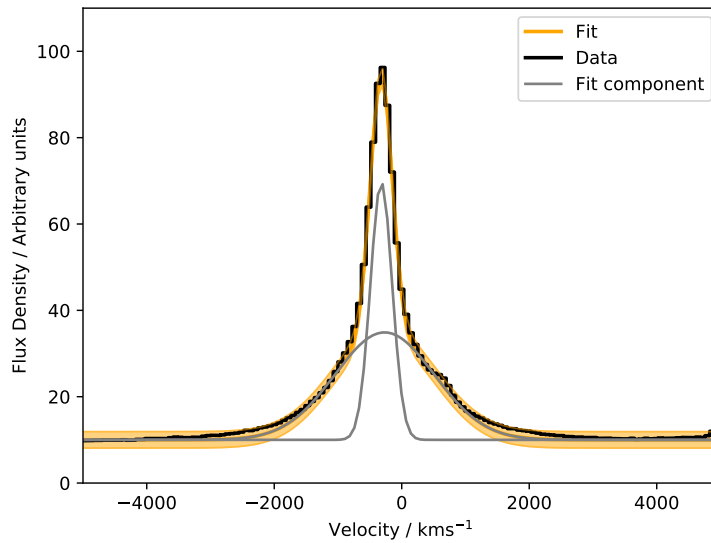


FIGURE 3.10: Multicomponent Gaussian fit to the only available spectrum of SN 2017gas. I was able to fit two Gaussian components, one broad and the other narrower. The thick black line is the data, the grey lines are the Gaussian components, and the shaded orange area is the total fit along with its 3σ uncertainty region.

TABLE 3.2: The sample of SNeIIn that were reclassified into the “silver” spectral category. From this sample of 115 transients within $z < 0.02$ with data, **50** SNe are classified as “silver” SNeIIn where the CSM interaction is apparent in some epochs but may be short-lived, or there is only one spectrum for the object. The table gives the common SN name, the discovery date, the common host name, the J2000 coordinates, and the redshift.

Name	Disc. Date	Host Name	R.A.	Dec.	z	OSC	TNS	SNID	Class	Source
SN2019el	2019/01/02	-	00:02:56.70	32:32:52.30	0.0005	IIn	IIn	-	Silver IIn	Zhang et al. (2019)
SN2017hcc	2017/10/02	GALEX 2.67E+18	00:03:50.58	-11:28:28.78	0.0173	IIn	IIn	Gal	Silver IIn	Mauerhan et al. (2017b)
SN2011fx	2011/08/30	MCG+04-01-48	00:17:59.56	24:33:46.00	0.0193	IIn	IIn	Ia	Silver IIn	Tomasella et al. (2011)
PTF11iqb	2011/07/23	NGC 151	00:34:04.84	-09:42:17.90	0.0125	IIn	-	Ic	Silver IIn	Parrent et al. (2011)
SN2018cvn	2018/06/26	ESO -476G	01:30:27.12	-26:47:06.79	0.0198	IIn	II	Ia-91bg	Silver IIn	Cartier et al. (2018)
SN2007pk	2007/11/10	NGC 579	01:31:47.07	33:36:54.10	0.0167	II	IIn	IIP	Silver IIn	Filippenko et al. (2007)
SN2016eem	2016/07/08	-	02:05:59.80	47:44:14.00	0.0200	IIn	-	Gal	Silver IIn	N. Blagorodnova
SN2002ea	2002/07/21	NGC 820	02:08:25.08	14:20:52.80	0.0148	II	IIn	IIP	Silver IIn	This work
SN1978K	1978/07/31	NGC 1313	03:17:38.60	-66:33:04.60	0.0016	II	-	IIn	Silver IIn	Dopita & Ryder (1990a)
SN2003lo	2003/12/31	NGC 1376	03:37:05.12	-05:02:17.30	0.0140	IIn	IIn	II-pec	Silver IIn	Matheson et al. (2004)
SN2005aq	2005/03/07	NGC 1599	04:31:38.82	-04:35:06.80	0.0130	IIn	IIn	AGN	Silver IIn	Modjaz et al. (2005a)
Gaia14ahl	2014/09/20	PGC 1681539	04:42:12.09	23:06:15.00	0.0170	IIn	-	IIn	Silver IIn	Ochner et al. (2014b)
SN2005ma	2005/12/24	MCG -02-13-13	04:49:53.91	-10:45:23.40	0.0150	II	IIn	AGN	Silver IIn	Puckett et al. (2005b)
SN2016hgf	2016/10/16	WEIN 69	04:51:45.97	44:36:03.06	0.0172	IIn	IIn	AGN	Silver IIn	Rui et al. (2016)
SN2016eso	2016/08/08	ESO -422G	04:59:30.04	-28:51:39.17	0.01606	IIn	IIn	II-pec	Silver IIn	Reynolds et al. (2016)
SN2018zd	2018/03/02	NGC 2146	06:18:03.18	78:22:00.90	0.0030	IIn	II	IIn	Silver IIn	Zhang et al. (2018)
SN2019rz	2019/01/14	UGC 3554	06:50:25.80	43:03:11.70	0.0189	IIn	IIn	Gal	Silver IIn	Tomasella et al. (2019)
AT2018lkg	2018/12/30	UGC 3660	07:06:34.76	63:50:56.90	0.0142	IIn	IIn	IIn	Silver IIn	Zhang et al. (2020b)
SN2002A	2002/01/01	UGC 3804	07:22:36.14	71:35:41.50	0.0096	II	IIn	Gal	Silver IIn	Benetti et al. (2002)
AT2014eu	2014/11/17	MCG+09-13-02	07:28:55.97	56:11:46.20	0.0179	IIn	-	IIP	Silver IIn	Zhang et al. (2014)
SN2017cik	2017/03/17	SDSS J075412.97+214729.9	07:54:13.07	21:47:35.80	0.0160	IIn	IIn	AGN	Silver IIn	Gutierrez et al. (2017)
SN2014ee	2014/11/12	UGC 4132	07:59:11.68	32:54:39.60	0.0174	IIn	IIn	IIP	Silver IIn	Ochner et al. (2014c)
SN2011an	2011/03/01	UGC 4139	07:59:24.42	16:25:08.20	0.0163	IIn	IIn	-	Silver IIn	Marion & Calkins (2011)
SN2001ir	2001/12/19	MCG-02-22-22	08:36:28.12	-11:50:03.50	0.0200	II	IIn	AGN	Silver IIn	Matheson et al. (2002a)
SN2002fj	2002/09/12	NGC 2642	08:40:45.10	-04:07:38.50	0.0140	II	IIn	IIn	Silver IIn	M. Hamuy
SN2017dwq	2017/05/04	2MASX J09033237-2120017	09:03:32.49	-21:20:02.99	0.0182	IIn	IIn	IIn	Silver IIn	Kankare et al. (2017)

SN2015bh	2015/02/07	NGC 2770	09:09:34.96	33:07:20.40	0.0064	II _n	II _n	LBV	Silver II _n	de Ugarte Postigo et al. (2015)
SN2014es	2014/11/20	MCG -01-24-12	09:20:46.91	-08:03:34.00	0.0196	II _n	II _n	II _n	Silver II _n	Li et al. (2014)
SN1997ab	1997/02/28	A095100+2004	09:51:00.40	20:04:24.00	0.0130	II	IIP	AGN	Silver II _n	Hagen et al. (1997)
SN2014P	2014/02/02	ESO 264-G49	10:54:04.00	-45:48:43.60	0.0190	II _n	II _n	AGN	Silver II _n	Ergon et al. (2014)
SN1996bu	1996/11/14	NGC 3631	11:20:59.18	53:12:08.00	0.0039	II	II _n	IIP	Silver II _n	Nakano et al. (1996)
SN2013L	2013/01/22	ESO 216-G39	11:45:29.55	-50:35:53.10	0.0170	II _n	II _n	Gal	Silver II _n	Morales Garoffolo et al. (2013)
SN2011ir	2011/11/21	UGC 6771	11:48:00.32	04:29:47.10	0.0199	II _n	II	II _n →IIL	Silver II _n	A. Pastorello
SN1987F	1987/03/22	NGC 4615	12:41:38.99	26:04:22.40	0.0160	II	IIP	Gal/AGN	Silver II _n	This work
SN2008ip	2008/12/31	NGC 4846	12:57:50.20	36:22:33.50	0.0151	II	II _n	IIP→II _n	Silver II _n	Challis & Calkins (2009)
SN2009au	2009/03/11	ESO 443-G21	12:59:46.00	-29:36:07.50	0.0094	II	II _n	II _n →IIP	Silver II _n	Stritzinger et al. (2009)
SN2016aiy	2016/02/17	ESO 323-G084	13:08:25.40	-41:58:50.10	0.0100	II _n	II _n	II _n	Silver II _n	Elias-Rosa et al. (2016)
SN1996cr	1996/03/16	ESO 97-G13	14:13:10.05	-65:20:44.40	0.0014	II	II _n	Gal	Silver II _n	F. Bauer
SN2006am	2006/02/22	NGC 5630	14:27:37.24	41:15:35.40	0.0089	II	II _n	Gal	Silver II _n	Blondin et al. (2006d)
SN1996ae	1996/05/21	NGC 5775	14:53:59.81	03:31:46.30	0.0056	II	II _n	II-pec	Silver II _n	Benetti & Zwitter (1996)
SN2003dv	2003/04/22	UGC 9638	14:58:04.92	58:52:49.90	0.0076	II _n	II _n	IIP	Silver II _n	Kotak et al. (2003)
SN2016bly	2016/04/09	2MASX J17224883+1400584	17:22:48.90	14:00:59.88	0.0194	II _n	II _n	Gal	Silver II _n	Zhang et al. (2016)
SN2018hpb	2018/10/25	-	22:01:34.52	-17:27:45.22	0.0177	II _n	II _n	II _n	Silver II _n	Bose et al. (2018)
SN2017gas	2017/08/10	2MASX J20171114+5812094	20:17:11.32	58:12:08.00	0.0100	II _n	II _n	Gal	Silver II _n	Bose et al. (2017)
SN2006bo	2006/04/05	UGC 11578	20:30:41.90	09:11:40.80	0.0153	II _n	II _n	LBV	Silver II _n	F. Taddia
ASASSN-15lx	2015/06/26	ESO 47-G4	20:36:05.24	-73:06:32.41	0.0126	II	-	II _n	Silver II _n	G. Hosseinzadeh
SN2016cvk	2016/06/12	ESO -344-G21	22:19:49.39	-40:40:03.20	0.0107	II-09ip	II _n -pec	AGN	Silver II _n	Bersier et al. (2016)
SN1989L	1989/05/04	NGC 7339	22:37:49.71	23:47:15.70	0.0044	II	II	IIP	Silver II _n	Uomoto (1989)
SN2015bf	2015/12/12	NGC 7653	23:24:49.03	15:16:52.00	0.014227	II _n	II _n	II _n	Silver II _n	J. Zhang
SN2013fs	2013/10/07	NGC 7610	23:19:44.70	10:11:05.00	0.0119	IIP	II _n	IIP	Silver II _n	Childress et al. (2013)

3.6.3 Previously misclassified type IIIn supernovae

There are 28 objects that I classify as not belonging to the SN IIIn class. This group includes SNe with spectra that cannot be positively identified as a SN IIIn owing to a noisy spectrum, underlying H II region pollution, not showing SN-like features or CSM interaction restricted to early times suggesting flash ionisation.

An example of a transient that is not a SN IIIn is SN 2009kr in NGC 1823. It was discovered on 2009 Nov. 6 with a 0.6 m reflecting telescope at a magnitude of ~ 16 (Nakano et al., 2009). Tendulkar et al. (2009a) obtained a spectrum of SN 2009kr with the Palomar 5 m telescope and used SNID to compare with standard templates. They concluded that the apparent prominent narrow feature in the $H\alpha$ emission line indicates that SN 2009kr is a SN IIIn. However, Steele et al. (2009b) analysed spectra of SN 2009kr from the 3 m Shane telescope at Lick Observatory and found that the narrow $H\alpha$ emission component is likely H II region pollution; the prior classification as an SN IIIn is due to this and blending of the [N II] lines on either side of $H\alpha$. They subsequently classify SN 2009kr as an ordinary SN II.

Analysis of images by Elias-Rosa et al. (2010) showed that SN 2009kr may be a SN IIL; however, Fraser et al. (2010) claim that the early-time light curve is more consistent with SN 2009kr being a SN IIP. Elias-Rosa et al. (2010) also found that the progenitor system of SN 2009kr may be a yellow supergiant. Fraser et al. (2010) concluded that the progenitor is ambiguous; if the progenitor was a single star it would be yellow supergiant, but the progenitor could not be ruled out as being in a cluster. The progenitor was quite luminous in *HST* images ($M_I \approx -8.5$ mag). Li et al. (2009c) stated that the progenitor may be in a compact star cluster, and Maund et al. (2015) suggested that the progenitor may be in a compact cluster with a mass of $\sim 6000 M_\odot$ after analysis of late-time observations of SN 2009kr.

I display a temporal series of spectra of SN 2009kr in Fig. 3.11. At early times (the three epochs before maximum brightness) there are narrow Balmer emission lines. A narrow feature superimposed upon the $H\alpha$ line persists over all observed epochs. The post-maximum spectra show a broadening $H\alpha$ line with a P Cygni profile. In Fig. 3.12 I show the fourth epoch of SN 2009kr (12.4 days post-maximum); this is when the $H\alpha$ emission line starts to broaden with a FWHM of $\sim 7500 \text{ km s}^{-1}$. I fit narrow features at $H\alpha$ and also [N II] $\lambda\lambda 6548, 6584$, consistent with the spectrum being contaminated by underlying emission from the local H II region. Furthermore, one can see probable emission features of [S II] $\lambda\lambda 6717, 6731$, supporting the argument that the narrow features previously interpreted as being due to CSM interaction are actually line pollution from the local

interstellar medium. My analysis is therefore consistent with that of [Steele et al. \(2009b\)](#). Despite the evidence that suggests SN 2009kr is not a SN IIn, the OSC has the primary classification of SN 2009kr as an SN IIn. SNID classifies SN 2009kr as an SN IIP.

Another example is SN 2002kg in NGC 2403. SN 2002kg was reported on 2002 Oct. 26 with KAIT as part of LOTOSS (the Lick Observatory and Tenagra Observatory Supernova Search), with a discovery magnitude of ~ 19.0 ([Schwartz et al., 2003](#)). Subsequent spectroscopic observations were carried out by [Filippenko & Chornock \(2003\)](#) using the Keck Observatory. I show the temporal series of spectra of SN 2002kg in Fig. 3.13, covering four epochs over 4309 days. Fig. 3.14 displays the $H\alpha$ profile of SN 2002kg, overlaid with Gaussian fits to the data. The spectra are mostly featureless apart from some Balmer emission and [N II] $\lambda\lambda 6548, 6584$ lines. SN 2002kg was initially classified as an SN IIn owing to the narrow $H\alpha$ feature ($\sim 300 \text{ km s}^{-1}$) and a possible broader component. However, [Filippenko & Chornock \(2003\)](#) drew comparisons to gap transients such as SN 2000ch ([Wagner et al., 2000](#)). They noted that the forbidden nitrogen lines, absence of any other forbidden lines, and an absolute magnitude of about -9 point toward a nitrogen-enriched wind or CSM consistent with the outburst of a massive star such as an LBV rather than an SN. However, these authors did not rule out an SN explosion until there is further evidence that this transient is an “impostor.”

KAIT photometry, Keck spectroscopy, archival data, and subsequent observations were used to constrain the properties of SN 2002kg. It was found that that the outburst is less energetic than most other “impostor” events and that the progenitor is the LBV V37 ([Tammann & Sandage, 1968](#)). It has been reported that the outburst may be forming an LBV nebula, with the eruption being consistent with an S Dor LBV phase and a progenitor mass of $60\text{--}80 M_{\odot}$ ([Weis & Bomans, 2005](#); [Van Dyk et al., 2006](#); [Maund et al., 2006](#); [Humphreys et al., 2017](#)). There is no multicomponent $H\alpha$ feature present in the spectra, and the spectra are not at an early stage, so I classify SN 2002kg as not being an SN IIn. SNID classifies SN 2002kg as an AGN (though it certainly was *not* an AGN as the transient is not central to the host).

A third example of a transient I do not classify as an SN IIn is SN 2001fa in NGC 673, which was discovered on 2001 Oct. 18 with KAIT as part of LOTOSS, with a discovery magnitude of ~ 16.9 . Later, a spectrum obtained with the Lick 3 m Shane telescope was interpreted as SN 2001fa being a young SN IIn that also exhibited WR features including He II, C III, and N III emission lines ([Papenkova & Li, 2001](#)). There are spectra at eleven epochs spanning 86 days that I present in Fig. 3.15. The early-time spectra are mostly featureless with the exception of the Balmer lines, in particular $H\alpha$, as is characteristic

of SNe IIn. SN 2001fa exhibited signatures of CSM interaction that were only visible for ~ 5 days and the spectrum subsequently resembled a more standard SN II with a broadened $H\alpha$ profile. There may be a narrow feature on the tenth epoch (0.76 days before maximum brightness), but it could be due to contamination from an H II region. I therefore do not classify SN 2001fa as an SNIIn, as the early-time CSM interaction is representative of flash ionisation and later spectra are consistent with those of a standard SN II. Light-curve analysis by [Faran et al. \(2014\)](#) presents SN 2001fa as part of a sample of SNe IIL. SNID classifies SN 2001fa as evolving from an SNIIn to an SN IIP, consistent with a flash ionisation SN evolving into a SN II.

Fig. 3.16 shows the $H\alpha$ profile for the fourth epoch of SN 2001fa. I fit two components to it, with the broad component having $\text{FWHM} \approx 1500 \text{ km s}^{-1}$ and the narrow component having $\text{FWHM} \approx 100 \text{ km s}^{-1}$.

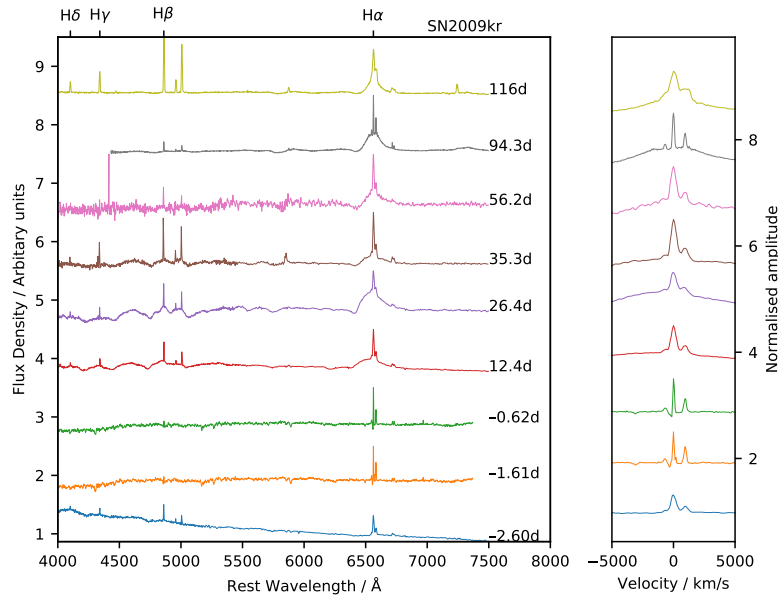


FIGURE 3.11: Temporal series of spectra of an example non-SNIIn classification – SN 2009kr. I display optical spectra over the range 4000–7500 Å at nine epochs, showing that the previously claimed CSM interaction features are likely due to the spectra being polluted by emission lines from the underlying H II region; the [N II] lines on either side of $H\alpha$ and the [S II] lines redward of $H\alpha$ are clearly visible at all epochs. This object therefore may be a standard SN II rather than an SNIIn. Each spectrum is shifted to the rest frame, a vertical offset is added for clarity, and the Balmer series from $H\alpha$ through $H\delta$ is indicated with tick marks. The numbers on the right of the spectra denote the days from maximum brightness (2009 Nov. 6) in the K band. (Right) Corresponding $H\alpha$ profiles in velocity space, with vertical offsets.

We find that 28 of the objects are not SNe IIn. In Table 3.3 I show that out of these, twelve may have been misclassified owing to H II region lines being interpreted as CSM

interaction. The remaining nine were gap transients that have retained their SN IIn classification in OSC and/or TNS.

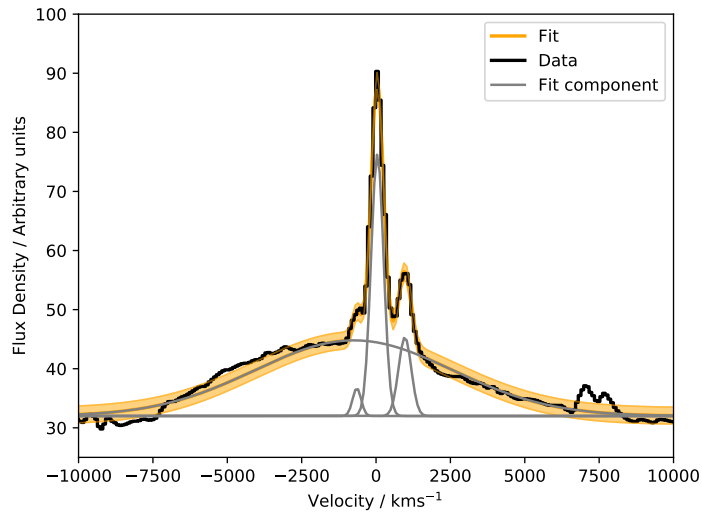


FIGURE 3.12: Multicomponent Gaussian fits to the fourth epoch of SN 2009kr just over 12 days past maximum brightness in the K band. I was able to fit a broad component to the $H\alpha$ profile along with three narrow components at $H\alpha$ and $[N\text{II}] \lambda\lambda 6548, 6584$. The $[S\text{II}] \lambda\lambda 6717, 6731$ lines are also visible. The presence of these lines indicates that the narrow features seen in this $H\alpha$ profile probably originate from the underlying H II region. The thick black line is the data, the grey lines are the Gaussian components, and the shaded orange area is the total fit along with its 3σ uncertainty region.

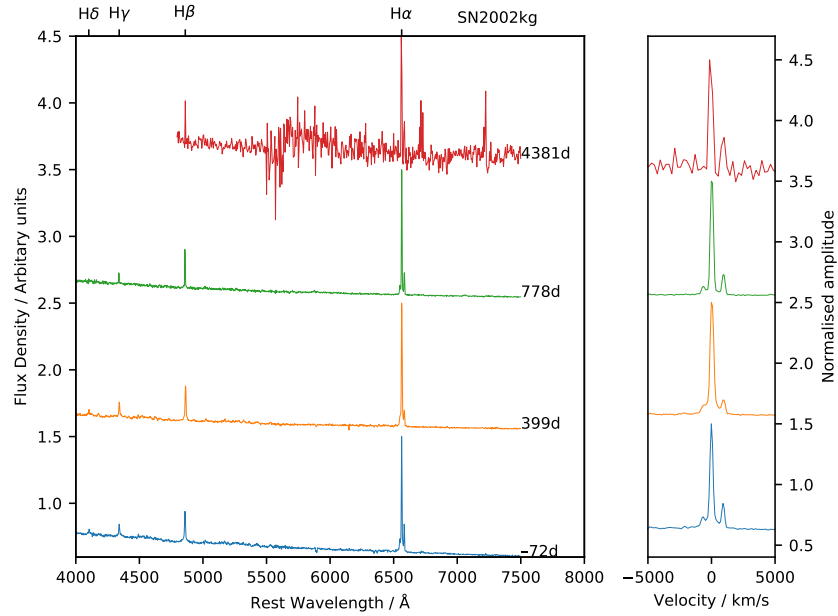


FIGURE 3.13: Time-series spectra of an example of a negative SN IIn classification - SN 2002kg. I show optical spectra from 4000-7500 Å over four epochs that are mostly featureless apart from Balmer emission and [N II]. The H α line is strong and narrow and the H β line is also apparent in these spectra. Each epoch is shifted to the rest-frame, an offset is added for clarity and the Balmer series from H δ -H α is marked with a tick. The numbers are the days from maximum (2002 Oct. 26) in the Clear band. (*Right*) Corresponding H α profiles in velocity space with offsets.

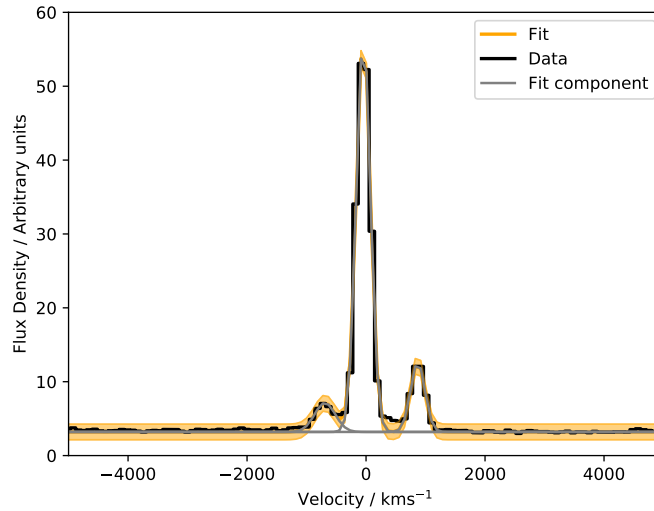


FIGURE 3.14: Multicomponent Gaussian fits to the H α profile of the third epoch (778 days post maximum brightness in the Clear band) of SN 2002kg. I fit a narrow H α profile with FWHM $\approx 300 \text{ km s}^{-1}$. The thick black line is the data, the grey lines are the Gaussian components, and the shaded orange area is the total fit along with its 3σ uncertainty region.

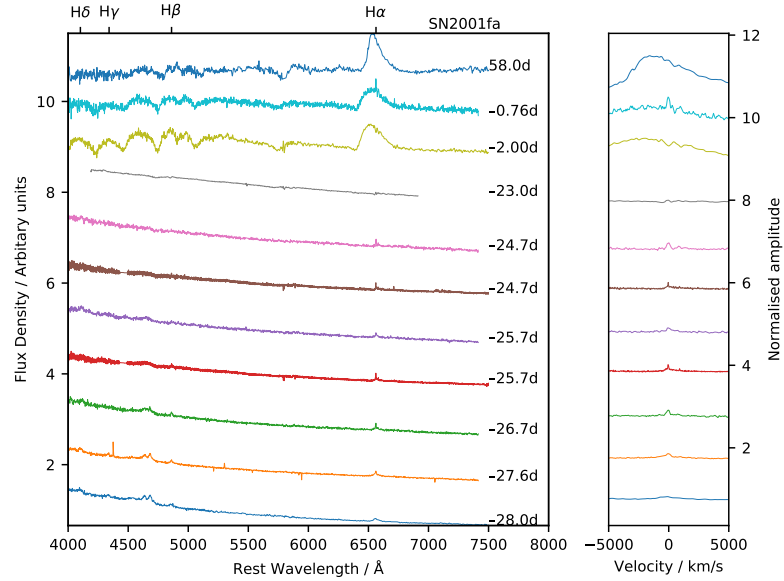


FIGURE 3.15: Time series of spectra of an exemplar silver-class SN IIn – SN 2001fa. I display optical spectra over the range 4000–7500 Å at nine epochs that show CSM interaction features at earlier times, followed by more-standard SN II characteristics with broad H α emission and possible P Cygni features in several lines. Each spectrum is shifted to the rest frame, a vertical offset is added for clarity, and the Balmer series from H α through H δ is indicated with tick marks. The numbers are the days from maximum (2001 Nov. 17) in the Clear band. (*Right*) Corresponding H α profiles in velocity space, with vertical offsets.

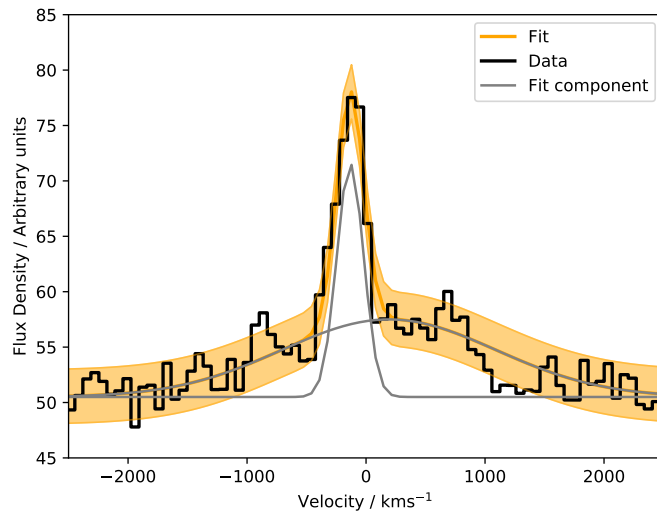


FIGURE 3.16: Multicomponent Gaussian fits to the fourth epoch (25.7 days before maximum brightness in the Clear band) of SN 2001fa. I was able to fit two Gaussian components to the data, one intermediate-broad and the other narrow. The thick black line is the data, the grey lines are the Gaussian components, and the shaded orange area is the total fit along with its 3 σ uncertainty region.

TABLE 3.3: Objects that are not SNeIIn and the reasons for classifications.

Name	Reason for a not SN IIn classification
SN 2001dk	Consistent with H II region contamination
SN 2001fa	Flash-ionisation SN
SN 2004F	Consistent with H II region contamination
SN 2001I	Consistent with H II region contamination
SN 2002bj	Consistent with H II region contamination
SN 2009kr	Consistent with H II region contamination
SN 2004gd	Consistent with H II region contamination
SN 2002kg	Gap transient
SN 1999gb	Consistent with H II region contamination
SN 2010al	Consistent with H II region contamination
SN 2002an	No narrow feature
SN 2003ke	Consistent with H II region contamination
SN 1999bw	Gap transient
SN 2000ch	Gap transient
SN 2014G	Flash-ionisation SN
SN 2001ac	Gap transient
SN 1997bs	Gap transient
SN 2002bu	Gap transient
SN 2017jfs	Gap transient
SN 2006bv	Gap transient
SN 2007cm	Flash-ionisation SN
SN 2001dc	No narrow feature
ASASSN-15hs	Consistent with H II region contamination
SN 2013by	Consistent with H II region contamination
SN 2001ad	No narrow feature
SN 2018dfy	Consistent with H II region contamination
SN 2006fp	Gap transient
SN 2008gm	Consistent with H II region contamination

TABLE 3.4: The sample of SNe II_n that were reclassified as not being SNe II_n. From my sample of 115 transients within $z < 0.02$ with data, **28** SNe are not SNe II_n. The CSM interaction may be confused with pollution from H II regions, or the data are noisy, or the object is a gap transient with a spectrum that resembles that of SNe II_n. The table gives the common SN name, the discovery date, the common host name, the J2000 coordinates, and the redshift.

Name	Disc. Date	Host Name	R.A.	Dec.	z	OSC	TNS	SNID	Class	Source
SN2001dk	2001/07/29	UGC 913	01:22:14.59	34:40:11.30	0.0171	IIP	IIP	II	H II region	Gal-Yam et al. (2001)
SN2001fa	2001/10/18	NGC 673	01:48:22.22	11:31:34.40	0.0170	II _n	II _n	II _n → IIP	Flash ionisation	Filippenko & Chornock (2001b)
SN2004F	2004/01/16	NGC 1285	03:17:53.80	-07:17:43.00	0.0175	II	-	Gal	H II region	This work
SN2001I	2001/01/15	UGC 2836	03:43:57.28	39:17:39.40	0.0170	II	II _n	Gal	H II region	Filippenko & Chornock (2001a)
SN2002bj	2002/02/28	NGC 1821	05:11:46.41	-15:08:10.80	0.0120	II	II _n	Ic	H II region	Matheson et al. (2002b)
SN2009kr	2009/11/06	NGC 1832	05:12:03.30	-15:41:52.20	0.0065	II _n	II	IIP	H II region	Tendulkar et al. (2009b)
SN2004gd	2004/11/06	NGC 2341	07:09:11.71	20:36:10.60	0.0170	II	II _n	Gal	H II region	This work
SN2002kg	2002/10/26	NGC 2403	07:37:01.83	65:34:29.32	0.0008	II _n	II _n	AGN	Gap transient	Schwartz et al. (2003)
SN1999gb	1999/11/22	NGC 2532	08:10:13.70	33:57:29.80	0.01751	II	II _n	II	H II region	Filippenko & Garnavich (1999)
SN2010al	2010/03/13	UGC 4286	08:14:15.91	18:26:18.20	0.0172	Ibn	II _n	Ic	H II region	Silverman et al. (2010)
SN2002an	2002/01/22	NGC 2575	08:22:47.76	24:17:41.70	0.0129	II	II	IIP	No narrow features	Gal-Yam et al. (2002)
SN2003ke	2003/11/23	MCG+06-22-09	09:45:52.96	34:41:01.40	0.0204	II	II _n	Gal	H II region	Matheson et al. (2003)
SN1999bw	1999/04/20	NGC 3198	10:19:46.81	45:31:35.00	0.0022	II _n ?	II _n	LBV	Gap transient	Filippenko et al. (1999)
SN2000ch	2000/05/03	NGC 3432	10:52:41.40	36:40:09.50	0.0017	LBV	II _n	AGN	Gap transient	Filippenko (2000)
SN2014G	2014/01/14	NGC 3448	10:54:34.13	54:17:56.90	0.00450	II _n	II _n	II _n → IIP	Flash ionisation	Ochner et al. (2014a)
SN2001ac	2001/03/12	NGC 3504	11:03:15.37	27:58:29.50	0.0051	II _n	II _n	AGN	Gap transient	Matheson et al. (2001)
SN1997bs	1997/04/15	NGC 3627	11:20:14.16	12:58:19.56	0.0019	II _n	II _n ?	AGN	Gap transient	This work
SN2002bu	2002/03/28	NGC 4242	12:17:37.18	45:38:47.40	0.0020	II _n	II _n	AGN/LBV	Gap transient	Ayani et al. (2002)
SN2017jfs	2017/12/26	NGC 4470	12:29:37.79	07:49:35.18	0.0080	II _n	II _n	AGN	Gap transient	Bufano et al. (2018)
SN2006bv	2006/04/28	UGC 7848	12:41:01.55	63:31:11.60	0.0084	II _n ?	II _n	LBV	Gap transient	Blondin et al. (2006a)
SN2007cm	2007/05/24	NGC 4644	12:42:45.18	55:08:57.10	0.0160	II	II _n	II _n → IIP	Flash ionisation	This work
SN2001dc	2001/05/30	NGC 5777	14:51:16.15	58:59:02.80	0.0071	II	IIP	IIP	No narrow feature	Hurst et al. (2001)
ASASSN-15hs	2015/04/24	2MASX J15333488-7807258	15:33:34.31	-78:07:23.46	0.0091	II _n	-	Gal	H II region	Childress et al. (2015)
SN2013by	2013/04/23	ESO 138-G10	16:59:02.43	-60:11:41.80	0.0038	II	II	IIP	H II region	Margutti et al. (2013)
SN2001ad	2001/03/11	NGC 6373	17:24:02.45	58:59:52.20	0.0110	II	I Ib	I Ib	No narrow features	Dong et al. (2001)
SN2018dfy	2018/07/10	UGC 11801	21:43:32.91	43:32:58.20	0.013519	II _n	IIP	IIP	H II region	Siebert et al. (2018)

SN2006fp	2006/09/17	UGC 12182	22:45:41.13	73:09:47.80	0.0050	LBV	IIn	Gal	Gap transient	Blondin et al. (2006b)
SN2008gm	2008/10/22	NGC 7530	23:14:12.39	-02:46:52.40	0.0117	IIn	IIn	Gal	H II region	Green (2008)

3.6.4 Comparing classifications from databases

TABLE 3.5: Breakdown of the number of objects in the OSC and TNS having non-SN IIn primary classifications (out of 115) and the number of occurrences where the OSC and TNS disagree on the primary classification.

Class	OSC	TNS	Disagreement
Gold	16	6	16
Silver	18	6	18
Not a SN IIn	16	10	15

3.6.5 Comparing to results from SNID

SNID was able to match 32 of the targets to template SNe IIn. In the instances where there was no match to an SN IIn spectrum, it is noted that there are 26 matches to AGN spectra and 39 have matches to other SN classes. I find that 18 match galaxy spectra and five match the spectra of LBV templates. I also find that six objects have spectra which evolve into/out of the SN IIn subclass according to SNID. These results are summarised in Table 3.6.

TABLE 3.6: Results of using SNID to match the spectral data to templates. In total, SNID matched 32 of the 115 targets to SN IIn templates.

Class	SNID IIn matches
Gold	15 out of 37
Silver	14 out of 50
Not SN IIn	3 out of 28

3.7 The spectral diversity of SNe IIn

In this work, I have explored the spectral diversity in the SN IIn subclass. I spectroscopically reclassified 115 objects within $z < 0.02$ that have at some point been classified as an SN IIn in the OSC. The main result is that 40% of the SNe in the sample had been misclassified when one takes account of the primary classification in OSC. Furthermore, $\sim 25\%$ of the objects in the sample are not SNe IIn when considering my classification scheme. Moreover, for objects that are not SNe IIn, eleven or 18 (OSC or TNS, respectively) claim a primary SN IIn classification. I also find that there is

disagreement in the classification for 45% of our sample between the OSC and TNS. Therefore, any work based on such catalogues of SNe IIn could have included SNe which are misclassified or miss some targets.

This disagreement is clearly problematic for work that relies upon samples and catalogues of SNe. Without this reclassification, the SN IIn catalogue would contain at least 28 targets that do not appear to be SNe IIn, possibly leading to erroneous conclusions in subsequent studies. Confusion in the classification of SNe IIn may come from a number of sources that contribute to the diversity in the SN IIn subclass.

3.7.1 SN 1978K and other caveats

We have chosen a simple classification scheme that only relies upon the Balmer line profiles. This allows these classifications to be independent of the complexities and heterogeneity of SN IIn spectra. However, there are a small number of objects that do not fit into this regime but are an important consideration.

SN 1978K in NGC 1313 was discovered in 1990 by [Dopita & Ryder \(1990b\)](#) and was initially classified as a classical nova system. Subsequent observations of NGC 1313 found that this “nova” was both a strong radio and X-ray source ([Schlegel et al., 1999](#)). Archival photographic plates reveal a dim, possibly dust-enshrouded source that those authors interpret as a SN at the “nova” location in mid-1978 and the object was designated SN 1978K ([Chapman et al., 1992](#)). A spectrum was taken over 13,000 days post-eruption ([Chugai & Della Valle, 1995](#)). The narrow $H\alpha$ line has a FWHM of $\sim 500 \text{ km s}^{-1}$. [Ryder et al. \(1993\)](#) observed SN 1978K at optical, X-ray, and radio wavelengths, and propose that the ongoing emission from the SN remnant may be explained by SN ejecta interacting with a dense shell of CSM. [Kuncarayakti et al. \(2016\)](#) made observations of SN 1978K with the Very Large Telescope and found that the CSM interaction is ongoing over 35 years post-explosion. Furthermore, SNID matches the spectrum of SN 1978K to the template spectrum of SN 1996L 322 days post-explosion.

Very early-time SN IIn spectra may exhibit a strong blue continuum but no broad component in the $H\alpha$ profile, yet show narrow $H\alpha$ emission ([Filippenko, 1997](#)). In the case of SN 1978K, the broad SN ejecta components have faded, leaving only the relatively narrow lines from ongoing CSM interaction. Therefore, it is important to consider the age of the spectrum relative to maximum light (which would be extrapolated for the case of SN 1978K). This is not always possible, however, as observation dates are not recorded on public databases in every instance.

As discussed previously, caution must be taken to ensure that gap transients and AGNs do not infiltrate the SN IIn sample, since their $H\alpha$ profiles can be similar (Filippenko, 1989). I did not identify any AGNs in the sample, but after comparing peak magnitudes and searching the literature I find that nine of the objects are gap transients. One of these transients, SN 2017jfs (also known as AT 2017jfs), has a SN IIn-like spectrum and was initially classified as a SN IIn, but photometric and spectroscopic analysis revealed that this transient was a LRN (Pastorello et al., 2019a).

This classification scheme may miss late-time CSM interaction that does not conform with the “Eiffel Tower” $H\alpha$ profile shape. I do not classify SN 2014G as an SN IIn, since the apparent CSM interaction features were seen only at early times and are thus indicative of flash ionisation. Terreran et al. (2016) found that SN 2014G photometrically behaved as an SN IIL, but at ~ 100 days post-maximum luminosity, the spectrum started forming a feature on the blue side of $H\alpha$. This feature grew over time along with the [O I] $\lambda\lambda 6300, 6363$ doublet. The authors interpreted this unusual feature as late-time interaction with a highly asymmetric CSM. As this classification scheme is localised to the $H\alpha$ region, I would not consider this possible CSM interaction feature.

3.7.2 Supernova impostors

Follow-up observations are the key to add clarity to the SN IIn classifications. Current transient surveys such as ZTF find enormous numbers of transients with thousands of SNe discovered each year (Feindt et al., 2019), and the Vera Rubin Observatory (formerly the Large Synoptic Survey Telescope; LSST Science Collaboration et al., 2009) might discover $\sim 10^5$ SNe per year. While this may be advantageous for catching the early-time flash spectra, prompt follow-up observations of enormous numbers of transients will be challenging. Such data are particularly important for gap transients. Suspected SN impostors may be dust-obscured SNe leading to a substantially reduced observed brightness, so a gap transient actually being a fully fledged SN cannot always be ruled out. Late-time observations of gap transients can confirm the survival of the progenitor. An example of a debated gap transient is SN 2008S, which is often used as a prototypical SN “impostor”; however, Adams et al. (2016) suggest that extreme dust behaviour must be invoked to account for a star surviving while SN 2008S became dimmer than its progenitor. Conversely, as discussed in Section 3.7.2, some transients such as the final eruption of SN 2009ip may be interpreted as a terminal CCSN explosion (Pastorello et al., 2013; Smith et al., 2014), but this is disputed (Fraser et al., 2013a, 2015). Nonterminal

eruptions cannot be ruled out until late-time observations can confirm the survival or death of the progenitor.

In the group of SNe that are not reclassified as SNe II_n, the gap transients such as SN 2002kg have primary classifications as SNe II_n in OSC or TNS. As previously discussed, in the case of SN 2002kg, [Schwartz et al. \(2003\)](#) recognise that SN 2002kg may be a SN impostor but hold an SN II_n classification until further evidence of a nonterminal explosion is revealed. [Van Dyk et al. \(2006\)](#) found that the photometric and spectroscopic properties of SN 2002kg represent LBV outbursts in the S Dor phase. [Weis & Bomans \(2005\)](#) found that the position of SN 2002kg in Isaac Newton Telescope (INT) observations was coincident with the LBV NGC 2403-V37; however, the classifications in the public databases were not updated to reflect the new evidence.

3.7.3 Circumstellar Medium Geometry

In Section 3.1, I described the classic “Eiffel Tower” H α profile of SNe II_n. The actual H α profile may deviate from the classic profile, possibly complicating efforts to classify the object. The standard symmetrical SN II_n profile is formed from a spherical shell of H-rich CSM, but [Dwarkadas \(2011\)](#) find that a clump of CSM is sufficient to create SN II_n-like features. These high-density clumps may be formed as a result of instabilities in the CSM or the ejected material. Indeed, there seems to be a variety of H α profile shapes observed which may result from the CSM having a variety of different geometries, with the inclination to the line of sight also having an effect. [Harvey et al. \(2020\)](#) shows how different shell morphologies and viewing angles can affect line profiles. Those authors present models of CN shells, fitting to data trialling viewing angles and shell geometry. An example of a deviation from a symmetrical profile is shown in the middle spectral epochs of SN 2009ip (Fig. 3.7), where there may be a double-peaked H α profile, and at later epochs a “hump” appears on the red side of the profile. A further example of this profile diversity is the proposed subclass SN II_d (with a narrow P-Cygni on the H α line [Benetti, 2000](#)); examples of SNe II_d within the catalogue may include SN 2009kn and SN 2013gc ([Reguitti et al., 2019](#)). There are signs of an aspherical CSM exhibited by SN 1998S ([Leonard et al., 2000](#)), and the CSM may be contained in a disc around PTF 11iqb ([Smith et al., 2015](#)).

3.7.4 Flash ionisation supernovae and type Ia-CSM supernovae

Flash ionisation SNe are characterised by CSM interaction in the very early time optical spectra. Ultraviolet emission from the shock breakout of the SN ionises CSM surrounding the SN and then we see the optical CSM emission features when the CSM undergoes recombination (Khazov et al., 2016). Mass loss events directly preceding the SN may produce a confined CSM, resulting in the interaction lasting a short period of time, typically under ten days.

Since the CSM interaction that causes the SNe IIn phenomenon is an environmental effect, I include SNe IIn that may be SNe Ia-CSM or flash-ionisation SNe in my analysis; they might be counted in the lower-mass progenitor channel, or in the case of the flash ionisation SNe not be SNe IIn at all. In the sample, it is possible that some of the silver SNe IIn may show short-lived flash-ionisation behaviour where the progenitor undergoes mass loss shortly before the SN explosion, creating a confined CSM shell (Khazov et al., 2016). For example, SN 2007cm may exhibit a flash-ionisation spectrum on day 0, when there is a SNe IIn-like H α profile, but by day 15 this narrow feature has faded and the spectrum represents a fairly standard SNe II spectrum. When there is data to show the transition to a standard SNe II, I do not classify it as a SNe IIn. Khazov et al. (2016) have the “weak” SNe IIn PTF 11iqb in their sample of flash ionisation SNe. While many flash ionisation SNe evolve into standard SNe II with no subsequent CSM interaction (Bruch et al., 2021), others exhibit CSM interaction at later times, such as PTF 11iqb (Smith et al., 2015). Moreover, this flash-ionisation phase is similar to the spectra of many young SNe IIn, with a mostly featureless continuum and narrow CSM interaction signatures on the H α emission line. I therefore cannot rule out young SNe with single spectral epochs, and these are classified in the silver category. The CSM around SNe IIn is complex, and in order to better understand the nature of these objects, longer-term observations are needed to determine whether CSM interaction re-emerges. These weaker SNe IIn may indicate that the mass loss required for the SNe IIn-like features has a continuum starting from “normal” SN progenitors such as RSGs, rather than being exclusive to the massive LBVs. SNe that are classified at early times may be classified as SNe IIn owing to flash-ionisation features that endure for ~ 10 days post-explosion. Without follow-up data there may be a number of misclassifications, as some of these SNe might evolve into “standard” SNe II.

To be able to promote a silver-class object to the gold class, follow-up observations are required. The silver-class SNe IIn with a single spectrum and young SNe IIn with no immediate follow-up data may show strong CSM interaction over multiple epochs and be

promoted to the gold category if subsequent observations indicate ongoing interaction. The SN may have short-lived CSM interaction at later times and be more like the proposed SNIIn-L or SNIIn-P subclasses. Additional observations of the objects that I did not classify as SNe IIn may reduce uncertainty in their classification if the H II regions were omitted from the spectra. Observations of the H II regions in the host galaxies could be utilised to create templates that can be subtracted from the spectra to remove the contamination, and then CSM interaction features would become clearer if present. Conversely, if the only CSM interaction shown is fleeting and at early times (i.e., flash ionisation), with the spectrum then evolving into a standard SN II, we can demote a silver SN IIn to not being an SN IIn. Three such transients in this study: SN 2001fa, SN 2007cm, and SN 2014G were demoted.

SNe Ia-CSM are SNe Ia that explode in a dense CSM. However, perhaps the underlying thermonuclear spectral features may be hidden until later times when the SN ejecta and CSM become optically thin. This is another example of the great diversity in SNe IIn. While I include SNe Ia-CSM as a subset of SNe IIn (indeed, one of the gold class SNe IIn, SN 2008J may be a SN Ia-CSM), my sample may hold some still disguised SNe Ia-CSM. For example, SN 2006gy, the brightest SN ever observed at the time (classified as a SNIIn/SLSN-II) of observation may be a SN Ia-CSM (Jerkstrand et al., 2020). As the CSM interaction can act as a ‘veil’, hiding SN Ia characteristics and I can not rule out a SNIIn being thermonuclear in nature (despite this proportion expected to be small), I include SNe Ia-CSM in the SNIIn sample. When considering progenitor paths, this is an important consideration as a SNe Ia-CSM have WD progenitors and core-collapse SNe have massive progenitors.

3.7.5 H II region contamination leading to erroneous classifications

Most of the objects that are not SNe IIn were initially categorised as SNe IIn owing to contamination from the underlying H II regions. These H II region features include narrow $H\alpha$ and $[N II] \lambda\lambda 6548, 6584$ lines. If these lines are not considered, it is possible that the narrow features on top of the broad SN $H\alpha$ emission could be misinterpreted as signatures of CSM interaction, hence leading to an erroneous classification of SNIIn. An example of a SN with such H II contamination that has a primary classification of SNIIn in online databases is SN 2009kr (see Fig. 3.11). This SN has multiple spectral epochs with consistent H II contamination. Moreover, Steele et al. (2009b) point out the H II contamination of SN 2009kr, but the object still retains a primary SNIIn classification in OSC. This highlights the importance of keeping transient entries on

public databases up to date, to reflect new data. In cases where there may be H II region contamination superimposed upon an H α profile that shows genuine CSM interaction and there is blending with the [N II] lines, my classification scheme could be applied to H β where the relatively narrow features and intermediate width components may be present (Filippenko, 1997).

Template-matching routines such as SNID are a popular tool for the classification of SN spectra. These routines rely on templates of archetypal members of a spectral class. The heterogeneity found in SNe IIn spectra may cause issues with such template-matching methods that have a limited number of templates for less-common SN classes. This is apparent when we find that only 32 of the targets (all from the gold and silver groups) were matched to an SN IIn template by SNID (see Table 3.6). In the case of SN “impostors,” photometric data or late-time observations are required to differentiate an object as a gap transient rather than an SN IIn. Similarly, SNID classifies 23 objects in the sample as AGNs, but I do not identify any genuine AGNs in the sample, as none lie near the centre of their host galaxy and also the characteristic nebular [O III] $\lambda\lambda$ 4959, 5007 lines seen in AGN were not present.

For the SNe with H II region pollution, if a spectrum has low resolution ($R \lesssim 500$), or if a noisy spectrum is heavily smoothed, it is possible that the [N II] lines blend with H α to make an illusion of an SN IIn-like profile. However, this blending may be identified when considering the blending would produce an asymmetric profile as the [N II] 6584 Å line is stronger than the 6548 Å line in H II regions. Spectroscopic templates of the gold SNe IIn will be produced in the hope of increasing the sample of reference templates to better reflect the great diversity we see in SNe IIn.

3.8 Conclusions

We have outlined a simple classification scheme for SNe IIn which takes advantage of their characteristic H α profile. This was applied to a sample of 115 SN IIn candidates at $z < 0.02$ which have publicly available data or data that was collected from the original observers. The sample is based on a catalogue collected for an environmental survey of SNe IIn, and candidates outside of this sample (e.g., at a higher redshift) are beyond the scope of this project. Here I briefly summarise my key findings and recommendations for future work.

1. I compiled a catalogue of 115 reclassified transients that have at some point held an SNIIn classification.
2. 87 of the 115 SNe have been reconfirmed to be SNe IIn based on their multicomponent H α profile.
3. Gold SNe IIn exhibit CSM interaction over multiple epochs. Silver-category transients are consistent with SNe IIn, but they may have short-lived CSM interaction in the case of transitional objects (e.g., when the classification evolves from SNIIn to SNIIP), or they have quite limited data. Silver SNe IIn can be promoted to gold SNe IIn with more data from follow-up observations. Objects can also be demoted if it becomes apparent that the CSM interaction features are due to flash ionisation.
4. There are 37 gold and 50 silver category spectra.
5. 28 of the SNe are reclassified as not being SNe IIn. In most cases, H II region lines contaminate the spectrum and were interpreted as CSM interaction. Other sources of misclassification were gap transients, or flash ionisation SNe.
6. 34 of the SNe IIn have a primary classification from the OSC that is not a SNIIn, and TNS has twelve such cases.
7. OSC reports that eleven of the targets I classified as not being SNe IIn are SNe IIn, and TNS reports 18 such cases.
8. The public databases OSC and TNS disagree on the classification of 51 of the objects; however, TNS primary classifications seem more reliable, despite lacking classifications for twelve objects.
9. SNID classifies 15 out of 37 gold SNe IIn as SNe IIn, 14 out of 50 silver SNe IIn as SNe IIn. Even where SNID finds a match to a SNIIn spectrum, other factors can overturn this classification. The three SNe with early narrow components which disappear over time, consistent with flash-ionisation signatures had a SNID match to a SNIIn spectrum.
10. Inconsistencies and ambiguities in the classification of SNe IIn may be due to the great range in properties that SNe IIn exhibit. The heterogeneity in the spectral features is perhaps a result of multiple progenitor paths and different environments.

To solidify classifications of SNe IIn, follow-up observations are vital. They provide information on the evolution of the spectra, allowing estimations of the duration of

CSM interaction. Furthermore, when an SN IIn classification is found to be erroneous, it is important that the new data are reflected in public databases, particularly in cases where specific SNe have been studied in depth in the literature. My classification scheme should be applied to a larger sample of SN IIn candidates, since the current catalogue is limited. My SN IIn classifications will be integrated into the survey of SN IIn environments presented in the following chapter.

Chapter 4

The H α environments of type IIIn supernovae

4.1 Environmental studies of supernovae

As discussed in Chapter 2, the local environment of a SN within its host galaxy can offer information on the possible progenitor systems. For example, one can examine the association of SNe to ongoing star-formation as traced by H α emission. H α emission indicates a characteristic time-scale of under 10 Myr (Tamburro et al., 2008; Haydon et al., 2020; Flores Velázquez et al., 2020). Generally speaking, CCSNe trace regions of recent star formation and the most massive stars may trace ongoing star formation. Possible high mass and short lived progenitors, such as LBVs, would be expected to be found in regions of ongoing star formation, which would be traced by H α emission.

In the case of associating star formation to SN locations, James & Anderson (2006); Anderson et al. (2012) developed the pixel statistics technique, normalised cumulative ranking (NCR) which utilises H α images of SN hosts. This technique will be explained in detail in Section 4.3.

Using NCR analysis, Anderson & James (2008) found that SNe IIIn in their sample did not follow the H α emission in their hosts. Those authors did, however, note that the SNe IIIn more closely followed near-ultraviolet (NUV) emission when comparing data from the *Galaxy Evolution Explorer* (GALEX). NUV traces recent star-formation rather than ongoing star-formation with a characteristic time-scale of over 19.6 Myr for GALEX NUV (Haydon et al., 2020).

[Anderson et al. \(2012\)](#) set out to constrain progenitor properties using the SN association to H α and NUV emission. They found that there was a mass ladder in terms of association to H α emission with the most massive progenitors being most associated with ongoing star formation, owing to their shorter lifetimes. It was found that the mass sequence, starting with SNIc as the most massive and most associated, went as such,

$$\text{SNIc} \rightarrow \text{SN Ib} \rightarrow \text{SN II} \rightarrow \text{SN Ia}.$$

The authors noted that the SNe IIn in their sample did not trace ongoing star formation as traced by H α emission, and on average had weaker association than other SNe II. They did, however, follow recent star formation as traced by near-UV emission. They suggested that this result indicated that the majority of SNe IIn do not have high-mass progenitors, such as LBVs. Furthermore, [Anderson et al. \(2014\)](#) expanded the sample of SNIa (on the bottom rung of the mass ladder) by 102 transients and once again found there was little association with H α or NUV emission. However, [Smith & Tombleson \(2015\)](#) noted that some LBVs are not associated with clusters of O-stars as one would expect of a massive progenitor. Instead those authors suggest that many LBVs may form in binary systems where the LBV is a mass gainer and a WR star is a donor in situ in the home O-star cluster.

[Haberman et al. \(2014\)](#) investigated the environments of SNe IIn and SN impostors. There were 24 SNe IIn in their sample and again it was found that these transients did not follow star formation as traced by H α , utilising the NCR method. The authors conclude that as some SNe IIn do have LBV progenitors, there may be multiple progenitor channels for SNe IIn as the NCR results suggest that LBVs are not the only progenitor route.

Another way the environments of SNe have been probed is the radial distributions of SNe in terms of the observed flux in a particular filter (we describe this method in Section 4.4). [Haberman et al. \(2014\)](#) found that the radial distribution of SNe IIn in their sample was very different from the radial distribution of SNe Ic, where SNe Ic were much more centrally concentrated. This suggests that the two classes arise from different stellar populations. Other environmental studies have used such radial analysis, for example, [Haberman et al. \(2010\)](#) investigated the radial distribution of 178 CCSNe in terms of *R*-band and H α emission. The authors found that when the hosts are split into disturbed and undisturbed galaxies, there was a central excess of the higher mass progenitor SNe (SNe Ib, Ic and Ib/c) in the disturbed hosts. The authors conclude that this may

suggest a stellar initial mass function (IMF) biased towards high mass progenitors at the centre of disturbed hosts. Moreover, [Habbergham et al. \(2012\)](#) expanded on the previous work on SN distribution in disturbed galaxies. The authors found that there was a significant increase of stripped-envelope SNe in the centre of the hosts further suggesting a top-heavy IMF and that in undisturbed galaxies, the distributions of SNe Ib and SNe Ic were very different, with the authors concluding that this may be due to a metallicity gradient in the hosts. Additionally, IFU studies have found that there is a group of SNe IIn in old populations and another group that is found in younger populations ([Galbany et al., 2018](#)). Moreover, NCR studies of the LMC and M33 have focused on the NCR distributions of SN progenitor type stars such as RSGs and LBVs, finding that LBVs in those hosts did follow star-formation as traced by H α emission ([Kangas et al., 2017](#)).

Additionally to the study of SN environments in terms of the association to star formation using H α emission, one can measure the local metallicity of the SN sites. [Habbergham et al. \(2014\)](#) use the O3N2 diagnostic ([Pettini & Pagel, 2004](#)) to compare the metallicity at the sites of different SN classes. It was found that SNe IIn sites are more metal rich than those of SNe IIP and that the local metallicities of SN impostors tend to be lower than for types Ic, IIn or IIP. [Taddia et al. \(2015\)](#) use optical spectra of the environments of 60 interacting transients (SNe IIn, SNe Ibn and SN impostors) using data from archives and the Nordic Optical Telescope. It was found that the impostors in the sample were generally in regions of lower metallicity when compared to SNe IIn. SNe IIn similar to SN 1998S were found in higher metallicity regions than SNe IIL and SNe IIP, and long lasting SNe IIn, such as SN 2005ip and SN 1988Z, were in regions of lower metallicity as seen in the environments of SN impostors. The authors conclude that these different metallicities found among SNe IIn suggests there may be multiple progenitor paths rather than solely LBVs. They go on to suggest that LBVs may be the progenitors of the long lasting, SN 1988Z-like SNe IIn and that RSGs may account for the SN 1998S-like transients.

4.1.1 Environmental tracers of underlying stellar population

Star formation is triggered by the collapse of massive clouds of neutral, molecular hydrogen. After enough material has collapsed such that the central pressure is sufficient to initiate the fusion of hydrogen, the star is born. In these stellar nurseries, massive stars are born, and depending on how massive those stars are, also die there. Young massive stars are hot and radiate ultra-violet light energetic enough to ionise the surrounding

neutral hydrogen in the gas cloud. This process forms an H II region (Kennicutt, 1998). When the ionised hydrogen recombines, light is emitted. The Balmer series is part of this recombination process that emits optical light, such energy level transitions include $H\alpha$, $H\beta$, $H\gamma$ and $H\delta$. The Balmer series is the energy transition to the $n = 2$ energy level. $H\alpha$ is the transition between from $n = 3$ and in the rest frame emits a photon at a wavelength of 6563\AA . $H\beta$ is the transition from $n = 4$, emitting a photon at 4861\AA . $H\gamma$ is the transition from $n = 5$, emitting a photon at 4341\AA and $H\delta$ is the transition from $n = 6$, emitting a photon at 4102\AA . The strongest hydrogen Balmer line is $H\alpha$ and it can be used to trace H II regions and therefore ongoing star formation.

The clouds in which stars form have a lifespan and the tracers of star formation have characteristic time scales. As mentioned in Section 4.1, Haydon et al. (2020) discuss the characteristic timescales of different emission wavelengths. $H\alpha$ emission traces **ongoing** star formation. Haydon et al. (2020) find recent star formation (timescales over 10 Myr) is traced by Galaxy Evolution Explorer (GALEX) FUV and NUV emission (see also Tamburro et al., 2008; Flores Velázquez et al., 2020). GALEX NUV has a timescale of 19.6–39.1 Myr and GALEX FUV has a timescale of 17.1–34.2 Myr (Haydon et al., 2020).

4.1.2 Sample for environmental analysis

I use the catalogue described in the the previous chapter where the SNe IIn are drawn from the OSC within a redshift of 0.02. This redshift limit is imposed to ensure the host galaxies are close enough that $H\alpha$ regions can be detected and resolved with the ground-based, 2m-class telescopes used in this work (the resolved H II regions in my redshift cut-off will be a few hundred parsecs across). The selection of SNe IIn is robust, using the spectral reclassifications from Chapter 3 and discarding the non-SN IIn transients. I use the gold and silver spectral categories and also include the SNe that were not reclassified due to a lack of spectral data. Another limit on the SNe used in the environmental analysis is that I use a cut on the ratio between the major axis and minor axis of each host, these axes are taken from the NASA/IPAC Extragalactic Database (NED; Helou & Madore, 1988). This ratio cut off is 4:1, the same as used in previous studies such as in Habbergham et al. (2014). This ratio is used so that the hosts aren't so inclined that the SN position is ambiguous due to false association with the emission in the line of sight.

4.2 Observations

In the Northern Hemisphere, I utilised the Liverpool Telescope (LT; [Steele et al., 2009b](#)) and Isaac Newton Telescope (INT) at the Observatorio de Roque de las Muchachos on La Palma in the Canary Islands. For these observations on the LT, I used the IO:O instrument¹. I use the Wide Field Camera (WFC) on the INT². In the Southern Hemisphere, I use the Las Cumbres Observatory 2m (LCOGT 2m) at Siding Springs Observatory, New South Wales, Australia ([Brown et al., 2013](#)). I use Spectral³ on the LCOGT 2m.

My observations consist of 3×300 s exposures using the appropriate redshifted $H\alpha$ filter and a single 300 s exposure in the r' -band with 2×2 binning. These observations span 2019 to 2021. I limit these observations to nearby ($z < 0.02$) hosts as I require that HII regions are resolved for the pixel statistics described in Section 4.3, this exposure time is consistent with previous NCR work. Major and minor axes for each host were taken from the SIMBAD Astronomical Database ([Wenger et al., 2000](#)). Both IO:O and Spectral have a $10'$ field of view and all surveyed hosts were contained within the field of view. The LT has redshifted $H\alpha$ filters covering the range to around $z = 0.04$ and all of my targets are within $z = 0.02$. This redshift limit is consistent with previous work and corresponds to resolutions $\sim 15 - 400$ pc/" in this redshift range. I only use the LCOGT 2m for nearby targets as there is only a rest-frame $H\alpha$ filter. The filter passbands for the LT $H\alpha$ filters and the passband of the LCOGT 2m $H\alpha$ filter are shown on Fig. 4.1.

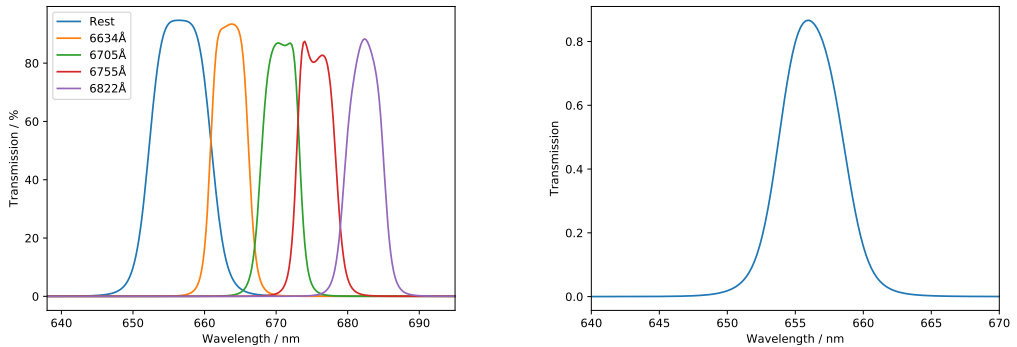


FIGURE 4.1: Filter transmission plots for the LT $H\alpha$ filters (*left*) and the single LCOGT 2m, rest frame $H\alpha$ filter (*right*).

¹<https://telescope.livjm.ac.uk/TelInst/Inst/IOO/>

²<https://www.ing.iac.es//Astronomy/instruments/wfc/>

³<https://lco.global/observatory/instruments/spectral/>

TABLE 4.1: The available H α filters on the LT and LCOGT 2m with their central wavelengths and corresponding redshift.

Telescope	Central wavelength (\AA)	Redshift (km s^{-1})
LT	6563	0.00
LT	6634	3250
LT	6705	6490
LT	6755	8870
LT	6822	11,800
LCOGT 2m	6563	0.00

4.2.1 Data reduction

Raw data from the LT and LCOGT 2m are reduced by the respective standard pipelines (Barnsley et al., 2016; Brown et al., 2013). These data were then downloaded from their respective data archives. The INT data arrived raw and un-reduced from the original observers, Prof. Philip James and Dr. Susan Percival.

The INT data were reduced using Python with astropy (The Astropy Collaboration et al., 2013). The INT data (from 2019) consists of biases, flats and science images (three H α and one R -band). Bias images are required in order to correct for imperfections in the detector CCD and also to subtract the bias level from the science images. Flats are required to correct for the imperfections in the optics of the telescope (mirrors etc). Flats also correct for the pixel-to-pixel sensitivity differences of the CCD. Flats and biases were taken on each night of observation with all the telescopes used in this thesis (LT, INT and LCOGT 2m). The bias frames were combined into a master bias image. The flats (with flats in each filter) were combined and the master bias was subtracted from the combined flat images to create a master flat. The INT data, using CCD 4 on WFC were windowed such that the field of view was 10' like the LT images. The science images were then bias subtracted with the master bias and flat corrected with the master flat by dividing the image by the master flat image.

The NCR analysis requires continuum-subtracted images. I use the methods in Anderson et al. (2012) but using IRAF (Tody, 1986), astropy (The Astropy Collaboration et al., 2013) and specutils (Earl et al., 2022). Continuum subtraction is necessary due to remove the continuum emission transmitted through the narrowband filter, to leave a pure emission line image.. To begin, I start with this reduced H α and r' / R -band images, example H α (6634 \AA) and r' -band images of the host of PTF 11iqb, NGC 151 are shown in Fig. 4.2.

Over the course of an observing night, the image of the host will slightly move on the

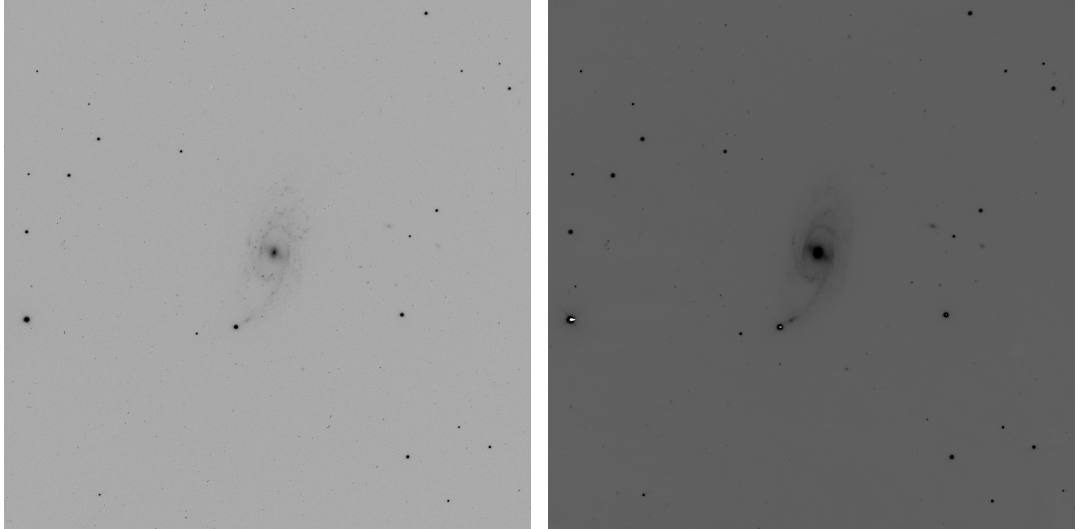


FIGURE 4.2: An example of the $6634 \text{ \AA} \text{ H}\alpha$ (*left*) and r' -band images (*right*) from the LT, in this case the host is NGC 151, the host of PTF 11iqb.

CCD as tracking is not perfect. This effect may be greater between changing the filters from the appropriate redshifted $\text{H}\alpha$ filter and the r' -band filter. Therefore, the images need to be aligned. The first $\text{H}\alpha$ image is taken as the reference image to which the other images are aligned. The reference image is also aligned to itself as a sanity check and also to keep the level of processing of each image the same. IRAF (Tody, 1986) is used to align these images. First the `starfind` routine is used on each image to find unsaturated stars with a maximum pixel value limit and detection limit along with an estimate of the FWHM of the point source function (PSF) of the stars (a value of $2.5''$ for the FWHM of the PSF was used most often here). `starfind` outputs a text file with the pixel values of all the stars it found in the image.

Next, the `xyxymatch` is used to match the stars in each image to each other. `xyxymatch` takes the reference `starfind` list and compares it to the stars found in another images, this is the input list. An example of matched stars is shown in Fig. 4.3 A matching limit in terms of the numbers of pixels between the stars being matched is specified, which can be up to \sim five pixels at this stage. The output match file holds the stars that were successfully matched along with the pixel coordinates in each image. Each `starfind` star list is matched with the stars from the reference image. After the stars are successfully mapped, the shifts needed to align the images must be calculated. To do this next stage, the routine `geomap` is used. `geomap` takes the matched star files and calculates the required shift and outputs a database file with the shifts. This shift is then used in conjunction with the matched star files in the next stage of the alignment, `geotran`. `geotran` takes the unaligned image, the shift file and the matched star file

and performs the shift to align the image to the reference image. This then produces an aligned image. To produce the final, aligned $H\alpha$ image, the three aligned images are combined with a median combine (in order to eliminate cosmic rays and in some cases, satellite streaks) using the `imcombine` command. I now have the aligned $H\alpha$ and r' -band images. To check that the alignment of the $H\alpha$ image to the r' -band was successful, I use `starfind` again on each aligned image and use `xyxymatch` to match the r' -band image to the $H\alpha$ images. In this case, the matching pixel limit is much more strict as the alignment must be sub-pixel level for effective continuum subtraction, this matching tolerance is set to 0.1 pix. The output matched star list is then used later on in the production of the continuum subtracted images.

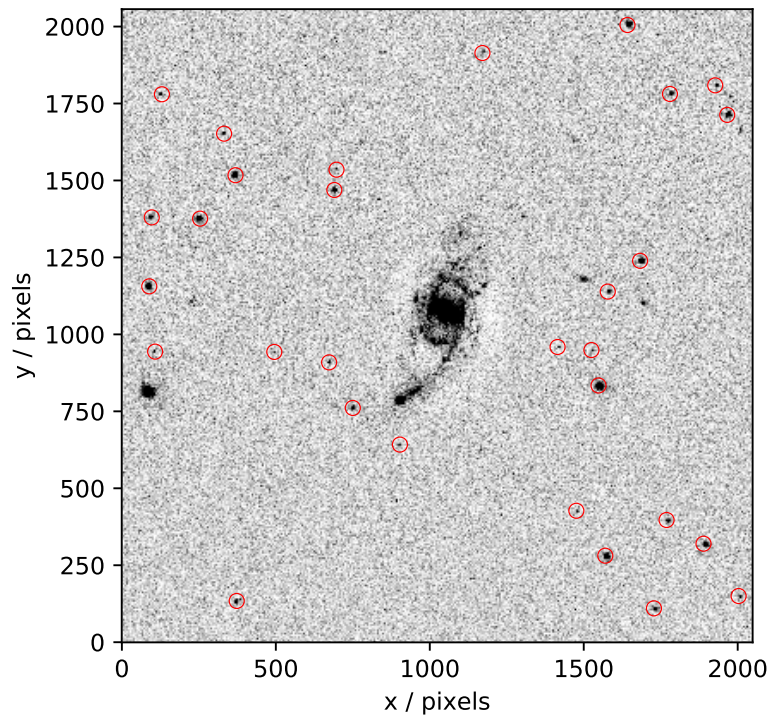


FIGURE 4.3: An example of matched, non-saturated stars as detected by the IRAF routine, `xyxymatch`. The stars are circled in red, in this case the image is the host of PTF 11iqb, NGC 151.

The remainder of the data reduction/production of the continuum subtracted images is now done using Python with `astropy`. The next step in the journey to a continuum subtracted image is flux scaling the r' image to the $H\alpha$ image. The non-saturated stars are used for this scaling. The matched star file is from the `xyxymatch` matching of the common unsaturated stars in the aligned r' -band and $H\alpha$ images. Using this list of common, non-saturated stars, I use the Python package, `photutils` (v 1.4.0 [Bradley](#)

et al., 2022). Using the common, unsaturated stars, aperture photometry is calculated for each star, see Fig. 4.3 for an example of the stars used in the aperture photometry. Flux calibration is not necessary for this work so all the fluxes are in terms of the pixel values. I now have a list of fluxes for each star in both bands. The fluxes of the stars scale linearly. The gradient of this line, or the average flux ratio of the stars is then the scaling factor to scale the r' -band to the $H\alpha$. The scaling factor is applied to the r' -band image and this scaled image is subtracted from the $H\alpha$ image, producing a continuum subtracted image as shown in Fig. 4.4. A 2D background is modelled with a (typically second order) polynomial fit using `photutils`, with the model using only the region around the host as to not include the host itself in the calculation of the background model (this is just calculated for the cropped image). This background is then subtracted from the continuum subtracted image. Continuum subtraction can leave some artefacts that can interfere with these pixel statistics, so these are masked out. Furthermore, any saturated stars are masked out as these will have large artefacts due to CCD bleeding. Finally, the images are cropped so that most of the image is the host (usually a box 1.5 times the size of the semi-major axis of the host as stated on SIMBAD) as shown in Fig. 4.4.

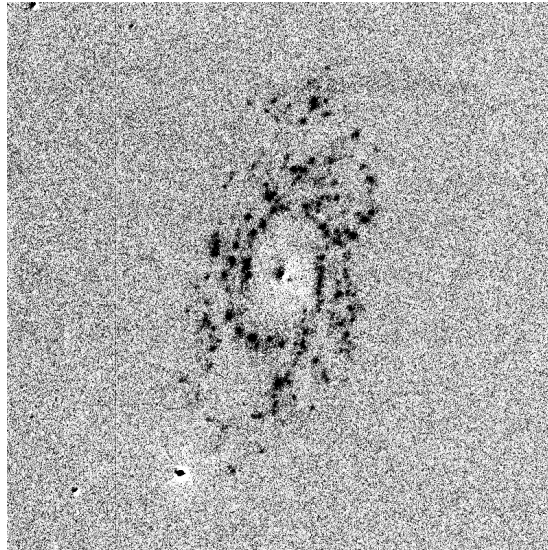


FIGURE 4.4: An example of a cropped continuum subtracted $H\alpha$ image (without masking), in this case it is NGC 151, the host of PTF 11iqb.

The PSF matching technique was trialled here. This is where the PSF of one image is matched with the other. In this case, the PSF of stars in the r' -band image are larger (a larger FWHM) than the $H\alpha$ PSFs. The $H\alpha$ star PSFs are then smoothed to conform with the PSF of the r' -band. This was done in an attempt to eliminate the artefacts (sometimes known as “doughnuts”) from the continuum subtractions. However, it was

found that this effectively reduced the resolution of the images and resulted in the H α emission regions being artificially spread out. This method was therefore abandoned.

4.3 Pixel statistics: normalised cumulative ranking

Previous studies that associate SN locations with H α emission focussed on the distance of the SN from an emission region (e.g. [Bartunov et al., 1994](#); [van Dyk et al., 1996](#)). However, that method may suffer from ambiguities in the identification in emission regions and also does not account for low surface brightness areas. NCR was first implemented by [James & Anderson \(2006\)](#) and subsequently utilised in environmental studies (e.g., [Anderson & James, 2008](#); [Anderson et al., 2012](#); [Habergham et al., 2014](#)). NCR traces the association of a pixel with some emission, in this case, to H α emission and therefore, the association to ongoing star-formation. Furthermore, the NCR statistic effectively gives the fraction of observed H α emission in low surface brightness areas of the host. NCR assigns every pixel a value between zero and one. A zero NCR value indicates no H α emission and therefore no association with ongoing star-formation. An NCR value of one indicates the strongest star-forming pixel within the entire galaxy image. A mean NCR value of 0.5 and a flat distribution would indicate a distribution that perfectly follows the H α emission (or indeed, whatever emission is being measured).

NCR is calculated by ordering the the pixel values of the continuum-subtracted H α image in ascending order, summing these values and normalising by the sum.

The NCR value of a pixel may be written as,

$$\text{NCR}_i = \frac{\sum_1^i x_i}{\sum_1^N x_j}, \quad (4.1)$$

where i is the current pixel, j is an iteration variable, N is the total number of pixels and x is the pixel value.

After continuum subtraction and sky background correction, some pixels will have negative values. Pixels before the sum turns positive are assigned an NCR value of zero.

To compute the NCR value, the average NCR value of a 3×3 pixel bin centred around the target pixel is taken. I apply this method to this sample and then make cumulative distributions. I split this sample into the spectral categories in Chapter 3 and then

compare these distributions to each other and also a hypothetical 1:1 relation which represents an NCR distribution that ‘perfectly’ follows the emission.

We can then implement Anderson-Darling (AD, [Anderson & Darling, 1952](#); [Stephens, 1974](#)) and Hartigan dip tests (HDT, [Hartigan & Hartigan, 1985](#)), as well as the bimodality coefficient ([SAS Institute, 1989](#)) in order to test whether there may be multiple populations of SNe IIn in terms of their association to ongoing star-formation as traced by H α emission.

The possible uncertainties in the NCR method are described in [James & Anderson \(2006\)](#). Those authors test the associated errors to assess the effect on the analysis. The most apparent error in the NCR analysis is the uncertainty in the SN location. [James & Anderson](#) used the median NCR value in the 3×3 bin surrounding the target pixel and found there was no significant difference between this and the exact SN pixel NCR value. Those authors found that the NCR method was robust for SN positional uncertainties at the $1'' - 2''$ level. The SNe IIn catalogue in this work is constructed from a variety of surveys/facilities with their own positional uncertainties. These results are robust even when assuming a SN is discovered by a survey with a relatively large positional uncertainty, for example, ASAS-SN. ASAS-SN has a median astrometric uncertainty of $1.17''$ and other surveys have sub-arcsecond positional uncertainties, with ZTF having a median uncertainty of $0.12''$ ([Yaron et al., 2019](#)). Furthermore, the effect due to the sky-level chosen and pixel-to-pixel noise was found to be not significant and the NCR method to be robust. [Crowther \(2013\)](#) note that the lifetimes of smaller H II regions are dictated by the lifetimes of (perhaps the single) massive stars that form them so are short lived compared to large H II complexes (this could lower the NCR value of SNe within them, as suggested by [Kangas et al., 2017](#)). The scales being studied here and in previous studies are in the order of 100 pc so the NCR analysis in these cases would not be sensitive to these small regions of emission. [Anderson et al. \(2012\)](#) found that the NCR method may assign a zero value to SNe in regions that have real, but low level emission due to still the cumulative sum being negative. The image quality may effect the NCR values, for example, in poor seeing the observed emission regions may ‘spread’ out, similar to what was seen in the PSF matching trial, where otherwise zero NCR SNe would have a non-zero NCR value. [Kangas et al. \(2017\)](#) investigated the effect of distance on NCR values and found that when images of the LMC were degraded to simulate a similar galaxy at higher redshift. Those authors found that while the overall effect was small, the ‘spreading’ of the emission regions as distance was increased may increase the NCR value of low NCR value SNe. Conversely, when adding noise, they found that low value NCR value SNe were lowered further, increasing the number of zero

NCR SNe. Generally, however, [Kangas et al.](#) found that the effect of distance (spatial resolution) and noise was not significant on the results of the NCR analysis and were consistent with the findings of [Anderson et al. \(2012\)](#).

As previously discussed, [Anderson & James \(2008\)](#) found that SNe IIn in their sample did not follow the $H\alpha$ emission in their hosts. Therefore in that sample, the SNe IIn did not trace ongoing star formation, but did follow NUV emission as observed by *GALEX*, suggesting SNe IIn may follow recent, rather than ongoing star formation.

[Anderson et al.](#) suggested that this indicated that the majority of SNe IIn do not have high-mass progenitors, such as LBVs (see also, [Haberman et al., 2014](#)). However, [Smith & Tombleson \(2015\)](#) noted that LBVs are often not associated with clusters of O-stars as one would expect of a massive progenitor. Instead those authors suggest that many LBVs may form in binary systems where the LBV is a mass gainer and a WR star is a donor in situ in the home O-star cluster.

4.4 Radial analysis

The radial distribution of SNe (i.e, the distribution relative to the centre of the galaxy in terms of the galaxy light) can indicate the general stellar population. In spiral galaxies, the bulge tends to have an older population while the discs have younger populations with active star formation. Furthermore, the spatial distribution within a galaxy may provide an analogue for metallicity as there is a metallicity gradient ([Henry & Worthey, 1999](#)) with central regions having a higher metallicity than further out in the disc regions. Progenitor mass loss may be influenced by the metallicity of the star. The rate of mass loss in a progenitor may increase with increasing metallicity due to metallicity dependent line driven winds ([Puls et al., 1996](#); [Mokiem et al., 2007](#)). Therefore, regions of higher metallicity may be inhabited by more stripped envelope SNe (i.e. types Ib and Ic) as these winds help the progenitors lose their outer layers.

However, the radial distribution of some SN classes may not be explained solely by metallicity gradients. SNe Ibc are found to be generally more centrally located than other SN classes ([Anderson & James, 2009](#); [Haberman et al., 2010, 2012, 2014](#)). SNe Ibc also follow the $H\alpha$ emission better than the other SN classes ([Anderson et al., 2012](#); [Haberman et al., 2014](#)). However the $H\alpha$ NCR values are not correlated to the radial distribution, as shown by [Anderson et al. \(2012\)](#) as the brightest $H\alpha$ emission may be in the spiral arms. This central distribution of SNe Ibc was also seen in interacting/disturbed

hosts (Habergham et al., 2012) where there is less of a pronounced metallicity gradient (if one exists at all, Kewley et al., 2010).

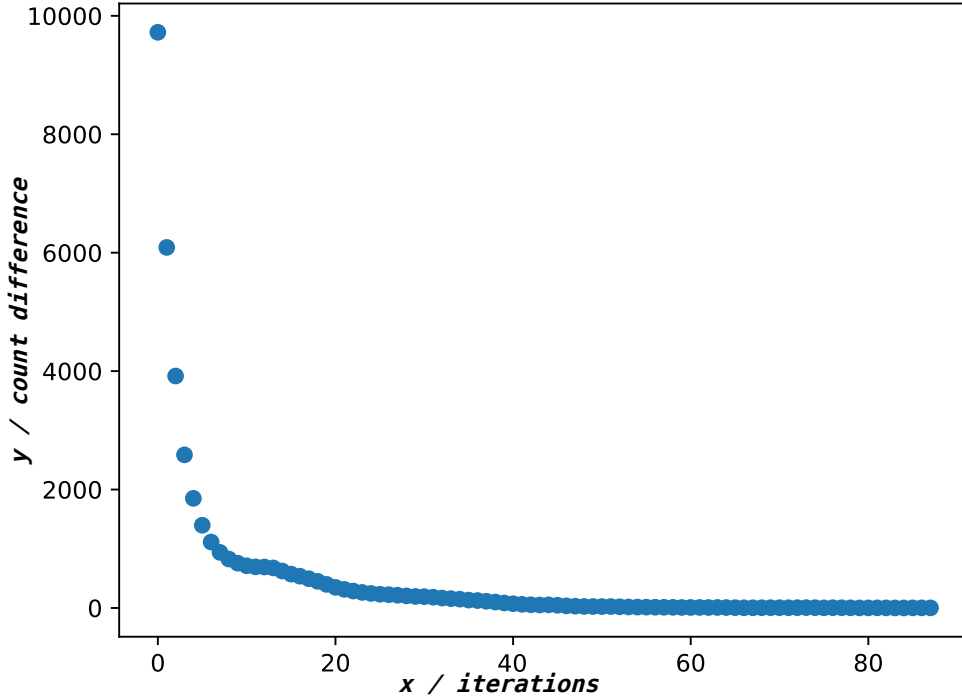


FIGURE 4.5: The radial light profile of the host of PTF 11iqb, NGC 151 in the r' -band. The y-axis is the difference in the contained flux between two ellipses. This profile flattens out when the sky level is reached. The x-axis is the number of iterations (i.e., number of expanding ellipses used).

I measure and compare the radial distribution of these SNeII in terms of the r' -band and $H\alpha$ flux in their host galaxies. I adopt the method used in Anderson & James (2009). This is achieved by calculating the ratio of the flux contained within ellipses that cover the extent of the host r' -band light and the ellipse enclosing the SN position. Ellipse parameters were taken from NED (Helou & Madore, 1988). For each galaxy, the ellipse covering the total r' -band emission from the host, the semi-major axis is increased by 2.5" until the ellipse has reached the sky level on the r' -band image. The sky level of the image is determined such that the difference in enclosed flux between ellipses has flattened out to being around zero. This ellipse is then used with the continuum subtracted $H\alpha$ image. This gives us $Fr(R)$, the fraction of r' -band light contained within the SN ellipse and $Fr(H\alpha)$, the fraction of $H\alpha$ emission contained in the SN ellipse. Therefore each SN will have a $Fr(R)$ and a $Fr(H\alpha)$ value of between 0 and 1, where 0 indicates the SN is at the centre of the host and a value of 1 indicates the SN is at the

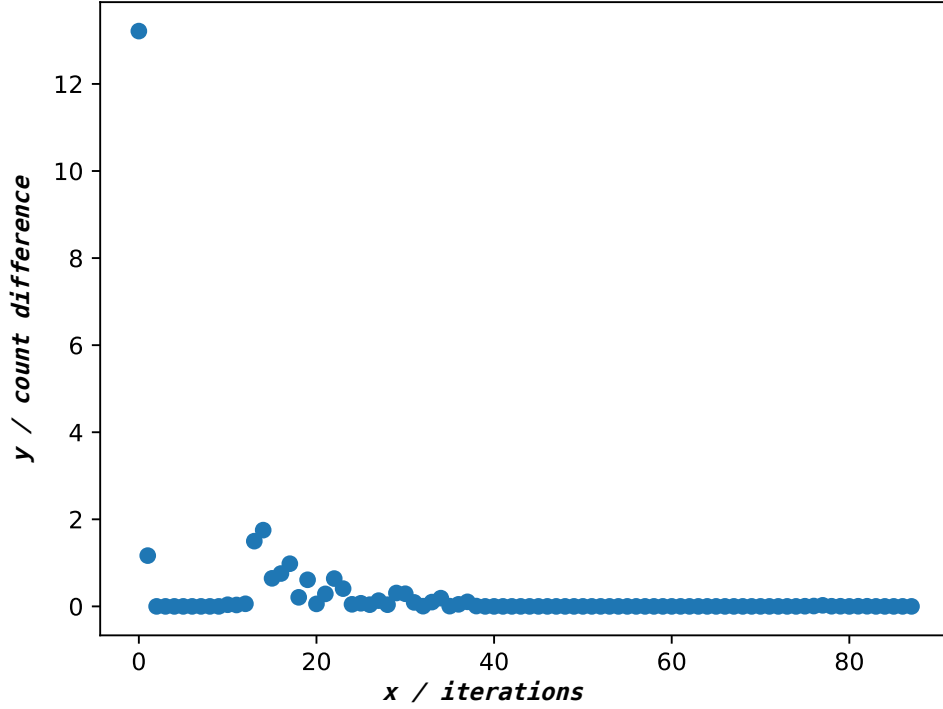


FIGURE 4.6: The radial light profile of the host of PTF 11iqb, NGC 151 in $H\alpha$. The y-axis is the difference in the contained flux between two ellipses. This profile flattens out when the sky level is reached. The x-axis is the number of iterations (i.e. number of expanding ellipses used) and this number of iterations is from the r' -band radial profile

extreme periphery of the host. In Fig. 4.7 I present an example of this radial analysis, where I show the ellipse enclosing the full r' -band flux of the host galaxy and the ellipse that just encloses the SN pixel. Some hosts with smaller radii are excluded from the radial analysis (with a semi-major axis less than $\sim 1'$) in order for a well defined radial profile to be constructed. Hosts with smaller semi-major axes therefore have blank $Fr(H\alpha)$ and $Fr(R)$ values in Table 4.2. One caveat to note however, is that (consistent with previous studies) I do not correct for $H\alpha + [NII]$ flux due to AGNs (as can be seen in the central peak in NGC 151).

Using these statistical measures, I will now analyse the SNIIn populations in host galaxies within $z = 0.02$.

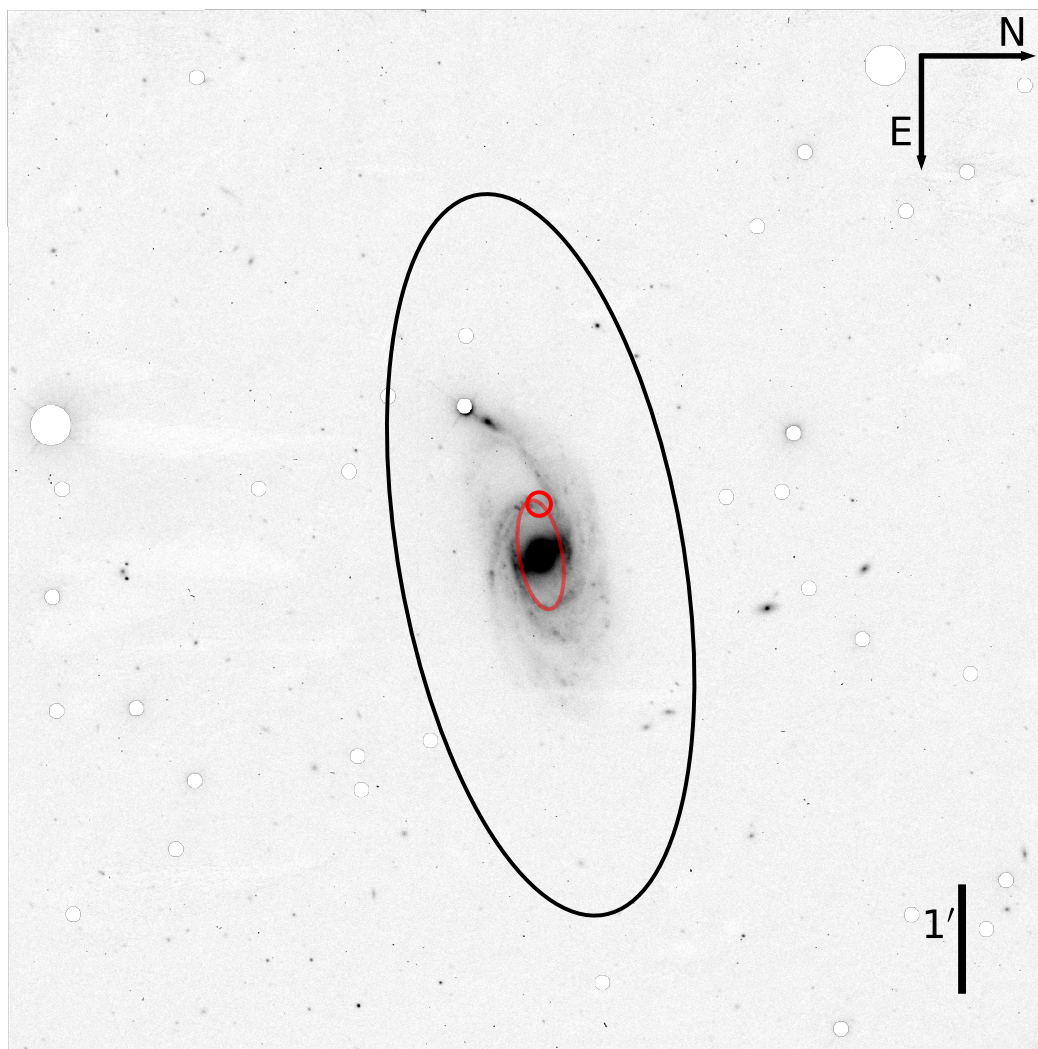


FIGURE 4.7: An example of the radial analysis employed in this chapter. Shown is the r' -band image of the host of PTF 11iqb, NGC 151. The transparent red ellipse just intercepts the SNII site (red circle). The black ellipse encloses the galaxy r' -band flux. These ellipses are also used in the continuum subtracted $H\alpha$ image. In order to measure the emission from the host, foreground stars were masked.

4.5 Results from the pixel statistics analysis

In Table 4.2 I present this full sample of 79 SNe IIn with their NCR values, classification from Chapter 4, $\text{Fr}(\text{H}\alpha)$ values, $\text{Fr}(\text{R})$ values, and the telescope used in the observations. Most of these observations were from the Northern Hemisphere, however three of these SNe IIn are southern targets observed with LCOGT 2m. The Southern Hemisphere sub-sample is somewhat small due to the lack of redshifted $\text{H}\alpha$ filters available at LCOGT 2m.

TABLE 4.2: The sample of 79 SNe II_n and their hosts with the discovery date, coordinates, NCR value, Fr(H α) values, Fr(R) value, the telescope I used for the observation and the classification from Chapter 3.

Name	Disc. Date	Host	R.A. (J2000)	Dec.	Telescope	NCR value	Classification	Fr(H α)	Fr(R)
SN 2005db	2005/07/19	NGC 214	00:41:26.79	25:29:51.60	LT	0.387	Gold	0.528	0.526
SN 2005gl	2005/10/05	NGC 266	00:49:50.02	32:16:56.80	LT	0.765	Gold	0.644	0.526
SN 2010jj	2010/11/03	NGC 812	02:06:52.23	44:34:17.50	LT	0.000	Gold	0.103	0.179
SN 2003G	2003/08/01	IC 208	02:08:28.13	06:23:51.90	LT	0.000	Gold	-	-
SN 2008J	2008/01/15	MCG -02-07-33	02:34:24.20	-10:50:38.50	LT	0.808	Gold	0.069	0.077
SN 2000eo	2000/11/16	MCG -02-09-03	03:09:08.17	-10:17:55.3	LT	0.000	Gold	-	-
SN 2006gy	2006/09/18	NGC 1260	03:17:27.06	41:24:19.5	LT	0.907	Gold	0.014	0.030
SN 1989R	1989/10/14	UGC 2912	03:59:32.56	42:37:09.20	LT	0.199	Gold	-	-
SN 1995G	1995/02/23	NGC 1643	04:43:44.26	-05:18:53.70	LT	0.007	Gold	0.549	0.620
SN 2006jd	2006/10/12	UGC 4179	08:02:07.43	00:48:31.50	LT	0.879	Gold	0.411	0.580
SN 2009kn	2009/10/26	MCG -03-21-06	08:09:43.04	-17:44:51.30	LT	0.000	Gold	-	-
SN 2005kj	2005/11/17	A084009-0536	08:40:09.18	-05:36:02.20	LT	0.000	Gold	-	-
SN 1994ak	1994/12/24	NGC 2782	09:14:01.47	40:06:21.50	LT	0.000	Gold	0.955	0.869
SN 2005ip	2005/11/05	NGC 2906	09:32:06.42	08:26:44.40	LT	-	Gold	0.685	0.540
SN 1989C	1989/02/03	MCG +01-25-25	09:47:45.49	02:37:36.10	LT	0.830	Gold	-	-
SN 2011ht	2011/09/29	UGC 5460	10:08:10.56	51:50:57.12	LT	0.000	Gold	0.090	0.197
SN 1993N	1993/04/15	UGC 5695	10:29:46.33	13:01:14.00	LT	0.000	Gold	0.485	0.490
SN 1998S	1998/03/02	NGC 3877	11:46:06.13	47:28:55.40	LT	0.780	Gold	-	-
SN 1994W	1994/07/29	NGC 4041	12:02:10.92	62:08:32.70	LT	0.000	Gold	0.698	0.510
SN 2011A	2001/01/02	NGC 4902	13:01:01.19	-14:31:34.80	LT	0.000	Gold	0.385	0.607
SN 2016bdu	2016/02/28	-	13:10:13.95	32:31:14.07	LT	0.707	Gold	-	-
SN 1997eg	1997/12/04	NGC 5012	13:11:36.73	22:55:29.40	LT	0.784	Gold	0.454	0.523
SN 2015da	2015/01/09	NGC 5337	13:52:24.11	39:41:28.60	LT	0.997	Gold	0.447	0.564
SN 1994Y	1994/08/19	NGC 5371	13:55:36.90	40:27:53.40	LT	0.000	Gold	0.112	0.320
SN 1995N	1995/05/05	MCG-02-38-17	14:49:28.29	-10:10:14.40	LT	0.000	Gold	-	-
SN 2008B	2008/01/02	NGC 5829	15:02:43.65	23:20:07.80	LT	0.000	Gold	0.201	0.383
SN 1987B	1987/02/24	NGC 5850	15:07:02.92	01:30:13.20	LT	0.107	Gold	0.998	0.999
SN 2008S	2008/02/01	NGC 6946	20:34:45.35	60:05:57.80	LT	0.000	Gold	-	-

SN 1999el	1999/10/20	NGC 6951	20:37:18.03	66:06:11.90	INT	0.000	Gold	0.277	0.321
SN 2009ip	2012/07/14	NGC 7259	22:23:08.30	-28:56:52.40	LCOGT 2m	0.000	Gold	0.788	0.891
SN 2019el	2019/01/02	-	00:02:56.70	+32:32:52.30	LT	0.003	Silver	-	-
SN 2017hcc	2017/10/02	GALEX 2.67E+18	00:03:50.58	-11:28:28.78	LT	0.993	Silver	-	-
SN 2011fx	2011/08/30	MCG+04-01-48	00:17:59.56	24:33:46.00	LT	0.726	Silver	-	-
PTF 11iqb	2011/07/23	NGC 151	00:34:04.84	-09:42:17.90	LT	0.845	Silver	0.059	0.334
SN 2007pk	2007/11/10	NGC 579	01:31:47.07	33:36:54.10	LT	0.785	Silver	0.248	0.108
SN 1999eb	1999/10/02	NGC 664	01:43:45.45	04:13:25.90	LT	0.750	Silver	0.324	0.258
SN 2016eem	2016/07/08	-	02:05:59.80	47:44:14.00	LT	0.231	Silver	-	-
SN 2002ea	2002/07/21	NGC 820	02:08:25.08	14:20:52.80	LT	0.096	Silver	0.124	0.308
SN 1978K	1978/07/31	NGC 1313	03:17:38.60	-66:33:04.60	LCOGT 2m	0.705	Silver	-	-
SN 2003lo	2003/12/31	NGC 1376	03:37:05.12	-05:02:17.30	LT	0.000	Silver	0.288	0.391
SN 2005aq	2005/03/07	NGC 1599	04:31:38.79	-04:35:06.80	LT	0.370	Silver	0.399	0.291
Gaia14ahl	2014/09/20	PGC 1681539	04:42:12.09	23:06:15.00	LT	0.000	Silver	-	-
SN 2005ma	2005/12/24	MCG-02-13-13	04:49:53.91	-10:45:23.40	LT	0.262	Silver	0.374	0.373
SN 2016hgf	2016/10/16	WEIN 69	04:51:45.97	44:36:03.06	LT	0.000	Silver	0.280	0.217
SN 2019rz	2019/01/14	UGC 3554	06:50:25.80	43:03:11.70	LT	0.926	Silver	0.028	0.001
AT 2018lkg	2018/12/30	UGC 3660	07:06:34.76	63:50:56.90	LT	0.880	Silver	0.092	0.001
AT 2014eu	2014/11/17	MCG+09-13-02	07:28:55.97	56:11:46.20	LT	0.228	Silver	-	-
SN 2014ee	2014/11/12	UGC 4132	07:59:11.68	32:54:39.60	LT	0.590	Silver	0.796	0.655
SN 2002fj	2002/09/12	NGC 2642	08:40:45.10	-04:07:38.50	LT	0.414	Silver	0.268	0.348
SN 2015bh	2015/02/07	NGC 2770	09:09:34.96	33:07:20.40	LT	0.000	Silver	0.601	0.603
SN 2014es	2014/11/20	MCG -01-24-12	09:20:46.91	-08:03:34.00	LT	0.000	Silver	0.900	0.876
SN 1997ab	1997/02/28	A095100+2004	09:51:00.40	20:04:24.00	LT	0.000	Silver	-	-
SN 2014G	2014/01/14	NGC 3448	10:54:34.13	54:17:56.90	LT	0.000	Silver	-	-
SN 1996bu	1996/1/14	NGC 3631	11:20:59.18	53:12:08.00	LT	0.026	Silver	-	-
SN 1987F	1987/03/22	NGC 4615	12:41:38.99	26:04:22.40	LT	0.000	Silver	0.132	0.152
SN 2008ip	2008/12/31	NGC 4846	12:57:50.20	36:22:33.5	LT	0.000	Silver	0.227	0.902
SN 2006am	2006/02/22	NGC 5630	14:27:37.24	41:15:35.40	LT	0.555	Silver	0.894	0.683
SN 2003dv	2003/04/22	UGC 9638	14:58:04.92	58:52:49.90	LT	0.180	Silver	1.000	0.777
SN 2016bly	2016/04/29	2MASX J17224883+1400584	17:22:48.90	14:00:59.88	LT	0.840	Silver	-	-
SN 2017gas	2017/08/10	2MASX J20171114+5812094	20:17:11.32	58:12:08.00	LT	0.920	Silver	-	-
SN 2006bo	2006/04/05	UGC 11578	20:30:41.90	09:11:40.80	LT	0.000	Silver	-	-

SN 2018hpb	2018/10/25	-	22:01:34.52	-17:27:45.22	LT	0.000	Silver	-	-
SN 2013fs	2013/10/07	NGC 7610	23:19:44.70	10:11:05.00	LT	0.345	Silver	0.515	0.660
SN 2015bf	2015/12/12	NGC 7653	23:24:49.03	15:16:52.00	LT	0.657	Silver	0.349	0.630
PS 15cwt	2015/08/20	-	02:33:16.24	19:15:25.20	LT	0.012	-	-	-
SN 2011js	2011/12/31	NGC 1103	02:48:04.96	-13:57:51.10	LT	0.000	-	0.262	0.385
SN 2006qt	2006/10/11	A034002-0434	03:40:02.72	-04:34:18.70	LT	0.000	-	-	-
SN 2005kd	2005/11/12	PGC 14370	04:03:16.88	71:43:18.90	LT	0.000	-	-	-
SN 2007ak	2007/03/10	UGC 3293	05:20:40.75	08:48:16.00	LT	0.000	-	0.184	0.130
SN 2013ha	2013/11/06	MCG +11-08-25	06:15:49.85	66:50:19.40	LT	0.808	-	-	-
SN 1987C	1987/03/21	MCG+09-14-47	08:30:01.30	52:41:33.00	LT	0.146	-	0.632	0.926
SN 2016ehw	2016/07/20	MCG+12-08-47	08:36:37.60	73:35:03.70	LT	0.041	-	-	-
ASASSN-15lf	2015/06/15	NGC 4108	12:06:45.56	67:09:24.00	LT	0.000	-	0.638	0.645
SN 2012ab	2012/01/31	A122248+0536	12:22:47.60	05:36:25.00	LT	0.912	-	-	-
PS 15aip	2015/05/02	KUG 1319+356	13:21:55.23	35:21:32.00	LT	0.860	-	-	-
SN 2006M	2006/01/17	PGC 47137	13:27:19.76	31:47:14.50	LT	0.575	-	-	-
SNhunt248	2014/05/21	NGC 5806	14:59:59.50	01:54:26.0	LT	0.000	-	0.817	0.681
SN 1978G	1978/11/24	IC 5201	22:20:48.30	-46:01:22.00	LCOGT 2m	0.000	-	-	-
SN 2006dn	2006/07/05	UGC 12188	22:47:37.84	39:52:50.16	LT	0.434	-	0.059	0.053

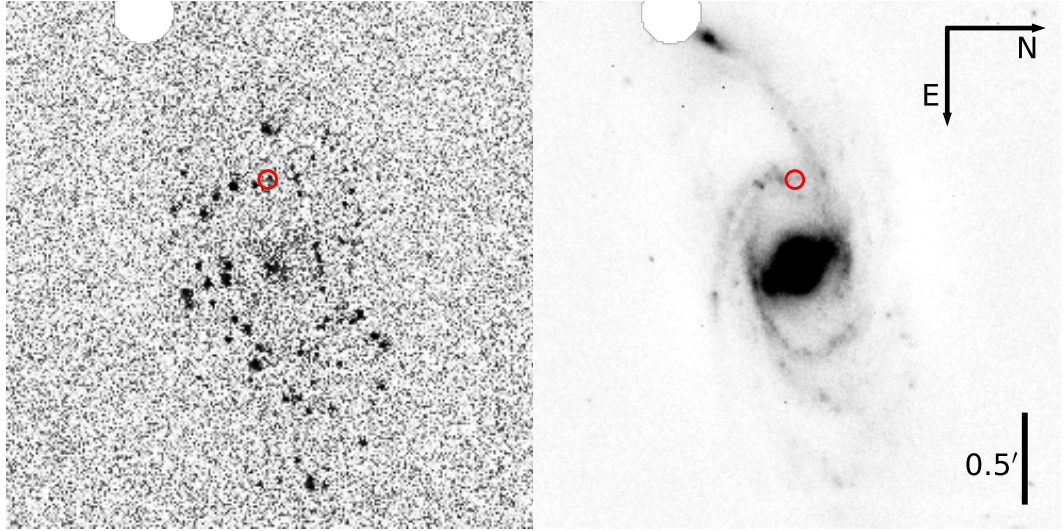
4.5.1 Examples of the SN II_n hosts

FIGURE 4.8: The continuum-subtracted $H\alpha$ (*left*) and r' -band (*right*) environments of PTF 11iqb in NGC 151 ($z=0.0126$). The position of PTF 11iqb is marked with the red circle. PTF 11iqb is an example of a SN II_n associated with star-formation as traced by the $H\alpha$ emission, resulting in an NCR value of 0.845. The foreground star at the top of the image has been masked out in the $H\alpha$ image as the continuum subtraction leaves artefacts which may interfere with the NCR value calculation.

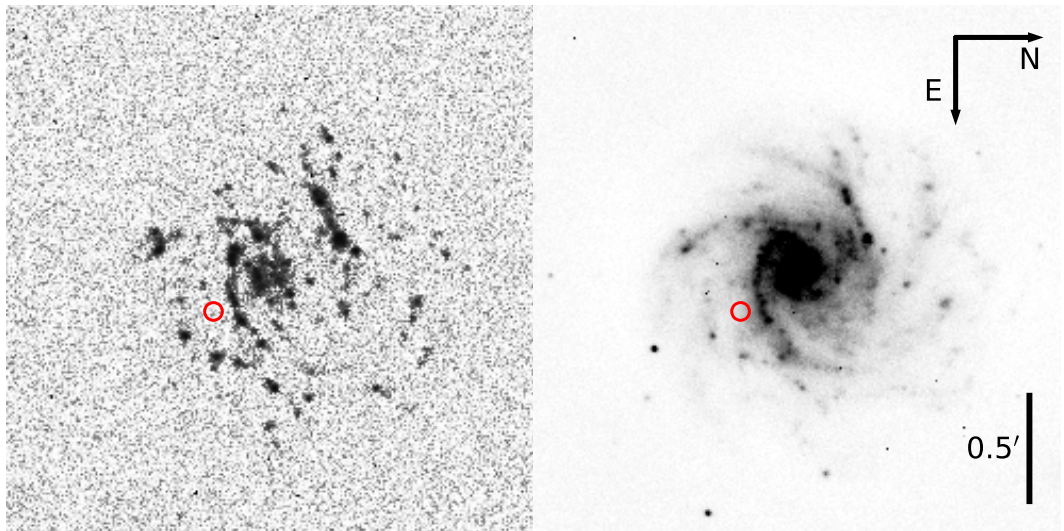


FIGURE 4.9: The continuum-subtracted $H\alpha$ (*left*) and r' -band (*right*) environments of SN 2003lo in NGC 1376 ($z=0.0139$). The position of SN 2003lo is marked with the red circle. SN 2003lo is an example of a SN II_n that is not associated with star-formation as traced by the $H\alpha$ emission (NCR value of zero). In the case of SN 2003lo, the transient resides in an apparent inter-arm gap.

4.5.2 NCR analysis results

I show the results of the NCR analysis in Fig. 4.10 in a cumulative distribution of the NCR values of 79 SNe IIn. These are split up into subcategories; the gold and silver samples and the non-zero NCR population. I compare sub-samples of SN IIn NCR values to a 1:1 NCR value relationship, which represents a hypothetical population of transients that perfectly traces H α emission (and therefore, ongoing star formation). The full sample has a mean NCR value of 0.318 ± 0.042 and the non-zero NCR subsample has a mean of 0.559 ± 0.049 . A mean NCR value of around 0.500 would suggest a population that follows the H α emission.

In Table 4.3 I present the AD p-values of different sub-samples of the NCR values when compared to each other and to a hypothetical population that perfectly follows H α emission. An AD test p-value ≤ 0.05 suggests that two populations differ significantly and are likely to be drawn from separate parent populations. I find that this full sample (blue line in Fig. 4.10) of SNe IIn does not follow star-formation as traced by H α emission when compared with the hypothetical population that traces star-formation perfectly, with an AD p-value $\sim 10^{-6}$. I then split this full sample into the gold and silver spectral subcategories from Chapter 3 and again these sub-samples likely do not follow the H α emission. Furthermore, the gold and silver populations are likely to follow each other in terms of NCR value. However, when I split the sample and isolate the non-zero NCR SNe IIn I find that the AD p-value (0.12) is consistent with the non-zero NCR sub-sample being drawn from the same population as the perfectly 1:1 relation. Therefore, the non-zero NCR SN IIn sub-sample is likely to follow the H α emission and therefore appears correlated with (on-going) star formation.

The statistics so far suggest that I am observing multiple populations within the SN IIn class when considering NCR distributions. In order to test for multi-modality, I utilise HDT and the bimodality co-efficient. A HDT p-value ≤ 0.05 indicates the sample is significantly multi-modal and a p-value of 0.05 – 0.10 suggests multi-modality of marginal significance. The bimodality coefficient uses the skew and kurtosis of a distribution and bimodality coefficient of $> 5/9$ suggests a bimodal distribution. The bimodality coefficient (for a finite sample) is given by,

$$b = \frac{g^2 + 1}{k + \frac{3(n-1)^2}{(n-2)(n-3)}}, \quad (4.2)$$

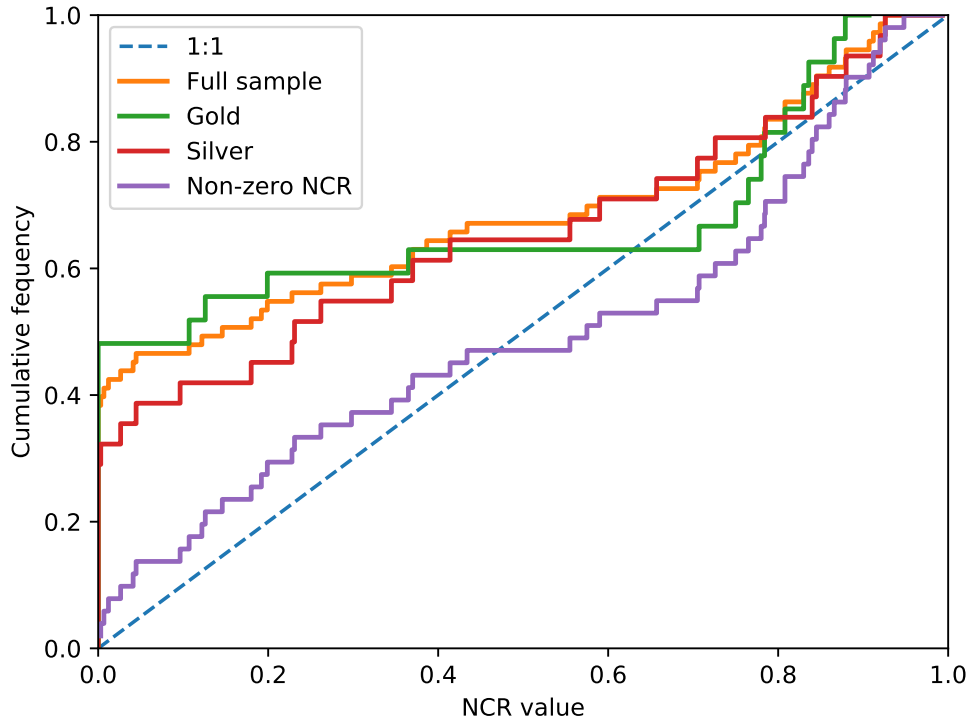


FIGURE 4.10: Cumulative distribution of the NCR values of the subsamples of the SNeIIn environments. The solid blue line is the full sample, the orange dashed line is the gold sample, the solid green line is the silver sample and the red dashed line is the non-zero NCR value sample. Also plotted is the 1:1 relationship (purple dashed line) which represents a population of progenitors which are strongly associated with star formation as traced by $H\alpha$ emission.

where b is the bimodality coefficient, g is the skewness, k is the kurtosis and n is the sample size.

I have applied these tests to these sub-samples with the results presented in Table 4.4. The HDTs indicate that the full and gold samples are at least bimodal with a dip test p-values in the order $\sim 10^{-3}$. However the silver and non-zero NCR sub-samples do not show significant levels of bimodality according to the dip test. None of these sub-samples have a bimodality coefficient $> 5/9$, which suggests the NCR values do not show bimodality. However this does not rule out multi-modality as suggested by the dip test p-values for the full sample and gold spectral classification sub-sample.

4.5.3 Comparisons between subsamples

Here, I compare the NCR distributions of the SN IIn sub-samples. The samples being compared and their AD p-values are presented in Table 4.3.

TABLE 4.3: The multi-sample Anderson-Darling test results comparing the NCR values of the sub-samples of SNe IIn. These tests probe whether or not the sub-samples are drawn from the same parent population.

Sample	AD p-value
Full sample – 1:1	8.1×10^{-6}
Gold – 1:1	2.1×10^{-5}
Silver – 1:1	8.2×10^{-4}
Non-zero NCR – 1:1	0.34
Gold – Silver	0.44

4.6 Results from the radial analysis

I present histograms showing the distributions of the fraction of r' -band or $H\alpha$ flux contained within the ellipse that just intersects the SN pixel. Fig. 4.11 shows the histogram for the distribution of the $H\alpha$ fraction, $\text{Fr}(H\alpha)$, and r' -band fraction, $\text{Fr}(R)$.

The sample of 46 SN IIn hosts (out of a full sample of 79 hosts) used in the radial analysis is smaller than the full sample as this analysis requires hosts that are well defined such that a radial profile can be constructed. In total, 33 of the hosts were unsuitable for the radial analysis. This will rule out hosts with semi-major axes of under $\sim 1'$. A limit of $1'$ was placed on the semi-major axes of the SN IIn hosts. The mean $\text{Fr}(R)$ value is 0.459 ± 0.040 and the mean $\text{Fr}(H\alpha)$ values is 0.421 ± 0.043 . From the histograms in Fig. 4.11, it can be seen that there may be a hint of a peak at lower $\text{Fr}(H\alpha)$ values which indicates centrally concentrated SNe (in terms of $H\alpha$ emission) but generally, the radial $H\alpha$ distribution is evenly distributed. The $\text{Fr}(R)$ distribution tells a similar story, the radial distribution is evenly distributed. More data is needed in order to determine any possible trends here. This is consistent with the findings of [Habergham et al. \(2014\)](#). The lack of a definite central concentrations seen in SN classes with massive progenitors such as SNe Ic seen in [van den Bergh \(1997\)](#) and [Habergham et al. \(2012\)](#) suggests that massive, SN Ic-like progenitors are not the main progenitor route for SNe IIn.

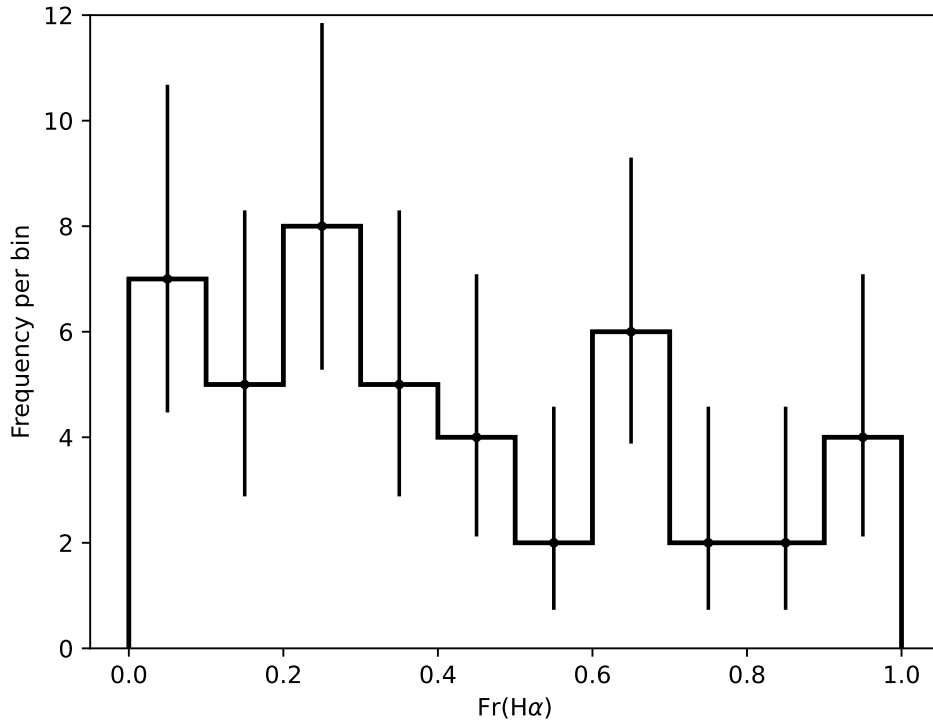


FIGURE 4.11: Fraction of $H\alpha$, $Fr(H\alpha)$ flux contained within an ellipse that just encloses the SN pixel.

In Fig. 4.13 and Fig. 4.14, the $Fr(H\alpha)$ and $Fr(R)$ distributions of SNe IIn with a zero NCR value are presented as histograms. In this case, there may be a central concentration of SNe IIn in terms of the $H\alpha$ emission but the $Fr(R)$ distribution is fairly even.

In Fig. 4.15 and Fig. 4.16, the $Fr(H\alpha)$ and $Fr(R)$ distributions of SNe IIn with a zero NCR value are presented as histograms. Compared to the zero NCR value subsample, the $Fr(H\alpha)$ distribution seems more even, with less of a central concentration. The $Fr(R)$ distribution is even however with some gaps at intermediate and low $Fr(R)$ values.

In Fig. 4.17, the $Fr(H\alpha)$ and $Fr(R)$ subsamples are plotted as a cumulative distribution and compared against the 1:1 relation that would denote an evenly distributed population. In this plot we see that all subsamples are consistent with each other and also consistent with being evenly distributed as shown by the 1:1 relation.

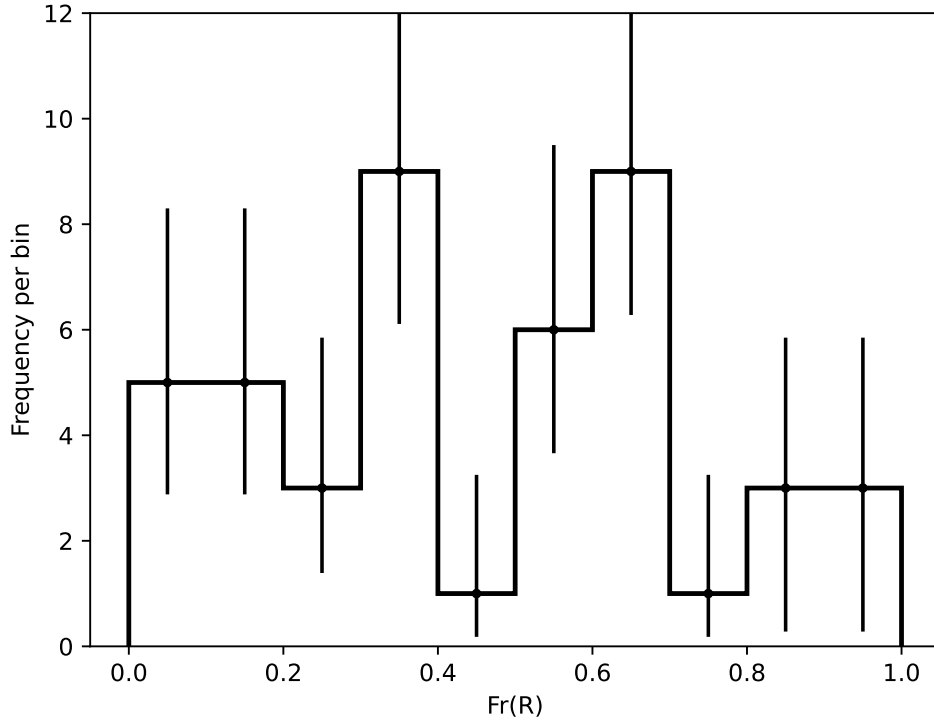


FIGURE 4.12: Fraction of r' -band flux, $Fr(R)$ contained within the ellipse that just enclosed the SN pixel.

In Table 4.4 I show the results of the HDT and the bimodality coefficients for the $Fr(R)$ and $Fr(H\alpha)$ value distributions. For both of these distributions, no bimodality was found by either the dip test or the bimodality coefficient.

TABLE 4.4: The Hartigan's dip test and bimodality coefficients for this sub-samples of SNe IIn and the flux fractions.

Sample	Dip test	Bimodality coefficient
Full sample	4.3×10^{-3}	0.23
Gold	1.8×10^{-4}	0.16
Silver	0.79	0.25
Non-zero NCR	4.7×10^{-2}	0.19
$Fr(H\alpha)$	0.87	0.29
$Fr(R)$	0.38	0.26

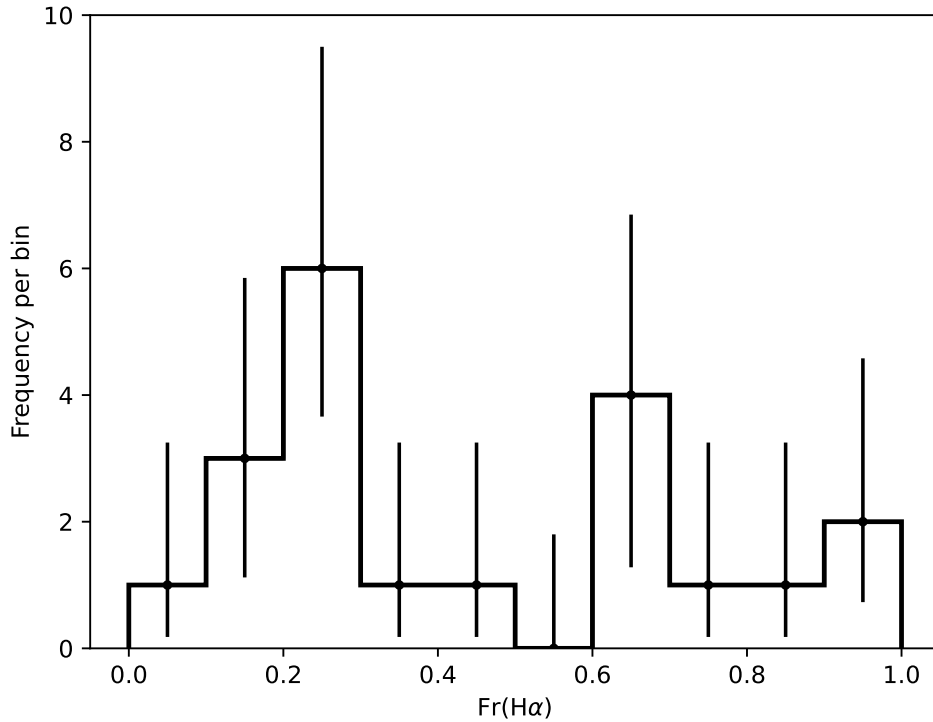


FIGURE 4.13: Fraction of H α , Fr(H α) flux contained within the ellipse that just enclosed the SN pixel. This is the subsample of SNe IIIn with a zero NCR value.

4.7 Using the environments of type IIIn supernovae to constrain possible progenitor systems

4.7.1 High mass progenitors

4.7.1.1 Luminous blue variables

LBVs arise from massive stars undergoing a transition phase from an O-type star to a Wolf-Rayet (WR) star where the outer H-rich layer has been expelled (Humphreys & Davidson, 1994; Weis & Bomans, 2020). LBVs are characterised by mass loss through winds at a rate of up to $\sim 10^{-4} M_{\odot} \text{ yr}^{-1}$ (Vink, 2018) and also episodic eruptions. The mass loss from these eruptive episodes (for example, the great eruption of η Car) can reach up to $10 M_{\odot}$ with $\dot{M} \approx 1 M_{\odot} \text{ yr}^{-1}$ (Smith et al., 2003, 2010). The H-rich CSM that surrounds SNe IIIn may originate from the material ejected in these dramatic mass-shedding events (see Smith, 2014, and references therein). Notable examples of the LBV class include P Cygni (Smith & Hartigan, 2006) and η Car (Smith et al., 2003)

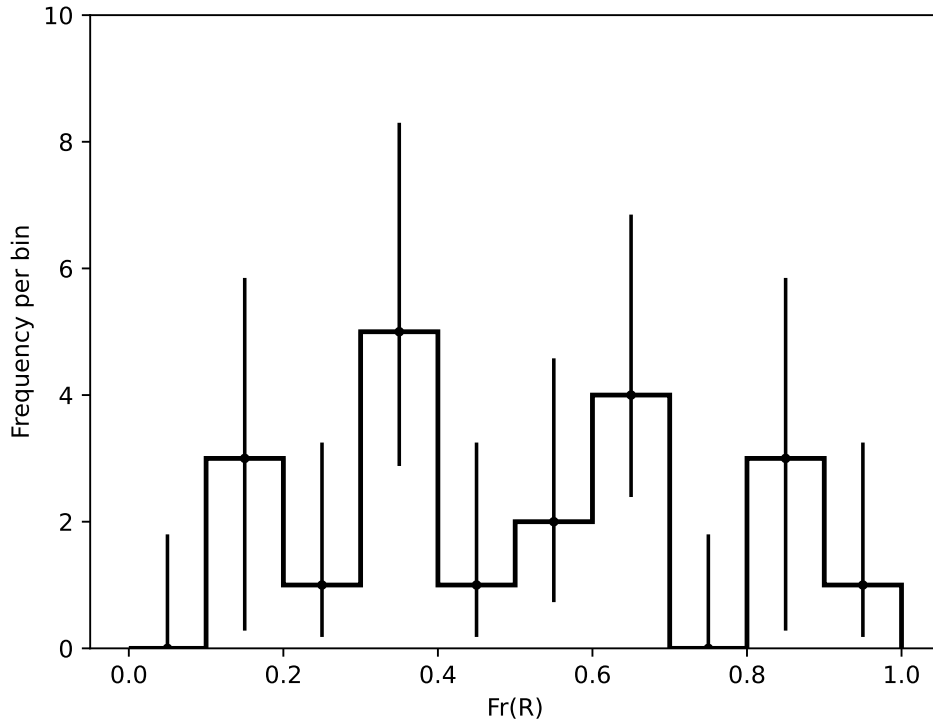


FIGURE 4.14: Fraction of r' -band flux contained within the ellipse that just enclosed the SN pixel. This is the subsample of SNe IIIn with a zero NCR value.

in the Milky Way and S Doradus in the Small Magellanic Cloud (Smith & Tombleson, 2015). These mass-loss periods of LBVs correspond to increases in the luminosity of the star. Ofek et al. (2014) found that some SN IIIn progenitor systems (at least five of their sample of 16) experience such brightening at least 120 days before the final terminal SN explosion. This behaviour may be consistent with the dramatic mass-loss events seen in LBVs (see also Strotjohann et al., 2021). According to Gal-Yam et al. (2007), archival data show that SN 2005gl in NGC 266 had an LBV progenitor. Gal-Yam & Leonard (2009) found that the LBV progenitor had a mass that exceeded $50 M_{\odot}$. This was the first confirmed LBV progenitor system for an SN IIIn.

As LBVs are high-mass stars, they are expected to reside in young environments close to O-type stars. However, Smith & Tombleson (2015) found that many LBVs are isolated from any cluster of O-stars. The authors propose a scenario where a WR star is a mass donor in an interacting binary system with an LBV mass gainer. The majority of massive stars are in binary systems (Sana et al., 2012) and if the separation between the stars is small enough, mass transfer occurs. Through these interactions the LBV may be kicked out of its place of birth when its companion explodes as a SN Ibc, leading to

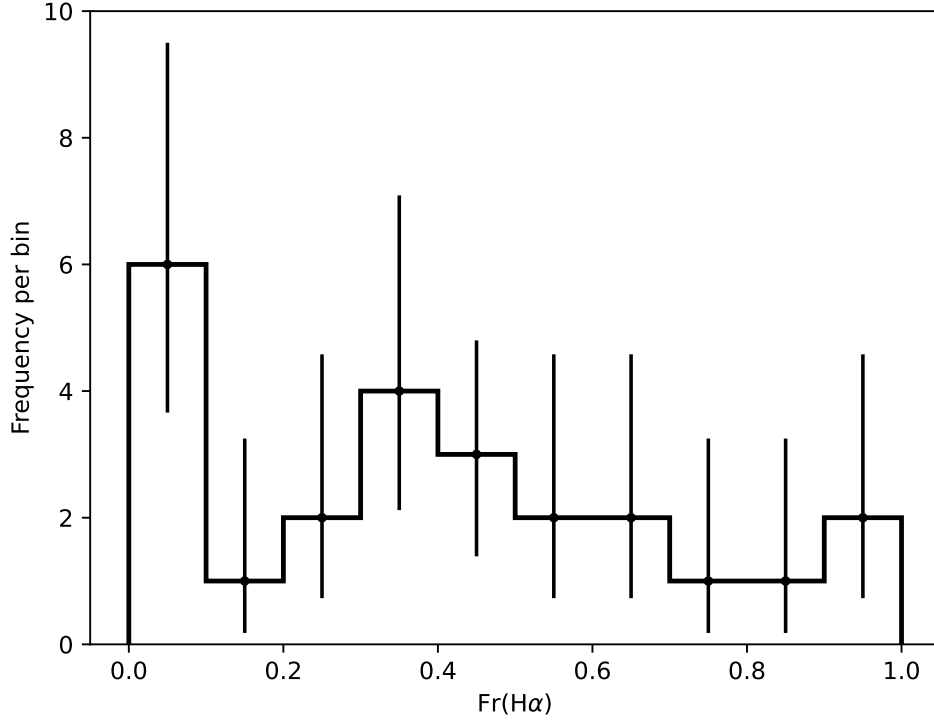


FIGURE 4.15: Fraction of H α flux contained within the ellipse that just enclosed the SN pixel. This is the subsample of SNe IIIn with a non-zero NCR value.

the observed isolation. This is consistent with the findings of [Habbergham et al. \(2014\)](#) described previously: many SNe IIIn reside in environments devoid of star formation. Another route for LBV formation is through binary mergers which may account for their apparent isolation ([Justham et al., 2014](#); [Aghakhanloo et al., 2017](#)).

The relations in the NCR values presented in Section 4.5 enable inferences to be made on the underlying stellar population. [Kangas et al. \(2017\)](#) utilised the NCR method with resolved massive stars in the Large Magellanic Cloud (LMC) and M33. [Kangas et al.](#) compare the NCR distributions of the massive stars in their sample with the NCR distributions of the different classes of SNe in [Anderson et al. \(2012\)](#). [Kangas et al.](#) note that SNe IIIn are a diverse class, possibly with multiple progenitors. [Kangas et al.](#) found that LBVs had an average NCR value around 0.5, indicating a population that follows star formation well. Those authors suggest that when combining the NCR values of RSGs ($M \lesssim 8 M_{\odot}$) and LBVs (with RSGs making up 70% and LBVs accounting for 30% of the NCR values), the average SNe IIIn NCR value can be reproduced.

Some SNe Ic progenitors are WR stars ([Georgy et al., 2009](#)) and LBVs may be a

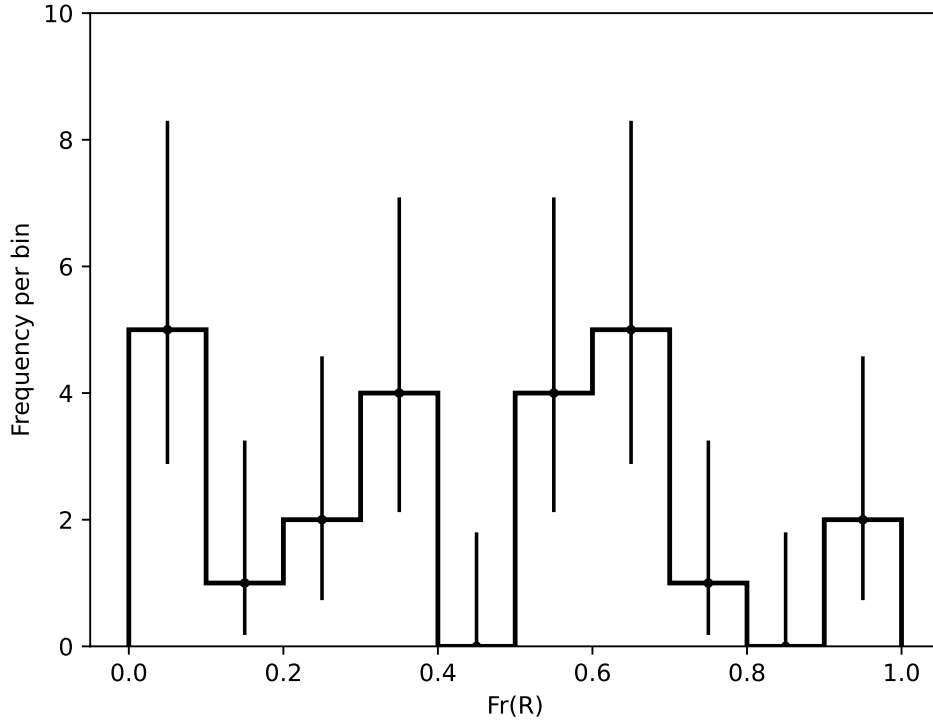


FIGURE 4.16: Fraction of r' -band flux contained within the ellipse that just enclosed the SN pixel. This is the subsample of SNe IIIn with a non-zero NCR value.

preceding evolutionary stage to WR stars. It is known that at least some SNe IIIn have LBV progenitors (e.g, SN 2005gl Gal-Yam et al., 2007). One would therefore expect that SNe IIIn would follow ongoing star-formation as traced by $H\alpha$ emission if the main progenitor path for SNe IIIn were LBVs. However, this is not what I observe in this environmental analysis. I found that over 40% of this sample had an NCR value of zero, indicating the SN pixel had **no** association with the $H\alpha$ emission. When I isolate the non-zero NCR values I find that when I compare the NCR values to a 1:1 relationship, the non-zero NCR values follow this 1:1 distribution as indicated by the AD test p-value. This may indicate that there are at least two populations of SNe IIIn: a non-zero NCR group that follows $H\alpha$ emission and a population of zero NCR values. This may indicate that these SNe IIIn have different progenitor stars. Instead, if I assume that LBVs are the progenitor system of the vast majority of SNe IIIn (with the rest being made up of transients such as SNe Ia-CSM or ecSNe) then this may inform us about the evolution and environments of LBVs.

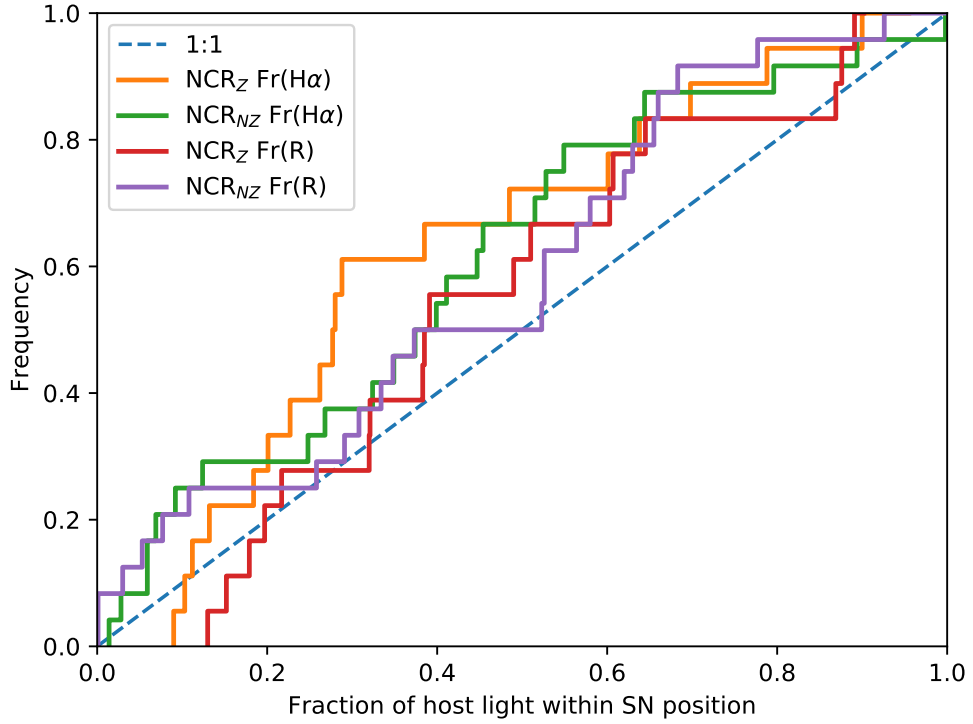


FIGURE 4.17: Cumulative frequency plot showing the Fr(H α) and Fr(R) distributions compared with the 1:1 relation which would be a hypothetical SN IIIn population that is evenly distributed in the host in terms of H α or r' -band emission.

4.7.1.2 Yellow hypergiants

Yellow hypergiants (YHGs) are evolved post-red-supergiant (RSG) stars with $M_{\text{ZAMS}} \approx 20\text{--}60 M_{\odot}$ which undergo enhanced mass loss that may form the required CSM for the SN IIIn phenomenon (for a review, see [de Jager, 1998](#)). [Brennan et al. \(2022a,b\)](#) present a detailed analysis of the SN IIIn candidate AT 2016jbu, which was found to be an SN 2009ip-like object with a double-peaked light curve and a dusty circumstellar shell. Using archival *Hubble Space Telescope* (*HST*) imaging, [Brennan et al.](#) found that the progenitor of AT 2016jbu was consistent with a YHG of $M \approx 20 M_{\odot}$. With age estimates of the possible progenitor of AT 2016jbu and the age of the environment of the transient, a CCSN scenario was favoured over a nonterminal explosion while an “impostor” event could not be ruled out.

4.7.2 Intermediate mass progenitors

4.7.2.1 Electron capture supernovae

At the lower end of the progenitor mass range for CCSNe, the SN IIn phenomena may also arise from ecSNe rather than the very high-mass stars which become LBVs. In the case of an ecSN, the collapse of the degenerate core of an 8–10 M_{\odot} star is triggered by electron capture in ^{24}Mg and ^{20}Ne . The resulting explosion is less energetic than regular SNe II, leaving behind a neutron star (Miyaji et al., 1980; Nomoto, 1984, 1987). A recent example of an ecSN is SN 2018zd in NGC 2146 (Zhang et al., 2020a; Hiramatsu et al., 2021a).

Smith (2013) and Moriya et al. (2014) explore the possible link between these lower-mass ecSN progenitors and SNe IIn by analysis of the Crab Nebula (M1), the remnant of the Galactic SN 1054 (Mayall & Oort, 1942; Duyvendak, 1942). Historical accounts of SN 1054 seem to contradict predictions that an ecSN would be less luminous than a regular SN II, and Moriya et al. (2014) explore CSM interaction as a possible solution to this. In the 8–10 M_{\odot} progenitor mass range, there may be super-AGB stars which undergo mass loss via massive winds, in turn forming the CSM required for the SNe IIn phenomenon. As discussed in Section 3.7.2, a possible progenitor path for SN 2008S-like transients is dust-enshrouded super-AGBs that explode as ecSNe; however, this cannot be confirmed without late-time imaging showing that the progenitor has disappeared. Adams et al. (2016) found that SN 2008S had dimmed to levels below its progenitor, but the dimming of a surviving progenitor can also be explained by extreme dust (dusty environments are typical in SN 2008S-like transients).

Cai et al. (2021) examine the intermediate luminous red transient (ILRT) phenomenon and the possible connection to ecSNe. It was found that all five of the ILRTs analysed by Cai et al. (2021) resembled SN 2008S which as well as being a prototypical impostor/transitional impostor to SNe IIn is also considered a prototypical ILRT. The spectra show SNe IIn-like narrow components to the $H\alpha$ profiles so would be classified as such by the classification scheme in Chapter 3. The NCR value of SN 2008S was zero and ILRTs could make up a zero or low NCR value population of SNe IIn. SN 2008S exploded in a dusty environment.

Another example of a possible SNe IIn with ecSN origin that is in this sample is SN 2015bf. This object has an NCR value of 0.657, which indicates a moderately strong region of ongoing star-formation. This contrasts with the zero NCR value of SN 2008S. Lin et al. (2021) present a study on SN 2015bf, finding that the spectrum evolves into a more

standard SN II spectrum. SN 2015bf had a fairly high peak luminosity of -18 but the light curve then started to decay rapidly with a similar light curve morphology to other fast-declining SN II, including the ecSN candidate, SN 2018zd. [Lin et al. \(2021\)](#) argue that the brief CSM interaction seen in the spectral evolution points towards the CSM being fairly confined. This was interpreted as a violent mass loss episode shortly before the SN explosion. As ecSNe are expected to have progenitors on the low end of the progenitor mass range for CCSNe, they would be lower down the NCR value mass ladder. SN 2015bf eventually evolved as a SN II. [Anderson et al. \(2012\)](#) found that around 30 per cent of SNe II had zero NCR values, 10 per cent lower than the proportion of zero NCR SNe IIn. Furthermore around 75 per cent of these SNe had an NCR value under 0.500, so SNe IIn from ecSNe may make up some of this lower or zero NCR population.

SNe from lower mass progenitors such as these ecSNe exemplify that mass loss sufficient to create enough CSM to produce the SN IIn phenomenon can be experienced by progenitors on the lower mass range for CCSNe. SNe IIn from lower mass progenitors such as RSGs may be classified as SNe IIn-P or SNe IIn-L depending on their light curves.

SN 2011ht in UGC 5460 was initially observed during a possible SN impostor event ([Roming et al., 2011](#)) and then later died in a terminal SN explosion. [Fraser et al. \(2013a\)](#) presents a study into a pre-explosion outburst. They used data from the Panoramic Survey Telescope and Rapid Response System 1 (Pan-STARRS1) survey. The authors found that there was an outburst with an absolute magnitude ~ -11.8 . This was linked with a coincident source from archival Catalina Sky Survey data from 258-138 d prior to the terminal explosion of SN 2011ht. This may have been a single outburst, or a series of eruptions similar to that of SN 2009ip that preceded the (potential) terminal eruption (see Section 4.7.7). [Ofek et al. \(2014\)](#) also comments on the precursor eruption of SN 2011ht and suggests precursor eruptions may be common among SNe IIn based on observations of other SNe IIn from the Palomar Transient Factory (PTF). [Smith \(2013\)](#) links SNe such as SN 2011ht to ecSNe, the Crab Nebula and also the SN IIn-P subclass. The Crab Nebula is the remnant of SN 1054 which must have been a CCSN due to the SN producing the Crab Pulsar. While the explosion had low kinetic energy, the transient was not subluminal with an estimated absolute magnitude (based on historical accounts) of around -18. The chemical abundances in the Crab Nebula reveal He and C but was not O-rich unlike other CCSN remnants. Nucleosynthesis and stellar models of ecSNe and super-AGB stars suggest a progenitor with a mass at the low end of the mass range for CCSNe ($8-10 M_{\odot}$) may be responsible for these abundances observed in the Crab Nebula ([Nomoto et al., 1982](#); [Nomoto, 1984](#); [Wanajo et al., 2009](#)). [Smith \(2013\)](#) suggests SN 1054 was a ecSN with similar properties to those of SN 1994W and

SN 2011ht. [Mauerhan et al. \(2013\)](#) presents a study on SN 2011ht and its membership into the SN II_n-P subclass. The optical light curve of SN 2011ht exhibited a plateau phase in the light curve decline which lasted around 120 days post explosion. The bolometric luminosity tail of the light curve suggests that there was a low ^{56}Ni yield which may be consistent with an 8–10 M_{\odot} progenitor or perhaps in the case of a fallback SN (where ejecta falls back onto the core, forming a black hole), a more massive progenitor over 25 M_{\odot} .

In this work there are four examples of possible ecSNe, the aforementioned SN 2011ht, SN 1994W, SN 2009kn and SN 2015bf. All but SN 2015bf are found to have an NCR value of zero. This may be consistent with these objects having lower mass progenitors.

[Boian & Groh \(2020\)](#) model early time spectra of SNe that exhibit early time CSM interaction. They use these models to explore the possible progenitors of a sample of 24 SNe with early time interaction. A wide range of mass loss rates, wind speeds and SN luminosities were calculated for this sample along with finding that there was increased mass loss immediately preceding the SN explosions. The authors conclude that the progenitors of these objects were massive RSGs. This early time interaction is not exclusive to the classic SN II_n class however, as flash spectrum SNe exhibit this behaviour and may have RSG progenitors ([Khazov et al., 2016](#); [Dessart et al., 2017](#); [Kochanek, 2019](#)). Using the classification criteria in Chapter 3, it is possible that some of the silver class SNe II_n that have a limited number of spectra are actually flash spectroscopy SNe but further data is needed to demote these objects from silver SNe II_n.

4.7.3 Red supergiants

RSGs are the progenitors of “normal” SNe, such as SNe IIP. RSGs suffer mass loss through massive winds and can lose a lot of their H-rich envelope, which may result in a SNIIL. However, some SNe II_n may have RSG progenitors. [Smith et al. \(2009a\)](#) present a study on the galactic RSGs, Betelgeuse and VY CMa. Those authors found that while Betelgeuse had steady mass loss via winds, VY CMa suffered more episodic mass loss. [Smith et al.](#) conclude that when considering the density of the CSM surrounding VY CMa, this RSG could be the progenitor for a SN 1988Z-like SN II_n. Another SN II_n with a possible RSG progenitor is SN 1998S where the CSM was produced by a strong wind and also is very dusty ([Meikle et al., 2003](#); [Mauerhan & Smith, 2012](#); [Taddia et al., 2015](#)). [Kangas et al. \(2017\)](#) found that the NCR value distribution of RSGs in M33 was consistent with the NCR distribution of the SNe II_n sample in [Anderson et al. \(2012\)](#) suggesting that RSGs may make up a large proportion of SNe II_n progenitors.

4.7.4 Low mass progenitors

4.7.4.1 Type Ia-CSM supernovae

Another scenario that may contribute to the SN II phenomenon are SNe Ia-CSM. SN Ia systems are old and will outlive their parent star formation region as there needs to be sufficient time for the star to evolve into a WD and then to grow to the Chandrasekhar mass. [Habbergham et al. \(2014\)](#) compares the NCR values of their sample of SNe II with other classes of SNe, including 98 SNe Ia. Just under 60% of the SNe Ia in that sample had a zero NCR value and most of the remainder had low NCR values, the slope on the cumulative frequency plot flattens out after around an NCR value of 0.600. The mean NCR value of the SNe Ia in [Habbergham et al.](#) is 0.157. SNe Ia have mostly low or zero NCR values, therefore, SNe Ia-CSM may account for some of the zero and low NCR value SNe II in this sample.

A distinction between core-collapse SNe II and SNe Ia-CSM would not be directly picked up by the selection criteria set out in Chapter 3 as the classification system uses only the $H\alpha$ line profile and would require the transient to be a recognised SN Ia-CSM. In this study there are two possible SN Ia-CSM, SN 2006gy and SN 2008J for which I have continuum subtracted $H\alpha$ data. However, I find that SN 2008J has an NCR value of 0.808 and SN 2006gy has a very high NCR value of 0.907, indicating these transients are in a strong, active star forming region. Alternatively to the thermonuclear origin of SN 2006gy, this transient may have a massive progenitor. For example, [Smith et al. \(2010\)](#) suggest that the $\sim 20 M_{\odot}$ of CSM required a very high mass progenitor with mass $\sim 100 M_{\odot}$. As most SNe Ia are not associated with $H\alpha$ emission ([Anderson et al., 2012](#); [Habbergham et al., 2014](#)) this is unusual but one of the SNe Ia in the previous studies was in a region with an NCR value of over 0.900. As the thermonuclear origin of some of these transients becomes apparent at later times such as with SN 2006gy, it is possible that some of the transients in the sample would be made up of hitherto unknown SNe Ia-CSM. These could therefore make up some of the zero and low NCR value SNe II, assuming that SNe Ia-CSM are in similar environments to SNe Ia. However, [Silverman et al. \(2013\)](#) investigated 16 SNe Ia-CSM and found that all of them were found in spiral galaxies, suggesting that SNe Ia-CSM generally occur in younger populations when regular SNe Ia occur in all Hubble types (with some SN Ia subtypes preferring elliptical galaxies, see [Hakobyan et al., 2020](#)). Therefore, SNe Ia-CSM may, on average, have higher NCR values than regular SNe Ia (for example those in [Anderson et al., 2012](#); [Habbergham et al., 2014](#)). As the CSM may be created by a super-AGB companion, it is possible that SNe Ia-CSM may have a similar average NCR value to SNe IIP or ecSNe as discussed

in Section 4.7.2.1. SNe Ia-CSM are rare (Graham et al., 2019) and for example, out of 127 SNe Ia observed by ZTF, only one was observed to be a SN Ia-CSM (Yao et al., 2019). This rate may be overstated as SNe Ia-CSM are more luminous than SNe Ia, thus more easily observed. Due to the rarity of CSM interaction in SNe Ia, they likely do not make up a large “hidden” proportion of the SNe IIIn sample, despite SNe Ia being the most numerous observed SN class (Li et al., 2011). On the other hand, a number of SNe Ia show late time CSM interaction, such as SN 2015cp that showed CSM interaction 664 days post-explosion (Graham et al., 2019) so some SNe Ia may be unrecognised as SNe Ia-CSM if they lack late time observations.

4.7.5 Luminous blue variables outside of their parent star forming region

Generally, I have found that the progenitors of SNe IIIn are longer lived than their host star forming regions which is indicated by the low average NCR values. I also found that the non-zero NCR subsample follows the $H\alpha$ emission, indicating that the progenitors in the non-zero NCR subsample resided in their star formation regions. This may indicate two populations of SNe IIIn in terms of the age of the underlying population, a younger population (tracing the $H\alpha$ emission) and an older population (less associated or unassociated with the $H\alpha$ emission). These environmental differences may suggest there being multiple progenitor paths for SNe IIIn when considering LBVs are a known progenitor channel of SNe IIIn. While some zero-NCR SNe IIIn may originate in small, unresolved H II regions (e.g. Crowther, 2013), previous studies found that massive SN progenitors have NCR distributions that do not have a large fraction of zero-NCR values (see Anderson et al., 2012; Kangas et al., 2017). There is potential degeneracy in the environments of LBVs or LBV-like objects which may contaminate the non-zero NCR sample. Perhaps the contrast I see in environments cannot simply be pinned to two sets of separate progenitors, with a higher mass component following ongoing star-formation and another population with lower mass progenitors that are less or unassociated with star formation. What if there are high mass progenitor stars unassociated to star forming regions?

Some LBVs may reside in areas outside of a star formation region in their hosts (Smith & Tombleson, 2015). Smith & Tombleson found that the neither the Galactic LBVs or LBVs in the LMC and SMC were well associated with O-type star clusters. Further to this, Smith & Tombleson note that in the LMC, the LBVs were more isolated than the Galactic or SMC LBVs and were more isolated than the known WR stars in the

LMC. Those authors suggest that LBVs may not be single stars but evolve in binaries (as many O-type stars do, [Gies, 1987](#); [García & Mermilliod, 2001](#); [Evans et al., 2006](#)). Furthermore, LBVs that are isolated and apparently in single star systems may have evolved in a multiple star system and then either the companion star has exploded as a SN or the LBV got kicked out of the system due to interactions with nearby stars and became a “runaway” star. This may cause a spin-up of the LBV, which is consistent with the models of [Groh et al. \(2013b\)](#) where the LBVs in their models exploded as SNe II_n when a rotational element was added. [Aghakhanloo et al. \(2017\)](#) implemented models of LBV isolation and found that the observed isolation of some LBVs is consistent with binary evolution. [Smith et al. \(2020\)](#) present a study on the LBV candidate, MCA-1D (also known as UIT003) in the outskirts of M33. [Smith et al.](#) find that similarly to some observed SN impostors, MCA-1D had an outburst in 2010 that had a similar light-curve to other LBV outbursts. This LBV candidate is associated with a small cluster but is on the outskirts of the galaxy and the environment is similar to that of the impostor turned (possible) SN II_n, SN 2009ip (see Section 4.7.7). [Humphreys et al. \(2016\)](#) found that the velocities of seven M31 LBVs and seven M33 LBVs were inconsistent with a runaway star scenario. Additionally, [Kangas et al. \(2017\)](#) noted that a small proportion of observed LBVs may outlive their local H α emitting star forming region simply by being formed towards the end of its life.

4.7.6 SN2005ip and the long-lasting type II_n supernovae

A sub-category of SNe II_n are the long lasting SNe II_n. These are SNe II_n where the light curve decay is slow and has greater longevity than what may be expected from a radioactive decay powered light curves. While SNe II_n are generally more long lived than other classes due CSM interaction, these long-lived SNe II_n may be bright for years post explosion. Examples of this phenomenon include SN 1988Z ([Turatto et al., 1993](#); [Chugai & Danziger, 1994](#)), SN 1995G ([Pastorello et al., 2002](#); [Chugai & Danziger, 2003](#)), SN 2005ip ([Stritzinger et al., 2012](#); [Haberman et al., 2014](#); [Smith et al., 2016](#)) and KISS15s ([Kokubo et al., 2019](#)). As previously mentioned in Section 4.1, [Taddia et al. \(2015\)](#) suggested that long lasting SNe II_n have LBV progenitors, but [Chugai & Danziger \(1994\)](#) found that SN 1988Z was most consistent with a lower mass 8–10 M_{\odot} progenitor, however [Aretxaga et al. \(1999\)](#) suggest previous estimates of the energy of the explosion were underestimated and the mass could be larger. [Kokubo et al. \(2019\)](#) note that KISS15s either has an RSG progenitor or an LBV progenitor. [Pastorello et al. \(2002\)](#) studied SN 1995G and after calculating the SN luminosity and wind speeds, they calculate the mass loss rates and ejecta velocities and find that the progenitor may have

had a mass of 15–20 M_{\odot} . However, this is an upper limit as if the efficiency factor of the conversion of kinetic energy into observed light is less than one, then the mass estimate would be lower.

SN 2005ip in NGC 2906 is perhaps the most well known long-lasting SN IIIn (Modjaz et al., 2005b). Smith et al. (2009b) present photometry and spectroscopy of SN 2005ip ranging over three years post-explosion. Those authors found that initially, (the first ~ 160 days), SN 2005ip resembled a SN IIL with a fast linear decline. However then the light curve plateaued. Smith et al. suggest that the presence of coronal lines in the spectrum of SN 2005ip and the longevity of the light curve indicate that the CSM is clumpy. They suggest that the progenitor of SN 2005ip may be an extreme RSG with $M \sim 20\text{--}40 M_{\odot}$. A clumpy CSM scenario is supported by Stritzinger et al. (2012). Those authors present photometric and spectroscopic observations of SN 2005ip up to six and a half years post-explosion. Stritzinger et al. suggest that the presence of coronal lines in the spectrum suggests a clumpy wind mode of mass loss of the progenitor pre-explosion. Alternatively to the RSG progenitor scenario, Fox et al. (2009, 2010) suggest that the dust detected in observations of SN 2005ip may have been formed by episodic mass loss consistent with an LBV progenitor ~ 100 years prior to explosion. Haberman et al. (2014) found that SN 2005ip was still the strongest $H\alpha$ source in its host, three years post explosion. Fox et al. (2020) present a study on SN 2005ip, including late time photometry (> 5000 days post explosion) and find that SN 2005ip had only just started to decline in 2015. In this study I find that SN 2005ip is no longer the strongest $H\alpha$ source in the host in observations in 2020, with an NCR value of 0.866. However, I do not include SN 2005ip in the analysis as it is not known if the transient has dimmed to quiescent levels.

Another example of a long-lasting SN IIIn in my sample is SN 2015da. Tartaglia et al. (2020) found that SN 2015da was still slowly declining four years post-explosion. Those authors suggest that the slow decline was due to ongoing CSM interaction with a CSM mass of $\sim 8 M_{\odot}$ with an extreme pre-explosion mass loss rate of $\sim 0.6 M_{\odot} \text{ yr}^{-1}$. SN 2015da has a NCR value of 0.997 (observed in 2020), indicating that SN 2015da is in one of the strongest $H\alpha$ emission regions in the host. The host of SN 2015da is shown in Fig. 4.19. SN 2015da is clearly in the strongest $H\alpha$ emission region in its host, or the SN itself is still being detected. Possibly this bright $H\alpha$ excess is due to the ongoing CSM interaction. This very high NCR value may be skewed by the ongoing interaction and is therefore not included in the NCR analysis.

A further example of a long-lasting SN IIIn is SN 2010jl in UGC 5189A (Yamanaka et al.,

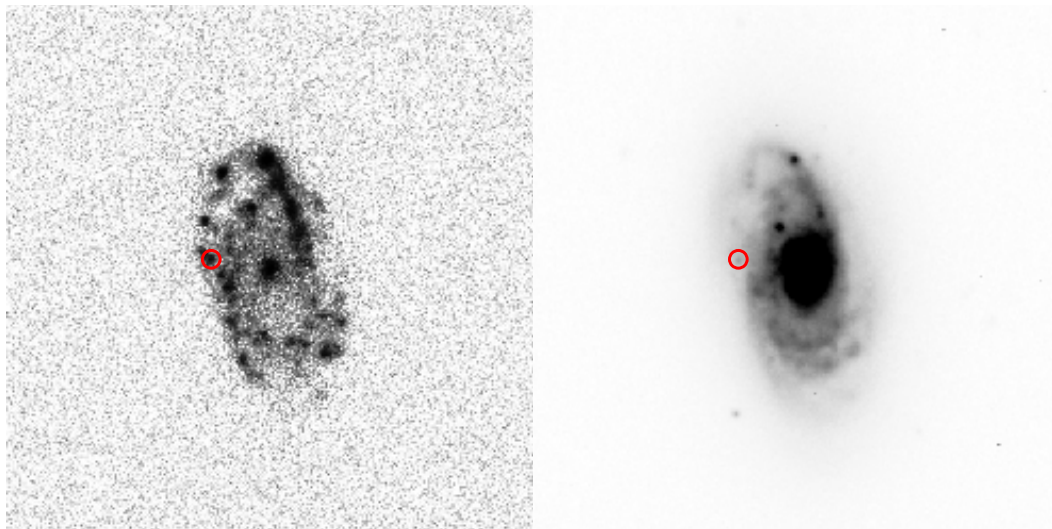


FIGURE 4.18: The host of SN 2005ip, NGC 2906. The continuum subtracted H α image is on the left and the right panel is the r' -band image of the host. The location of SN 2005ip is marked by the red circle.

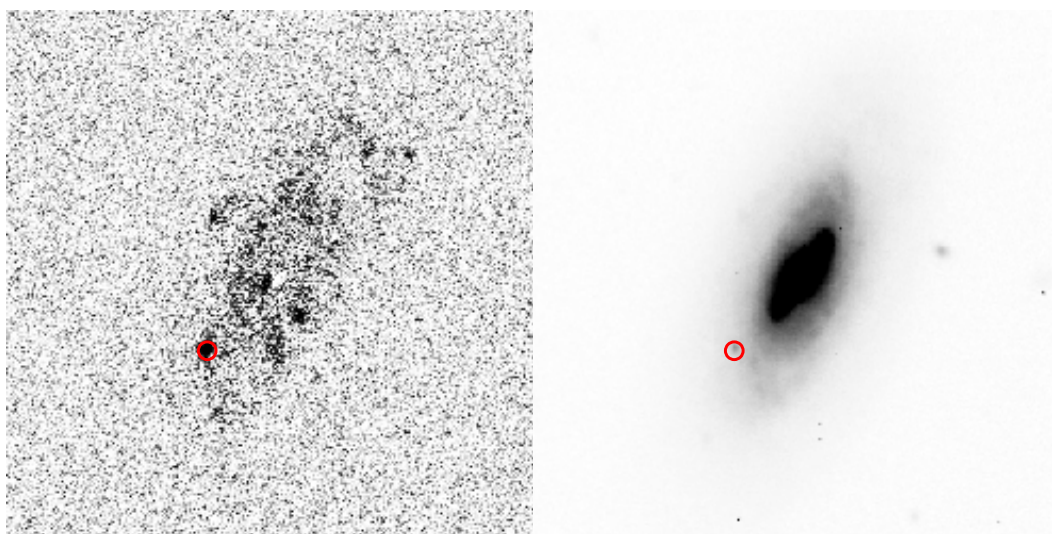


FIGURE 4.19: The host of SN 2015da, NGC 5337. The continuum subtracted H α image is on the left and the right panel is the r' -band image of the host. The location of SN 2015da is marked by the red circle. Note that SN 2015da is in one of the strongest star formation regions in NGC 5337 and the observed excess may be (at least in part) due to the ongoing CSM interaction.

2010). This transient was found to remain much brighter than would be expected from the decay of a ^{56}Ni powered light curve. Indeed, light curve modelling of SNe II_n may only consider CSM interaction as the light curve may have a higher peak and last longer than a radioactive light curve, however some models combine radioactive decay and CSM

interaction (Chatzopoulos et al., 2012; Villar et al., 2017). Ofek et al. (2019) present the light curve of SN 2010jl over a six year period up to 2300 days after maximum light. Those authors conclude that the persistence of the light curve of SN 2010jl may be explained by ongoing interaction with CSM that was ejected in the decades preceding the explosion. The CSM surrounding SN 2010jl is asymmetric and may extend to $\sim 10^{17}$ cm (Dwek et al., 2021). Furthermore, Fox et al. (2017) show that the source of the emission from the SN is offset from the blue source previously attributed to the progenitor of SN 2010jl in pre-explosion HST imaging. They suggest that the massive progenitor may have been obscured by dust but the association with a young cluster suggests a massive progenitor with $M > 30 M_{\odot}$. As SN 2010jl is persistent and it is unknown if the transient has faded in H α , it is not included in the NCR analysis. Moreover, as the transient is in a disturbed host, it is not included in the radial analysis.

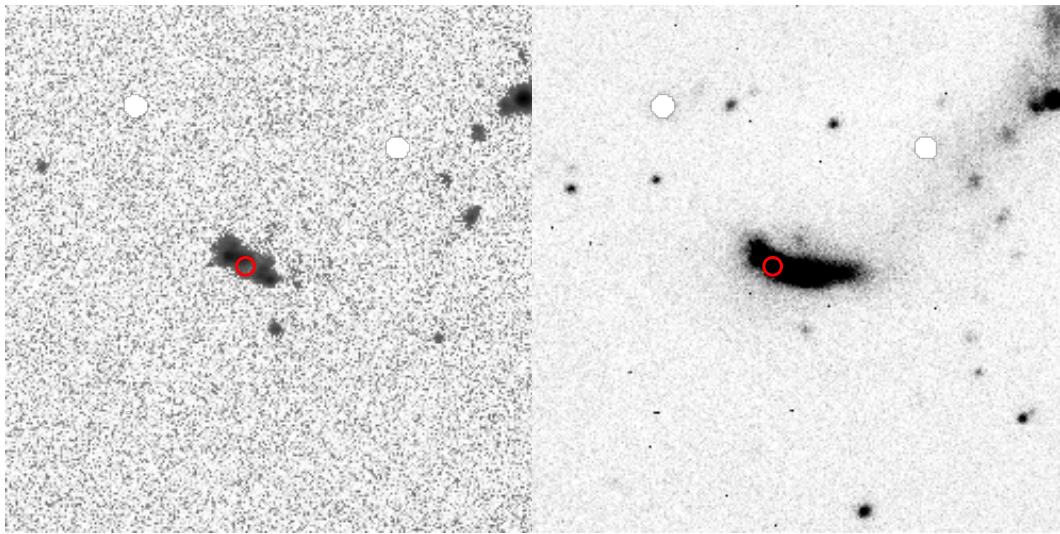


FIGURE 4.20: The host of SN 2010jl, NGC 5189A. The continuum subtracted H α image is on the left and the right panel is the r' -band image of the host. The location of SN 2010jl is marked by the red circle. Note that SN 2010jl is in a disturbed host.

4.7.7 SN2009ip and precursor eruptions

Ofek et al. (2014) and Strotjohann et al. (2021) found that many SNe II_n suffer from precursor explosions which may be LBV-like great eruptions. Notable examples include SN 2009ip (Foley et al., 2011; Mauerhan et al., 2013; Pastorello et al., 2013), SN 2011ht (Roming et al., 2011), and SN 2015bh (Boian & Groh, 2018; Thöne et al., 2017).

I find that SN 2009ip is a very isolated transient, with an NCR value of zero and the similar transients, SN 2015bh and SN 2011ht were also zero NCR SNe II_n. If these

precursor “impostor” events are LBV eruptions, these could be further examples of LBV isolation, possibly showing the effects of binary evolution. The location of SN 2009ip in its host is shown in Fig. 4.21.

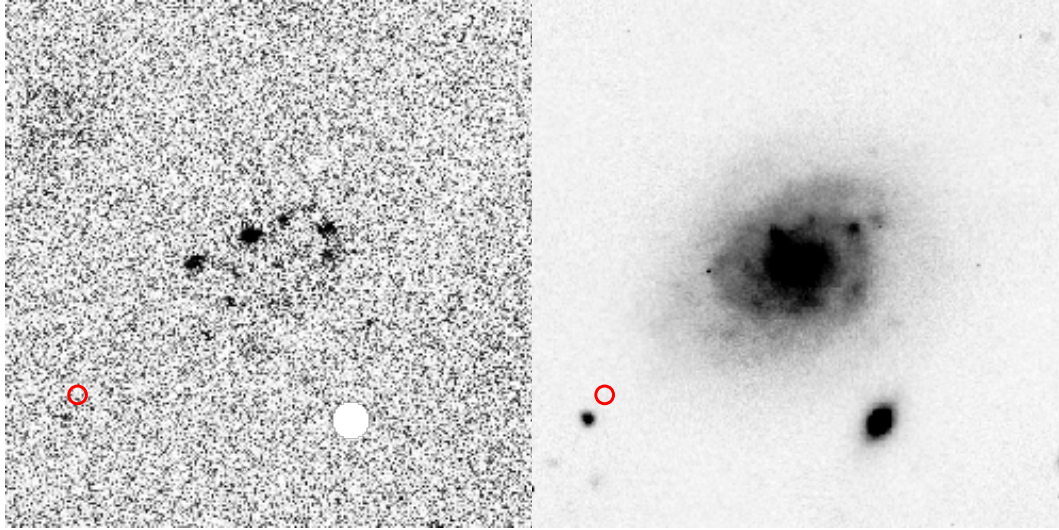


FIGURE 4.21: The host of SN 2009ip, NGC 7259. The continuum subtracted $H\alpha$ image is on the left and the right panel is the r' -band image of the host. The location of SN 2009ip is marked by the red circle. Note that SN 2009ip is isolated from the main disc of the host and has an NCR value of zero.

In some cases there is little pre-explosion data. [Groh et al. \(2013a\)](#) present models of single star LBVs and found that LBVs in the mass range $20\text{--}25 M_{\odot}$ can explode as SN when rotation is introduced to the models. Those authors suggest that if the archival images of the progenitor of SN 2005gl were taken at the time the progenitor was suffering a pre-SN II_n outburst, then the mass estimates for the progenitor may be overestimated. This is because the pre-explosion progenitor would appear brighter than at quiescence. If this were the case, the progenitor may have a mass of around $20\text{--}25 M_{\odot}$ and would be consistent with the findings of [Groh et al. \(2013a\)](#).

As discussed previously, SN 2009ip in NGC 7259 is a well studied example of a SN II_n that possibly had a precursor eruption before a terminal SN II_n explosion. Initially, SN 2009ip erupted in 2009 in an SN impostor style event ([Berger et al., 2009a](#); [Smith et al., 2010](#)), with an absolute magnitude of around -13.7 . Prior to the “final” eruption in 2012, there was a period of erratic eruptions and then the final eruption occurred with an absolute magnitude of around -18 which may have been a terminal, SN II_n explosion ([Mauerhan & Smith, 2012](#); [Prieto et al., 2012](#); [Pastorello et al., 2013](#); [Margutti et al., 2014](#); [Ofek et al., 2014](#); [Smith et al., 2014](#)). [Pastorello et al. \(2013\)](#) and [Smith et al. \(2013\)](#) make energetics arguments to suggest that the 2012 explosion was terminal, with

them finding an SN explosion energy of around 10^{51} ergs. [Fraser et al. \(2013a\)](#) argue that the spectrum of the 2012 eruption was very similar to that of the 2009 eruption and lacked the nucleosynthesised elements one would expect from a SN. [Fraser et al. \(2015\)](#) found that SN 2009ip had not dimmed beneath the quiescent pre-discovery images and still had not entered the nebular phase expected in CCSNe. This may suggest a nonterminal explosion mechanism, but those authors do not rule out continuing CSM interaction after core collapse being responsible for these features. I find that SN 2009ip is a very isolated transient, with an NCR value of zero. [Foley et al. \(2011\)](#) and [Smith et al. \(2011\)](#) present studies on the precursor events to the possible terminal SN explosion of SN 2009ip. Both papers find that these eruptions are consistent with the giant eruption of an LBV.

[Pessi et al. \(2022\)](#) present a ten year study on SN 2011fh in NGC 4806. The authors find that similar to SN 2009ip, SN 2011fh experienced a brightening phase ($M_r \sim -16$) which preceded a possible terminal explosion ($M_r \sim -18$). The mass loss rate of the progenitor of SN 2011fh was consistent with the mass loss rates of SN 2009ip and other SNe II_n. MUSE data revealed that SN 2011fh was in a region of ongoing star formation and inferring from the age of the local cluster, the progenitor may have had a mass of around $60 M_{\odot}$ which is consistent with estimates of SN 2009ip and the mass may indicate that the progenitor was an LBV. [Elias-Rosa et al. \(2018\)](#) found that SN Hunt151 was remarkably similar to the eruption of SN 2009ip; they suggested that SN Hunt151 may be an η Car-like LBV eruption within a dense CSM cocoon.

4.7.8 Supernova impostors

Some transients are initially classified as SNe II_n because they exhibit the multicomponent and narrow $H\alpha$ emission features. However, it later becomes apparent, when the progenitor star is reobserved after the brightening phase, that some events originate from nonterminal explosions within dense CSM. These transients typically lie within gaps in the timescale-luminosity phase space of exploding transients ([Kasliwal, 2011](#)). With absolute magnitudes ranging from -10 to -14 (between novae and SNe), they may be generally termed “gap transients.” A subset of them are sometimes named SN impostors; they have spectra similar to those of SNe II_n, but they are subluminous, typically $M_V \approx -11$ to -14 ([Kochanek et al., 2012](#)). Such events may be due to mass-loss episodes from LBVs, similar to the great eruption of η Car ([Smith et al., 2011](#)). After this initial eruption, the progenitor may be obscured by dust that forms after the initial eruption ([Kochanek et al., 2012](#)) however some objects such as SN 2002kg do not produce

much dust [Kochanek et al. \(2012\)](#); [Humphreys et al. \(2014, 2017\)](#). Other examples that appear in this work include; SN 1997bs, SN 1999bw, SN 2000ch, SN 2001ac and SN 2002kg ([Kochanek et al., 2012](#)). These outbursts can sometimes precede a possible full SN explosion — for example, SN 2006jc (an SN Ibn rather than an SN II_n; [Pastorello et al., 2007](#); [Smith et al., 2013](#)), SN 2009ip ([Foley et al., 2011](#); [Mauerhan et al., 2013](#); [Pastorello et al., 2013](#)), and SN 2015bh ([Boian & Groh, 2018](#); [Thöne et al., 2017](#)). The precursor eruptions of the aforementioned SN 2009ip may be considered SN impostor events.

Other notable (possible) impostors include SN 2008S (the namesake for a group of similar objects; [Thompson et al., 2009](#)) in NGC 6946 ([Arbour, 2008](#)), where a progenitor was unable to be recovered. [Prieto et al. \(2008\)](#) reported that the culprit may have been a lower-mass ($\sim 10 M_{\odot}$) star in a dusty environment, hence this object could be an enshrouded “impostor”. [Kochanek \(2011\)](#) argued that SN 2008S and the similar transient NGC 300-OT are consistent with an explosion taking place in an environment with very dusty winds. [Berger et al. \(2009a\)](#) found that the progenitor of NGC 300-OT may be a compact object such as a WR star or blue supergiant (BSG), contrary to the RSG interpretation of [Kochanek \(2011\)](#). [Andrews et al. \(2021\)](#) suggested that the progenitor of the SN 2008S-like transient AT 2019krl is a BSG/LBV, based on archival *HST*, *Spitzer Space Telescope*, and Large Binocular Telescope data. They also discussed the possibility that the transient was caused by binary interaction in the form of a merger that resembled an LBV eruption (briefly discussed in Section 4.7.1.1, but see also [Smith et al., 2016, 2018](#)). An alternative scenario to the LBV/BSG and nonterminal path ([Berger et al., 2009b](#); [Bond et al., 2009](#); [Kochanek, 2011](#); [Smith et al., 2009c](#); [Andrews et al., 2021](#)) for SN 2008S-like transients may be RSG/super-AGB (asymptotic giant branch) progenitors which suffer terminal electron-capture supernova (ecSN) explosions, discussed in Section 4.7.2.1. [Botticella et al. \(2009\)](#) found that the bolometric light curve of SN 2008S was consistent with the decay of ^{56}Co and suggested that the progenitor was a super-AGB star with $M \approx 6$ to $8 M_{\odot}$ that ended its life as an ecSNe. [Adams et al. \(2016\)](#) reported that SN 2008S had become fainter than its progenitor, arguing that the explosion was terminal. The dusty environments of SN 2008S-like transients complicates attempts to detect a surviving progenitor; as such, the nature of these objects remains elusive.

While SN impostors are subluminous, there may still be luminosity overlap with some genuine SNe such as SNe II_n-P and SNe that are obscured by dust — as in the aforementioned terminal scenario for SN 2008S-like transients. The outbursts of SN 2009ip reached absolute magnitudes of -15 and -18 ([Smith et al., 2013](#)); if the final 2012 event

was not terminal, then SN impostors driven by CSM interaction may overlap most of the luminosity space of SNe. Indeed, the possible SN impostor, SN 1961V in NGC 1058 (Zwicky, 1964) had a peak absolute magnitude of -17.8, well into the range of fully fledged SNe IIIn (Humphreys, 2005). The true nature of SN 1961V is debated; Kochanek (2011) suggest that the stars identified as possible surviving progenitors were around an order of magnitude less luminous than the possible progenitor observed pre-eruption (Zwicky, 1964; Utrobin, 1987). Kochanek suggest that the presence of a dust-obscured progenitor may support the SN impostor scenario. However, when observed in the mid-IR, there was no detection of a progenitor and those authors concluded that SN 1961V was a fully fledged SN IIIn. Conversely, Van Dyk & Matheson (2012) report a recovered progenitor for SN 1961V using improved astrometric data. Those authors suggest that the progenitor observed is consistent with an LBV, indicating an η Car-like great eruption and therefore it is a SN impostor. Therefore, distinguishing between “impostor” events and genuine SNe can be difficult without late-time imaging showing the surviving progenitor (or the lack thereof).

SN impostors are an important consideration, and I can not rule out there being contamination in this sample (especially in the case of the silver SNe IIIn). An environmental study of this nature, with a sample of SN impostors is difficult due to selection effects involved. Impostors are generally dim events so I may be biased towards exceptional, bright objects, especially if the objects are superimposed on a bright H II region.

Over the course of the observation campaign, the hosts of eight SN impostors were observed. Due to the limited number of impostors, the NCR distributions were not compared to the full sample of SNe IIIn. The impostor sample is presented in Table 4.5. Apart from SN 2006fp in UGC 12182 (Blondin et al., 2006b), all the impostors had a zero NCR value. Again, this result is surprising as SN impostors are often interpreted as great eruptions of LBVs. For example, SN 1997bs in NGC 3627 may have a massive progenitor and if the progenitor was an LBV (not in outburst) then it would have a mass $\sim 60 M_{\odot}$ (Van Dyk et al., 2000). Van Dyk et al. found that the light curve from KAIT and HST flattens off around 0.5 mag below the level of the possible progenitor observed pre-explosion. Those authors conclude that SN 1997bs was not a bona fide SN IIIn but rather an impostor. Furthermore those authors conclude that SN 1997bs may be an η Car great eruption analogue due to a similar peak magnitude. Moreover, SN 2000ch in NGC 3432 (Filippenko, 2000) has an LBV progenitor that has undergone multiple eruptions. Pastorello et al. (2010) showed that SN 2000ch had suffered from numerous great eruptions since its discovery reaching an absolute magnitude of -12.8 and the photometric properties are consistent with LBV eruptions. SN 2000ch erupted

again in 2013 which was designated PSN J10524126+3640086 but was recognised as the reappearance of this restless impostor (Van Dyk et al., 2013).

TABLE 4.5: The sample of eight SN impostors observed. All but one of these transients is unassociated with star forming regions as traced by H α emission.

Name	Host	RA (J2000)	Dec	NCR value
SN1997bs	NGC 3627	11:20:14.16	12:58:19.56	0.000
SNhunt248	NGC 5806	14:59:59.50	01:54:26	0.000
SN1999bw	NGC 3198	10:19:46.81	45:31:35	0.000
SN2002kg	NGC 2403	07:37:01.83	65:34:29	0.000
SN2006fp	UGC 12182	22:45:41.13	73:09:48	0.433
SN2006bv	UGC 7848	12:41:01.55	63:31:12	0.000
SN2002bu	NGC 4242	12:17:37.18	45:38:47	0.000
SN2000ch	NGC 3432	10:52:41.40	36:40:10	0.000

4.7.9 The possible progenitor routes and explosion mechanisms that produce the type II_n phenomenon

As shown in Fig. 4.22, there are numerous phenomena and mechanisms that form the heterogeneous SN II_n class. As the SN II_n phenomenon is an environmental effect, the various explosion mechanisms and progenitor paths are included.

As previously mentioned, RSGs are a possible progenitor route of SNe II_n (e.g. Kangas et al., 2017). The NCR distributions of SNe IIP were explored by Anderson et al. (2012). The NCR distribution of the SNe IIP from Anderson et al. (2012) are presented in Fig. 4.23. It can be seen that the full sample of SN IIP are less well associated to star-formation as traced by H α emission when compared to the full sample of SNe II_n. This is mirrored in the NCR distribution of the non-zero NCR value SNe IIP where they follow the 1:1 line less well than the non-zero NCR SNe II_n. Considering NCR distributions may show a mass ladder in terms of progenitor mass, this suggests that even if we assume that some SNe II_n have RSG progenitors, there may be a higher mass progenitor route that make up some SN II_n progenitors. The AD test p-values of the full SN IIP sample to the 1:1 line is ~ 0 and the p-value for the non-zero NCR SNe IIP is 0.003. This suggests that SNe IIP are inconsistent with a population that follows star formation as traced by H α emission. The non-zero SNe II_n and SNe IIP have a p-value of 0.017, therefore the non-zero NCR distributions of SNe II_n and SNe IIP are inconsistent with being drawn from the same population. This may support there being a high mass component in the SN II_n progenitor channel if the non-zero component of the NCR distribution for SN II_n is consistent with high mass progenitors.

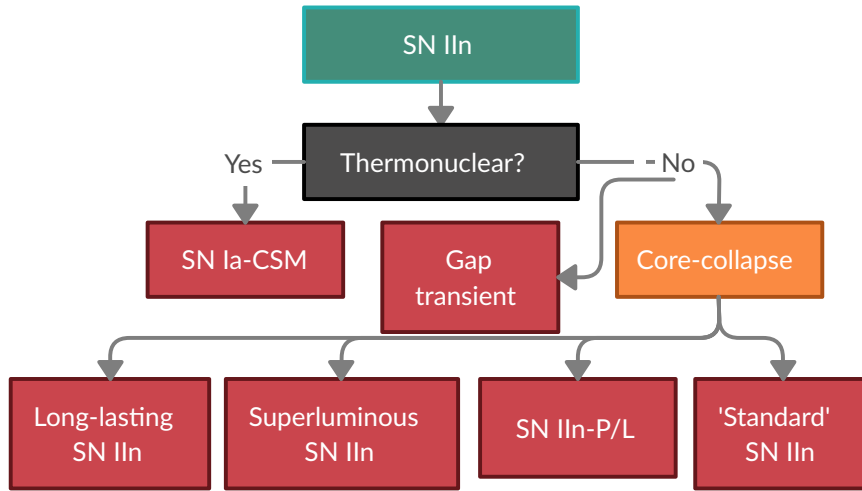


FIGURE 4.22: The routes that a SN IIIn can take in terms of the different possible explosion mechanism (i.e. thermonuclear vs core collapse) and the photometric properties. Within these types there may be further subdivisions in terms of the progenitor types.

4.8 Possible biases

I collated this sample from online databases which compile transients from many sources which include surveys that may be targeted or untargeted. Any bias inherent in these surveys will persist through to this target list. For example, large surveys such as the Palomar Transient Facility (PTF, [Law et al., 2009](#)) may introduce bias when transients are selected for spectroscopic followup.

The NCR method may lead to missing low level $H\alpha$ emission. As the zero NCR population are the SNe where the cumulative sum is under zero, there may be a skew towards the positive pixel values and negative values, indicating that the low level emission is being missed. This was seen in [Anderson et al. \(2012\)](#) where for a sample of 15 SNeIIP that had a zero NCR value, nine of them fell on a pixel with intrinsic low level $H\alpha$ emission, suggesting that a lack of sensitivity can result in low level $H\alpha$ emission regions being missed in the NCR statistic. Therefore, the number of SNe IIIn with a zero NCR value may be overestimated. This could be remedied with larger telescopes with capabilities to perform deeper observations to increase the sensitivity. Moreover, $H\alpha$

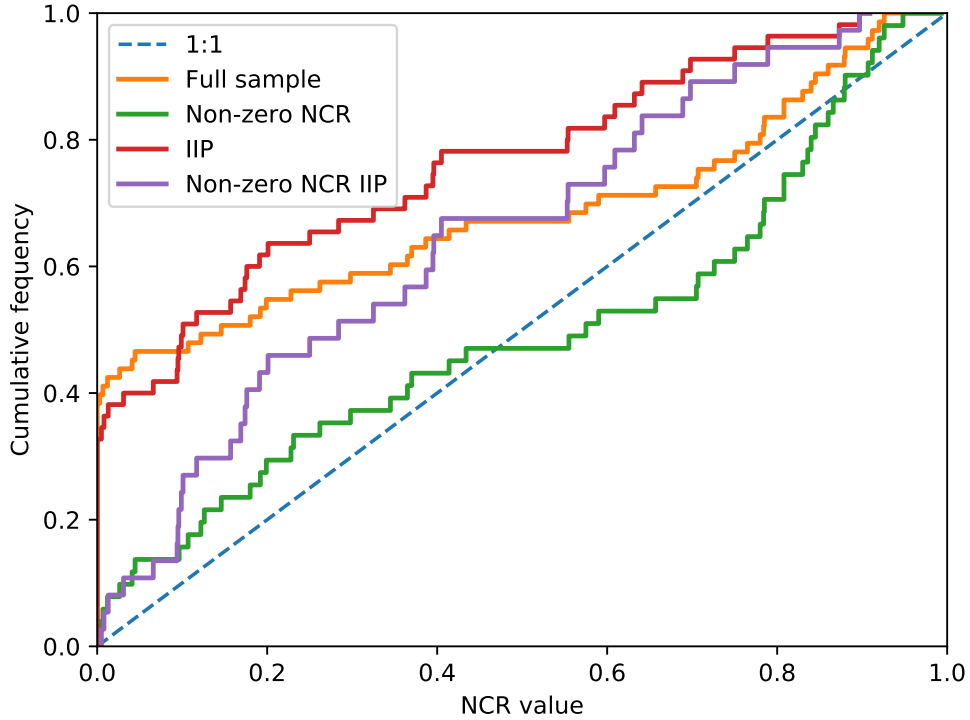


FIGURE 4.23: NCR distributions of the SNe IIn in this work split into the full sample and the non-zero NCR SNe IIn and also the NCR distribution of the SNe IIP from [Anderson et al. \(2012\)](#), with both the full SN IIP and non-zero NCR distributions plotted. The 1:1 relation is marked with a dashed blue line.

absorption from line underlying stars may reduce the observed emission and therefore NCR value.

Another potential source of bias in this work is that I exclude hosts with smaller angular diameters from the radial distribution analysis. The majority of the SNe IIn where there is no $\text{Fr}(\text{H}\alpha)$ or $\text{Fr}(\text{R})$ value in Table 4.2 have hosts that have too small an angular diameter to calculate the radial offset in terms of the galaxy light.

SNe IIn are on average more luminous than other SN classes, but with their great diversity, a small number may be sub-luminous (e.g. SN 2008S if it is a true SNe IIn rather than an impostor). Therefore some of the dimmer SNe IIn may be missed by surveys if they are within a bright H II region.

Furthermore, some SNe IIn explode in dusty regions in their hosts and the progenitors may be dust factories. Therefore it is possible that there is underlying $\text{H}\alpha$ emission from star formation regions that are being missed in optical observations due to absorption by dust. For example, SN 2008S is in a very dusty region ([Adams et al., 2016](#)). [Haberman](#)

[et al. \(2014\)](#) explored the possibility that there was dust absorbing any $H\alpha$ emission from star forming regions. They used *Spitzer* $24\mu\text{m}$ data of the hosts in their sample and did not find any strong IR emission. Therefore this effect may be small if at all present in the expanded SN IIn sample in this work. As mentioned previously, some of the zero NCR SNe IIn may be found in regions where the H II region has already dissipated or is otherwise too small to be resolved. Furthermore, $H\alpha$ absorption from intermediate mass stars may lead to an underestimate in the NCR value. [James & Anderson \(2006\)](#) found that the pixel values of zero-NCR values SNe tend towards positive values, indicating that real, low level emission may be missed. However my conclusions drawn from the comparison of the NCR distributions remains unchanged as all NCR measurements will be effected.

4.9 Conclusions and summary

I have presented the results of the largest environmental study of SN IIn hosts to date using 79 SNe IIn with most having robust spectral classifications. The conclusions of this study can be summarised as:

1. As a whole, SNe IIn do not follow the 1:1 NCR distribution that represents a hypothetical SN population that perfectly follows the $H\alpha$ emission. This may indicate that the SNe IIn in my sample generally do not follow star formation as traced by $H\alpha$ emission.
2. Around **40%** of SNe IIn are not associated with any $H\alpha$ emission as calculated by NCR. However some zero-NCR values may be accounted for by unresolved/dissipated H II regions, $H\alpha$ absorption from the underlying stellar population or low level emission being missed by the NCR technique. These caveats will affect all NCR samples so the comparisons remain robust.
3. The non-zero NCR population is consistent with the hypothetical star-formation following population.
4. These findings suggest there may be multiple progenitor routes to SNe IIn (e.g. ecSNe or SNe Ia-CSM). Bimodality is not detected in these NCR distributions but I see multimodality in the full, gold and non-zero NCR value subsamples.
5. There are no significant differences in the NCR distributions of the gold and silver classes. This suggests that many of the silver SNe IIn may be promoted to gold SNe IIn given more spectral epochs.
6. SN impostors predominantly lie in regions devoid of ongoing star formation, with an NCR value of zero.
7. The radial distributions of SNe IIn follow the r' -band and $H\alpha$ emission equally well. However I do note there are more centrally located SNe IIn than previous studies. While there is no central excess found in the distribution, there may be some SNe IIn progenitors that are similar to the progenitors of the massive, centrally concentrated SNe Ic.

Future surveys will provide a huge amount of data and transient discoveries. Surveys such as the ZTF and the Legacy Survey of Space and Time (LSST) at the Vera C. Rubin Observatory ([LSST Science Collaboration et al., 2009](#)) will provide a wealth of SN IIn

candidates and will allow much larger samples to be used for constraining possible SN II progenitors.

Chapter 5

Introduction: Classical Novae

5.1 Classical novae

Classical novae (CNe) are a subset of the accreting binary systems known as the cataclysmic variables (CV). CN systems are comprised of a WD accreting mass from a companion star in a close binary orbit as proposed by [Walker \(1954\)](#). Observed donors include main-sequence and sub-giant stars. The mechanism for mass transfer is via Roche-lobe overflow and/or direct accretion from the stellar wind from a red giant companion (see [Darnley et al., 2012](#); [Williams et al., 2016a](#)). The hydrogen-rich material falls upon the surface of the WD from the donor via an accretion disc. However there may be sub-classes in the accretion regime with observational evidence of magnetic accretion ([Warner, 2003](#); [Darnley et al., 2012](#)).

5.1.1 The eruption

A CN eruption is the product of a thermonuclear runaway reaction (TNR). The TNR takes place at the surface of the WD at the bottom of the hydrogen-rich accreted envelope where the great pressure forces degeneracy. The TNR is initiated when enough of this material has been transferred from the donor to meet the conditions necessary for a TNR to occur. These conditions are when the base of the accreted layer becomes hot ($T > 10^8$ K) and the pressure is sufficient (10^{19} N m⁻²; [Starrfield et al., 1972](#)). Hydrogen burning initiates via the p - p chain but the temperature rapidly rises to the point at which most energy production is via the hot-CNO cycle where proton capture creates β^+ unstable nuclei such as ¹³N and ¹⁵O (see [Starrfield, 1971](#); [Starrfield et al., 1976, 2016](#)). The energy released from these β^+ decays, and the high temperatures lifting

the temperature/pressure degeneracy leads to the CN eruption and some proportion of the accreted envelope is ejected as the ejecta exceed the escape velocity of the WD. The CN eruption is observable with an X-ray flash (König et al., 2022) during a fireball phase in the eruption and then the ejecta form a pseudo-photosphere (Starrfield et al., 1976). The increase in luminosity is of the order 10^4 times the quiescent level and this can result in a peak absolute magnitude of $M_V = -10.5$ (see Shafter et al., 2008; Aydi et al., 2017), and as a result, bright CNe are observable out to the Virgo cluster (Della Valle & Livio, 1995). However, a more typical brightness of CNe is $\langle M_V \rangle = -7.5$ (e.g. Shafter, 2017; Selvelli & Gilmozzi, 2019, and Fig. 5.6).

The TNR ignition mass as a function of the WD mass and radius:

$$P_{\text{crit}} \approx \frac{GM_{\text{WD}}M_{\text{crit}}}{4\pi R_{\text{WD}}^4}, \quad (5.1)$$

where G is the gravitational constant, M_{WD} is the WD mass. M_{crit} is the critical mass of accreted material for TNR ignition and R_{WD} is the WD radius. This critical pressure is reached at the base of the accreted layers and P_{crit} is also a function of the mass accretion rate, temperature, and the WD composition (see Starrfield, 1989). This results in a range of required M_{crit} from $10^{-5} M_{\odot}$ for WDs approaching the Chandrasekhar mass (such as M31N 2008-12a, see Darnley et al. 2019) to $10^{-2} M_{\odot}$ for less massive WDs (around half a solar mass Bode & Evans, 2008).

5.1.2 Nova light-curves

5.1.2.1 Light-curve morphology

The rise to a nova's peak brightness after the initial eruption is rapid in almost every case, taking around one to three days (Bode & Evans, 2008). These light curves are used to determine the speed class of the nova. The anatomy of a nova light-curve is shown in Fig. 5.1 taken from McLaughlin (1960). Nova light-curves in most cases are similar to each other when compared on similar timescales (McLaughlin, 1945; McLaughlin, 1960). The lightcurve shape represents the effect on the brightness of the transient by the expanding ejecta forming an optically thick photosphere that subsequently recedes towards the WD as the optical thickness decreases and there may be shift towards shorter wavelengths as the hot central WD is exposed. Ongoing pseudo-stable burning on the surface of the envelope emit X-rays in what is known as the super soft source phase (van den Heuvel et al., 1992; Kahabka, 1997; Osborne, 2015). Furthermore, ongoing

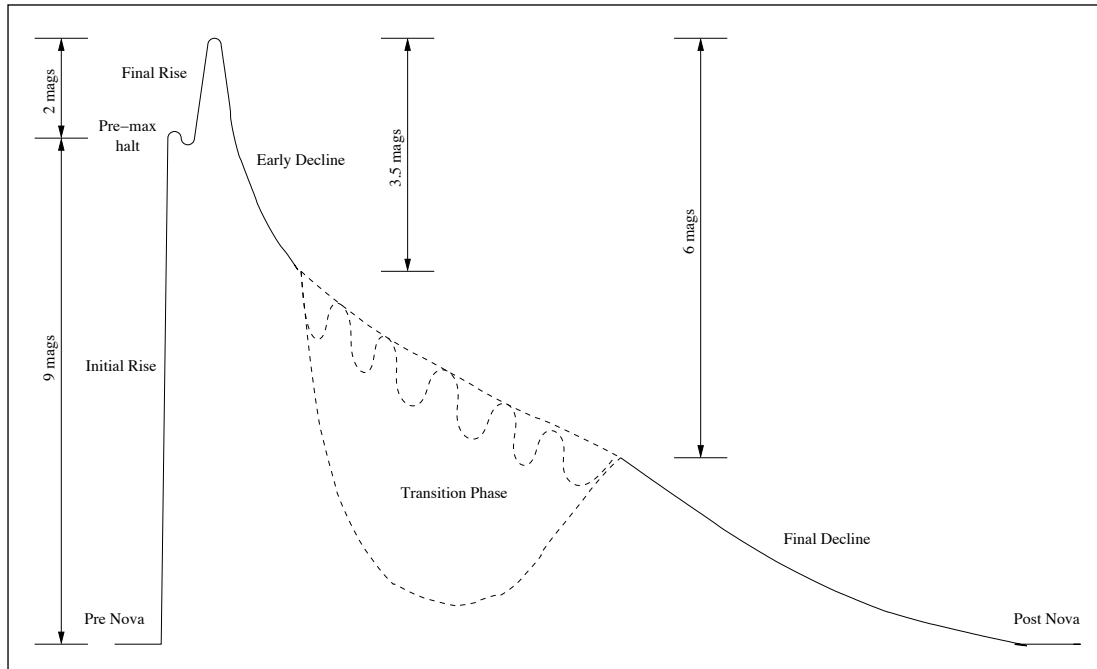


FIGURE 5.1: The anatomy of a nova light-curve. Courtesy of Prof. Matthew Darnley (PhD thesis), originally from McLaughlin (1960)

photoionisation of the ejecta driven by the central WD leads to radio emission (Bode & Evans, 2008) and dust processes the WD radiation and creates an infra-red excess (Hyland & Neugebauer, 1970; Gehrz, 1988). The light-curve evolution can be described in a series of steps:

Initial rise: The initial rise phase is very short and not many CNe are observed in this phase, but some novae are caught during the initial rise such as the June 2022 eruption of the Galactic nova, U Sco¹. The initial rise may halt at around two magnitudes before the peak brightness after no more than three days (Bode & Evans, 2008).

Pre-maximum halt and final rise to peak: Depending on the speed class of the nova this pre-maximum halt can last between a few hours and a few days after which the light-curve reaches its peak maximum brightness. This result contrasts with the relation that the duration of the pre-maximum halt is correlated to the speed class of the CN, where fast CNe have short duration pre-maximum halts (only a few hours, e.g. V598 Pup, KT Eri and V5583 Sgr Hounsell et al. 2010 and also see Hounsell et al. 2016), and slower CNe decreasing in brightness more slowly (may last over a month, e.g.

¹<http://ooruri.kusastro.kyoto-u.ac.jp/mailman3/hyperkitty/list/vsnet-alert@ooruri.kusastro.kyoto-u.ac.jp/thread/DZCBTEGDQPYCX4LSE3SDJNJ2J6JBRKTD/>

V2891 Cyg [Kumar et al., 2022](#)). This peak brightness period is short and lasts at most a few days.

Some explanations for the pre-maximum halt have been suggested, although the cause of the halt is still not fully understood. One such explanation proposed by [Orio & Shaviv \(1993\)](#) is that there may be a localised TNR on the WD surface due to the accretion of a non-homogeneous envelope. Furthermore, [Friedjung \(1992\)](#) suggested that the pre-maximum phase of HR Del was due to the CN having a low-mass WD ($\sim 0.52 M_{\odot}$) and the conditions for TNR may have been only just satisfied and there may be instabilities in the runaway. [Hachisu & Kato \(2004\)](#) modelled the lightcurves of two CNe with pre-maximum halts, V723 Cas and V463 Sct. Those authors found that when modelling an optically thick wind with WD that possessed a massive H-rich envelope, the star mimics a supergiant star. The WD expands to over $100 R_{\odot}$, this then decreases the effective temperature of the WD to ~ 7000 K. In these models, the changes to the photospheric radius and temperature are small compared to the increases in envelope mass, leading to the CN pre-maximum halt. However the steady-state wind model may only be applicable for very specific CN systems with the massive H-rich envelope. [Hillman et al. \(2014\)](#) present models of CN light curves, investigating the pre-maximum halt. They found that the pre-maximum halt may occur when the convective envelope boundary recedes towards the WD. [Hillman \(2022\)](#) found that model parameters that result in fluctuations in a prolonged light curve maximum also result in pre-maximum halts, with a possible lower mass WD and long accretion period.

Initial decline and the transition phase and final decline: In many novae the initial decline (a power law decline in flux, $f \propto t^{\alpha}$) is fairly smooth however novae of the slow speed class exhibit some brightness variations that occur on a time-scale of a few days. Once the brightness of the nova has declined by around three magnitudes the light-curves can show some diversity. Generally, three regimes arise:

1. The nova can fall in to a deep minimum well up to ten magnitudes below maximum that is caused by dust formation. This can be observed via infra-red observations showing a brightening in IR before a recovery to an extrapolated decline curve (see [Hyland & Neugebauer, 1970](#)). This “dust dip” phase of the light-curve’s evolution can last for months to years ([Bode & Evans, 2008](#)). For example, DQ Her had a dust dip lasting around four months ([Rosenbush, 1999](#)).
2. The second scenario is that oscillations in brightness may occur with amplitudes of around 1.5 mag and periods of between five and fifteen days (e.g. V603 Aql, GK Per and DK Lac; [Pejcha, 2009](#)) and more recently, V373 Scuti ([Bianchini et al., 1992](#)),

Speed class	t_2 (days)	\dot{m}_V (mag d ⁻¹)
Very fast	<10	>0.20
Fast	11-25	0.18-0.08
Moderately fast	26-80	0.07-0.025
Slow	81-150	0.024-0.013
Very slow	151-250	0.013-0.008

TABLE 5.1: The five nova speed classes from very fast to very slow as defined by Payne-Gaposchkin (1964) with the corresponding t_2 time in days and the magnitude rate of decline, \dot{m}_V in magnitudes per day.

V1186 Sco and V2540 Oph (Tanaka et al., 2011). These rebrightening episodes have been interpreted as being due to unstable envelope hydrogen burning (Pejcha, 2009).

3. The third possibility is that the nova light-curve is unaffected and smoothly transitions to the final decline and post-nova phase into quiescence.

5.1.3 Speed classes

One may categorise novae using speed classes. The speed class of a nova is determined by the decline time, when decline time is usually defined as the time taken for the magnitude of the nova system to drop by two magnitudes from maximum light (t_2). Sometimes other standards are used such as t_3 , the time taken for the nova to decrease by three magnitudes. The convention for the categorisation of nova speed class was set by Payne-Gaposchkin (1964) and is described in Table 5.1.

5.1.4 Maximum-Magnitude Rate of Decline (MMRD) relation

Historically novae have been proposed as standardisable candles for distance estimates. Hubble (1929) and Zwicky (1936) suggested a relation in the speed classes of novae, now known as the maximum magnitude rate of decline (MMRD) relation (McLaughlin 1945, Arp 1956b, Downes & Duerbeck 2000), which could be utilised for distance estimates. However the MMRD is probably a product of selection bias as there is now large scatter in the magnitudes of novae leading to 2-3 mag discrepancies in the MMRD (Shara et al., 2017b) and shown in the discovery of “faint and fast” novae (Kasliwal et al., 2011b) and rapid recurrent novae (RNe, Darnley et al. 2014a). Yaron et al. (2005) present simulations showing that nova explosions are not only dictated by the WD mass but also accretion rates, and the varying accreted envelope mass also results in a scatter in the

magnitudes. [Shara et al. \(2017b\)](#) used a sample of novae in M87 to explore the MMRD. They found that the presence of faint and fast novae reveal the relation as flawed, at least generally. However, with this in mind, there are some arguments still in support of the MMRD. [Shara et al. \(2018\)](#) proposed that novae that follow the t_{15} relation which does not refer to the time taken to drop 15 magnitudes but rather that the magnitudes of novae that remain detectable for 15 days tend to converge (using the de Vaucouleurs relation, see [de Vaucouleurs 1978](#)) with an absolute magnitude ~ -6.4 ([Ferrarese et al., 2003](#)). This results in distance estimates with 1σ errors of 20 per cent, however, all the CNe in the sample were similar, it discounts fast novae and the survey used did not detect any slow novae.

The MMRD persists despite the advent of Gaia DR2 ([Gaia Collaboration et al., 2018](#)) and the debate continues. [Schaefer \(2018b\)](#) found that the MMRD did not perform well for CNe with distances from Gaia, with a large scatter. [Selvelli & Gilmozzi \(2019\)](#) present a study on 18 CNe with Gaia distances (almost the same sample as [Schaefer, 2018b](#), with 15 of the same transients). They found that the decline time/speed class (in this case, t_3) was correlated with the MMRD where the most luminous CNe had the shortest t_3 . Furthermore, [Della Valle & Izzo \(2020\)](#) found that the MMRD could reproduce the distances to the CNe in their sample with uncertainties < 30 per cent. [Darnley & Henze \(2020\)](#) propose that the MMRD could be modified to use the bolometric luminosity of CNe as much of the output of some CNe such as the faint and fast CNe may be out of the visible wavelength realm (in the case of faint and fast CNe, the bulk of the emission may be in the UV).

5.1.5 Spectral classes

Spectroscopic studies show that novae can be broadly split into two spectroscopic classes based on signature non-Balmer emission lines that appear in the spectra soon after maximum. The principal spectrum in the case of CNe is observed between maximum brightness and the time at which the brightness of the CN has decreased by two magnitudes from maximum, t_2 . The two classes as described in ([Williams 1992, 1993](#) and [Williams et al. 1994](#)) are Fe II and He/N.

The Fe II class is characterised by the presence of a plethora of iron lines and by slower ejecta (with ejecta velocities under 2500 km s^{-1} [Shafter et al., 2011a](#)) and often exhibit P-Cygni absorption features. They show low-ionisation lines such as various Fe II lines and at the red-end of the spectrum one may find CNO product lines. The Fe IIb (“b” denoting broad) is a sub-class of Fe II CN where the Balmer emission lines are broader

(in this respect, more closely resembling the He/N class discussed below) than typically seen in Fe II novae. The FWHM distributions of H α emission lines from M31 CNe are illustrated in Fig. 5.2 from [Shafter et al. \(2011a\)](#). However it should be noted that this distribution may under represent the faster CNe (which are abundant in the disc of the Milky Way) as it is difficult to detect the faster CNe in M31.

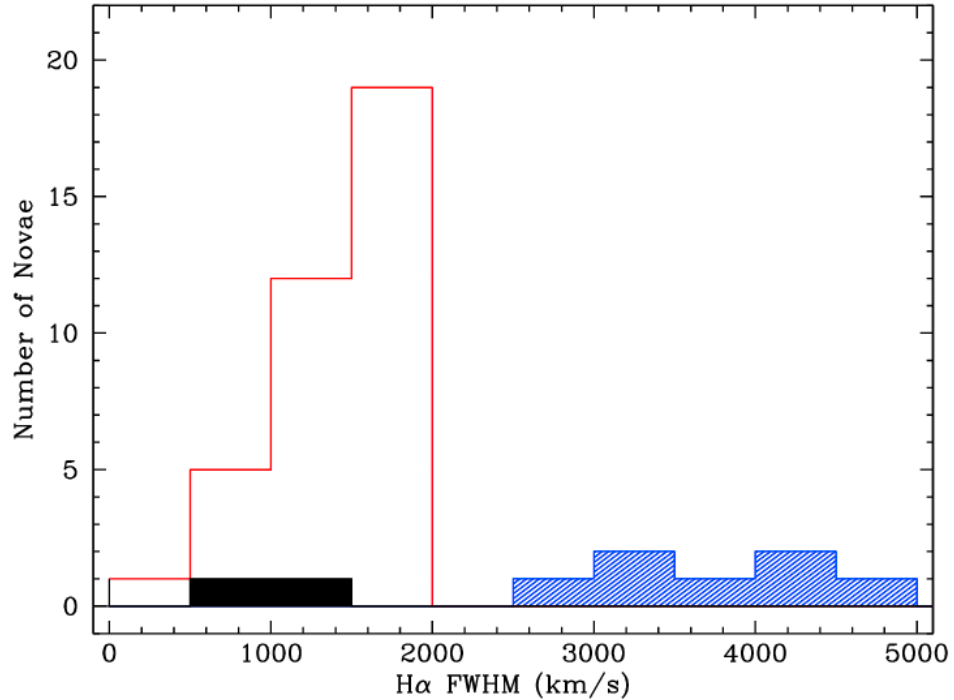


FIGURE 5.2: The distribution of the novae spectral classes in relation to their ejecta velocity as inferred from the widths of the H α emission line. It is clear that the Fe II novae in red have slower ejecta than He/N in the blue cross-hatch. The filled black region represents the He/Nn hybrid class. Taken from [Shafter et al. \(2011a\)](#) © AAS. Reproduced with permission

The He/N class CNe are characterised by an He and N enriched spectrum with faster ejecta (2500 km s^{-1} and above). They don't tend to be observed to show any absorption features as the ejecta in He/N CNe become optically thin quickly. He/N novae show higher levels of ionisation exhibiting more rectangular line profiles and He and N lines are observed ([Williams, 2012](#); [Shafter, 2013](#)). The He/Nn (“n” denoting narrow) are a sub-class of He/N CNe where the widths of the the Balmer emission lines are narrower than the “normal” He/N class but exhibit otherwise similar features. However, the He/Nn CNe may be a product of inclination to the observer.

[Shore \(2012\)](#) describe the taxonomy of the spectral classes being a sequence corresponding to the changing optical thickness of the ejecta. Fe II spectra are exhibited when the

ejecta are optically thick and the He/N features are subsequently revealed when the ejecta become thin. CNe could be observed when the ejecta are already optically thin. Some CNe ejecta can be optically thick or opaque for some time and seemingly be stuck in this phase and the He/N features are never seen as the CN has already passed to the later spectroscopic phases (coronal and nebular). Shore (2012) also show that some spectral features and line profile shapes may be affected by other factors such as inclination. Williams (2012) interpret the classes as features originating from different parts of the CN system. He/N CNe decline rapidly in luminosity and show wider line profiles (above 2500 km s^{-1}) and prominent H, He and N features and exhibit higher ionisation. Williams (2012) suggest that these He/N features originate from material ejected at high velocity from the WD. The Fe II CNe have narrower line profiles than those of the He/N class. The Fe II class exhibits many numerous Fe II lines and unlike the He N, shows P Cygni absorption features and the luminosity declines slowly. The Fe II CN features seem consistent with a stellar wind and may originate in a gas envelope with solar-like abundances that comes from the companion star (Williams, 2012). All CN outbursts eject He and CNO material that create the He/N spectrum. Some of these ejecta interact with the donor and may initiate elevated mass loss from the donor. The material that is lost by winds from the secondary may be responsible for the Fe II spectral features. The subsequent spectral class then depends on the mass loss rate of the donor and the geometry of the donor wind. If the amount of mass lost through these winds is small, the He/N may dominate. Conversely, if the mass loss is significant, then the mass loss from the secondary forms an expanding photosphere and the CN presents as a Fe II class nova. As the optical thickness of the ejecta decreases, the nebular spectrum emerges.

Examples of the spectra of the Fe II class and He/N class from Williams (1992) are given in Fig. 5.3 and Fig. 5.4.

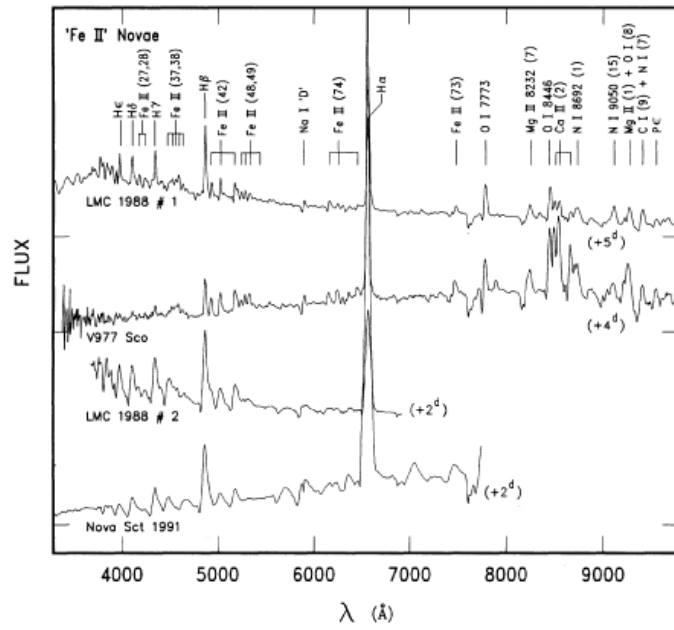


FIGURE 5.3: Template spectra for the Fe II class, taken from Williams (1992). © AAS. Reproduced with permission

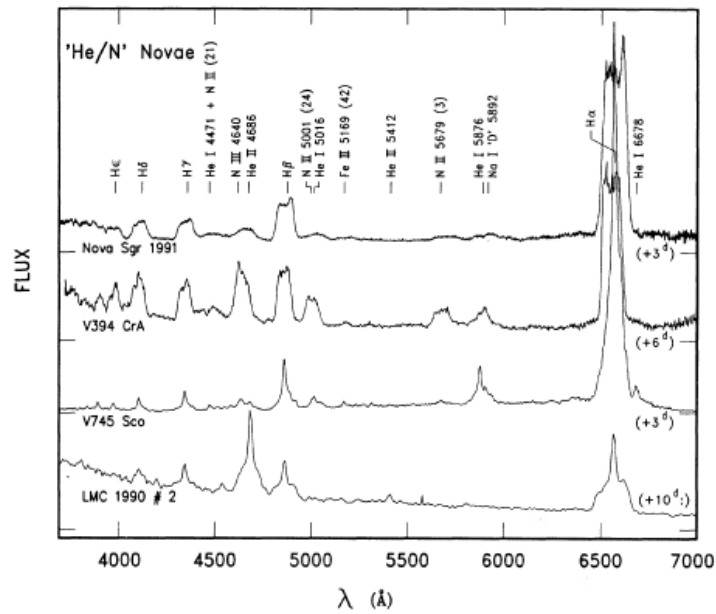


FIGURE 5.4: Template spectra of the He/N class, taken from Williams (1992). © AAS. Reproduced with permission

5.1.6 Ejecta velocity

One can approximate the velocities at which material is ejected from the CN eruption by measuring the widths of the emission lines (or P-Cygni profiles). The full-width half-maximum (FWHM) value of a line is an approximation of the line of sight ejecta velocity with broader lines suggesting higher ejecta velocities due to Doppler broadening (e.g. [Harvey et al., 2019](#)). The ejecta velocity may not directly yield the maximum velocity of the ejecta, however, as the emission lines originate from different parts of the ejecta, and may also be effected by the inclination of the system and the ejecta density profile.

The terminal velocity at which material reaches after being ejected from the WD is typically of the order a few thousand kilometres per second but can be in excess of $10,000 \text{ km s}^{-1}$. The $\text{H}\alpha$ profile FWHM differences between the Fe II and He/N classes are illustrated in Fig. 5.2.

5.2 The significance of classical novae

5.2.1 Type Ia Supernova progenitors

CNe are a plausible single-degenerate channel of SNe Ia (see [Whelan & Iben, 1973](#); [Hachisu et al., 1999](#); [Hillebrandt et al., 2000](#)). SNe Ia would arise from a CN system where the WD is a CO WD (oxygen-neon WDs collapse to form neutron stars; [Gutierrez et al., 1996](#)) and when the accreted mass over time is greater than the mass loss from eruptions. The mass of such a WD would eventually exceed the Chandrasekhar mass where electron degeneracy pressure can no longer prohibit a collapse and a supernova explosion would subsequently occur (see [Chandrasekhar, 1931](#)).

[Hillman et al. \(2015\)](#) investigated the single-degenerate route to SNe Ia by simulating the evolution of a CN system. Those authors began with a high mass WD. They then evolved the WD over thousands of CN eruptions, and found that the accreted mass was larger than the ejected mass in the CN eruptions. Therefore, the WD slowly grew in mass and those authors found that WDs with masses $1.0\text{--}1.38 M_{\odot}$ increased in mass steadily with a mass accretion rate of $5 \times 10^{-7} M_{\odot} \text{ yr}^{-1}$ and would evolve into a SN Ia. [Hillman et al. \(2016\)](#) extended these simulations and found that helium flashes from the ignition of a thick helium layer accumulated on the surface of the WD would not necessarily prevent the growth of the WD over the Chandrasekhar mass. Those authors

also found that there was a large valid range of accretion rates and WD masses for which the single-degenerate channel for SNe Ia was valid.

5.2.2 ${}^7\text{Li}$ production

As described by [Fields \(2011\)](#), observed lithium abundances in metal-poor halo stars are several orders of magnitudes smaller than the abundances predicted by primordial nucleosynthesis models. If Li is not primordial in nature, then other astrophysical processes must be the source. CNe are thought to be a major source of ${}^7\text{Li}$. ${}^7\text{Li}$ lines (in this case the 6703Å line) were first observed by [Izzo et al. \(2015\)](#) in the early spectra of V1369 Cen. This isotope of Li is produced by the decay of ${}^7\text{Be}$ which is a product of the TNR. The ${}^7\text{Be}$ formed in the TNR is ejected in the CN eruption and then decays into ${}^7\text{Li}$ via electron capture ([Izzo et al., 2018](#)). The first detection of ${}^7\text{Be}$ in a nova spectrum was by [Tajitsu et al. \(2015\)](#) in the post-outburst spectra of V339 Delphini. The ejecta of V5669 Sgr was found by [Molaro et al. \(2016\)](#) to be highly enriched in ${}^7\text{Be}$ and they conclude if the production rate seen in V5669 Sgr is common then CNe can account for all ${}^7\text{Li}$ production in the Galaxy.

[Izzo et al. \(2018\)](#) found ${}^7\text{Be}$ in the very fast Galactic CN, ASASSN-16kt that may have a ONe WD. Those authors concluded that ONe WDs produce a similar amount of ${}^7\text{Be}$ as CO WDs, despite the total ejected mass from ONe CNe being less than CO CNe.

5.2.3 Recurrent novae (RNe)

CNe are inherently recurring systems (see [Darnley & Henze, 2020](#), for a review). The WD and donor companion star both survive the CNe eruption and resume the mass-accretion process ([Darnley & Henze, 2020](#)). CN systems that have been observed to undergo multiple eruptions are classified as recurrent novae (RNe). RNe require a high M_{WD} so that less hydrogen rich material needs to be accreted from the donor for the eruption to take place. This is due to the higher surface gravity facilitating less accreted mass required to reach P_{crit} . This is coupled with a high accretion rate (\dot{M}) resulting in short recurrence times. This results in the CN erupting within timescales that are short enough to be in reliable astronomical records, hence recognised as RNe. RNe have a wide range in observed recurrence periods (P_{rec}) from 1yr in the case of the remarkable recurrent nova M31N 2008-12a (often referred to simply as 12a) to 98 yrs (see [Darnley et al., 2014a](#); [Pagnotta & Schaefer, 2014](#)). Observational limitations truncate the both ends of this range.

5.3 Extragalactic nova studies

Extragalactic CN studies have advantages over Galactic nova observations in that the CNe in a particular galaxy are essentially equidistant, furthermore foreground extinction/reddening is roughly constant across the field of view, which helps determining luminosities. Another advantage over Galactic CN studies is that if one is observing a galaxy such as M31 or M33 it is possible to determine a region of galaxy/stellar population a CN resides in which is difficult to do in Galactic CN studies due to uncertainties in distance and due to extinction.

The Andromeda galaxy (M31) is the best laboratory we have for the study of CNe. M31 is a large spiral galaxy that is close to edge on (not ideal for CN studies) with an inclination of 77° (de Vaucouleurs, 1958) at a distance of 761 ± 11 kpc (Li et al., 2021). Transients in M31 have been observed as close as $10''$ from the nucleus (Kerins et al., 2010) and novae were being discovered in M31 before it was recognised as a separate galaxy itself (indeed, before anyone knew there were separate galaxies!). Hubble (1929) published the first extragalactic CN sample in M31, along with the Cepheid survey that contained the distance estimates which showed M31 was beyond the Milky Way. The first spectroscopically confirmed novae in M31 were discovered by Ritchey (1917) in the early days of extragalactic novae studies and after previous discoveries are now recognised as supernovae (S Andromedae and Z Centauri). The CN rate for M31 is around 65 CNe per year (Darnley et al., 2004, 2006).

Extra-galactic nova studies historically have been partially motivated by the possibility of using CNe as an extra-galactic distance indicator (see Lundmark, 1922, 1923). CNe can provide a fair estimate to the distance to other galaxies assuming the chosen novae fit the MMRD relation (discussed in Section 5.1.4). Della Valle & Izzo 2020 provide a calibration to the MMRD based on distances to CNe from Gaia,

$$M_V = 2.5 \times \log t_3 - 11.6, \quad (5.2)$$

where M_V is magnitude and t_3 is the three magnitude decline time in days.

The observations and surveys of CNe beyond of the Milky Way afford us the opportunity to investigate the separate nova populations in more galaxies and different galaxy types that may differ in spatial distribution in relation to the host galaxy or their Hubble Sequence classification (see Hubble, 1926). Thirty CNe were discovered in the M31 survey by Arp (1956a), who found a bimodal distribution in the magnitude of the novae

at maximum light with a peak at around $m_{pg} = 16.0$ and another peak at around $m_{pg} = 17.5$ (Fig. 5.5), however this bimodality is due to selection effects (M. J. Darnley, private comm.). Until this work the largest M31 survey, the Asiago survey (see [Rosino, 1964, 1973](#); [Rosino et al., 1989](#)) found 142 CNe candidates. When these data were combined with the Hubble and Arp findings, the bimodal peaks in the magnitudes of the novae at maximum light were no longer present (Fig. 5.6). This highlights the importance of surveys that allow us to elucidate any correlations or patterns that may be real or simply a product of small number statistics and bias.

5.3.1 Extragalactic classical nova populations

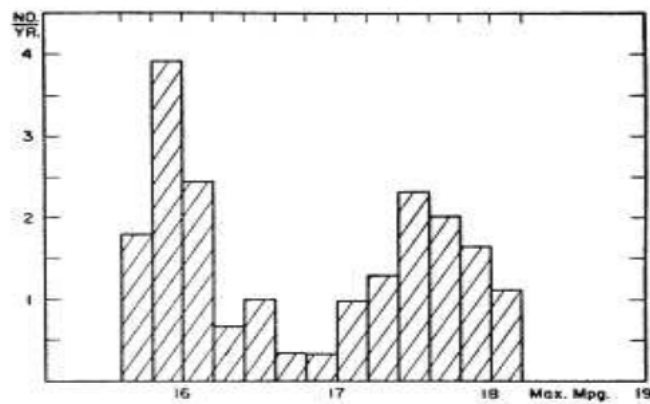


FIGURE 5.5: Histogram of the maximum apparent magnitude of M31 CNe showing the bimodal CN population proposed by [Arp 1956a](#) © AAS. Reproduced with permission

While the idea that there are multiple populations of CNe in terms of their peak brightness is now discredited, there still may be multiple populations of CNe. For Milky Way CNe, [Duerbeck \(1990\)](#) proposed that CNe had two populations. One population is associated with the disc of the galaxy and another associated with the bulge. [Duerbeck \(1990\)](#) also suggests that the disc novae are of the fast speed class and the bulge novae were slow CNe. [Della Valle et al. \(1992\)](#) expands on these results, finding that out of a sample of 19 Galactic CNe, fast (and brighter) speed class novae have a small scale heights, while slow (and dimmer) novae can be found up to 1 kpc above the plane of the Milky Way. However, selection effects may be in play here, [Özdönmez et al. \(2018\)](#) found that most novae were associated with the Galactic disc and previous results were due to catalogue incompleteness. [Della Valle et al. \(1992\)](#) also found that these

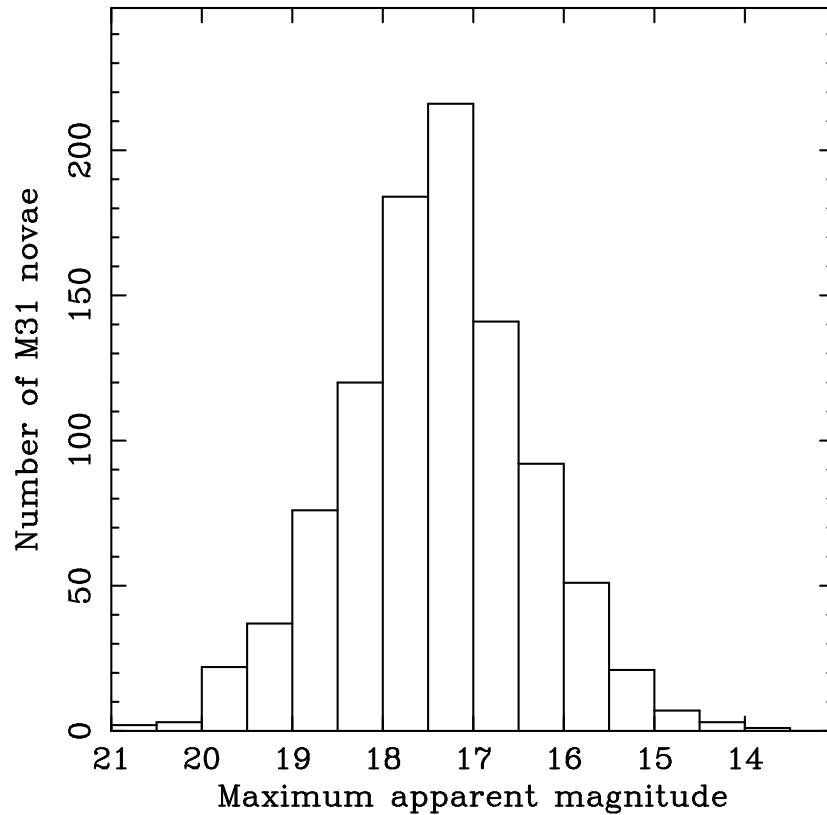


FIGURE 5.6: Histogram of the maximum apparent magnitude of M31 CNe using updated observations. The initial bimodal distribution found by [Arp 1956a](#) is no longer present when new observations are used. Plot from Prof. Matthew Darnley with data from the catalogue of [Pietsch \(2010\)](#).

correlations are consistent with the statistics of extragalactic CNe found in hosts such as M31 and the LMC. [Della Valle & Livio \(1998\)](#) then investigate the distribution of the spectroscopic classes from [Williams \(1992\)](#) (also see Section 5.1.5). Those authors found that the the bright, fast disc associated CNe tend to be He/N class and the dimmer, slow, bulge CNe tended to be classified as Fe II novae. This suggested that the He/N CNe may be associated to younger stellar populations found in the disc and the older populations in the bulge host the Fe II novae. CNe fade more slowly in the $H\alpha$ band because recombination time is longer than the decay time for the the continuum as noted in [Payne-Gaposchkin 1964](#). $H\alpha$ surveys of CNe exemplify a benefit of narrow-band imaging, as it reduces the effect of the host galaxy’s background light and allows a deeper survey. [Ciardullo et al. \(1987\)](#) presented a $H\alpha$ survey of CNe in M31. They found that the “hole” in the CN population in the bulge of M31 reported by [Arp \(1956a\)](#) was not present and the gap was due to selection effects. [Ciardullo et al. \(1987\)](#) also found that CNe in M31 are mainly associated with the bulge (also see [Capaccioli et al., 1989](#); [Shafter & Irby, 2001a](#)). [Darnley et al. \(2006\)](#) present the M31 CNe from the

POINT-AGAPE microlensing survey. Those reaffirmed that the CN population in M31 was bulge dominated and had a disc associated population and bulge population. These populations were found to have a CN rate of around 38 yr^{-1} for the bulge and around 27 yr^{-1} for the disc of M31. Along with [Ciardullo et al. \(1987\)](#) and [Shafter & Irby \(2001a\)](#), [Darnley et al. \(2006\)](#) present a model for the M31 CN distribution based on the contribution of the disc and bulge light. In this model, there is a parameter, θ that is the ratio of the eruption rate of disc and bulge CNe per unit light ($\theta = 0$ indicating a bulge population, $\theta = 1$ being a population that follows galaxy light and $\theta \rightarrow \infty$ is a disc dominated population). Based on the disc/bulge contributions in terms of the r' -band light, [Darnley et al. \(2006\)](#) determined a $\theta \approx 0.18$. Therefore, per unit r' -band light, the bulge CNe are five times more common than disc novae, however as there is more disc light than bulge light, the bulge/disc CN rates are similar. This distribution will be explored in Chapter 7.

[Shafter et al. \(2011a\)](#) found in their survey of M31 CNe that generally the He/N class were more luminous and decayed faster than their Fe II counterparts. This faster decay is due to there being higher ejecta velocity and therefore lower optical depth. [Shafter et al. \(2011a\)](#) investigated whether the mass of the WD may have an influence on spectral classification. They use radial distribution analysis to test for a bimodal population of bulge and disc novae. Less massive WDs in the bulge may give rise to Fe II novae as generally the bulge would host older stellar populations. Higher mass WDs may produce the He/N novae and compared to the Fe II which one would expect to only find in old populations, may also be associated with younger ones. The number of the lower mass, bulge CN progenitors is around five times that of the higher mass disc CN progenitors assuming a Salpeter initial mass function ([Cummings et al., 2018](#); [Della Valle & Izzo, 2020](#)). When accounting for a higher recurrence rate from higher mass WDs, [Della Valle & Izzo \(2020\)](#) calculate that the observed eruption fraction between disc and bulge CNe is ~ 3 . While [Della Valle & Izzo \(2020\)](#) find this rate consistent with observations of extragalactic CNe, [Shafter et al. \(2011a\)](#) did not find any significant difference in the radial distributions of the two main spectral classes in M31. This may be an expected result however, as both Fe II and He/N may be found in older populations (with some He/N associated with younger populations). Furthermore if the spectral classes were linked to the WD mass and underlying stellar populations then the proportion of each class should differ depending on the type of galaxy. For example, [Shafter et al. \(2012a\)](#) and [Shafter et al. \(2014\)](#) found half of the ten spectroscopically confirmed CNe in M33 were of the Fe II class and [Shafter \(2013\)](#) found that this was also the case in the LMC. M33 and the LMC may be considered ‘bulgeless’ galaxies

Conversely, in the large, ‘bulged’, spiral galaxy M31, Fe II class novae make up about 82 per cent of the nova population. It should be noted that selection effects could play a role in the classifications of novae. The Fe II class has a longer decline time than the He/N novae so is detectable for longer, however may be on average less luminous. Historically, observations of M31 CNe focus on the central regions of the galaxy as one is more likely to detect CNe near the bulge ([Darnley et al., 2019](#)), this bias should be considered when discussing CN surveys and samples.

Other galaxies have been surveyed such as the LMC ([Shafter, 2013](#)), M81 ([Shara et al., 1999](#)) and M87 ([Madrid et al., 2006](#); [Shara et al., 2017b](#)). Reviews on extragalactic CNe and their possible populations are given in [Shafter \(2019\)](#) and [Darnley & Henze \(2020\)](#).

Chapter 6

The spectral classification of classical novae in the Andromeda galaxy (M31)

6.1 The spectral classes of classical novae

As described in Chapter 5, spectroscopic studies of CNe show that, broadly, there are two spectroscopic classes based on signature non-Balmer emission lines which appear in the spectra soon after maximum. The two classes as described by ([Williams, 1992, 1995](#)) are Fe II and He/N (see also [Williams, 2012](#)).

Here I present the largest spectroscopic survey of CNe in M31 to date. In this chapter, I outline the spectroscopically confirmed M31 CN sample. Moreover, I spectroscopically classify CNe that had available LT SPRAT data. In Section 6.2 I describe why the classification is necessary and in Section 6.3 I describe where the CN sample came from. I set out the classification methods in Section 6.4. The classification of the M31 CNe are presented in Section 6.4.1 and the conclusions are discussed in Section 6.5.

6.2 Motivation for the classification of classical novae

For the environmental analysis of M31 CNe presented in Chapter 7, robust spectral classifications are required, ideally multiple times more than in previous studies such as in [Shafter et al. \(2011a\)](#) in order to obtain robust statistical results. A number of

CNe within online databases are recorded as spectroscopically unclassified, but they may have accessible data, for example in the LT archive (the CN community generally do not report much on large transient databases). Furthermore, some transients are initially classified as CNe but subsequent observations reveal that they are Galactic variable stars or dwarf novae.

Also as the distributions of the different spectral classes of CNe are being investigated here, it is important that as many of the CNe as possible are systematically investigated. Moreover, any of the CN spectroscopic sub-classes, the He/Nn and Fe IIb CNe must be noted and differentiated from other classes by estimating the widths of the Balmer emission lines ($H\alpha$ in this case) which gives an estimate of ejecta velocity. As will be discussed in Chapter 7, the spectral classes of CNe may be linked to the progenitor WD mass.

6.3 M31 classical nova catalogue

6.3.1 The database

Using the online database of extragalactic novae of [Pietsch et al. \(2007\)](#) and [Pietsch \(2010\)](#), the largest sample of spectroscopically confirmed CNe to date was constructed. Starting from the end of the previous M31 nova survey by [Shafter et al. 2011a](#) who present the initial 44 CNe used here, I assembled a catalogue of novae with confirmed spectra from January 2010 to February 2019. Despite there likely being a small number of unpublished nova spectra which won't appear on the catalogue this is an exhaustive list of M31 novae. References to photometry and spectroscopy of each nova are often in the form of a link to an Astronomical Telegram (ATel), an entry in the Central Bureau for Astronomical Telegrams (CBAT) or a Transient Name Server (TNS) posting. The CNe in this catalogue are reported from a variety of sources, with a large component being from amateur, or 'pro-am' astronomers. Sources of CNe discoveries include reports by individual astronomers¹, amateur surveys such as the Xingming Observatory Sky Survey (XOSS²) and professional surveys such as the Lick Observatory Supernova Search (LOSS; [Filippenko et al., 2001a](#)). Followup spectroscopic observations may be carried out using facilities such as the LT with SPRAT, the Spectral Camera with Optical

¹In some cases these astronomers coordinate observations through groups such as the American Association of Variable Star Observers (AAVSO), <https://www.aavso.org/>

²<http://xjltip.china-vo.org/about-xingming.html>

Reducer for Photometrical and Interferometrical Observations (SCORPIO) on the Large Azimuth Telescope (BTA-6) in Russia³ and others described in Table 6.1.

From the [Pietsch \(2010\)](#) database⁴, 180 more M31 CNe were recorded. Of this 180, 76 of these had SPRAT data. As the SPRAT data were available on the LT data archive⁵, these will be used for spectral classification. The ATel/CBET/TNS classifications will be used for the transients without LT SPRAT observations. This catalogue is over four times bigger than that of [Shafter et al. \(2011a\)](#) and their sample will be compared to the new, larger sample and then combined with the larger sample. The ‘new’ 180 CNe and which facility the spectra are from is outlined in Table 6.1. Out of these 180 CNe, 21 do not have spectral data.

TABLE 6.1: The number of CN spectra from our full sample of 180 observed by different facilities.

Telescope	Number of spectra
Liverpool Telescope (LT SPRAT)	76
BTA SCORPIO	25
Hobby-Eberly Telescope (HET)	24
Palomar 200"	17
Apache Point	7
Canada France Hawaii Telescope (CFH)	3
Isaac Newton Telescope (INT)	3
Keck	3
Lick	3
Araki	2
William Herschel Telescope (WHT)	2
Others	15

6.4 Data analysis

In order to determine independent spectral classifications of our novae, spectroscopic data were downloaded from the LT data archive. LT SPRAT data are processed by an automated pipeline, resulting in a reduced 1D spectrum ([Piasecik et al., 2014](#)). Most of the spectra had three exposures with some having multiple observations over time. Using the `scombine` routine in `IRAF` these spectra are combined and the median taken to eliminate any cosmic rays. A small number of our novae had only one observation so regions affected by the cosmic rays are omitted from these spectra.

³<https://www.sao.ru/hq/lsvfo/devices/scorpio/scorpio.html>

⁴<https://www.mpe.mpg.de/m31novae/opt/m31/>

⁵https://telescope.livjm.ac.uk/cgi-bin/lt_search

Using the nova spectral templates seen in Fig. 5.3 and Fig. 5.4 and more detailed lists of expected lines from Williams (2012), the spectra of each CN is examined by eye for the presence of their characteristic lines and also line shapes as, for example, the Balmer line profiles of He/N novae tend to be double peaked or ‘saddle’ shaped. Furthermore the FWHM of the Balmer emission lines can be used to estimate the ejecta velocity and a FWHM of over 2500 km s^{-1} is indicative of a Fe IIb or He/N CN and below this limit, the Fe II and He/Nn novae. To aid line identification, the `python` package, `lineid_plot`⁶ is used which also plots line labels on the figures presented in Section 6.4.1.

The H α line is isolated (5000 km s^{-1} either side of the line centre) and the `lmfit` (v1.0.3 Newville et al., 2021) module in `python` is used to fit a single Gaussian curve to the line profile and similarly to Chapter 3, the FWHM is calculated in order to estimate the ejecta velocity. These ejecta velocity are used in the classifications and aid in the differentiation between “normal” Fe II and He/N novae from the sub-classes Fe IIb and He/Nn.

6.4.1 The spectra

In this section, I present a selection of the CNe that have good spectral data from the LT. Out of the 76 CNe with spectral data on the LT archive, I was able to classify 60. In Section 6.4.1.1, I describe the features of a selection of Fe II CNe. The Fe II CNe are the most abundant classification in M31, comprising 80 per cent of the observed fraction in this sample. This is consistent with previous work presented in Shafter et al. (2012a). Spectra used in the classification of some of these Fe II CNe are presented in Fig. 6.1 and Fig. 6.2. Compared to previous studies (one in Shafter et al., 2011a), we find more Fe IIb CNe, these are presented in Section 6.4.1.2 with the spectra plotted in Fig. 6.3. The He N in our sample are described in Section 6.4.1.3 and the spectra are presented in Fig. 6.4. There is a single He/Nn CN that was classified in this sample and is presented in Fig. 6.4. The ‘new’ sample of 180 CNe that includes the 60 new classifications is presented in Table 6.3.

A breakdown of the spectral classifications in this sample are outlined in Table 6.2.

⁶https://github.com/phn/lineid_plot

TABLE 6.2: The number of each class of nova determined from the 60 CNe with spectra available on the LT database which were able to be used for our classification purposes.

Spectral class	Number
Fe II	48
Fe IIb	5
He/N	6
He/Nn	1

6.4.1.1 Fe II novae

M31N 2015-07d is a good example of an Fe II nova, with strong Balmer lines up to $H\gamma$ and clear Fe II (42), (48, 49) and (74) lines are exhibited. The NaI line at 5892 Å is present with a P-Cygni feature. The $H\alpha$ FWHM is $\sim 2200 \text{ km s}^{-1}$ and the Fe II(42) lines redward of $H\beta$ increase in strength with longer wavelengths.

M31N 2015-08c has numerous pronounced P-Cygni features. P-Cygni features can be seen on the Balmer series up to $H\gamma$ and can be seen on the Fe II (42) and to a lesser extent the Fe II (48, 49) complexes and also on the OI line at 7002 Å. The FWHM of the $H\alpha$ profile is $\sim 1400 \text{ km s}^{-1}$. The $H\alpha$ and $H\beta$ lines are similar in strength and the Fe II(42) lines increase in strength with wavelength.

M31N 2015-11c is a very clear case of an Fe II nova, whilst no P-Cygni lines are present the Balmer series is clear up to a tentative $H\delta$ and shows the Fe II (42), Fe II (49,48), Fe II (37, 38), Fe II (27, 28) and Fe II (53) complexes as well as some other lines. The $H\alpha$ FWHM is $\sim 1300 \text{ km s}^{-1}$ and the Fe II(42) increase in strength with wavelength.

M31N 2016-05a shows a fairly featureless spectrum apart from the $H\alpha$ and $H\beta$ lines. However one can see some iron lines such as Fe II (42) and also shows Fe II nova characteristic lines such as the MgI line at 5178 Å and OI at 7773 Å. The FWHM of the $H\alpha$ profile is $\sim 1600 \text{ km s}^{-1}$ with a much weaker $H\beta$ line compared to the $H\alpha$ line.

M31N 2017-04b is also fairly featureless apart from a strong $H\alpha$ and a less pronounced $H\beta$ emission line. The HeI line at 7593 Å is shown along with a tenuous HeI line at 6683 Å hence the classification as a nova of the Fe II class. The FWHM of the $H\alpha$ profile is $\sim 1500 \text{ km s}^{-1}$.

M31N 2017-06e shows Balmer emission lines up to $H\delta$ and shows a strong OI 7773 Å feature and displays various iron lines such as Fe II (48, 49), Fe II (49), Fe II (42) and other lines such as the NaI line at 5892 Å which has a P-Cygni feature. The FWHM of the $H\alpha$ profile is $\sim 1500 \text{ km s}^{-1}$ and the Fe II(42) group of lines have similar strengths.

AT 2018kjt shows the Balmer series up to a clear $H\delta$ and shows Fe II (42) lines as well as OI at 7773 Å AlII at 6237 Å NaI at 6159 Å and NaII at 5686 Å which also shows a P-Cygni feature. The FWHM of the $H\alpha$ profile is $\sim 1100 \text{ km s}^{-1}$ and the Fe II(42) group decreases in strength with wavelength.

M31N 2019-01b is another good example of an Fe II nova with Balmer emission visible up to $H\gamma$ and various iron lines being displayed such as Fe II (42), Fe II (49), Fe II (48, 49), Fe II (38) and Fe II (27). There is a strong OI feature at 7773 Å and an MgI line at 7896 Å. The FWHM of the $H\alpha$ profiles is $\sim 2100 \text{ km s}^{-1}$ and the Fe II(42) group appears to strengthen with wavelength while the Fe II(48, 49) group decreases in strength with wavelength.

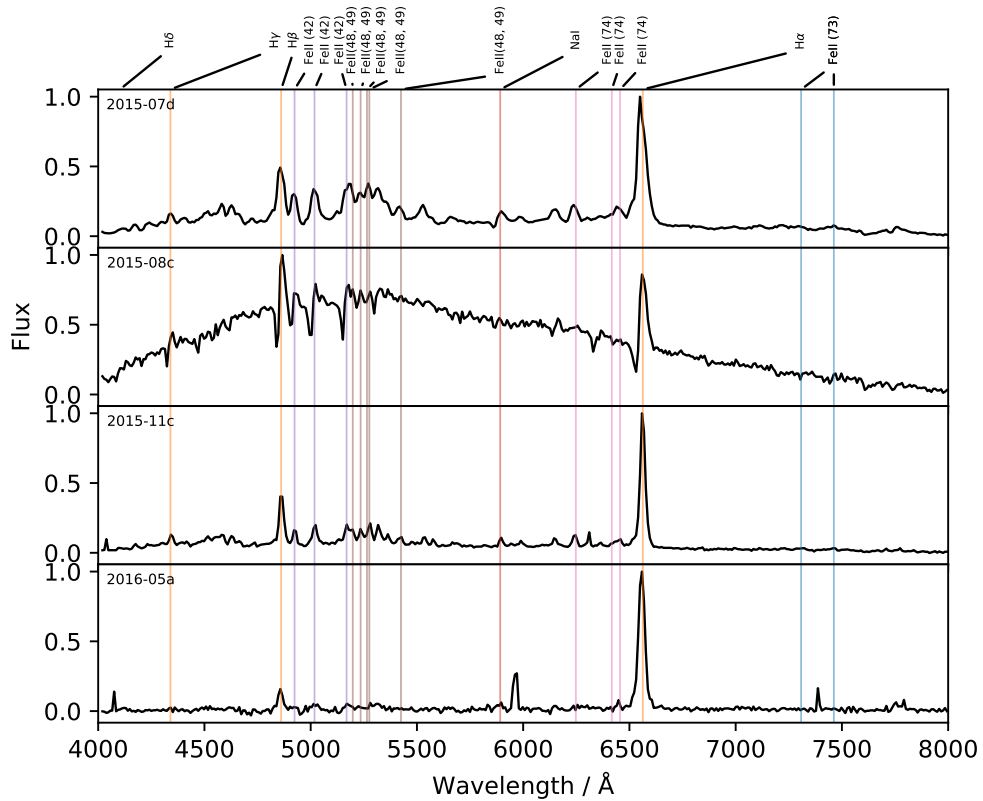


FIGURE 6.1: Spectra is presented for the first five of our chronologically ordered Fe II class CNe. Over-plotted are the more common Fe II characteristic lines. Note that the top spectra had a single SPRAT exposure so cosmic rays must be manually removed. M31N 2015-08c has numerous P-Cygni features that are easily visible.

6.4.1.2 Fe IIb novae

M31N 2016-01c exhibits broad single-peak Balmer series lines up to $H\gamma$ with $H\alpha$ being broad ($\sim 3600 \text{ km s}^{-1}$ therefore discounting this nova as being in the Fe II spectral

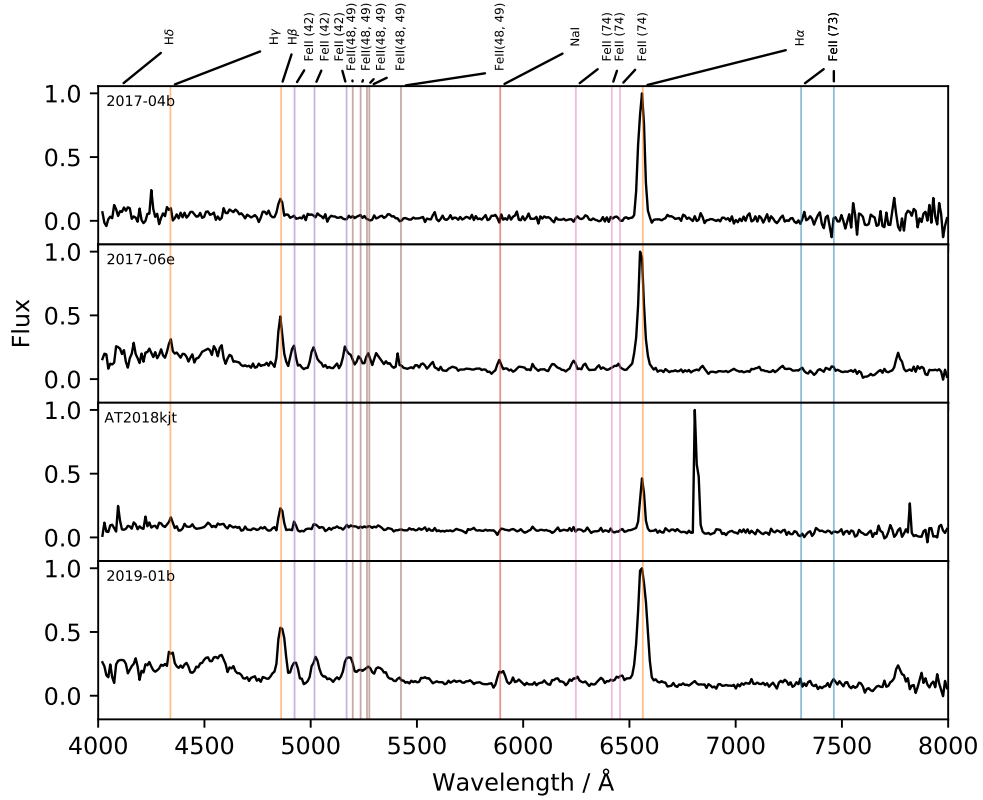


FIGURE 6.2: Spectra for the second group of five chronologically ordered Fe II class novae. M31N 2017-06e is a classic Fe II nova, exhibiting many of the Fe lines and the Balmer series extends to $H\delta$.

class where the FWHM of the $H\alpha$ line does not exceed 2500 km s^{-1} . Otherwise this nova exhibits a number of characteristic emission lines consistent with the Fe II class, hence we classify this nova as a broad lined Fe II nova or Fe IIb. The lines seen include a strong NaI line at 5892\AA , Fe II at 4352\AA , the Fe II (74) group is visible as well as some of the Fe II (42) and Fe II (48.49) lines and also a small OI feature at 7773 km s^{-1}

M31N 2016-02a shows sharp single peaked and broad Balmer lines up to a tenuous $H\gamma$ with the $H\alpha$ line having a width of $\sim 3200 \text{ km s}^{-1}$. This nova also shows a weak NaI feature at 5892\AA , OI at 7773\AA and some lines in the Fe II (42) and Fe II (48, 49) groups.

AT2018jas shows the Balmer series up to $H\delta$ with sharp and single peaks apart from the broad ($\sim 3500 \text{ km s}^{-1}$) $H\alpha$ feature that has a small feature on the red side. The lines seen in AT2018jas include several iron lines such as lines in the Fe II (49), Fe II (48, 49), Fe II (38) and Fe II (27) groups and accompanying the iron lines we see an MgI feature at 5178\AA and a possible OI line at 7773\AA .

AT2018lcl displays sharp, single peaked Balmer lines down to $H\delta$ with $H\alpha$ having a

M31N 2016-07d has saddle shaped Balmer lines with $H\alpha$ having a triple peak structure and Balmer emission can be seen to $H\delta$. The $H\alpha$ line is very broad, around 5500 km s^{-1} and shows lines such as the Fe II (42) at 5169\AA , NII at 5001\AA , HeI at 5016\AA along with Fe II (27) at 4417\AA and NII at 4517\AA .

M31N 2017-05a has a fairly narrow $H\alpha$ line for the He/N class ($\sim 3000 \text{ km s}^{-1}$ and shows double-peaked Balmer lines to a visible $H\delta$. Visible emission lines include HeI at 7065\AA , NIII at 4638\AA , NII at 5001\AA , HeI at 5016\AA and a possible blended NIV feature at 7703\AA .

M31N 2017-12d is tentatively classed as a He/N class here. The $H\alpha$ line emission is not obviously the classic saddle shape characteristic of He/N novae but is clearly has multiple components and is also only just in the accepted width range at $\sim 2600 \text{ km s}^{-1}$ however the $H\gamma$ line does appear to be double-peaked. There are however a number of emission lines consistent with an He/N nova such as HeI at 7065\AA , CII at 7234\AA , HeI at 6683\AA , a strong NII feature at 5479\AA , a strong Fe II (48) feature at 5363\AA , NV at 4945\AA , and HeII at 4200\AA .

AT2018cmi shows a very clearly double peaked, broad ($\sim 5200 \text{ km s}^{-1}$) $H\alpha$ emission line and Balmer lines are clear to $H\delta$ with these lines also being double-peaked or multi-component. Characteristic lines shown in this nova include HeI at 7281\AA , HeI at 7064\AA , HeI at 6016\AA and NIII at 4638\AA .

AT2018kcd has a less prominent double peak on the $H\alpha$ line with a width of $\sim 3400 \text{ km s}^{-1}$ and Balmer emission lines being visible down to $H\delta$ and all seem to have a double-peak. AT2018kcd shows He/N nova characteristic lines such as HeII at 7593\AA , Fe II (42) at 5018\AA , HeI at 5016\AA and CII at 4262\AA .

M31N 2016-04a has an incredibly flat spectra which only really shows the Balmer lines which are visible up to $H\gamma$ but the $H\alpha$ emission line is very narrow at around $\sim 1300 \text{ km s}^{-1}$. We make the classification of a He/Nn hybrid nova based on the narrow $H\alpha$ line and the few lines that can be seen are consistent with a He/N nova such as AlII at 7049\AA , HeI at 5876\AA , and a possible HeI line at 4712\AA . It is possible the spectra of this nova was taken very early in the eruption which may explain why only the Balmer series is prominent.

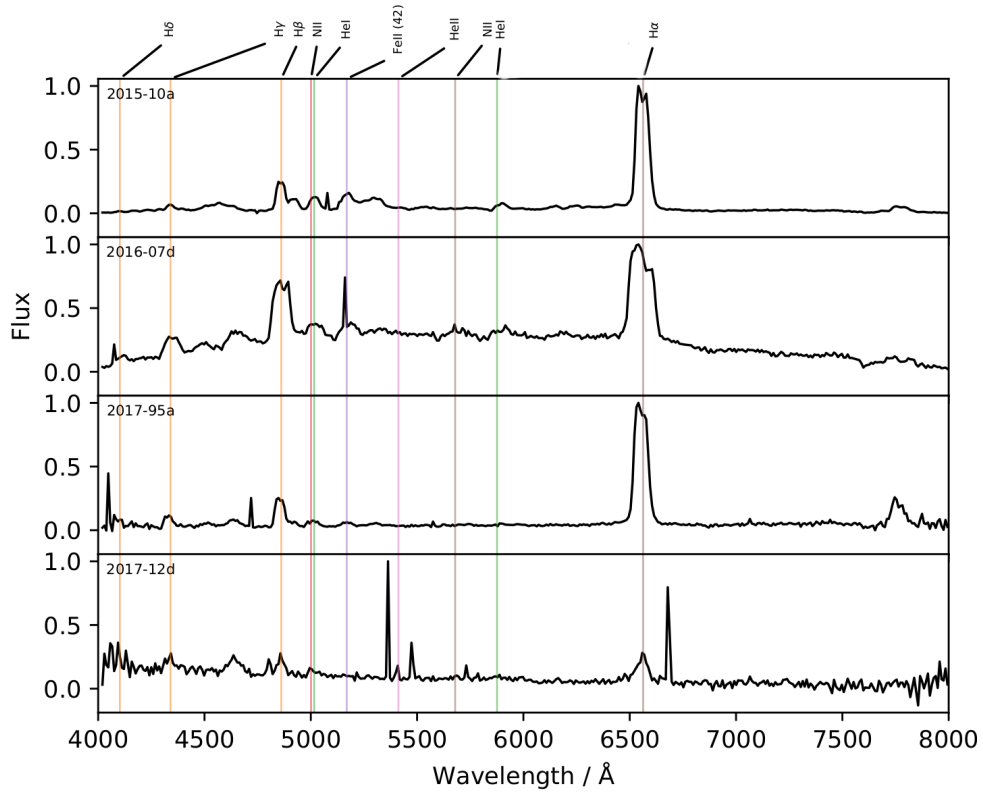


FIGURE 6.4: The first four chronologically ordered novae of the He/N class. Note that the first three spectra have the classic He/N feature of double peaked, or saddle shaped Balmer series lines. M31N 2017-12d has a fairly noisy spectra with an atypical H α profile but enough information was contained in the other lines to make a classification.

6.4.1.4 The H α profiles of classical novae

In Fig. 6.6, the H α line profiles are presented with a Gaussian fit. The FWHM of all of these Fe II CNe are below the 2500 km s^{-1} criteria for Fe II CNe. Some CNe such as M31N-2015-08c show a P-Cygni profile on the H α line. Fig. 6.7 shows a histogram of the H α FWHM velocities split into the Fe II spectral class and the combined He/N + Fe IIb + He/Nn classes.

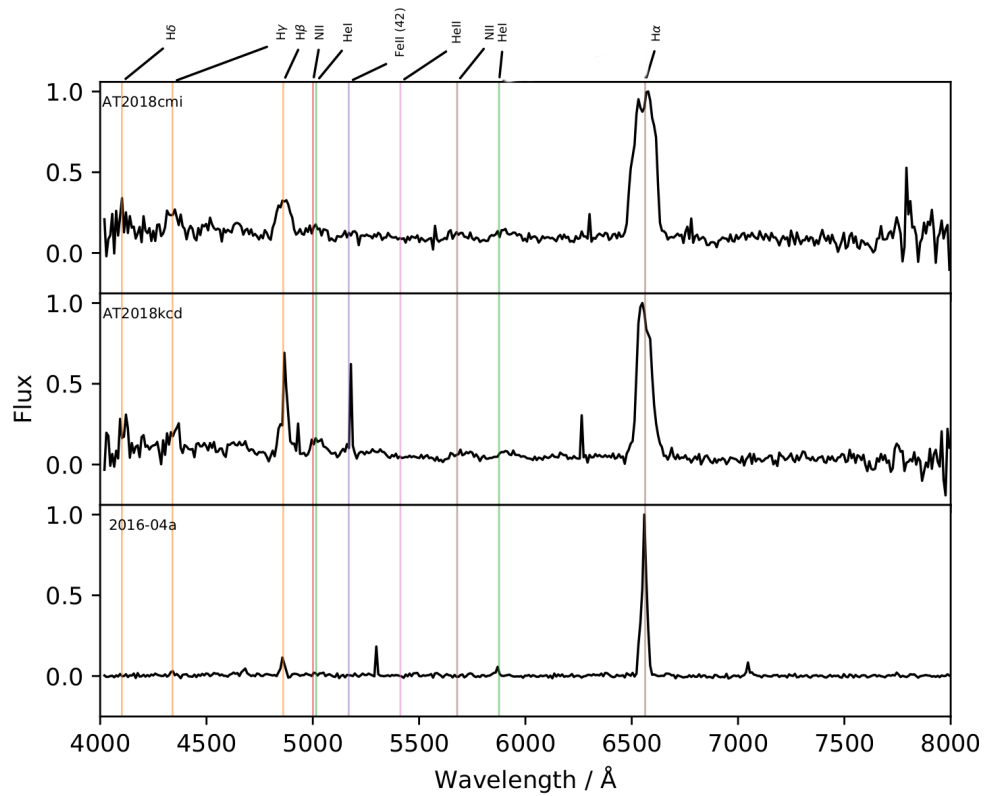


FIGURE 6.5: The final two of the chronologically ordered He/N class novae and our only He/Nn nova M31N 2016-04b. M31N 2016-04b has a very flat spectra apart from the blamer lines however the few lines that do appear on this spectra along with the very narrow H α profile allows us to make the tentative classification of He/Nn.

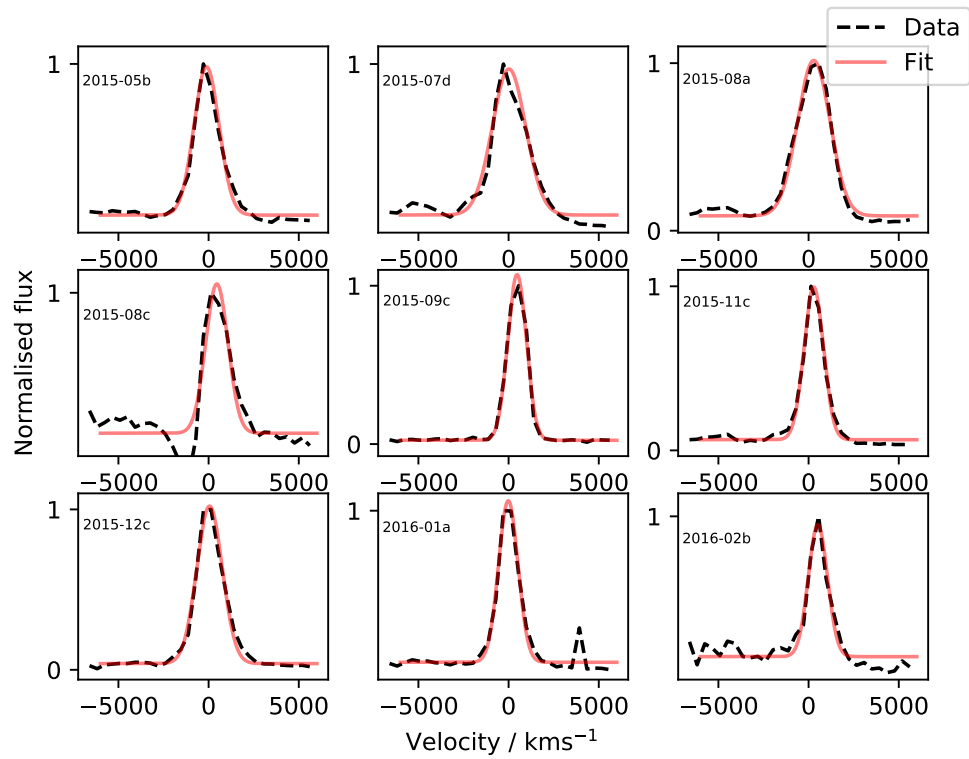


FIGURE 6.6: The isolated H α lines of nine of the FeII CNe in the sample of CNe that have LT SPRAT data. The red line is the Gaussian fit used to measure the FWHM of the H α profile in order to estimate the ejecta velocity.

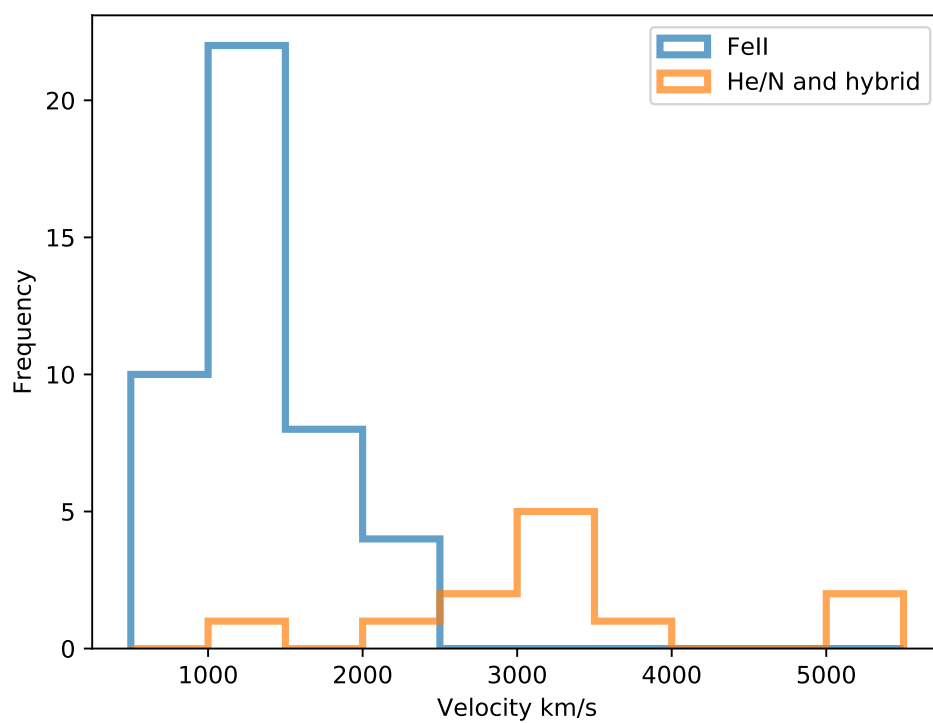


FIGURE 6.7: The H α FWHM of the LT SPRAT CNe. The sample is split into the spectral classes.

The full catalogue of 180 M31 CNe with their spectral classifications whether this be the LT classifications or classification from observers listed on the [Pietsch et al. \(2007\)](#) database.

*: LT SPRAT data

†: New classification

◊ Reclassification

Name (M31N -)	Date(JD)	RA (J2000)	Dec	Magnitude	Type	Reference
2010-01a	2455207.63	00:42:56.70	41:17:20.20	15.9	Fe II	Hornoch et al. (2010a)
2010-05a	2455344.54	00:42:35.90	41:16:38.20	17.1	Fe II	Hornoch et al. (2010b)
2010-06d	2455371.52	00:42:55.61	41:19:26.00	18.3	Fe II	Barsukova et al. (2010)
2010-06b	2455374.50	00:44:04.48	41:28:34.20	17.6	Fe II	Hornoch et al. (2010c)
2010-06a	2455374.53	00:43:07.56	41:19:49.00	16.9	Fe II	Hornoch et al. (2010c)
2010-07a	2455384.57	00:43:20.11	41:21:23.70	15.7	Fe II	Hornoch et al. (2010c)
2010-09c	2455421.74	00:38:09.06	40:37:25.90	17.0	Fe II	Shafter et al. (2010b)
2010-10b	2455427.55	00:42:41.55	41:03:27.70	17.4	Fe II	Shafter et al. (2010g)
2010-09a	2455440.87	00:42:23.32	42:17:08.60	17.2	Fe II	Shafter et al. (2010a)
2010-09b	2455469.73	00:43:45.55	41:07:54.50	16.4	Fe II	Shafter et al. (2010c)
2010-10a	2455474.29	00:42:45.82	41:24:22.00	17.0	Fe II	Yusa (2010)
2010-10f	2455481.01	00:42:43.58	41:12:42.60	15.5	-	Shafter et al. (2010h)
2010-10c	2455482.61	00:44:26.57	41:31:13.60	16.7	Fe II	Shafter et al. (2010d)
2010-10d	2455498.22	00:42:36.91	41:19:28.90	17.0	He/N	Shafter et al. (2010e)
2010-10e	2455500.20	00:42:57.75	41:08:12.30	17.8	He/N	Shafter et al. (2010f)
2010-11a	2455523.55	00:42:31.61	41:09:50.80	18.8	He/N	Fabrika et al. (2010)
2010-12c	2455545.59	00:42:56.67	41:17:21.20	16.5	-	Cao et al. (2012a)
2011-01a	2455568.89	00:42:42.68	41:19:14.80	14.9	Fe II	Henze et al. (2011a)
2011-06a	2455718.30	00:41:23.07	41:06:17.40	16.5	Fe II	Cao et al. (2011a)
2011-06e	2455731.00	00:36:15.30	38:51:31.70	19.0	Fe II	Cao et al. (2011b)
2011-06d	2455742.53	00:42:06.85	41:15:30.80	17.2	Fe II	Cao et al. (2011c)
2011-07a	2455765.19	00:42:44.83	41:18:00.70	15.9	He/N	Cao et al. (2011d)
2011-07b	2455770.57	00:41:41.12	41:20:11.70	17.4	Fe II	Cao et al. (2011d)
2011-08a	2455777.27	00:40:40.51	40:53:00.10	17.3	Fe II	Cao et al. (2011d)
2011-08b	2455778.25	00:44:47.94	41:38:09.60	16.5	Fe II	Cao et al. (2011d)
2011-09a	2455813.40	00:41:23.99	40:46:56.30	17.5	Fe II	Cao et al. (2011e)

Continued on next page...

TABLE 6.3: Table 6.3
 *: LT SPRAT data
 †: New classification
 ◇ Reclassification (continued)

Name (M31N -)	Date(JD)	RA (J2000)	Dec	Magnitude	Type	Reference
2011-09b	2455817.38	00:42:21.71	41:12:33.70	16.2	-	Henze et al. (2011b)
2011-10a	2455836.16	00:42:57.13	41:17:10.90	17.7	Fe II	Cao et al. (2011f)
2011-10d	2455854.22	00:42:55.74	41:17:52.30	16.8	Fe IIb	Shafter et al. (2011b)
2011-11a	2455877.09	00:42:10.07	41:05:13.80	17.7	Fe II	Shafter et al. (2011c)
2011-11c	2455878.23	00:41:58.24	41:24:01.10	17.9	Fe II	Shafter et al. (2011d)
2011-11e	2455885.20	00:42:38.31	41:16:31.30	17.4	Fe II	Shafter et al. (2011d)
2011-12a	2455902.58	00:42:06.28	41:01:28.70	18.6	Fe II	Shafter et al. (2011e)
2011-12b	2455919.63	00:43:55.84	41:21:26.60	17.4	Fe II	Shafter et al. (2011f)
2012-01a	2455931.34	00:41:41.01	41:19:44.30	18.7	Fe II	Shafter et al. (2012b)
2012-01b	2455947.92	00:42:38.04	41:08:41.70	17.1	He/N	Shafter et al. (2012c)
2012-02a	2455958.62	00:41:46.70	40:15:06.10	18.4	Fe II	Shafter et al. (2012d)
2012-05e	2456059.99	00:44:12.29	41:00:50.50	18.4	Fe II	Cao et al. (2012b)
2012-06b	2456084.96	00:40:23.22	40:36:10.30	19.8	Fe II	Cao et al. (2012c)
2012-06c	2456085.91	00:45:09.79	41:40:50.60	17.7	Fe II	Cao et al. (2012c)
2012-06d	2456086.90	00:38:56.60	40:29:49.80	19.4	Fe II	Cao et al. (2012c)
2012-06e	2456092.89	00:42:05.05	41:15:48.20	18.5	Fe II	Cao et al. (2012c)
2012-06a	2456096.55	00:43:21.92	41:20:24.40	16.6	Fe II	Cao & Kasliwal (2012)
2012-06f	2456101.54	00:42:37.07	41:22:16.00	18.6	Fe II	Cao & Kasliwal (2012)
2012-06g	2456105.25	00:42:42.20	41:13:01.60	17.4	He/N	Shafter et al. (2012e)
2012-07a	2456115.89	00:41:33.95	41:08:06.30	19.1	Fe II	Cao et al. (2012e)
2012-07b	2456124.53	00:42:23.71	41:10:14.20	18.3	-	Cao et al. (2012d)
2012-07c	2456127.49	00:42:39.91	41:26:57.30	18.0	Fe II	Cao et al. (2012d)
2012-09a	2456179.27	00:42:47.16	41:16:19.60	16.3	Fe IIb	Shafter et al. (2012f)
2012-09b	2456188.28	00:42:50.98	41:14:09.70	15.5	Fe IIb	Shafter et al. (2012g)
2012-10a	2456219.18	00:45:28.84	41:54:09.50	18.4	He/N	Shafter et al. (2012h)
2012-12a	2456271.53	00:42:49.13	41:17:02.50	18.5	Fe II	Shafter et al. (2012i)
2012-12b	2456287.09	00:46:19.12	41:44:36.40	16.7	Fe II	Shafter et al. (2012j)

Continued on next page...

TABLE 6.3: Table 6.3
 *: LT SPRAT data
 †: New classification
 ◊ Reclassification (continued)

Name (M31N -)	Date(JD)	RA (J2000)	Dec	Magnitude	Type	Reference
2013-01a	2456296.95	00:42:44.15	41:14:52.50	16.0	Fe II	Shafter et al. (2013a)
2013-01b	2456318.23	00:44:02.07	41:25:44.20	15.2	He/N	Shafter et al. (2013b)
2013-02a	2456332.98	00:39:25.67	40:37:45.10	17.2	Fe II	Cao et al. (2013b)
2013-05b	2456439.65	00:42:55.63	41:14:12.50	15.2	He/N	Cao et al. (2013c)
2013-06c	2456449.95	00:42:09.45	40:55:21.60	18.1	-	Tang et al. (2013a)
2013-06b	2456466.52	00:42:59.87	41:20:37.90	17.3	Fe II	Cao & Kasliwal (2013)
2013-08a	2456511.61	00:42:21.37	41:13:00.40	16.8	Fe II	Cao et al. (2013d)
2013-08e	2456532.89	00:44:01.52	41:32:01.30	17.8	Fe II	Tang et al. (2013b)
2013-09d	2456560.04	00:41:53.14	41:09:54.00	18.1	Fe II	Valeev et al. (2013)
2013-10a	2456567.25	00:42:24.22	41:18:19.20	16.4	Fe II	Valeev et al. (2013)
2013-10d	2456579.68	00:44:21.29	40:55:22.80	15.7	He/N	Fabrika et al. (2013a)
2013-10g	2456586.35	00:43:24.96	41:21:21.90	17.4	Fe II	Fabrika et al. (2013a)
2013-10h	2456595.58	00:43:04.83	41:16:30.60	14.8	Fe II	Fabrika et al. (2013b)
2013-11a	2456599.75	00:44:23.29	41:40:54.60	18.4	-	Tang et al. (2013c)
2013-12a	2456609.20	00:42:49.87	41:14:57.30	17.4	He/Nn	Fabrika et al. (2014a)
2013-12b	2456644.20	00:42:51.72	41:18:14.20	15.9	Fe IIb	Williams et al. (2014a)
2014-01a	2456659.63	00:43:13.62	41:14:46.90	16.2	Fe II	Fabrika et al. (2014b)
2014-01b	2456675.60	00:42:23.58	41:29:12.40	18.9	-	Tang et al. (2014)
2014-01c	2456683.23	00:42:34.92	41:14:56.30	17.1	Fe II	Fabrika et al. (2014c)
2014-02a	2456690.60	00:43:26.76	41:23:33.30	18.3	He/N	Fabrika et al. (2014c)
2014-06b	2456836.49	00:42:28.66	41:14:12.60	18.3	He/N	Cao & Miller (2014)
2014-07a	2456840.47	00:42:54.72	40:56:33.50	17.1	Fe II	Barsukova et al. (2014)
2014-09a	2456909.11	00:43:23.75	41:22:25.80	16.1	Fe II	Darnley et al. (2014b)
2014-09b	2456914.63	00:43:49.97	41:14:04.90	17.8	Fe II	Darnley et al. (2014b)
2014-10c	2456933.40	00:45:28.81	41:54:09.90	18.5	He/N	Sala et al. (2014)
2014-10a	2456936.48	00:42:39.72	41:20:11.70	17.7	Fe II	Williams et al. (2014b)
2014-11a	2456968.24	00:42:52.76	41:17:19.70	17.0	Fe II	Fabrika et al. (2015a)

Continued on next page...

TABLE 6.3: Table 6.3
 *: LT SPRAT data
 †: New classification
 ◇: Reclassification (continued)

Name (M31N -)	Date(JD)	RA (J2000)	Dec	Magnitude	Type	Reference
2015-01a	2457036.13	00:42:07.99	40:55:01.10	15.1	-	Fabrika et al. (2015b)
2015-02a	2457047.81	00:42:33.06	41:13:08.90	17.6	Fe II	Williams et al. (2015b)*
2015-02b	2457073.23	00:41:33.17	41:10:12.40	16.5	He/Nn	Williams et al. (2015b)
2015-05b	2457164.50	00:43:19.11	41:16:08.20	16.2	Fe II	Neric et al. (2015)*
2015-06a	2457174.54	00:42:42.53	41:15:13.90	14.9	Fe II	Williams et al. (2015c)
2015-07d	2457225.45	00:42:29.94	41:11:21.00	16.4	Fe II	Williams et al. (2015d)*
2015-08a	2457250.41	00:42:48.83	41:19:50.40	19.0	Fe II	Fabrika et al. (2015c)*
2015-08c	2457261.57	00:44:16.54	41:32:23.90	17.7	Fe II	Darnley et al. (2015)*
2015-08d	2457262.91	00:45:28.81	41:54:09.90	18.4	-	Darnley et al. (2015)
2015-09c	2457282.28	00:43:21.14	41:24:59.70	14.3	Fe II	Williams & Darnley (2015a)*
2015-10a	2457298.25	00:41:59.37	41:17:02.60	15.3	He/N ◇	Williams & Darnley (2015b)*
2015-10b	2457321.46	00:43:15.34	41:20:16.60	18.1	Fe II	Williams et al. (2015e)
2015-10c	2457326.52	00:42:57.73	41:08:12.30	17.9	He/N	Fabrika et al. (2015d)
2015-11a	2457333.49	00:44:28.40	41:32:32.90	19.0	Fe II	Williams & Darnley (2015c)
2015-11c	2455523.22	00:43:38.52	41:28:02.60	17.1	Fe II	Williams & Darnley (2015d)*
2015-12a	2457367.35	00:42:41.61	41:15:22.30	16.5	He/N	Williams & Darnley (2016b)
2015-12c	2456385.64	00:38:36.50	39:39:53.60	17.5	Fe II	Williams & Darnley (2016a)*
2016-01a	2457399.32	00:42:21.84	41:02:03.50	17.8	Fe II	Darnley & Williams (2016a)*
2016-01c	2457415.92	00:45:14.19	42:00:07.90	16.6	Fe IIb †	Darnley & Williams (2016b)*
2016-02a	2457426.07	00:44:43.49	41:53:40.10	18.7	Fe IIb †	Martin et al. (2018)*
2016-03c	2457430.24	00:42:49.14	41:16:40.10	17.9	-	Darnley & Williams (2016c)
2016-02b	2457430.37	00:44:37.03	41:42:26.40	18.8	Fe II	Williams & Darnley (2016d)*
2016-03b	2457446.28	00:42:19.51	41:11:13.70	18.1	-	Williams & Darnley (2016c)
2016-03d	2457464.27	00:43:01.54	41:14:09.00	17.6	-	Williams & Darnley (2016c)
2016-04a	2457488.53	00:45:28.12	41:41:17.60	18.6	He/Nn †	[Darnley & Williams (2016d)*
2016-05a	2457518.58	00:42:39.47	41:21:38.50	17.3	Fe II	Chinetti et al. (2016b)*
2016-05b	2457536.55	00:42:42.88	41:15:27.40	17.0	Fe II	Chinetti et al. (2016a)*

Continued on next page...

TABLE 6.3: Table 6.3
 *: LT SPRAT data
 †: New classification
 ◊ Reclassification (continued)

Name (M31N -)	Date(JD)	RA (J2000)	Dec	Magnitude	Type	Reference
2016-07b	2457581.94	00:44:41.05	40:08:35.90	16.3	Fe II	Ederoclite et al. (2016)*
2016-07c	2457591.20	00:43:57.94	41:34:54.60	17.9	Fe II	Williams et al. (2016b)*
2016-07d	2457595.98	00:40:03.15	41:45:19.10	16.5	He/N	Williams et al. (2016b)*
2016-07e	2457596.98	00:43:04.00	41:17:07.90	16.0	Fe II◊	Fabrika et al. (2016a)*
2016-08d	24576217.60	00:42:23.50	41:17:19.80	15.2	Fe II	Fabrika et al. (2016b)*
2016-08e	2457630.42	00:43:53.29	41:26:22.00	17.2	Fe II	Fabrika et al. (2016c)*
2016-09a	2457654.30	00:42:55.66	41:19:14.50	17.9	Fe II	Williams & Darnley (2016e)*
2016-09b	2457657.66	00:42:17.29	41:09:44.40	18.1	Fe II	Somero et al. (2016)*
2016-10d	2457678.02	00:43:36.60	41:56:32.10	17.7	Fe II	Darnley et al. (2016)*
2016-10b	2457678.29	00:42:52.45	41:18:41.20	16.8	Fe II	Darnley et al. (2016)*
2016-11a	2457696.27	00:42:41.81	41:13:43.30	15.9	Fe IIb	Fabrika et al. (2017a)
2016-12f	2457734.99	00:45:28.88	41:54:09.70	17.9	He/N	Fabrika et al. (2017b)
2016-12d	2457748.01	00:43:01.49	41:16:59.40	16.1	Fe II†	Williams & Darnley (2017a)*
2016-12e	2457750.02	00:41:31.54	41:07:13.60	16.2	He/N	Williams & Darnley (2017b)
2017-01c	2457769.25	00:42:21.33	41:12:01.80	16.8	Fe II	Williams & Darnley (2017c)
2017-01e	2457772.20	00:44:10.72	41:54:22.10	17.8	He/N	Williams et al. (2017a)
2017-03a	2457814.25	00:43:02.00	41:13:19.00	18.1	Fe II	Williams & Darnley (2017d)*
2017-04b	2457867.61	00:42:46.10	41:18:39.00	16.3	Fe II	Williams et al. (2017b)*
2017-05a	2457897.28	00:42:18.25	40:53:57.20	18.0	He/N ◊	Williams & Darnley (2017e)*
2017-05b	2457897.03	00:42:49.09	41:42:41.60	19.3	Fe II†	Williams & Darnley (2017e)*
2017-06c	2457913.50	00:42:32.91	41:12:23.60	18.0	Fe II	Williams & Darnley (2017f)*
2017-06e	2457912.72	00:41:05.43	40:30:46.70	17.4	Fe II	Williams & Darnley (2017g)*
2017-07a	2457953.60	00:43:14.50	41:33:57.20	17.1	Fe II	Barsukova et al. (2017)*
2017-07b	2457954.38	00:43:15.04	41:20:50.60	18.2	Fe II	Williams & Darnley (2017h)*
2017-07d	2457955.13	00:39:04.48	40:46:04.10	17.0	Fe II	Williams & Darnley (2017i)*
2017-09a	2457998.28	00:44:08.72	41:43:36.70	17.8	Fe II	Williams & Darnley (2017j)
2017-09b	2458005.36	00:42:58.94	41:26:27.20	17.0	Fe II	Williams & Darnley (2017k)*

Continued on next page...

TABLE 6.3: Table 6.3
 *: LT SPRAT data
 †: New classification
 ◊ Reclassification (continued)

Name (M31N -)	Date(JD)	RA (J2000)	Dec	Magnitude	Type	Reference
2017-09c	2458010.35	00:43:16.10	41:20:08.30	17.5	Fe II	Williams & Darnley (2017k)*
2017-09e	2458020.94	00:42:12.19	41:10:19.20	16.4	Fe II	Fabrika et al. (2017c)*
2017-10a	2458040.54	00:42:39.05	41:23:00.50	17.5	Fe II	Williams & Darnley (2017l)
2017-11a	2458055.35	00:42:54.22	41:30:42.30	17.7	Fe II	Fabrika et al. (2017e)*
2017-11c	2458069.01	00:41:44.35	41:08:28.70	17.4	Fe II	Shafter et al. (2017)
2017-11d	2458069.49	00:42:43.32	41:17:15.50	15.8	He/N	Fabrika et al. (2017d)
2017-11e	2458074.01	00:43:04.19	41:15:15.50	16.4	He/N	Williams et al. (2018)
2017-12b	2458103.24	00:44:01.52	41:30:18.40	17.4	Fe II	Williams & Darnley (2017m)*
2017-12a	2458111.57	00:43:29.46	41:17:13.70	16.8	He/N	Darnley et al. (2017)
2017-12e	2458119.27	00:45:28.88	41:54:09.70	18.2	-	Fabrika et al. (2018)
2018-01a	2458128.74	00:44:42.25	41:42:44.90	17.8	Fe II	Tomasella et al. (2018)
2018-01b	2458128.74	00:43:42.25	41:18:39.30	17.8	-	Fabrika et al. (2017c)
2018-02a	2458156.88	00:42:34.41	40:44:26.00	16.5	Fe II†	Sitaram & Darnley (2018a)*
2018-05b	2458256.68	00:43:42.11	41:22:34.80	18.1	-	Sitaram & Darnley (2018b)
2018-06a	2458282.67	00:42:19.67	40:56:40.70	18.9	He/N	Sitaram & Darnley (2018b)*
2018-06b	2458295.51	00:42:41.44	41:17:37.70	17.1	Fe II	Darnley et al. (2018a)*
2018-07a	2458299.53	00:41:48.89	41:09:14.80	17.9	Fe II	Darnley et al. (2018a)*
2018-07b	2458312.25	00:42:07.65	41:19:43.80	17.3	Fe II	Darnley et al. (2018b)*
2018-07c	2458314.50	00:42:52.61	41:18:40.90	17.6	Fe II	Darnley et al. (2018b)*
2018-08a	2458331.60	00:42:42.12	41:14:45.70	17.5	Fe II	Wayland et al. (2018)
2018-08b	2458344.08	00:39:21.90	40:15:48.80	18.2	Fe II	Conseil (2018)
2018-08d	2458349.91	00:45:15.87	42:10:26.90	18.7	Fe II	Conseil (2018)
2018-09a	2458364.46	00:44:19.85	41:29:26.50	18.2	Fe II	Sun & Gao (2018)
2018-10a	2458402.10	00:42:49.84	41:23:35.00	18.2	-	Yin & Gao (2018)
2018-10b	2458405.32	00:42:40.09	41:17:27.70	17.5	-	San Julian-Jacques et al. (2019)
2018-10c	2458406.96	00:42:03.10	41:02:33.10	16.3	Fe II	Xu & Gao (2018)
2018-10d	2458417.62	00:42:54.96	41:12:28.80	17.2	-	Darnley et al. (2018c)

Continued on next page...

TABLE 6.3: Table 6.3
 *: LT SPRAT data
 †: New classification
 ◊ Reclassification (continued)

Name (M31N -)	Date(JD)	RA (J2000)	Dec	Magnitude	Type	Reference
2018-11b	2458449.28	00:43:44.56	41:27:52.40	16.4	Fe IIb ◊	Williams et al. (2019)*
2018-12a	2458455.32	00:42:40.65	41:11:08.00	18.0	Fe II	Zhang & Gao (2019a)
2018-12b	2458470.05	00:42:42.41	41:19:41.00	17.6	Fe II	Zhang & Gao (2019a) *
2018-12c	2458470.16	00:39:44.80	40:35:34.50	16.2	He/N ◊	Zhang & Gao (2019a) *
2018-12d	2458474.09	00:43:24.62	41:20:22.30	18.6	Fe II †	Zhang & Gao (2019a) *
2018-12e	2458475.60	00:42:43.80	41:17:20.80	15.5	Fe II	Zhang & Gao (2019a) *
2018-12f	2458483.36	00:42:26.24	41:04:01.09	16.4	Fe IIb	Zhang & Gao (2019a) *
2019-01d	2458485.25	00:43:00.08	41:18:34.00	19.1	-	Gorbovskoy et al. (2019)
2019-01a	2458499.31	00:45:59.36	41:56:29.70	17.1	-	Hornoch (2019)
2019-01b	2458504.44	00:42:45.03	41:14:24.80	18.0	Fe II †	Zhang & Gao (2019b) *
2019-01c	2458504.44	00:42:02.90	41:07:14.20	18.2	-	Carey (2019)
2019-01f	2458511.24	00:42:29.25	41:14:00.30	16.7	Fe II †	Tonry et al. (2019) *
2019-01e	2458511.96	00:43:54.57	41:17:33.00	17.5	Fe IIb †	Zhang (2019) *
2019-02a	2458518.05	00:42:51.00	41:21:03.80	18.8	Fe II †	Zhang (2019)*

Continued on next page. . .

6.5 Conclusions and summary

From 76 novae, we could make a spectral classification for 60 of our novae. We find that 48 of our novae belong to the Fe II class, five to the Fe IIb hybrid class, six He/N class novae and one tentative He/Nn nova.

The proportions of each class of novae we have classified (both the LT SPRAT novae and the remainder of the 180) are similar to the findings of [Shafter et al. \(2011a\)](#), in their earlier survey of CNe in M31 where they find that around 80% of novae are of the Fe II class and 20% of the novae are either of the He/N class or a subclass. In this chapter, the LT SPRAT data has 80 per cent Fe II novae, with the remainder being He/N or hybrid class. Out of the 180 CNe that include the LT SPRAT CNe, 75 per cent of the spectroscopically confirmed CNe are Fe II CNe with the remaining 25 per cent being He/N or hybrid CNe. This also corroborates with the findings of [Shafter \(2007\)](#) and [Della Valle & Livio \(1998\)](#) who both performed surveys of Galactic novae. This suggests star-forming late Hubble-type spiral galaxies have similar novae populations. In this work, five of the CNe with LT spectra were reclassified from their original ATel/CBET classification. We find that the Fe IIb class is roughly as common as the He/N class which may present an argument for treating the Fe IIb spectral class as a main class of nova or that the upper limit of 2500 km s^{-1} for the Fe II class is not valid. Further to this, Fig. 6.7 shows that the He/N and hybrid classes almost merge with the FWHM of the Fe II CNe.

Furthermore due to observational biases we can not be certain nova surveys are representative of the entire galaxy's nova population. Firstly many nova searches concentrate on the central bulge of the galaxy as historically this is where most novae are found which may lead to a bias in the spectral classifications if a bulge population is expected to host more Fe II class novae. Secondly the cadence of most surveys may not be high enough to be able to detect all the fast and very fast novae which as discussed previously are exclusively of the He/N or Fe IIb class. If such biases are common and we miss many of the fast or very fast novae or even the proposed ultra-fast nova speed class (see [Shara et al. \(2017b\)](#) which looked at the simulation parameter space of [Yaron et al. \(2005\)](#) to predict t_2 decline times in the order of a few hours) then not only the population proportions inaccurate but nova rate estimates will also be off. Moreover if He/N novae are thought to be associated with a young disc population then we may be missing some of these novae due to extinction from dust at the disc. A higher cadence (sub-daily) survey is needed which observes all of M31 to avoid such observational biases.

6.5.1 Distribution of the different spectral classes

The M31 CN catalogue can be split into the spectral classes and also the RNe can be isolated. The M31 CN positions are overlaid over an M31 image shown in Fig. 6.8 with the spectral classes split. A Palomar 48" image is used in Fig. 6.8 to be illustrative as the *GALEX* mosaic has gaps and incomplete sections outside of the disc due to the circular fields. If the He N CNe are from a younger population than the Fe II novae, one may expect them to be more concentrated in the disc of a spiral galaxy such as M31 where star formation is concentrated in the spiral arms.

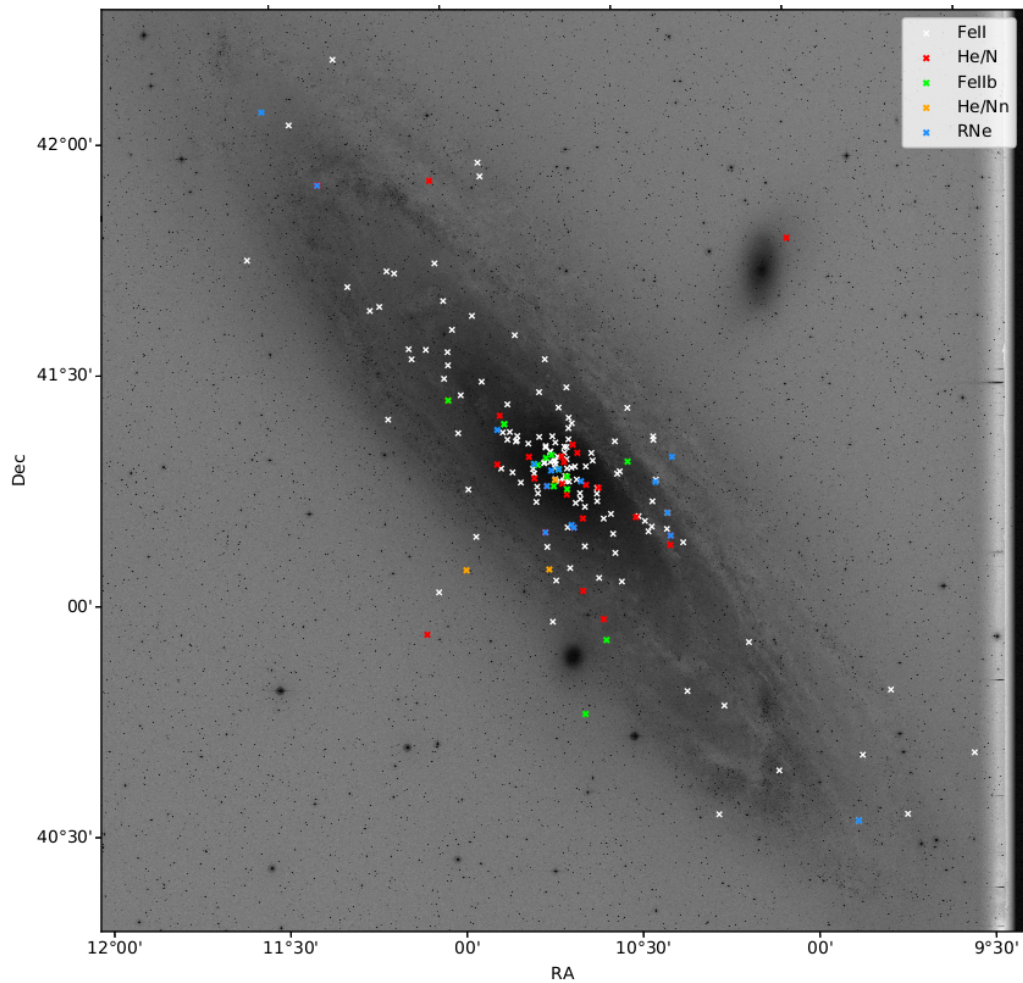


FIGURE 6.8: Overlay of the positions of our catalogue (the ‘new’ CNe combined with the 44 [Shafter et al. \(2011a\)](#) novae) of M31 novae over an image from the Palomar 48-inch telescope. The catalogue novae have been split into their spectral classes and also RNe are featured.

6.5.2 Summary

The findings of this chapter can be summarised as such:

1. From 76 M31 CNe with LT SPRAT data, discovered after the survey of [Shafter et al. \(2011a\)](#), I was able to make 60 spectral classifications. These classifications were based on spectral templates, $H\alpha$ profile widths and line lists from [Williams \(2012\)](#).
2. Of these 60 CNe, 48 were Fe II novae, five were Fe IIb, six were He/N and there was a single He/Nn nova.
3. These proportions are consistent with [Shafter et al. \(2011a\)](#), however in this sample, there are more Fe IIb novae.
4. The number of He/N (six) novae is similar to the number of Fe IIb (five). This may be an argument to support the Fe IIb class being a “main” CN spectral class, or that the 2500 km s^{-1} $H\alpha$ profile FWHM cut-off for Fe II novae should be reassessed.

These spectral classifications will be used in Chapter 7, investigating the environments of M31 CNe in terms of their association with UV emission and also their radial distributions.

Chapter 7

The environments of classical novae in the Andromeda galaxy (M31)

7.1 Multiple populations of classical novae

7.1.1 Spatial populations

It has been proposed that there may be separate populations of CNe based on their membership of the disc or bulge of M31. [Shafter et al. \(2011a\)](#) suggested the faster CNe in their sample (that tend to be He/N spectral class) may be more spatially extended in M31 than the slower novae in their sample (that tend to be Fe II CNe). Therefore the spectral class may be correlated with the underlying stellar population and host metallicity (the centre of M31 having higher metallicity than the outer regions [Gajda et al., 2021](#)). The spectral class of a CN may be dependent on the WD mass and younger populations, i.e. the disc in spiral galaxies has higher mean mass WDs than the bulge of the galaxy. A more massive WD needs to amass less hydrogen rich material for the TNR to initiate. A portion of the material is ejected at high velocity in a discrete shell (these objects may give rise to the He/N CNe). A less massive WD must accrete more material and more material is ejected at lower velocities, first in a discrete shell and followed by a slower optically thick wind (forming the P Cygni features observed in Fe II CNe).

7.2 Methods

7.2.1 The spectroscopically confirmed sample

The spectroscopically confirmed catalogue of M31 CNe is described in Chapter 6. The number of each CN class is presented in Table 7.1. This table include the classifications from ATel/CBET/TNS and also my classifications from Chapter 6 where I classify 60 M31 CNe that have LT SPRAT data.

TABLE 7.1: The spectral classes in the full sample of 222 M31 CNe from the [Pietsch \(2010\)](#) catalogue and the [Shafter et al. \(2011a\)](#) survey.

Spectral class	Number
Fe II	144
Fe IIb	11
He/N	33
He/Nn	6
Unclassified	28

7.3 GALEX map of the Andromeda galaxy

The image data we use in this study was obtained from the Galaxy Evolution Explorer ([Martin et al., 2003](#)). These data are publicly available at the Mikulski Archive for Space Telescopes (MAST)¹ website, we use M31 mosaics taken in 2004 in both NUV and FUV ([Thilker et al., 2005](#)). For our analysis we used our own `python` and `astropy` routines to crop the image, subtract the average background flux and mask bright foreground stars.

The *GALEX* NUV filter has a central wavelength of 2310 Å with a passband of 1750–2800 Å. The FUV filter has a central wavelength of 1540 Å with a passband of 1350–1750 Å. A transmittance plot of the *GALEX* NUV and FUV filters is presented in Fig. 7.1²

¹<https://archive.stsci.edu/>

²Filter information from https://asd.gsfc.nasa.gov/archive/galex/Documents/instrument_summary.html

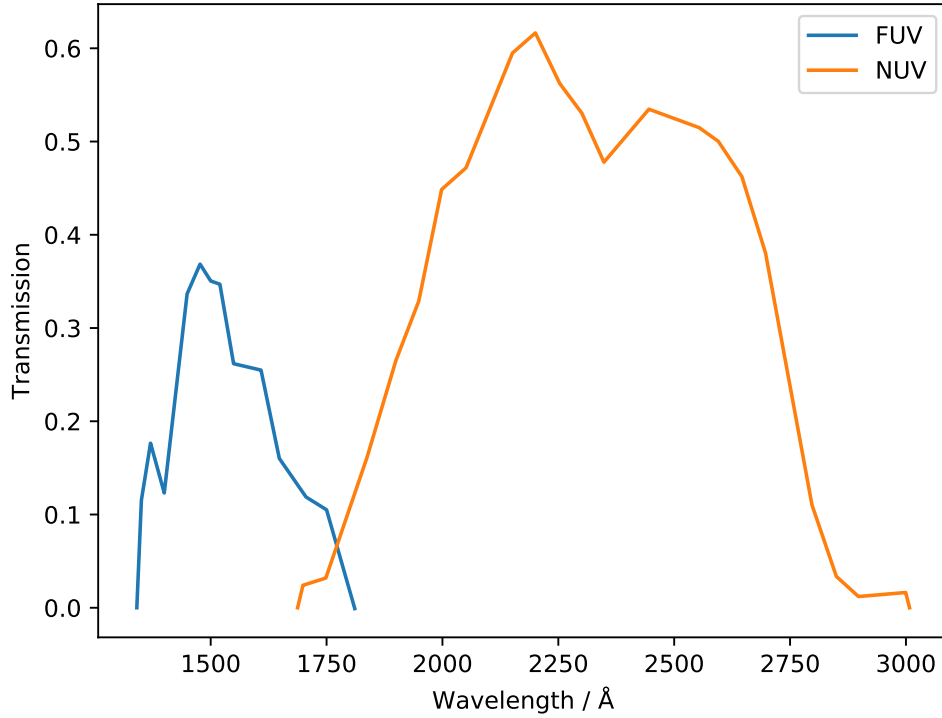


FIGURE 7.1: Transmittance plot of the *GALEX* NUV and FUV filters. The transmittance is in terms of the fraction of transmission and the wavelength axis is in Å.

7.4 Methods

7.4.1 Pixel statistics: normalised cumulative ranking

The NCR pixel statistics method used for the M31 CNe is much the same as that as employed in the analysis of SNe IIn in Chapter 4. There are some key differences, however. Firstly, there is only one host, M31, with many CNe rather than one host per transient like in the SNe IIn work. Furthermore, here I use *GALEX* NUV and FUV rather than $H\alpha$ images. *GALEX* NUV and FUV are tracers of recent star formation, however, not ongoing star formation like $H\alpha$ emission traces, with characteristic emission lifetimes of 17.1–34.2 Myr for the FUV emission and 19.6–39.1 Myr for the NUV emission (Haydon et al., 2020). As CN systems are old, one would not expect any association with ongoing star formation as traced by $H\alpha$ emission, so is not used in this work. This is the first time the NCR analysis has been applied to CNe.

One difference to the previous NCR analysis in this thesis is that the NCR value of a CN is calculated using the median value of a square ‘annulus’ around the CN location.

This was to avoid the hot accretion disc in quiescent CN systems that may be bright in the UV (the *GALEX* pixel size is 1.5", subtending ~ 5 pc on M31, with a diffraction limit ~ 0.1 "). However, the *GALEX* FWHM in FUV and NUV are 4.2" and 4.9" respectively³. Therefore if there was a point source at the CN location, there would be contribution to the UV flux in the annulus, this caveat may be particularly important if the CN is in outburst (i.e. a recurrent nova).

7.4.1.1 NCR map of Andromeda

Imaging from *GALEX* was collected from the MAST archives. *GALEX* fields are circular and a mosaic can be made on the MAST archive. This mosaic covers the disc of M31 and also some surrounding sky. Sky subtraction is required for the NCR analysis. The sky level was taken as the median pixel value of a selection of regions in the outer *GALEX* circular frames. Bright foreground stars are identified by eye and are masked out as to not interfere with the NCR statistic. The NCR algorithm described in Chapter 4 is applied to the cropped *GALEX* images and the cropped *GALEX* NUV NCR image is presented in Fig. 7.2.

As the *GALEX* filters used here are broadband filters, there is no continuum subtraction. As such, some of the emission in these images may not be related to star formation. Indeed, the bulge of M31 is one of the brightest UV emission regions in the *GALEX* NUV and FUV images due to the additive effect of high stellar density. I therefore mask out the central region (the bulge can't be isolated due to the inclination) using parameters from [Blaña Díaz et al. \(2017\)](#). I approximate the bulge of M31 as an ellipse with a semi-major axis of 700" (~ 2.7 kpc, at which point the bulge isophotes stop increasing in ellipticity) with an ellipticity of $\epsilon = 0.4$ and position angle of 38° . The bulge holds between $4 \times 10^{10} M_\odot$ (the upper limit from [Kent, 1989](#)) and $2.5 \times 10^{10} M_\odot$ (lower limit from [Widrow & Dubinski, 2005](#)) and at 700", around 3.0×10^{10} is enclosed. The half mass radius of the bulge is 340" (~ 1.3 kpc). I compare two ways of computing the NCR for the remaining region. Firstly, I mask the inner region after the NCR processing to get a 'global' view of the NCR distributions. Secondly, I mask the inner region before NCR processing so that the only flux being considered is that from the outer regions of M31. Fig. 7.3 shows an example *GALEX* NCR image of M31 with the bulge masked out.

³<http://www.galex.caltech.edu/researcher/techdoc-ch5.html>

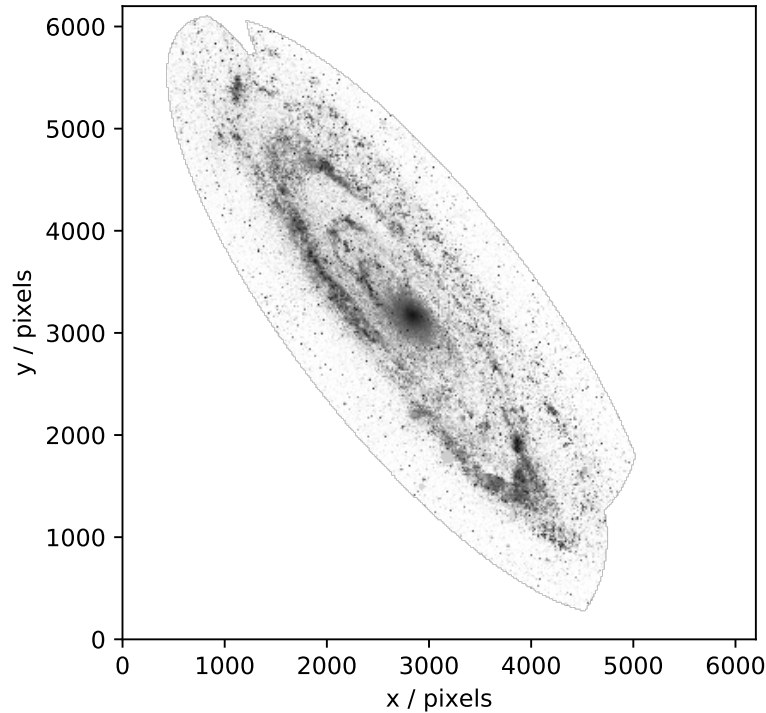


FIGURE 7.2: A cropped GALEX NUV mosaic that has had the normalised cumulative rank processing applied. This image is the entire galaxy, unmasked.

To investigate the NCR distributions of the inner region (and for the sake of completeness), I also include analysis of inside the masked region itself. The masked region in *GALEX* NUV is shown in Fig. 7.4.

7.4.2 Radial analysis

In addition to our NCR analysis we also investigate the spatial distribution of our nova catalogue in relation to the offset from the centre of M31. No significant difference between the radial distributions of the spectral classes according to the KS tests were reported in [Shafter et al. \(2011a\)](#), however the faster novae were possibly more spatially extended. We approach this question in three ways and repeat AD tests to determine if there is a statistically significant difference in the distributions.

Firstly I look at the offsets of the novae from the centre of M31 as they appear on the sky. This method was used in [Williams et al. \(2016a\)](#) in their investigation of red-giant nova systems.

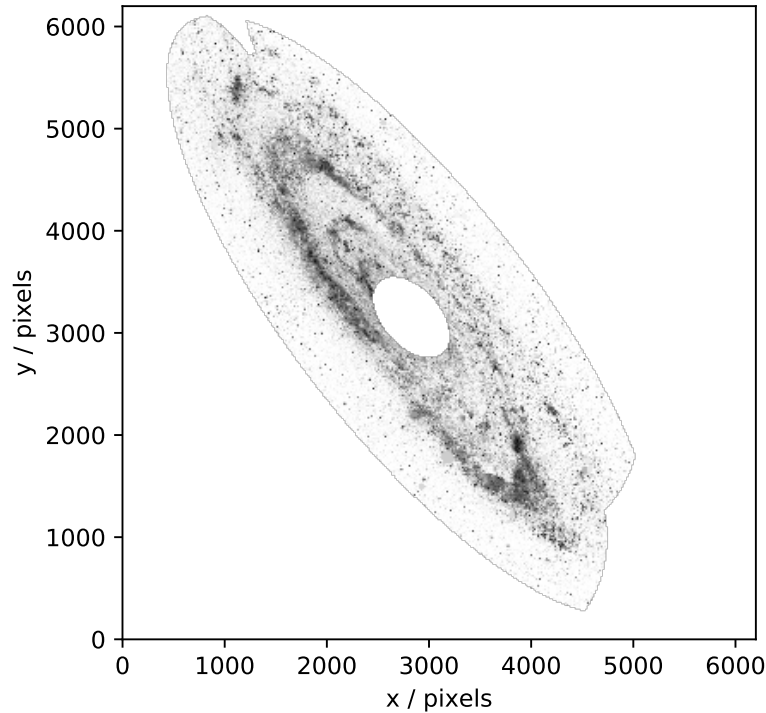


FIGURE 7.3: A cropped GALEX NUV mosaic which has had the normalised cumulative rank processing applied. In this image, the inner region of M31 is masked as to discount high NCR values contained within the bulge and therefore biasing any attempt to associate UV emission with regions of recent star-formation.

Secondly as from our viewpoint M31 has an inclination angle of 77° the radial extension of some novae are impossible to assess as we can not know if they belong to the disc or the bulge of M31. I therefore approximate M31 as an inclined circular thin disc and deproject the nova coordinates and then calculate the offsets from the centre of the deprojected M31.

Finally we adopt the method used in [Shafter et al. \(2011a\)](#) where they use the isophotal radius of each nova position. The isophotal radius is defined as the semi-major axis of an ellipse of the isophote that passes through the position of a CN. Isophotal radius is calculated using a `python` translation of `Fortran` routines formulated by [Ciardullo et al. \(1987\)](#). The translated code uses isophotes as defined by [Kent 1983](#) and [Kent \(1987\)](#) in their surface brightness photometry work on M31. The isophotal radius is determined as the semi-major axis of an ellipse fitted to an isophote that intercepts a CN position, with an ellipse centre defined as the centre of M31. Firstly, the two isophotes bounding the CN position are calculated by iteratively decreasing the size of an interval window

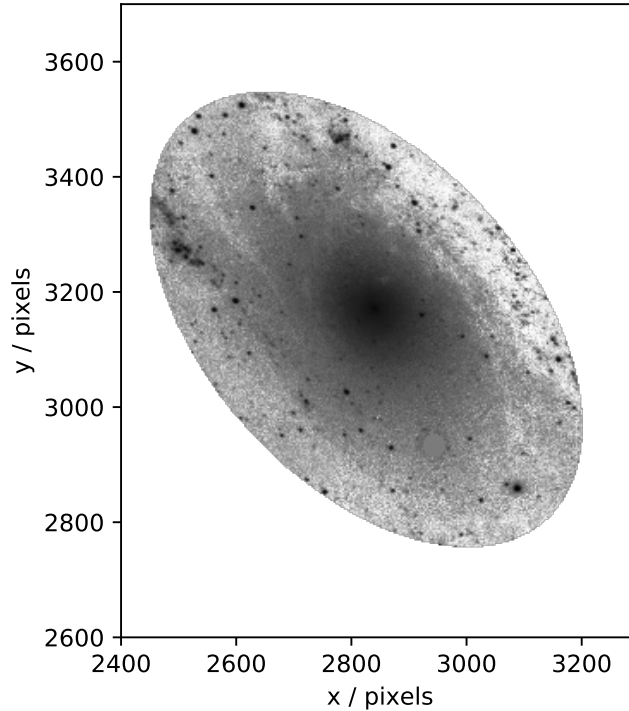


FIGURE 7.4: A cropped GALEX NUV mosaic which has had the normalised cumulative rank processing applied. This image is just the inner region of M31.

until the bounding isophotes are found and then then interpolated to find the distance to CN and therefore the semi-major axis which is the isophotal radius.

Furthermore the full M31 CN catalogue presented by [Pietsch \(2010\)](#) that holds all CNe (mostly without spectroscopic information) observed in M31 in the last ~ 120 years will also be compared as this may show the selection effects in M31 CN surveys. However it should be noted that not all the entries in this historical catalogue will be M31 novae, there may be contamination from transients such as Galactic dwarf novae and Mira variables.

In order to quantify any differences in the distribution of our spectral classes, we employ an AD test. For consistency we use the R K-Samples implementation (version 1) of these tests as the `python scipy` implementation of the AD test is capped. This tests the null hypothesis that two distributions are drawn the same parent distribution. We use an AD test instead of the Kolmogorov-Smirnov (KS) test as the AD tests are more sensitive to differences in the tails of distributions. If the p-value from the tests is below 0.05, we reject the null hypothesis (therefore the distributions are consistent with being drawn

from different parent populations), if the p-value is above 0.05, the null hypothesis is that the distributions are drawn from the same parent population.

7.4.3 Modelling CN spatial distributions

Previous M31 CN surveys have indicated that the CN populations are bulge dominated (see [Shafter & Irby, 2001a](#)). While the CNe mostly follow the bulge, [Darnley et al. \(2006\)](#) show that there is a contribution to the CN population that belongs to the disc of M31. [Darnley et al. \(2006\)](#) observationally derived a spatial distribution model comprised of one population which follows the disc light and one population which follows the bulge light (r' -band). This model is ultimately determined by the parameter θ in the equation formulated by [Ciardullo et al. \(1987\)](#) when investigating the spatial distribution of M31 CNe:

$$\Psi_i = \frac{\theta f_i^d + f_i^b}{\theta \sum_j f_j^d + \sum_j f_j^b}, \quad (7.1)$$

where Ψ is the probability of a CN eruption occurring at a certain location i , θ is the ratio of disc and bulge CN eruption rates per unit r' -band flux, f^b and f^d are the disc and bulge contributions to the r' -band flux at that location. The denominator in this expression sums over the contributions over the whole galaxy (locations j) normalised such that the sum of the probabilities, $\sum_i \Psi_i = 1$. Therefore $\theta = 0$ would indicate an entirely bulge based population and $\theta = 1$ would indicate that the population follow the galaxy light and as θ tends towards infinity the population is associated with the disc.

The θ parameter was originally determined by comparing the contributions of the disc and bulge flux of M31 to the novae observed in the POINT-AGAPE microlensing survey of M31 (see [Darnley et al., 2004, 2006](#)). In [Darnley et al. \(2006\)](#), θ is determined (with 1σ limits) to be $\theta = 0.18_{-0.10}^{+0.24}$. We take $\theta = 0.18$ in this study. This value leads to a nova rate of $65 \pm 15 \text{ year}^{-1}$ and when split into the bulge and disc populations there is a rate of $38 \pm 8 \text{ year}^{-1}$ in the bulge and $27 \pm 6 \text{ year}^{-1}$ in the disc ([Darnley et al., 2006](#)). Using this (or any) value for θ and the modelled M31 light distribution of [Darnley et al. \(2006\)](#) (and the associated C code), I generate model CN distributions. This will be compared to the radial distribution of the observed CN sample.

7.5 Results and discussion

7.5.1 Radial analysis results

In this section, the radial distributions of M31 CNe are presented. The relations between the subsamples in all three of the trialled methods to calculate (on-sky offset, deprojected offset and isophotal radius) are consistent. All three methods therefore may be valid ways of measuring the radial extent of CNe in M31. Here I will present the isophotal radius, the method employed by [Shafter et al. \(2011a\)](#). The AD-test results are presented in Table 7.2. I also compare the distributions to the sample in [Shafter et al. \(2011a\)](#) which is tabulated in Table 7.3.

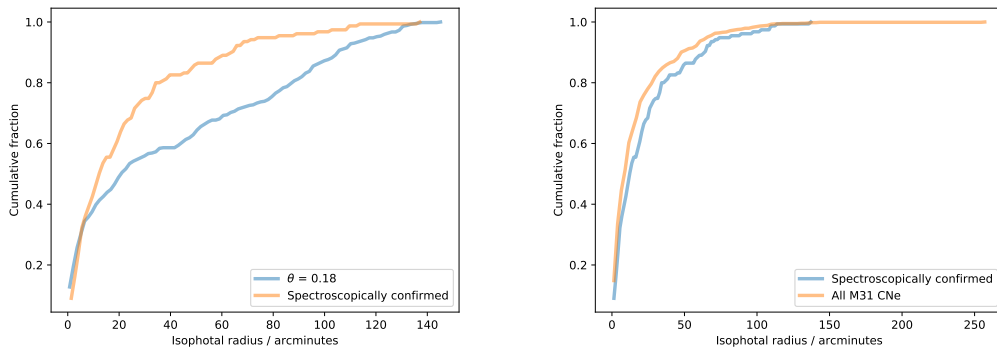


FIGURE 7.5: (*Left:*) The isophotal radial distributions of the modelled radial CN distribution with $\theta = 0.18$ and the spectroscopically confirmed CNe from Chapter 6. When compared, these distributions have an AD p-value of ~ 0.00 . (*Right:*) the radial distribution of the spectroscopically confirmed CNe and the full M31 CN catalogue from [Pietsch \(2010\)](#). Comparing these distributions, I find an AD p-value of 0.022.

The radial distributions of the spectroscopically confirmed sample from Chapter 6 and the modelled radial distribution with $\theta = 0.18$ are presented on the left panel of Fig. 7.5. It can be seen that these distributions differ significantly (with an AD p-value of ~ 0) with the modelled distribution having a more extended distribution compared to the spectroscopically confirmed distribution where there is a more central concentration of CNe. As the modelled distribution does not follow the observed distribution of the spectroscopically confirmed CNe, they will not be considered further in this work as the model uses a completeness map that is not reflected in the real data. The panel on the right shows the distributions of the spectroscopically confirmed CNe and the full catalogue from [Pietsch \(2010\)](#). The historical CNe (986 CNe) extend out to $\sim 250'$ while the spectroscopically confirmed CNe (180 CNe) extend to $\sim 140'$. The historical catalogue are more centrally concentrated due to selection effects. This is because

‘traditionally’, CN surveys of M31 concentrate on the central regions of the galaxy as one is more likely to observe a CN in this region. The AD p-value when comparing these two distributions is 0.022, suggesting that they are not drawn from the same parent population. Due to this result and also because I will split the samples by spectral class, the historical catalogue will not be considered further in either the radial analysis or the NCR distributions.

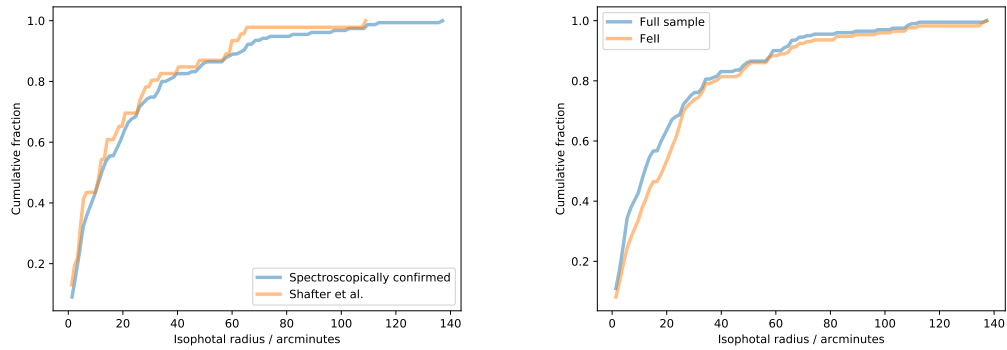


FIGURE 7.6: (*Left:*) the isophotal radial distributions of the spectroscopically confirmed CN sample from Chapter 6 and the sample in [Shafter et al. \(2011a\)](#). (*Right:*) the isophotal radial distribution of the combined, full sample (i.e the Chapter 6 sample and the [Shafter et al. \(2011a\)](#) sample) and the combined Fe II spectral class CNe.

In Fig. 7.6, the left panel shows the radial distribution of the spectroscopically confirmed sample from Chapter 6 and the distribution of the sample of 44 CNe presented in [Shafter et al. \(2011a\)](#). These two distributions are similar by eye. The AD p-value when these two distributions are compared is 0.60, suggesting that these two samples are consistent with being drawn from the same population. The distribution of the [Shafter et al. \(2011a\)](#) sample is always above the larger sample of spectroscopically confirmed CNe, suggesting that the ‘new’ novae are more spatially extended and perhaps shows that smaller telescopes such as the LT that can get on target quickly are improving the completeness of CN surveys compared to surveys on large telescopes such as the Hobby-Eberly Telescope used in [Shafter et al. \(2011a\)](#). As these are consistent samples, I will combine the [Shafter et al. \(2011a\)](#) with my sample from Chapter 6, bringing the full sample to 222 M31 CNe. The panel on the right of Fig. 7.6 shows the radial distribution of the aforementioned extended sample and the Fe II spectral class CNe. Again, by eye, these distributions are similar (the full sample may be slightly more centrally concentrated), but this is to be expected considering that around 80 per cent of M31 CNe are of the Fe II spectral class, this is reflected in the AD p-value of 0.10. This p-value suggests the distributions are consistent with being drawn from the same parent population. However, it should be noted that this AD p-value is low and almost

of marginal significance, indicating there may be some difference in this population that could be revealed with more data.

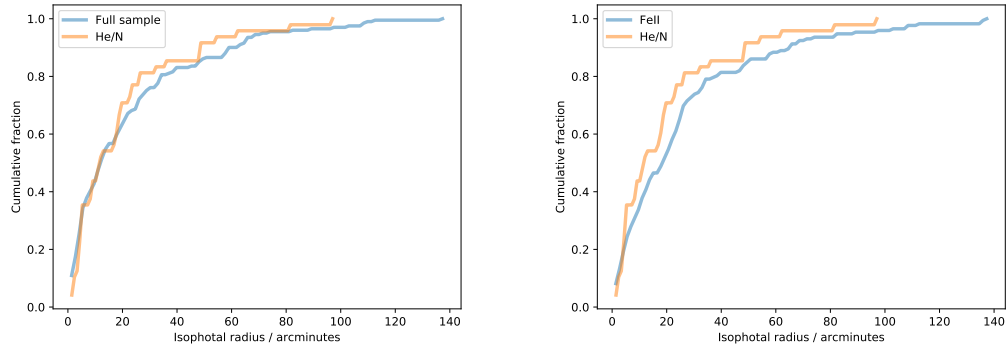


FIGURE 7.7: (*Left:*) the isophotal radial distributions of the combined full sample and the combined He/N spectral class CNe. (*Right:*) the isophotal radial distribution of the combined He/N spectral class CNe and the combined Fe II spectral class CNe.

The left panel of Fig. 7.7 shows the isophotal radial distribution of the full combined sample and the He/N spectral classification. These distributions appear similar, with perhaps the full sample being more extended than the He/N CNe as the He/N distribution tends to be above the full combined sample distribution. The AD p-value when comparing these two distributions is 0.75, suggesting that are consistent with being drawn from the same parent population. The panel on the right of Fig. 7.7 shows the radial distributions of the Fe II spectral class and the He/N spectral class. The He/N CNe seem more centrally concentrated than the Fe II CNe (as expected considering the previous comparison with the full combined sample) with the distribution being above the full sample distribution. Furthermore, the Fe II distribution extends further ($\sim 140'$) than the He/N distribution ($\sim 100'$). The AD p-value when comparing these two distributions is 0.14, suggesting these distributions are consistent with being drawn from the same parent population. Therefore, with this expanded sample, there is no significant evidence that the two spectral classes have different radial distributions as suggested by [Shafter et al. \(2011a\)](#), where there was a hint that the faster novae may be more spatially extended than the slower novae, with a KS p-value of 0.23. The He/N novae tend to be faster evolving than the Fe II novae, however, when comparing the spectral classes, [Shafter et al. \(2011a\)](#) found a KS p-value of 0.81, indicating that the distributions of the spectral classes are consistent (I find a KS p-value of 0.40 between the two spectral classes). If the He/N class were more spatially extended, they may be more associated with younger stellar populations in the disc of M31. However, their result was not statistically significant but a test with a larger sample size (222 vs 44) was needed for a more robust result. It can be seen in the right panel that the He/N may actually be more centrally concentrated

than the Fe II CNe, contrasting the suggestion from [Shafter et al. \(2011a\)](#). Furthermore, I combine the Fe IIb ‘hybrid’ class CNe into the He/N group similarly to [Shafter et al. \(2011a\)](#).

TABLE 7.2: The Anderson-Darling test results for the radial distributions.

Spectral classes	p-value
Spectroscopically confirmed vs $\theta = 0.18$	~ 0.00
Spectroscopically confirmed vs Historical CNe	0.022
This work vs Shafter et al. (2011a)	0.60
Fe II vs He/N	0.14

In terms of the radial positions of CNe, the existence of a disc and bulge CN population in M31 has been hypothesised and explored. As discussed previously in Chapter 5, there have been a variety of suggestions relating to multiple CN populations. [Della Valle et al. \(1992\)](#) and [Della Valle & Livio \(1998\)](#) propose that Galactic CNe originate from two separate populations dependent on their scale height, and linked this to the spectral class. They suggest He/N novae were associated with the thin disc and slower, Fe II CNe tended to have a larger scale height and were associated with the thick disc or bulge. However, as previously mentioned [Özdönmez et al. \(2018\)](#) did not find any dependence on scale height and suggested these previous results were due to observational biases.

There is a similar story in M31, [Ciardullo et al. \(1987\)](#) investigated the spatial distributions and possible populations of CNe in M31. They surveyed CNe in M31 in a narrowband H α filter. This allowed for greater contrast and observations into the inner region of the nucleus (the ‘hole’ found by [Hubble, 1929](#); [Arp, 1956a](#)) and found the CNe distribution extended into this central region. They also found that CNe were bulge dominated with the bulge nova rate to disc nova rate ratio was over ten. [Shafter & Irby \(2001b\)](#) also conducted an H α survey of M31 CNe and found 82 CNe extending to the outer disc of M31. [Shafter & Irby](#) found that generally, the M31 CNe followed the galaxy light but when the galactic light (B-band) was split into disc and bulge components, the CN distribution best fit the bulge light. Those authors found that around 70 per cent of the CNe in M31 were associated with the bulge. [Darnley et al. \(2006\)](#) present 20 M31 CNe from the POINT-AGAPE microlensing survey. They test the two population disc/bulge hypothesis with an observationally derived model. [Darnley et al.](#) found that the CN rate in the bulge is around five times that of the disc per unit r' -band flux. [Shafter et al. \(2011a\)](#) present a spectroscopic and photometric survey of M31 CNe and in total investigated the radial distributions of 91 CNe. Those authors did not find any significant dependence on the radial distribution for the spectral classes, however they do report that the He/N class may be slightly more spatially extended than the Fe II

CNe. Furthermore, [Williams et al. \(2016a\)](#) used *HST* imaging data to identify possible CN progenitors and found that around 30 per cent of CNe had a red giant companion and these red giant CNe were more associated with the disc, contrasted to the generally bulge-based CN population.

With this stage set, we can now discuss these findings. I have compared the radial distributions of various subsamples of M31 CNe. I find that the radial distributions of the Fe II and He/N classes are consistent with being drawn from the same parent population. I therefore find no evidence that there is a significant radial dependence for the spectral classifications and therefore there may not be a dependence between the spatial distribution of M31 CNe and their spectral classes. In all cases the Fe II CNe were consistent with the spectroscopically confirmed CNe presented in Chapter 6 but this is to be expected when 80 per cent of M31 CNe are Fe II class. Moreover, the He/N CNe are not distributed differently to the spectroscopically confirmed sample. As discussed previously, surveys of CNe in M31 tend to concentrate on the bulge of the galaxy as the CN rate is higher, therefore possibly biasing this sample to a more centrally concentrated distribution than what is seen in more recent surveys that venture out further into the disc. The observational bias towards the central regions of M31 may have a contribution due to some disc CNe being missed due to the effect of dust. However, to test the effect of this possible selection effect, [Shafter & Irby \(2001a\)](#) look at the distribution of planetary nebulae which are not strongly dependent on a stellar population and would be similarly effected by extinction as CNe. [Shafter et al.](#) found that when considering these planetary nebulae, the CNe were still bulge-dominated and at least in $H\alpha$ the CNe were no significant difference in the extinction experienced between CNe and the planetary nebulae. Furthermore as the He/N novae are more likely to be of the fast or very-fast speed class ([Shafter et al., 2011a](#)), the cadence of nova surveys may miss some of these CNe. If He/N are more associated with a disc population, their speed class may be biasing the number of He/N in catalogues as some may be missed. Conversely, slow speed class CNe are also difficult to observe due to their faintness. If such biases are common and we miss many of the fast or very fast novae or even the proposed ultra-fast nova speed class (see [Shara et al. 2017b](#) which looked at the simulation parameter space of [Yaron et al. 2005](#) to predict t_2 decline times in the order of a few hours) then the population proportions and CN rates may need reassessing. Conversely, slow CNe tend to be Fe II CNe and slow speed class CNe are also more difficult to detect due to the slow decay, hence some Fe II CNe may be missed. In order to overcome some of these selection effects and observational biases, a face-on galaxy such as M33 could be used for future radial analysis.

7.5.2 Pixel statistics results from the UV data

In this section, the NCR distributions of the M31 CNe are presented. The NCR values for the M31 CNe are tabulated in Table 7.5, this table includes the NCR values in both NUV and FUV. In Table 7.5, where there is no NCR value recorded, the CN is in a masked region of the image or lay outside of the cropped M31 image. The NCR plots shown here also show the one-to-one relation that traces a hypothetical population that perfectly follows the emission being measured. The two approaches used for masking the inner region of M31 were trialed here and the NCR distributions were consistent so only the masking after the NCR will be presented here.

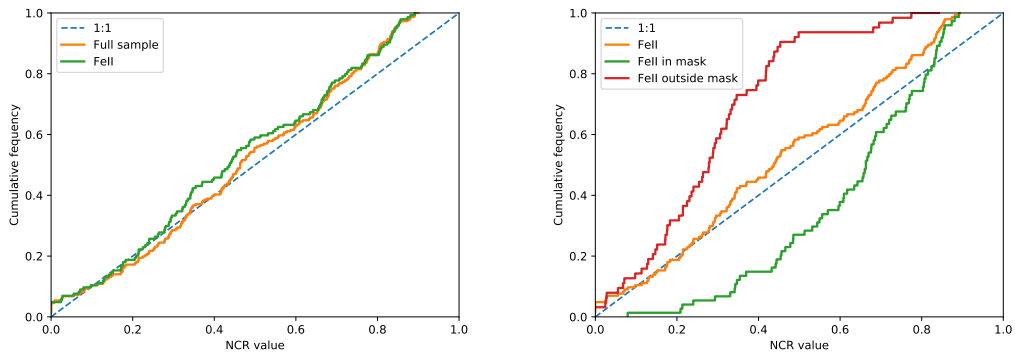


FIGURE 7.8: (*Left:*) The NUV NCR distributions of the full sample and the Fe II spectral class CNe. (*Right:*) The NUV NCR distributions of the decomposition of the full sample when it is broken down into a central region and an outer region that has the central region masked.

The left panel in Fig. 7.8 shows the NUV NCR distributions of the full sample and the Fe II spectral class. As most of the full sample are Fe II CNe, the two distributions are consistent, with an AD p-value of 0.89. There may be an upturn at higher NCR values (until the cut off at ~ 0.9). The two distributions follow the one-to-one distribution with AD p-values of 0.10 for the full sample and 0.16 for the Fe II CNe. Therefore, the full sample and Fe II CNe are consistent with being drawn from the same population as a population that follows the NUV emission. The panel on the right shows the decomposition of the Fe II CNe when the region around the bulge is isolated and we look at the NUV NCR distributions in either the masked region of the bulge or the region outside the masked region, towards the disc of M31. It can be seen that the NCR distribution inside the masked region tends towards the higher NCR values, with the distribution lying beneath the one-to-one distribution and has an upturn. This corresponds to the NCR values in the region that contains the centre of M31 which is bright in the NUV. This distribution is not consistent with the one-to-one distribution

with an AD p-value of ~ 0 . Conversely, the NCR distribution of the CNe that lay outside of the masked region lies above the one-to-one distribution, indicating that this distribution tends towards lower NCR values. This region corresponds to the outer regions of M31. This sample also has an ~ 0 AD p-value when compared with the one-to-one distribution. When combined, it can be seen how the combined distributions create the full sample that follows the NUV emission. The inside mask and outside mask distributions have a ~ 0 AD p-value when compared. The distributions for the FUV are similar.

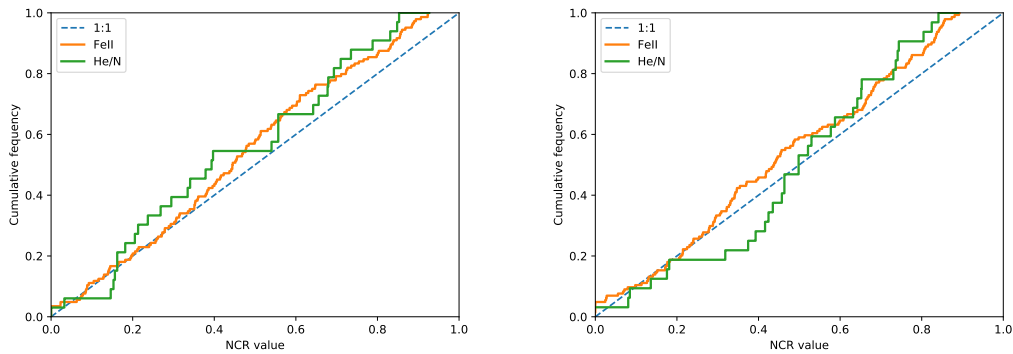


FIGURE 7.9: (*Left:* the FUV NCR distributions of the He/N and FeII spectral classes. (*Right:*) The NUV NCR distributions of the FeII and He/N spectral classes of CNe.

In Fig. 7.9, I compare the NCR distributions of the spectral classes, Fe II and He N. Here, the Fe IIb ‘hybrids’ are included in the He/N sample similarly to [Shafter et al. \(2011a\)](#). The left panel shows the FUV NCR distributions comparing the Fe II class CNe and the He/N class CNe. These distributions by eye look very similar and have an AD p-value of 0.78, indicating they are consistent with each other. Both of these distributions are consistent with the one-to-one distribution with AD p-values of 0.20 for the Fe II CNe and 0.36 for the He/N CNe. Therefore, in the FUV there is no significant difference between the spectral classes in terms of the FUV emission and also the two classes follow the FUV emission. The right panel shows a similar story for the Fe II and He/N class NUV NCR values. The distributions are similar, perhaps the He/N CNe have fewer intermediate NCR values indicated by a flattening at an NCR value of ~ 0.3 . The two classes are consistent with being drawn from the same parent population with an AD p-value of 0.46. Furthermore, the two spectral classes seem to follow the one-to-one distribution. The Fe II class CNe have an AD p-value of 0.16 when compared to the one-to-one distribution and the He/N CNe have a p-value of 0.36, indicating both are consistent with being drawn from the same parent population as the one-to-one distribution. Therefore there is no difference between the two spectral classes in terms

of their association to NUV or FUV emission and they also follow the NUV and FUV emission. It should be noted that the NCR values do not extend past a value of ~ 0.90 . So the CNe are not associated with the very strongest emission regions. The highest NCR value pixels are in the spiral arms rather than the central region which has a maximum NCR value of 0.962. The highest UV NCR values in M31 are therefore consistent with a star formation region. This is shown in Fig. 7.10 that shows the central region of M31, with all NCR values above 0.9 and a region in the spiral arms (see also Fig. 7.12).

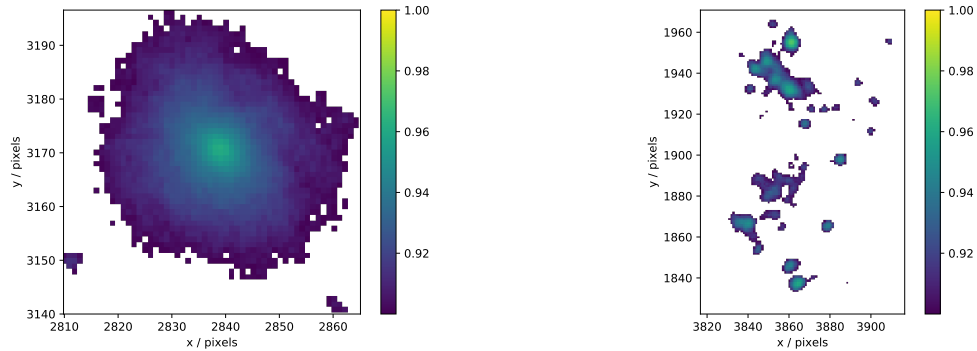


FIGURE 7.10: (*Left:* the centre of M31 in the NUV NCR colourmap with the colourbar starting at an NCR value of 0.9, here the maximum value is 0.962. (*Right:*) The NUV NCR image of one of the star forming regions in the spiral arms of M31, here the NCR values reach 0.975.

The NCR values of the various subsamples in Table 7.5 show that seven of the CNe in the full sample lay outside of the M31 UV images and therefore have no associated NCR values. The AD p-values when all the different permutations of subsamples are presented in Table 7.4.

As previously discussed, the spectral class observed in a CN may have some dependence on the WD mass. He/N CNe may have higher mass progenitors than those of Fe II CNe as the He/N spectrum originates in the ejected shell of the WD (Williams, 2012) and if the WD is higher mass, then for a given accretion rate, requires less accreted mass to initiate a TNR. Therefore less mass is ejected at a high velocity, the optical thickness decreases more quickly and therefore the decline time is faster. This is consistent with observations that show He/N CNe are more likely to be of the faster speed classes as defined by Payne-Gaposchkin (1964). Furthermore, in the Williams (2012) scheme, there may be less interaction with the companion with a small ejected mass and less winds that form the spectral features seen in Fe II CNe (however this mode of Fe II class spectral formation is unproven). The NCR technique, already described in depth in this thesis has been used to probe the association of SNe to star formation regions. In this chapter, I have applied the NCR analysis to CNe in order to explore any possible differences in

the association to UV emission between the spectral classes. I use UV emission as seen by *GALEX* as CNe aren't considered to be associated with ongoing star formation as they are old systems, enough time is required for an intermediate/low mass star (under $8 M_{\odot}$) to evolve into a WD, and then enough time passing to accrete enough material from its companion to undergo a CN eruption. The UV emission however, traces recent star formation as opposed to ongoing star formation. This NCR analysis is applied in three separate ways; the full galaxy has NCR processing applied, the central region is masked out after the NCR processing, and a focus on just the central region. I found that the central regions were biased towards high NCR values and the outer regions tended towards lower NCR values, combining to form an NCR distribution that follows the UV emission (both FUV and NUV). This highlights one of the issues with using broadband data as opposed to the narrowband, continuum subtracted data in Chapter 4. Unlike $H\alpha$ emission that has had the continuum subtracted, broadband filters suffer from the stars in M31 contributing their continuum flux rather than the UV emission being from just ionised gas associated with star formation.

If He/N novae are created by more massive WDs then a spatial difference and NCR result difference would be expected as higher mass WDs are thought to inhabit a young disc population. However none of the tests comparing Fe II and He/N novae show any significant difference between the populations. Generally speaking, there is no evidence to suggest that there is a significant difference in the NCR distributions in the *GALEX* FUV and NUV images. Therefore this shows that in general, CNe are associated with UV emission.

As well as the selection effects at play when considering studies of CNe, the geometry of M31 will effect the NCR distributions. The high inclination of M31 obscures the spiral arms and inter-arm gaps, this makes the determination of the NCR values in the star formation regions in the spiral arms difficult. M31 is close to the major-minor axis ratio cutoff of 4:1 used in previous SN work such as [Habergham et al. \(2014\)](#) and in Chapter 4. Due to this inclination, our observations may be more susceptible to dust, so some emission may be lost. Moreover, due to this inclination, the disc is in front of the bulge, so determination of the membership of a CN to the disc or bulge requires a statistical treatment such as the model in [Darnley et al. \(2006\)](#) and [Williams et al. \(2016a\)](#). The NCR plots show that the NCR distribution inside the masked region tends towards higher NCR values and the CNe outside of this region tend towards lower NCR values and when combined, they form a fairly even distribution. In the case of these *GALEX* UV images and the NCR analysis, the comparison of populations with each other (e.g. Fe II and He/N CNe) in the same host (in this case, M31) can be used to

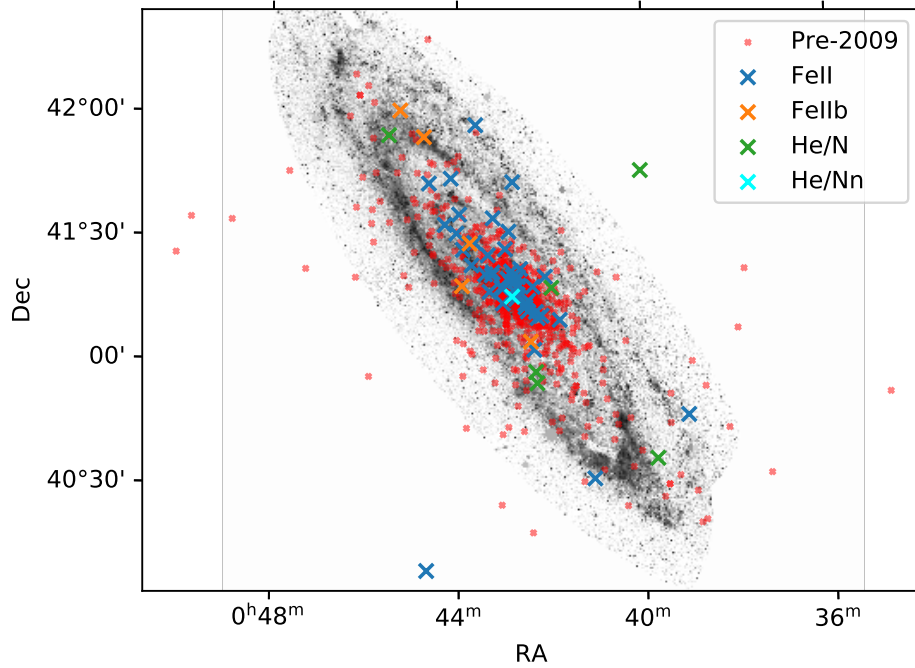


FIGURE 7.11: A cropped GALEX NUV mosaic which has had the normalised cumulative rank processing applied. Overlaid are the CNe classified previously and the CNe from the [Pietsch et al. \(2007\)](#) catalogue.

test for multiple populations. However it may not be testing purely the association to the UV emission due to star formation regions. The bulge of M31 is very bright in the UV due to the additive effect of the stellar concentration in the nucleus of M31. This therefore contributes to the high NCR values seen in the bulge, contrasted to the $H\alpha$ images where in many cases the continuum subtraction effectively erases the bulge. Therefore, the NCR analysis may only provide comparisons within the same host if the narrow band imaging is not continuum subtracted. However, it should be noted that *GALEX* UV images were used in SN work (such as [Anderson et al., 2012](#); [Haberman et al., 2014](#)) and similar relations to the $H\alpha$ NCR distributions were found.

A solution to this (if we want to assess the association to star forming regions) would be to use continuum subtracted $H\alpha$ images of M31 for the NCR analysis (such as imaging from the Local Group Galaxy Survey [Massey et al., 2006](#)). Additionally, to eliminate the possible inclination effects of M31, it would be interesting to see what the NCR distributions of more face on galaxies (and galaxies with different proportions of Fe II and He/N CNe) such as M33 and the LMC. Furthermore, to explore a relation to WD mass, the distributions of recurrent novae should be explored as these all have high mass

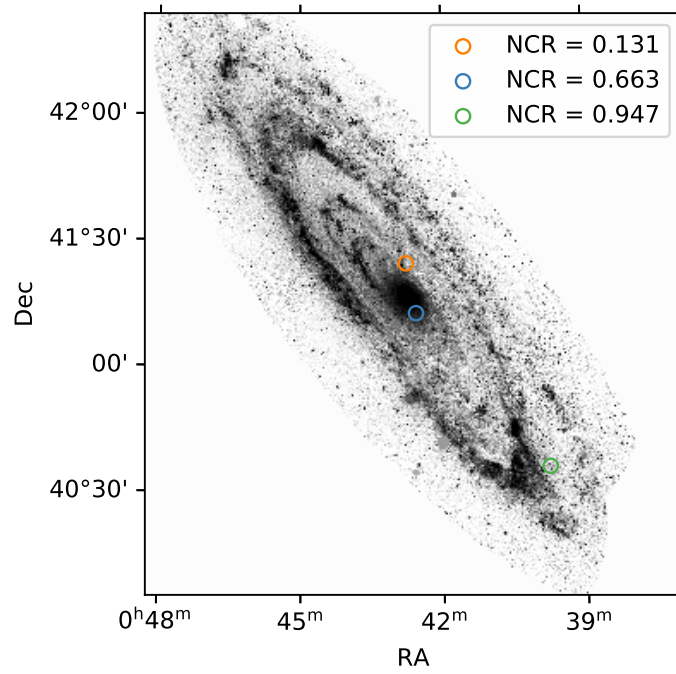


FIGURE 7.12: A cropped GALEX NUV mosaic which has had the normalised cumulative rank processing applied. Overlaid are the CNe in increasing NCR value. Note that the highest NCR value is near a spiral arm.

WD and some of the most frequently recurring CNe approach the Chandrasekhar mass. These extensions to this chapter will be discussed in Chapter 9.

Name (M31N-)	RA (J2000)	Dec	Type
1992-11b	00:42:36.20	41:11:54.00	FeII
1993-06a	00:42:49.20	41:17:27.50	FeII
1993-08a	00:42:45.10	41:14:27.00	He/N
1993-10g	00:42:47.70	41:18:01.00	FeII
1993-11c	00:42:50.10	41:17:28.00	FeII
1998-09d	00:42:46.60	41:14:49.20	FeII
1999-06a	00:42:49.70	41:15:05.60	FeII
1999-08f	00:42:41.10	41:19:12.20	FeII
1999-10a	00:42:49.70	41:16:32.00	FeII
2001-10a	00:43:03.30	41:12:11.50	FeII
2001-12a	00:42:41.40	41:16:24.50	FeII
2002-01b	00:42:33.90	41:18:23.90	He/N
2002-08a	00:42:30.92	41:06:13.10	FeII
2004-08b	00:43:26.84	41:16:40.80	FeII
2004-09a	00:42:40.27	41:14:42.50	FeII
2004-11a	00:42:42.81	41:18:27.90	FeII
2004-11b	00:43:07.45	41:18:04.70	He/N
2005-01a	00:42:28.39	41:16:36.20	FeII
2005-07a	00:42:50.79	41:20:39.80	FeII
2006-09c	00:42:42.38	41:08:45.50	FeI
2006-10a	00:41:43.23	41:11:45.90	FeII
2006-10b	00:39:27.38	40:51:09.80	FeIIb
2006-11a	00:42:56.81	41:06:18.40	FeII
2006-12a	00:42:21.09	41:13:45.30	FeII
2006-12b	00:42:11.14	41:07:43.40	FeII
2007-02a	00:40:59.02	40:44:52.70	FeII
2007-02b	00:41:40.32	41:14:33.50	FeII
2007-06b	00:42:33.14	41:00:25.90	He/N
2007-08d	00:39:30.27	40:29:14.20	FeII
2007-10a	00:42:55.95	41:03:22.00	He/Nn
2007-11b	00:43:52.99	41:03:36.20	He/Nn
2007-11c	00:43:04.14	41:15:54.30	FeII
2007-11d	00:44:54.60	41:37:40.00	FeII
2007-11e	00:45:47.74	42:02:03.50	FeII
2007-12a	00:44:03.51	41:38:41.10	FeII
2007-12b	00:43:20.00	41:13:46.60	He/N
2007-12d	00:41:54.96	41:09:47.30	He/N
2008-09a	00:41:46.72	41:07:52.10	FeII
2008-09c	00:42:51.42	41:01:54.00	FeII
2008-10a	00:43:35.46	41:54:44.20	FeII
2008-10b	00:43:02.42	41:14:09.90	FeII
2008-11a	00:41:32.00	41:06:01.00	He/N
2009-01a	00:44:44.03	41:23:28.30	FeII
2009-02a	00:43:43.81	41:36:38.80	FeII

TABLE 7.3: The CN sample presented in [Shafter et al. \(2011a\)](#).

TABLE 7.4: Grid presenting the Anderson-Darling test results for the subsamples of M31 CNe NCR values. The values shown are the AD p-values. The lower triangle are the FUV AD p-values and the upper triangle shows the AD p-values for the NUV NCR distributions.

-	1:1	Full sample	Fe II	He/N	In mask	Out of mask	In mask Fe II	In mask He/N	Out of mask Fe II	Out of mask He/N
1:1	-	0.1	0.16	0.36	0	0	0	0	0	0.051
Full sample	0.21	-	0.89	0.8	0	0	0	0.028	0	0.056
Fe II	0.2	0.98	-	0.46	0	0	0	0.013	0	0.11
He/N	0.36	0.86	0.78	-	0	0	0.008	0.1	0	0.083
In mask	0.011	0	0	0.0085	-	0	0.95	0.96	0	0
Out of mask	0.0017	0.0037	0.022	0.224	0	-	0	0	0.45	0.3
In mask Fe II	0.063	0.009	0.005	0.034	0.98	0	-	0.94	0	0
In mask He/N	0.57	0.4	0.24	0.37	0.94	0.012	0.89	-	0	0
Out of mask Fe II	0	0	0.0032	0.062	0	0.24	0	0.005	-	0.06
Out of mask He/N	0.13	0.17	0.24	0.53	0.0015	0.84	0.0064	0.046	0.48	-

Name (M31N-)	Type	NUV NCR	FUV NCR	NUV in mask	FUV in mask	NUV out of mask	FUV out of mask
2010-01a	FeII	0.768	0.759	0.768	0.759	-	-
2010-05a	FeII	0.810	0.828	0.810	0.828	-	-
2010-06d	FeII	0.677	0.602	0.677	0.602	-	-
2010-06b	FeII	0.306	0.289	-	-	0.306	0.289
2010-06a	FeII	0.642	0.551	0.642	0.551	-	-
2010-07a	FeII	0.444	0.293	0.444	0.293	-	-
2010-09c	FeII	0.266	0.230	-	-	0.266	0.230
2010-10b	FeII	0.332	0.194	-	-	0.332	0.194
2010-09a	FeII	-	-	-	-	-	-
2010-09b	FeII	0.225	0.128	-	-	0.225	0.128
2010-10a	FeII	0.131	0.306	-	-	-	-
2010-10f	-	0.805	0.824	0.805	0.824	-	-
2010-10c	FeII	0.437	0.610	-	-	0.437	0.610
2010-10d	He/N	0.558	0.328	0.558	0.328	-	-
2010-10e	He/N	0.498	0.162	-	-	0.498	0.162
2010-11a	He/N	0.587	0.146	0.587	0.146	-	-
2010-12c	-	0.779	0.759	0.779	0.759	-	-
2011-01a	FeII	0.676	0.562	0.676	0.562	-	-
2011-06a	FeII	0.341	0.139	-	-	0.341	0.139
2011-06e	FeII	-	-	-	-	-	-
2011-06d	FeII	0.209	0.116	0.209	0.116	-	-

2011-07a	He/N	0.804	0.788	0.804	0.788	-	-
2011-07b	FeII	0.183	0.923	-	-	0.183	0.923
2011-08a	FeII	0.419	0.561	-	-	0.419	0.561
2011-08b	FeII	0.322	0.206	-	-	0.322	0.206
2011-09a	FeII	0.309	0.302	-	-	0.309	0.302
2011-09b	-	0.596	0.547	0.596	0.547	-	-
2011-10a	FeII	0.770	0.744	0.770	0.744	-	-
2011-10d	FeIIb	0.759	0.701	0.759	0.701	-	-
2011-11a	FeII	0.293	0.104	-	-	0.293	0.104
2011-11c	FeII	0.279	0.444	-	-	0.279	0.444
2011-11e	FeII	0.854	0.833	0.854	0.833	-	-
2011-12a	FeII	0.447	0.684	-	-	0.447	0.684
2011-12b	FeII	0.395	0.273	-	-	0.395	0.273
2012-01a	FeII	0.254	0.444	-	-	0.254	0.444
2012-01b	He/N	0.424	0.205	0.424	0.205	-	-
2012-02a	FeII	-	0.000	-	-	-	-
2012-05e	FeII	0.000	0.143	-	-	0.000	0.143
2012-06b	FeII	0.696	0.837	-	-	0.696	0.837
2012-06c	FeII	0.425	0.609	-	-	0.425	0.609
2012-06d	FeII	0.489	0.698	-	-	0.489	0.698
2012-06e	FeII	0.240	0.531	0.240	0.531	-	-
2012-06a	FeII	0.442	0.416	0.442	0.416	-	-
2012-06f	FeII	0.793	0.629	0.793	0.629	-	-

2012-06g	He/N	0.741	0.735	0.741	0.735	-	-
2012-07a	FeII	0.205	0.166	-	-	0.205	0.166
2012-07b	-	0.570	0.351	0.570	0.351	-	-
2012-07c	FeII	0.215	0.211	-	-	0.215	0.211
2012-09a	FeIIb	0.901	0.934	0.901	0.934	-	-
2012-09b	FeIIb	0.774	0.757	0.774	0.757	-	-
2012-10a	He/N	0.435	0.557	-	-	0.435	0.557
2012-12a	FeII	0.856	0.884	0.856	0.884	-	-
2012-12b	FeII	0.555	0.197	-	-	0.555	0.197
2013-01a	FeII	0.852	0.886	0.852	0.886	-	-
2013-01b	He/N	0.521	0.642	-	-	0.521	0.642
2013-02a	FeII	0.278	0.400	-	-	0.278	0.400
2013-05b	He/N	0.731	0.679	0.731	0.679	-	-
2013-06c	-	0.477	0.609	-	-	0.477	0.609
2013-06b	FeII	0.635	0.567	0.635	0.567	-	-
2013-08a	FeII	0.608	0.470	0.608	0.470	-	-
2013-08e	FeII	0.296	0.314	-	-	0.296	0.314
2013-09d	FeII	0.264	0.414	-	-	0.264	0.414
2013-10a	FeII	0.347	0.164	0.347	0.164	-	-
2013-10d	He/N	0.000	0.153	-	-	0.000	0.153
2013-10g	FeII	0.342	0.379	0.342	0.379	-	-
2013-10h	FeII	0.670	0.625	0.670	0.625	-	-
2013-11a	-	0.253	0.272	-	-	0.253	0.272

2013-12a	He/Nn	0.833	0.835	0.833	0.835	-	-
2013-12b	FeIIb	0.802	0.772	0.802	0.772	-	-
2014-01a	FeII	0.532	0.455	0.532	0.455	-	-
2014-01b	-	0.316	0.527	-	-	0.316	0.527
2014-01c	FeII	0.807	0.777	0.807	0.777	-	-
2014-02a	He/N	0.375	0.335	0.375	0.335	-	-
2014-06b	He/N	0.744	0.710	0.744	0.710	-	-
2014-07a	FeII	0.141	0.315	-	-	0.141	0.315
2014-09a	FeII	0.466	0.353	0.466	0.353	-	-
2014-09b	FeII	0.681	0.801	-	-	0.681	0.801
2014-10c	He/N	0.463	0.557	-	-	0.463	0.557
2014-10a	FeII	0.485	0.307	0.485	0.307	-	-
2014-11a	FeII	0.815	0.831	0.815	0.831	-	-
2015-01a	-	0.446	0.158	-	-	0.446	0.158
2015-02a	FeII	0.720	0.603	0.720	0.603	-	-
2015-02b	He/Nn	0.287	0.372	-	-	0.287	0.372
2015-05b	FeII	0.556	0.478	0.556	0.478	-	-
2015-06a	FeII	0.881	0.923	0.881	0.923	-	-
2015-07d	FeII	0.655	0.648	0.655	0.648	-	-
2015-08a	FeII	0.688	0.610	0.688	0.610	-	-
2015-08c	FeII	0.176	0.383	-	-	0.176	0.383
2015-08d	-	0.463	0.557	-	-	0.463	0.557
2015-09c	FeII	0.354	0.200	0.354	0.200	-	-

2015-10a	He/N	0.176	0.213	-	-	0.176	0.213
2015-10b	He/N	0.577	0.540	0.577	0.540	-	-
2015-10c	He/N	0.498	0.162	-	-	0.498	0.162
2015-11a	FeII	0.439	0.640	-	-	0.439	0.640
2015-11c	FeII	0.453	0.468	-	-	0.453	0.468
2015-12a	He/N	0.890	0.927	0.890	0.927	-	-
2015-12c	FeII	-	0.000	-	-	-	-
2016-01a	FeII	0.262	0.145	-	-	0.262	0.145
2016-01c	FeIIb	0.328	0.401	-	-	0.328	0.401
2016-02a	FeIIb	0.694	0.829	-	-	0.694	0.829
2016-03c	-	0.879	0.915	0.879	0.915	-	-
2016-02b	FeII	0.176	0.780	-	-	0.176	0.780
2016-03b	-	0.479	0.354	0.479	0.354	-	-
2016-03d	-	0.679	0.611	0.679	0.611	-	-
2016-04a	He/Nn	0.467	0.673	-	-	0.467	0.673
2016-05a	FeII	0.293	0.214	0.293	0.214	-	-
2016-05b	FeII	0.891	0.925	0.891	0.925	-	-
2016-07b	FeII	-	0.000	-	-	-	-
2016-07c	FeII	0.371	0.404	-	-	0.371	0.404
2016-07d	He/N	-	0.00E+00	-	-	-	-
2016-07e	FeII	0.707	0.679	0.707	0.679	-	-
2016-08d	FeII	0.456	0.240	0.456	0.240	-	-
2016-08e	FeII	0.498	0.711	-	-	0.498	0.711

2016-09a	FeII	0.714	0.547	0.714	0.547	-	-
2016-09b	FeII	0.432	0.244	0.432	0.244	-	-
2016-10d	FeII	0.147	0.258	-	-	0.147	2.58
2016-10b	FeII	0.776	0.766	0.776	0.766	-	-
2016-11a	FeIIb	0.780	0.800	0.780	0.800	-	-
2016-12f	He/N	0.463	0.557	-	-	0.463	0.557
2016-12d	FeII	0.725	0.723	0.725	0.723	-	-
2016-12e	He/N	0.846	0.237	-	-	0.846	0.237
2017-01c	FeII	0.596	0.539	0.596	0.539	-	-
2017-01e	He/N	0.642	0.848	-	-	0.642	0.848
2017-03a	FeII	0.617	0.514	0.617	0.514	-	-
2017-04b	-	0.780	0.743	0.780	0.743	-	-
2017-05a	He/N	0.181	0.268	-	-	0.181	0.268
2017-05b	-	0.415	0.583	-	-	0.415	0.583
2017-06c	FeII	0.663	0.572	0.663	0.572	-	-
2017-06e	FeII	0.842	0.501	-	-	0.842	0.501
2017-07a	FeII	0.152	0.843	-	-	0.152	0.843
2017-07b	FeII	0.549	0.182	0.549	0.182	-	-
2017-07d	FeII	0.775	0.894	-	-	0.775	0.894
2017-09a	FeII	0.127	0.708	-	-	0.127	0.708
2017-09b	FeII	0.215	0.279	-	-	0.215	0.279
2017-09c	FeII	0.454	0.437	0.454	0.437	-	-
2017-09e	FeII	0.370	0.351	0.370	0.351	-	-

2017-10a	FeII	0.213	0.141	0.213	0.141	-	-
2017-11a	FeI	0.231	0.271	-	-	0.231	0.271
2017-11c	FeII	0.172	0.423	-	-	0.172	0.423
2017-11d	He/N	0.841	0.853	0.841	0.853	-	-
2017-11e	He/N	0.653	0.393	0.653	0.393	-	-
2017-12b	FeII	0.418	0.340	-	-	0.418	0.340
2017-12a	He/N	0.457	0.295	0.457	0.295	-	-
2017-12e	-	0.463	0.557	-	-	0.463	0.557
2018-01a	FeII	0.711	0.856	-	-	0.711	0.856
2018-01b	-	0.381	0.194	-	-	0.381	0.194
2018-02a	FeII	0.000	0.741	-	-	0.000	0.741
AT2018bto	-	0.644	0.708	-	-	0.644	0.708
AT2018cmi	He/N	0.319	0.341	-	-	0.319	0.341
2018-06b	FeII	0.803	0.724	0.803	0.724	-	-
2018-07a	FeII	0.346	0.445	-	-	0.346	0.445
2018-07b	FeII	0.130	0.233	-	-	0.130	0.233
2018-07c	FeII	0.761	0.736	0.761	0.736	-	-
2018-08a	FeII	0.849	0.889	0.849	0.889	-	-
2018-08b	-	0.008	0.213	-	-	0.009	0.213
2018-08d	FeII	0.680	0.881	-	-	0.680	0.881
AT2018fhy	-	0.681	0.502	0.681	0.502	-	-
AT2018fsy	-	0.340	0.484	-	-	0.340	0.484
AT2018ggg	-	-	0.000	-	-	-	-

AT2018had	-	0.319	0.341	-	-	0.319	0.341
AT2018hcd	FeII	0.171	0.360	-	-	0.171	0.360
AT2018hfs	-	0.748	0.739	0.748	0.739	-	-
AT2018hho	-	0.800	0.772	0.800	0.772	-	-
2018-10c	FeII	0.280	0.256	-	-	0.280	0.256
2018-10d	-	0.603	0.485	0.603	0.485	-	-
2018-11b	FeII	0.335	0.335	-	-	0.335	0.335
2018-12a	FeII	0.599	0.540	0.599	0.540	-	-
2018-12b	FeII	0.657	0.499	0.657	0.499	-	-
2018-12c	FeIIb	0.947	0.137	-	-	0.947	0.137
2018-12d	FeII	0.485	0.452	0.485	0.452	-	-
2018-12e	FeII	0.832	0.856	0.832	0.856	-	-
2018-12f	FeIIb	0.250	0.203	-	-	0.250	0.203
2019-01d	-	0.703	0.659	0.703	0.659	-	-
2019-01a	-	0.260	0.380	-	-	0.260	0.380
2019-01b	FeII	0.824	0.803	0.824	0.803	-	-
2019-01c	-	0.505	0.458	-	-	0.505	0.458
2019-01f	FeII	0.769	0.726	0.769	0.726	-	-
2019-01e	FeIIb	0.662	0.743	-	-	0.662	0.743
2019-02a	FeII	0.570	0.407	0.570	0.407	-	-
1992-11b	FeII	0.663	0.351	0.663	0.351	-	-
1993-06a	FeII	0.844	0.857	0.844	0.857	-	-
1993-08a	He/N	0.825	0.831	0.825	0.831	-	-

1993-10g	FeII	0.805	0.798	0.805	0.798	-	-
1993-11c	FeII	0.837	0.847	0.837	0.847	-	-
1998-09d	FeII	0.836	0.860	0.836	0.860	-	-
1999-06a	FeII	0.835	0.869	0.835	0.869	-	-
1999-08f	FeII	0.660	0.514	0.660	0.514	-	-
1999-10a	FeII	0.873	0.907	0.873	0.907	-	-
2001-10a	FeII	0.544	0.456	0.544	0.456	-	-
2001-12a	FeII	0.892	0.924	0.892	0.924	-	-
2002-01b	He/N	0.632	0.397	0.632	0.397	-	-
2002-08a	FeII	0.343	0.396	0.343	0.396	-	-
2004-08b	FeII	0.513	0.359	0.513	0.359	-	-
2004-09a	FeII	0.831	0.839	0.831	0.839	-	-
2004-11a	FeII	0.762	0.698	0.762	0.698	-	-
2004-11b	He/N	0.652	0.656	0.652	0.656	-	-
2005-01a	FeII	0.736	0.647	0.736	0.647	-	-
2005-07a	FeII	0.609	0.585	0.609	0.585	-	-
2006-09c	FeII	0.478	0.262	0.478	0.262	-	-
2006-10a	FeII	0.288	0.278	-	-	0.288	0.278
2006-10b	FeIIb	0.007	0.209	-	-	0.007	0.209
2006-11a	FeII	0.241	0.477	-	-	0.241	0.477
2006-12a	FeII	0.667	0.508	0.667	0.508	-	-
2006-12b	FeII	0.331	0.130	0.331	0.130	-	-
2007-02a	FeII	0.977	0.354	-	-	0.977	0.354

2007-02b	FeII	0.289	0.381	-	-	0.289	0.381
2007-06b	He/N	0.736	0.693	-	-	0.736	0.693
2007-08d	FeII	0.245	0.885	-	-	0.245	0.885
2007-10a	He/N _n	0.530	0.678	-	-	0.530	0.678
2007-11b	He/N _n	0.806	0.325	-	-	0.806	0.325
2007-11c	FeII	0.686	0.591	0.686	0.591	-	-
2007-11d	FeII	0.277	0.485	-	-	0.277	0.485
2007-11e	FeII	0.113	0.630	-	-	0.113	0.630
2007-12a	FeII	0.729	0.855	-	-	0.729	0.855
2007-12b	He/N	0.393	0.379	0.393	0.379	-	-
2007-12d	He/N	0.416	0.182	-	-	0.416	0.182
2008-09a	FeII	0.236	0.386	-	-	0.236	0.386
2008-09c	FeII	0.322	0.577	-	-	0.322	0.577
2008-10a	FeII	0.328	0.754	-	-	0.328	0.754
2008-10b	FeII	0.682	0.511	0.682	0.511	-	-
2008-11a	He/N	0.136	0.156	-	-	0.136	0.156
2009-01a	FeII	0.399	0.442	-	-	0.399	0.442
2009-02a	FeII	0.418	0.479	-	-	0.418	0.479

TABLE 7.5: The M31 CNe and their NCR values in FUV and NUV. These distributions are also split into the contributions from within and outside of the masked region. The CNe presented in [Shafter et al. \(2011a\)](#) are towards the end of this table and are separated with a horizontal line after M31N-2018-02a.

7.6 Conclusions and Summary

In this chapter, I have implemented NCR analysis for the first time to the environments of CNe, in this case the CNe in M31. The sample used here included the spectroscopic confirmed sample outlined in Chapter 6 and also the full catalogue of M31 CNe from [Pietsch \(2010\)](#). The radial distributions of various CN subsamples were compared as well as the NCR distributions in order to explore any possible differences in the M31 CN population. My results can be summarised as:

1. The radial distributions of the spectral classes, are consistent with each other, this is in agreement with the findings of [Shafter et al. \(2011a\)](#).
2. When comparing the full M31 catalogue with around 1000 CNe in it, we find that the radial distributions are largely inconsistent with the spectroscopically confirmed sample. This may be due to selection effects in how CN surveys are often carried out.
3. Generally, M31 CNe follow UV emission as measured by the NCR method. This suggests that the novae in M31 follow regions of recent star formation. This is a surprising result as classical novae are thought to be old systems that have had time for a WD to form and accrete enough material to undergo a TNR. In the context of SNe, this result would suggest high mass progenitors, but this is not the case with CNe.
4. There is no significant difference in the NCR distributions of the CN spectral classes in M31 in either the *GALEX* NUV or FUV. Therefore there is no evidence for a strong WD mass dependence on spectral class.
5. While the NCR distributions followed the UV emission, no CNe were associated with the strongest UV regions (NCR values over around 0.90) which were in pixels not in the central regions.

Future work can further explore these results by looking at other, more face on galaxies such as M33, integrated with high cadence, spatially non-biased surveys and also the analysis of $H\alpha$ data. Furthermore, the distributions of RNe should be explored as these all have high mass WDs.

Chapter 8

Conclusions

In this thesis I have presented the results of the environmental analysis of two transient classes that inhabit very different regions of the timescale-luminosity phase-space. As part of this work I also present the largest spectroscopically confirmed samples of each transient used in environmental studies. Additionally, for the SNe IIn, I also present a classification scheme. These robust samples were used in the environmental analysis.

Below, I summarise the findings and conclusions presented in each chapter.

8.1 Chapter 3: Type IIn supernovae spectral classifications

The classification of SNe IIn has been problematic with out of date classifications or misclassifications recorded in online databases being common. The environmental work presented in Chapter 4 depends on a robust sample. I have therefore presented a classification scheme that is dependent on the $H\alpha$ profile, using a Gaussian decomposition of the different components present. Combined with a peak luminosity cut for impostors (with a literature search to filter out brighter impostors), this scheme was applied to a sample of 115 transients from the OSC that at some point has held a SN IIn classification.

Based on the presence and persistence of CSM interaction features, the reclassified transients were split into three groups, the gold, silver and not SNe IIn. The gold SNe exhibited persistent CSM interaction over multiple epochs over a period greater than the flash-ionisation timescale. The silver SNe have short lived CSM interaction (but still longer than the flash-ionisation timescale, limited data, with either one spectrum or multiple spectra but during a possible flash-ionisation phase. The reasons why a

transient may be discounted as being a SN IIIn include an evolution to a regular SN II, H II region pollution, being an impostor or there was no evidence CSM interaction and there was an erroneous classification.

I found that 87 of the 115 SNe IIIn candidates could be classified as SNe IIIn with my scheme. Of these, 37 were gold and 50 were silver. There were 28 non-SNe IIIn where the main reason they were discounted was possible contamination from the underlying H II region. I also found that the two main databases used here, the OSC and TNS disagreed on the primary classifications of 51 of the transients. The OSC had non-IIIn classifications for 34 of my reclassified SNe and the TNS had twelve. The OSC has eleven transients classified as SNe IIIn that I classify as not being a SN IIIn, the TNS had 18 such cases. It should be noted however, that the now offline OSC was an aggregate database with no direct input but was widely used in the SN community. I also presented the SNID classifications of the transients and showed the limitations of template matching routines when there is a limited spectral library.

To solidify classifications of SNe IIIn, follow-up observations are vital. They provide information on the evolution of the spectra, allowing estimations of the duration of CSM interaction. Furthermore, when a SN IIIn classification is found to be erroneous, it is important that the new data are reflected in public databases, particularly in cases where specific SNe have been studied in depth in the literature. The classification scheme presented here should be applied to a larger sample of SN IIIn candidates, since the current catalogue is limited.

8.2 Chapter 4: The environments of type IIIn supernova

Using the spectroscopic sample from the Chapter 3, I presented the observations of the host galaxies of 79 SNe IIIn using the LT, INT and LCOGT 2m. These data were used to construct continuum subtracted $H\alpha$ images of the hosts. The pixel statistics technique, normalised cumulative ranking, was applied to these images in order to associate the SN position with $H\alpha$ emission which traces ongoing star formation. The NCR distributions were compared between subsamples, such as the gold and silver spectral categories from Chapter 3. It was found that in general, SNe IIIn do not follow the $H\alpha$ emission and therefore do not follow star formation. This result is unexpected if LBVs are the main progenitor route for SNe IIIn. Around 40 per cent of the SNe in this sample were unassociated with emission regions. However the non-zero NCR distribution is consistent with a population that does follow the emission and therefore, ongoing star formation.

This result may point towards there being multiple progenitor routes for SNe IIn with lower mass progenitors making up some of the zero NCR population. Possible lower mass progenitor systems include ecSNe and SNe Ia-CSM. Furthermore, when considering the gold and silver samples from the spectroscopic classification in the previous chapter, it was found that there was no significant difference between these distributions. This suggests that given more data at later epochs, many of the silver class SNe IIn would be promoted to gold SNe IIn. I also found that the SN impostors were almost all had an NCR value of zero.

The radial distributions of SNe IIn in terms of the r' -band and $H\alpha$ emission is consistent with being flat. However I do note there are more centrally located SNe IIn than previous studies. While there is no central excess found in the distribution, there may be some SNe IIn progenitors that are similar to the progenitors of the massive, centrally concentrated SNe Ic.

Future surveys will provide a huge amount of data and transient discoveries. Surveys such as the ZTF and the Legacy Survey of Space and Time (LSST) at the Vera C. Rubin Observatory ([LSST Science Collaboration et al., 2009](#)) will provide a wealth of SNe IIn candidates and will allow much larger samples to be used for constraining possible SNe IIn progenitors.

8.3 Chapter 6: The spectral classification of M31 classical novae with SPRAT

In this chapter I presented the spectral classifications of M31 CNe that had LT SPRAT data. These classifications were used for the environmental analysis presented in Chapter 7.

In total, there are 222 CNe in our catalogue, starting from an initial 44 CNe from [Shafter et al. \(2011a\)](#). Of these, 76 have LT SPRAT data. Out of these 76 CNe, 60 were able to be (re)classified. These classifications were made by measuring the $H\alpha$ profile widths along with the line lists from [Williams \(1992\)](#); [Williams \(2012\)](#).

From these 60 spectrally classified CNe, there were 48 Fe II class novae, five Fe IIb novae, six He/N novae and a single He/Nn nova. These proportions are consistent with the findings of [Shafter et al. \(2011a\)](#), however with more Fe IIb novae. The number of Fe IIb nova in this work is similar to the number of He/N, this may be an argument to support

the Fe IIb class being a ‘main’ class along with the He/N, or that the typical 2500 km s^{-1} cut-off for Fe II novae should be reassessed.

8.4 Chapter 7: The environments of classical novae in the Andromeda galaxy

In this chapter, I explored possible CN populations in M31. I investigate this using both the radial distributions of the CNe as well as for the first time for CNe, NCR with *GALEX* NUV and FUV images. The radial distributions and NCR distributions between the spectral classes were compared.

There is no significant difference between the radial distributions of the spectral classes. This result is consistent with the findings of [Shafter et al. \(2011a\)](#) who reported a hint at a more extended population (however not statistically significant). Furthermore, when comparing my sample to the full historical sample from [Pietsch \(2010\)](#) with ~ 1000 M31 novae, I find that the radial distributions are inconsistent with the two populations being drawn from the same parent population. This result highlights the selection effects in play how CN surveys were conducted, the historical CNe were more centrally located as CN surveys tended to concentrate on the centre of M31 due to the higher CN rate.

Furthermore, the NCR distributions in both the NUV and FUV suggest that CNe follow UV emission. When the sample is split into the spectral classes, it is found that there is no significant difference between the Fe II and He/N (plus subclasses). This suggests there is no strong dependence on the WD mass and which spectral class is observed. While the NCR distribution followed the UV flux of M31, no CNe were found in the strongest UV emission regions.

Future work can include looking at the CNe in other galaxies such as M33 and the LMC which may have different proportions of Fe II and He/N CNe. Furthermore M33 is face on so will not suffer from the inclination effects experienced by M31. The NCR distributions can be recalculated with $H\alpha$ images from [Massey et al. \(2006\)](#) to gauge the association of the M31 CNe and ongoing star formation. The NCR and radial distributions of RNe could be explored also as these transients are known to have high mass WDs.

Chapter 9

Future work

The environmental tools I have used in my previous work have proven to be very powerful, namely the pixel statistics method, NCR which allows us to associate a pixel with emission. New surveys such as ZTF are finding a huge number of transients, many of which will be exotic and poorly understood. This offers a fantastic opportunity to exploit these surveys to create large catalogues for studies of such transients and their environments.

9.1 Metallicity of the environments of type II_n supernovae with the New Technology Telescope

Another avenue that can be explored is the local metallicities of SNe II_n (not including the radial distribution analogue for metallicity discussed previously). Using the O3N2 diagnostic of [Pettini & Pagel \(2004\)](#), [Habergham et al. \(2014\)](#) investigated the local metallicities of SNe II_n. However only six of their sample had a direct measurement, the others were conversions from other methods of measuring metallicity. They found that SN impostors were found in lower metallicity regions than SNe II_n, IIP and Ic. [Taddia et al. \(2015\)](#) investigated the metallicities of the environments of interacting transients (i.e. SNe II_n split into further subtypes and also impostors). Similarly, to [Habergham et al. \(2014\)](#), [Taddia et al. \(2015\)](#) found that the impostors were in regions of lower metallicity than SNe II_n. Further to this, SN II_n-L (SN 1998S-like) were in regions of higher metallicity than the longer lasting SNe II_n, with metallicities similar to ‘regular’ SNe IIP/L.

9.1.1 The New Technology Telescope

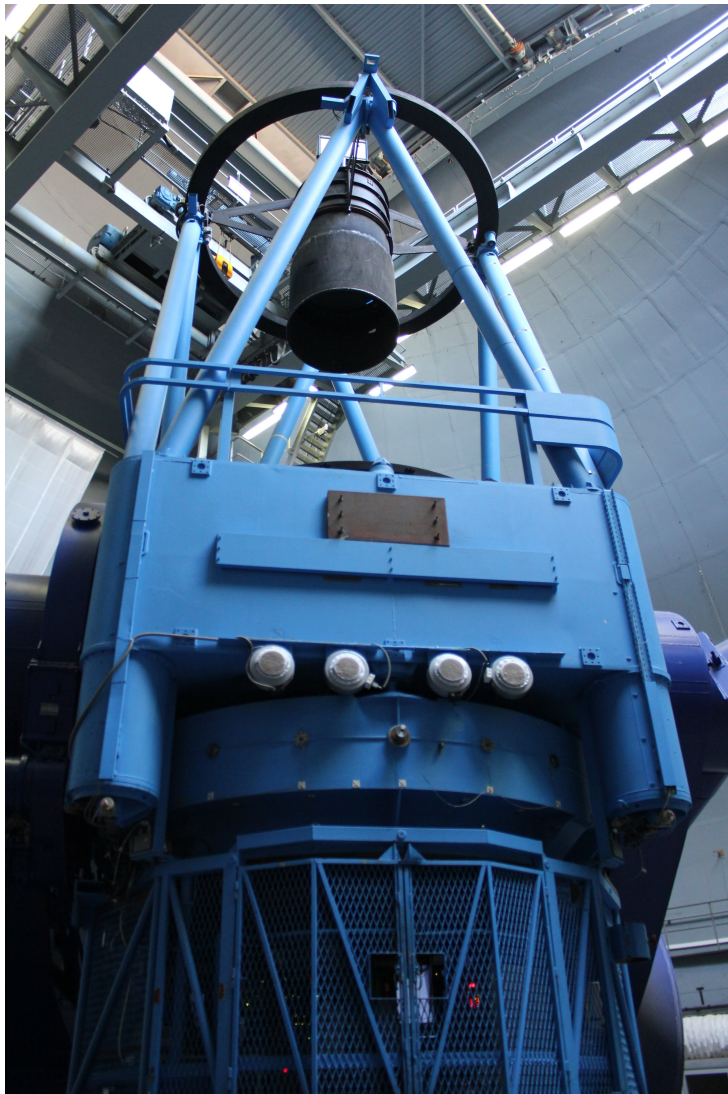


FIGURE 9.1: The New Technology Telescope (NTT). Photo courtesy of Dr. Stacey Habergham-Mawson.

The New Technology Telescope (NTT) at the European Southern Observatory La Silla Observatory in Chile. The NTT has a 3.58 m mirror and has an alt-azimuth mount. The NTT holds three instruments, ESO Faint Object Spectrograph and Camera version 2 (EFOSC2), ESO Multi-mode Instrument (EMMI, a wide field camera, long slit spectrograph, multi object spectrograph and echelle spectrograph) and the Son of ISAAC (SOFI, an infrared camera and spectrograph).

Using IDS on the INT and EFOSC2 on the NTT (shown in Fig. 9.1), I am in the process of taking spectroscopic observations of the hosts of the SNe II_n presented in this thesis.

When complete, this will be the largest spectroscopic survey of the environments of SNe IIIn and impostors and will reinforce constraints on possible progenitor paths.

9.1.2 Other possible projects

As well as the SN IIIn metallicity project, there are a number of other future projects that extend the work presented in this thesis. Possible future projects include:

- Applying the environmental tools in this thesis to other types of transients. I will use the pixel statistics techniques defined previously and possibly data from integral field units to study local environments in terms of the local population and their ages and H II regions along with local metallicities. This will allow the creation of a ‘family tree’ of possible progenitors for each transient type. Example transients would include intermediate luminosity red transients (ILRTs) which may be electron-capture SNe or be interpreted as SN impostors (e.g. SN 2008S). SNe Ibn and SNe Icn (a new class [Perley et al., 2022](#); [Davis et al., 2022](#), however there are only five examples of this class as of Dec. 2022, e.g. SN 2019jc, SN 2019hgp, SN 2021ckj, SN 2021csp and SN 2022ann;) are stripped envelope SNe showing CSM interaction. I could investigate whether these transients share the same environments as non-interacting SNe Ib and Ic.
- Recent findings (see [Nyholm et al., 2020](#)) suggest that there may be separate photometric classes within SNe IIIn. There may be ‘fast’ and ‘slow’ SNe IIIn when considering their rise times. Generally speaking, SNe IIIn are longer-lasting photometrically due to ongoing CSM interaction, and those authors found that the slow risers were also slow decliners. This may be linked to the CSM density, with less dense CSM causing a sharper decline and vice versa. I could explore these possible photometric classes by following up new SNe IIIn found by ZTF or future surveys at the Rubin Observatory. A larger sample of SNe IIIn may reveal greater heterogeneity if the light-curves are diverse in terms of their rise/decline times, but also their peaks. Light-curve modelling may reveal clustering in the derived parameters which may be linked with photometric types of SNe IIIn.
- SN impostors are non-terminal eruptions which are sometimes mistaken for SNe and may be SN precursors. With the notable example of SN 2009ip, the 2009 eruption was a precursor to the full SN. SN 2009ip had mass loss events up until the (possibly) terminal eruption in 2012 and may be interpreted as giant LBV eruptions. [Strotjohann et al. \(2021\)](#) found that a quarter of SNe IIIn discovered

by ZTF had precursor events in the three months prior to terminal explosion. This fraction may be higher due to incompleteness in the survey coverage. Using previous precursor events a training set can be created for an “early warning” system that can be used for monitoring transients, using it as a predictive tool. This would offer the opportunity to catch SNe IIⁿ at early times with targeted observations.

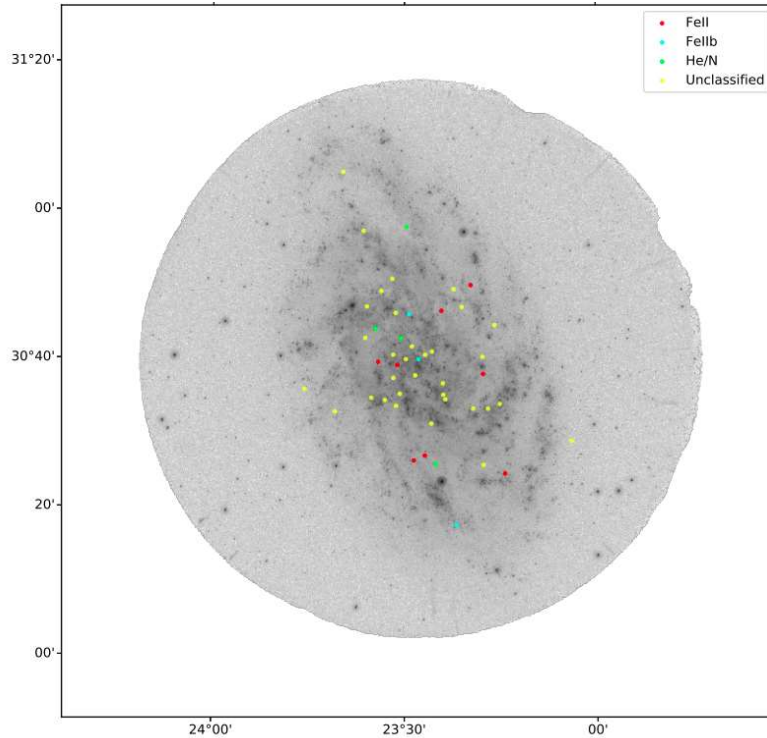


FIGURE 9.2: Classical novae in M33

Furthermore, building from the CN work presented in this thesis, I could explore the CN populations of galaxies other than M31. As discussed previously, different galaxies have different proportions of CN spectral classes, for example, M33 (shown in Fig. 9.2) has equal proportions of He/N and Fe II CNe, while M31 is 80 per cent Fe II and He N and hybrids making up for the remaining 20 per cent. As M33 does not have a classical bulge, exemplifying how the galaxy morphology and underlying populations may effect the CN spectral classes observed. [Shafter et al. \(2011a\)](#) also investigated the photometric properties of M31 CNe and found that the brighter, faster declining CNe tended to be of the He/N class. This photometric analysis could be extended to the CN sample in this thesis and compared to the NCR distributions to probe for any differences in these

populations. Furthermore, the NCR distributions of the M31 CNe in terms of the H α emission could be measured using data from the Local Group Galaxy Survey ([Massey et al., 2006](#)). Also the distributions of RNe could be measured and compared to the spectral classes as these are likely to have high mass WDs.

Appendix A

Appendix

A.1 Anderson-Darling test

I use the k-samples AD test in R to test the similarities between the various distributions presented in this thesis (see [Scholz & Stephens, 1987](#)). This differs from the ‘regular’ AD test where rather than testing a distribution against a known distribution (i.e. a normal distribution), tests two empirical distributions against each other. The AD statistic is calculated using:

$$D_{AD} = \frac{n-1}{n^2(k-1)} \sum_{i=1}^k \left[\frac{1}{n_i} \sum_{j=1}^L h_j \frac{(nF_{ij} - n_i H_j^2)}{H_j(n - H_j) - \frac{nh_j}{4}} \right], \quad (\text{A.1})$$

where h_j is the number of values in the combined samples equal to z_j which is the values of the data ordered from smallest to largest. H_j is the number of values in the combined samples which are less than z_j plus half the number of values in the combined samples equal to z_j . F_{ij} is the number of values in the i -th group which are less than z_j plus a half the number of values in the group equal to z_j . k is the number of groups (the samples) and n is the number of observations.

A.2 Isophotal radius code in Python

Routine to determine the semi-major axis of the isophote which goes through position (x,y), with (0,0) being the centre of the galaxy Input is table of semi-major axis radius

(r), ellipticity (b/a), and the sin and cos of the position angle of the ellipse Input 'n' is the number of items in that table (x,y) is the input position

```
import numpy as np
import matplotlib.pyplot as plt
from tqdm import tqdm

M31RA = 10.6847929
M31Dec = 41.2690650

kent_data = np.loadtxt('m31rlight.csv', delimiter = ',')
nova = np.loadtxt('PaperHeNdegs.csv', delimiter = ',')

r = kent_data[:,0]
ell = kent_data[:,1]
sinpa = np.sin((90-kent_data[:,2])*np.pi/180)
cospa = np.cos((90-kent_data[:,2])*np.pi/180)
n = len(kent_data)
x = (nova[:,0] - M31RA)* 60 * np.cos((nova[:,1])*np.pi/180)

itop = n
ibot = 0
vtop = -1.0
vbot = -1.0

radell = []
twistaxis = []

radius = np.sqrt(x**2 + y**2)

print(len(kent_data))
```

This loop finds the two isophotes that bound the position of the object It simply keeps dividing the interval in half until the boundaries are found

```
for m in tqdm(range(len(nova))):
```

```
    if radius[m] == 0:

twistaxis.append(0)

xp = y[m] * cospa - x[m] * sinpa
yp = (-x[m] * cospa) - (y[m] * sinpa)

slope = (yp/xp)**2

for i in range(len(kent_data)):

    if r[i] == 0:

        radell.append(0)

    if xp[i] == 0:
        radellipse = r[i] * (ell[i])
        radell.append(radellipse)
        radiellipse = r[i] * (ell[i]) * np.sqrt((slope[i] + 1.0)/(slope[i] + (ell[i])**2))
        radell.append(radiellipse)

    while (itop - ibot) > 1:

        k = (itop + ibot) / 2
        v = radell[int(k)]

        v_check = np.where(radius == v)[0]

    if len(v_check) != 0:

twistaxis.append(r[int(k-1)])
```

```
if v < radius[m]:

    ibot = k
    vbot = v

    if v > radius[m]:

        itop = k
        vtop = v

    if vbot < 0:

        vbot = radell[0]

    if vtop < 0:

        vtop = radell[-1]

    frac = (radius - vbot) / (vtop - vbot)

    t_axis = r[int(ibot-1)] + (frac * (r[int(itop-1)] - r[int(ibot-1)]))

    twistaxis.append(t_axis)

print(twistaxis)
```

A.3 The SNIIn hosts

In this appendix, I present the full set of SNIIn hosts from the survey presented in chapter 4.

A.3.1 Gold

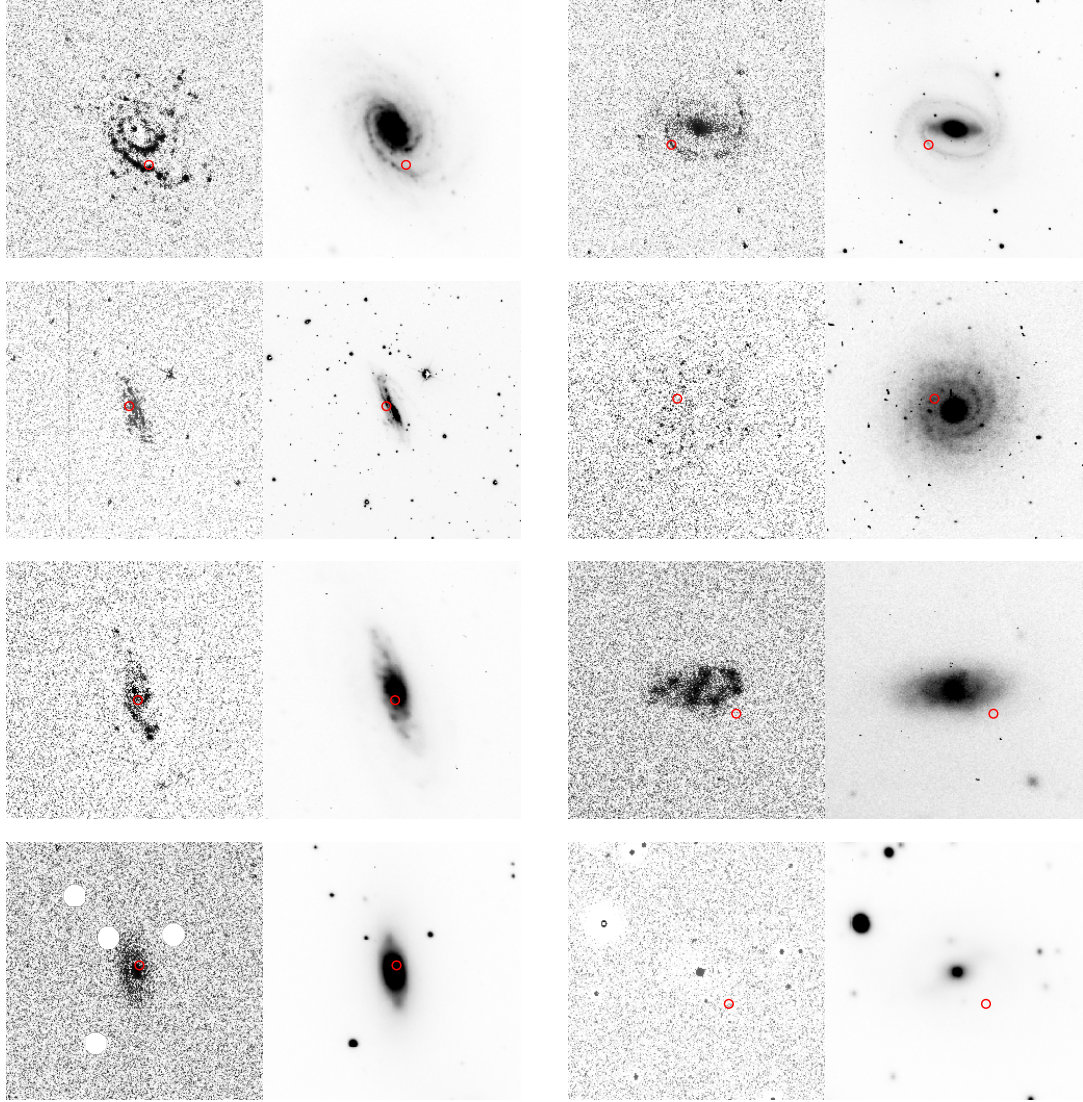


FIGURE A.1: Continuum-subtracted $H\alpha$ images (left panel of each sub-plot) and r' -band images (right panel of each sub-image). The SN positions are marked with a red circle. Reading left to right, the hosts of SN 2005db, SN 2005gl, SN 2010jj, SN 2003G, SN 2008J, SN 2000eo, SN 2006gy and SN 1989R are shown.

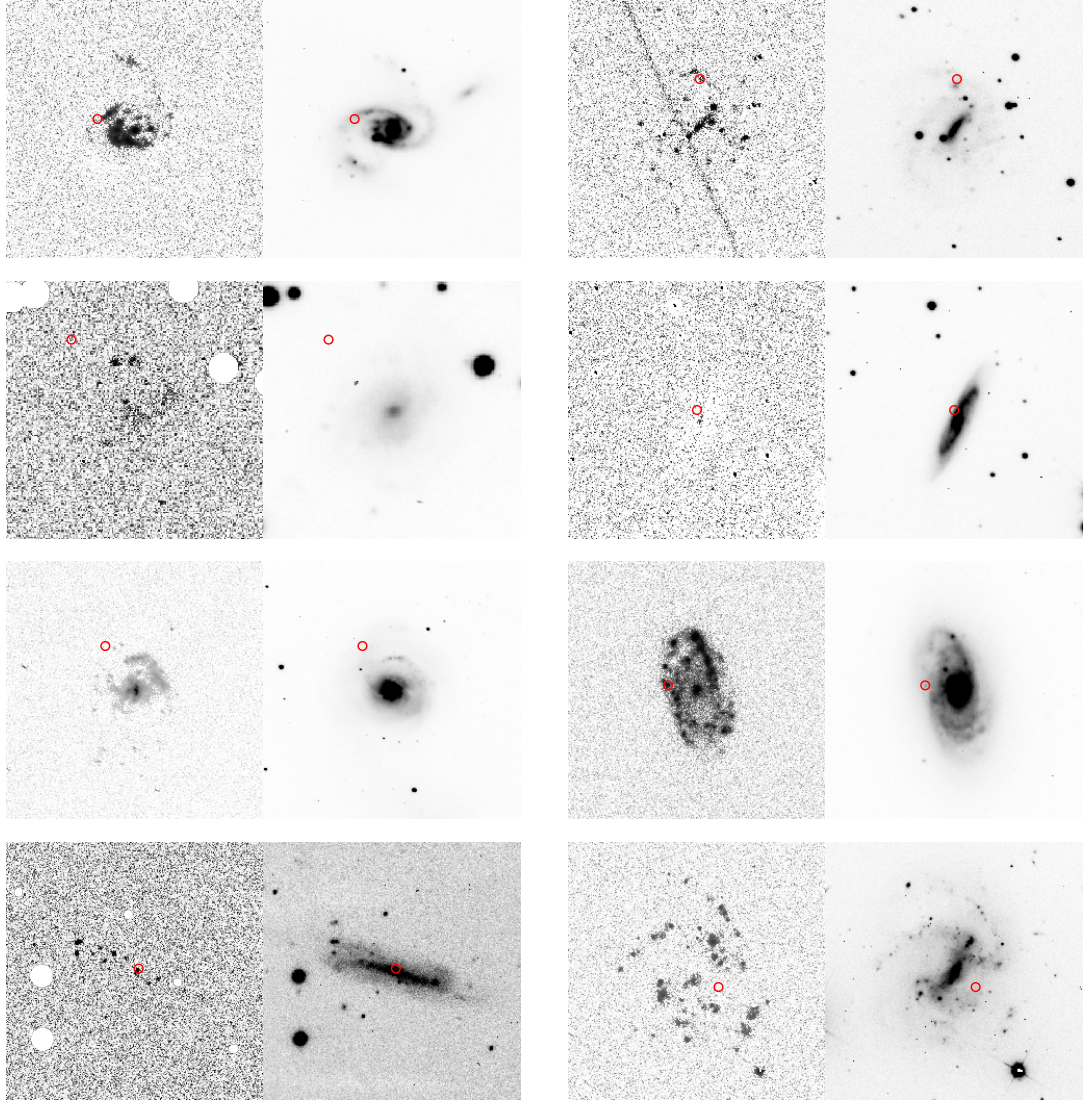


FIGURE A.2: Continuum-subtracted $H\alpha$ images (left panel of each sub-plot) and r' -band images (right panel of each sub-image). The SN positions are marked with a red circle. Reading left to right, the hosts of SN 1995G, SN 2006jd, SN 2009kn, SN 2005kj, SN 1994ak, SN 2005ip, SN 1989C and SN 2011ht are shown.

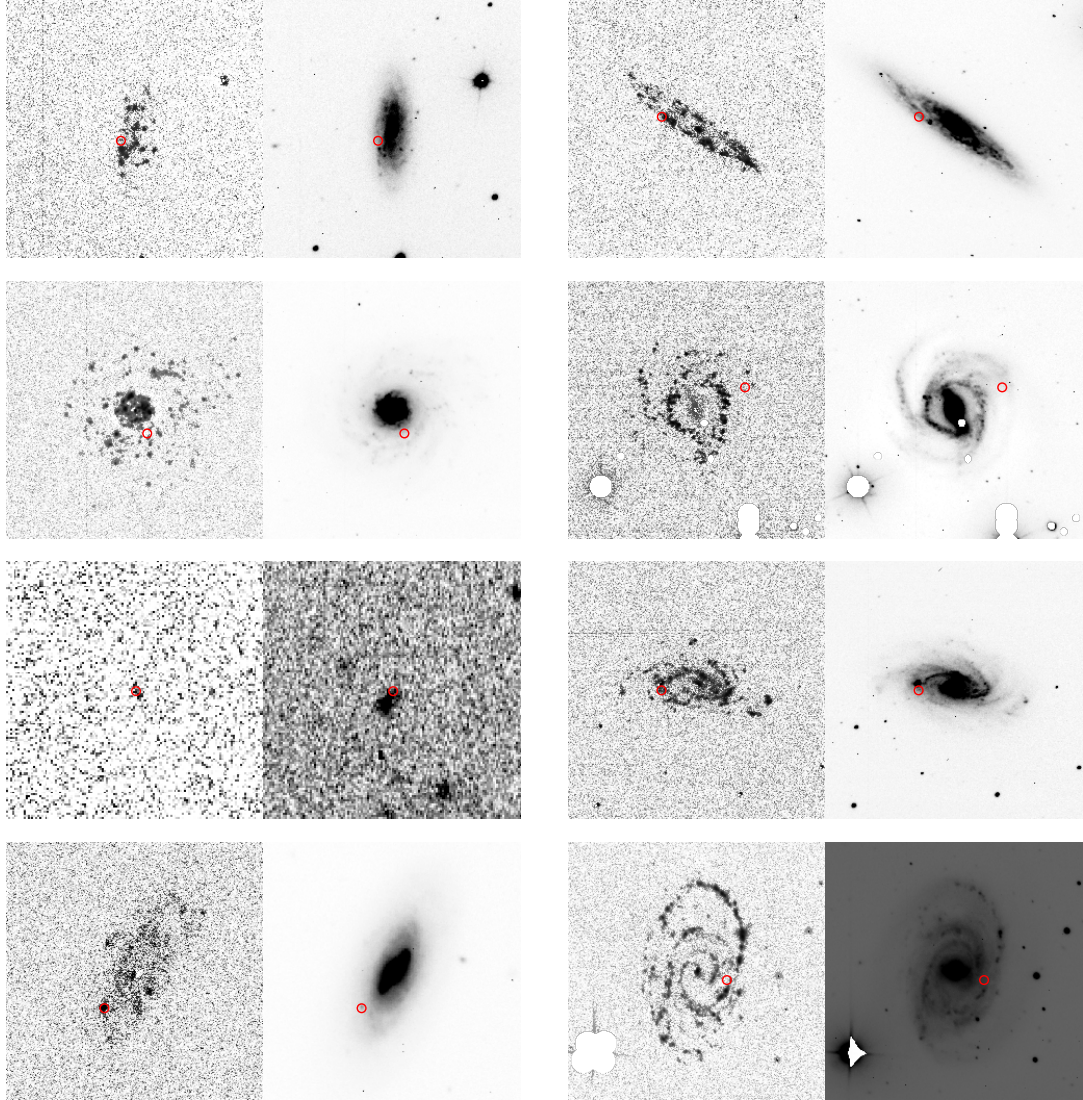


FIGURE A.3: Continuum-subtracted H α images (left panel of each sub-plot) and r' -band images (right panel of each sub-image). The SN positions are marked with a red circle. Reading left to right, the hosts of SN 1993N, SN 1998S, SN 1994W, SN 2011A, SN 2016bdu, SN 1997eg, SN 2015da, SN 1994Y are shown.

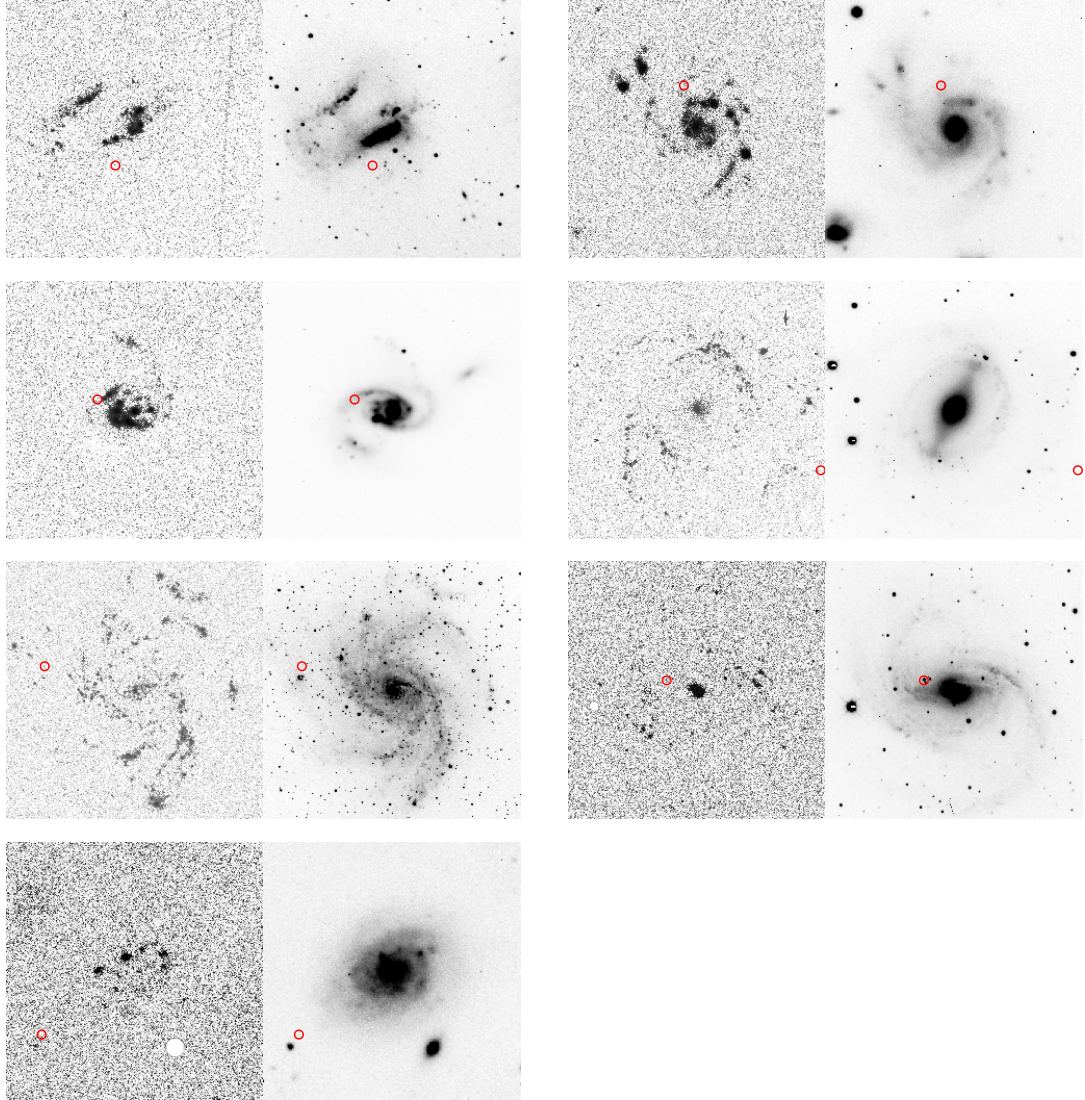


FIGURE A.4: Continuum-subtracted $H\alpha$ images (left panel of each sub-plot) and r' -band images (right panel of each sub-image). The SN positions are marked with a red circle. Reading left to right, the hosts of SN 1995N, SN 2008B, SN 1995G, SN 1987B, SN 2008S, SN 1999el, SN 2009ip are shown.

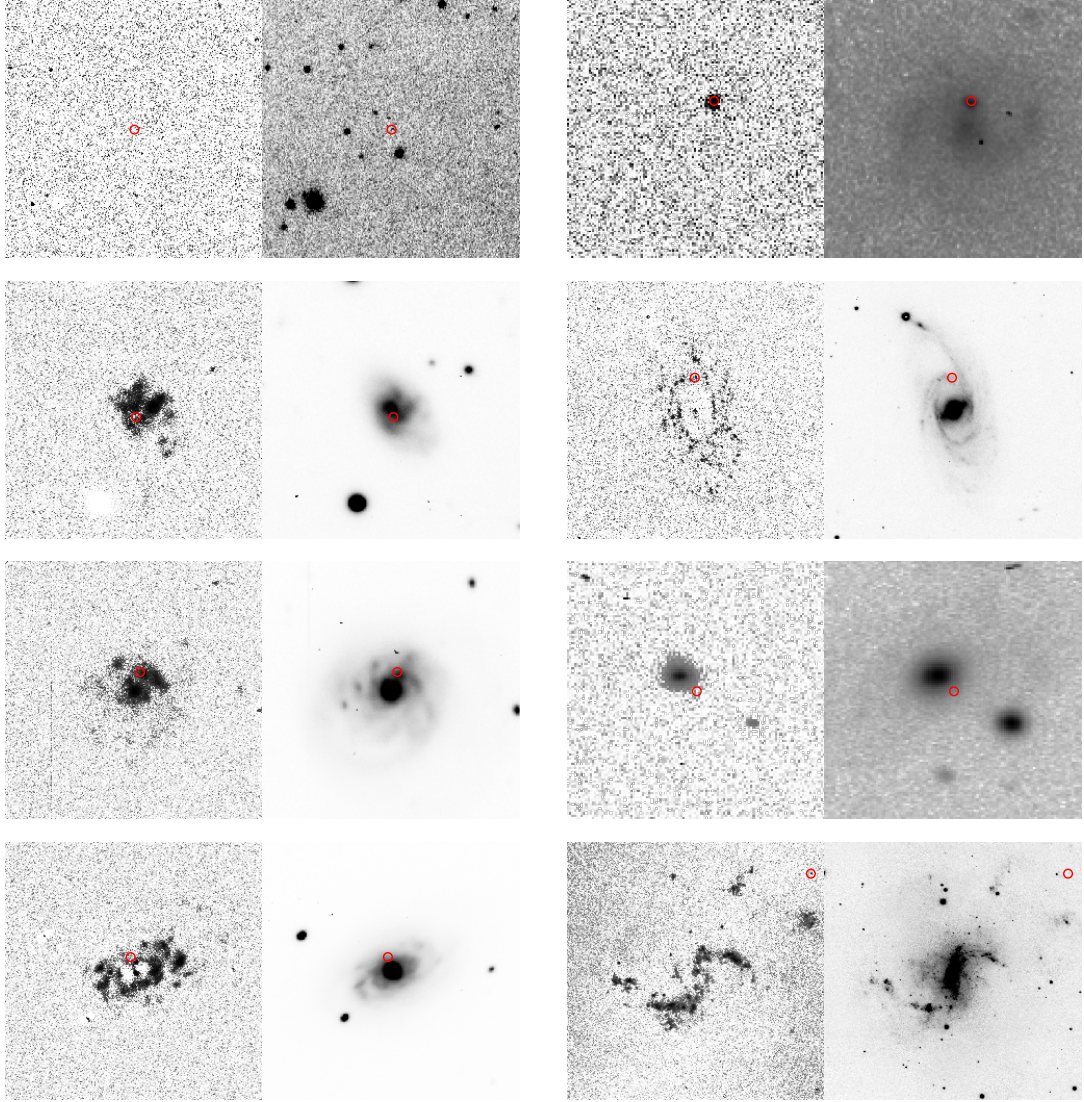


FIGURE A.5: Continuum-subtracted $H\alpha$ images (left panel of each sub-plot) and r' -band images (right panel of each sub-image). The SN positions are marked with a red circle. Reading left to right, the hosts of SN 2019el, SN 2017hcc, SN 2011fx, PTF 11iqb, SN 2007pk, SN 2016eem, are shown.

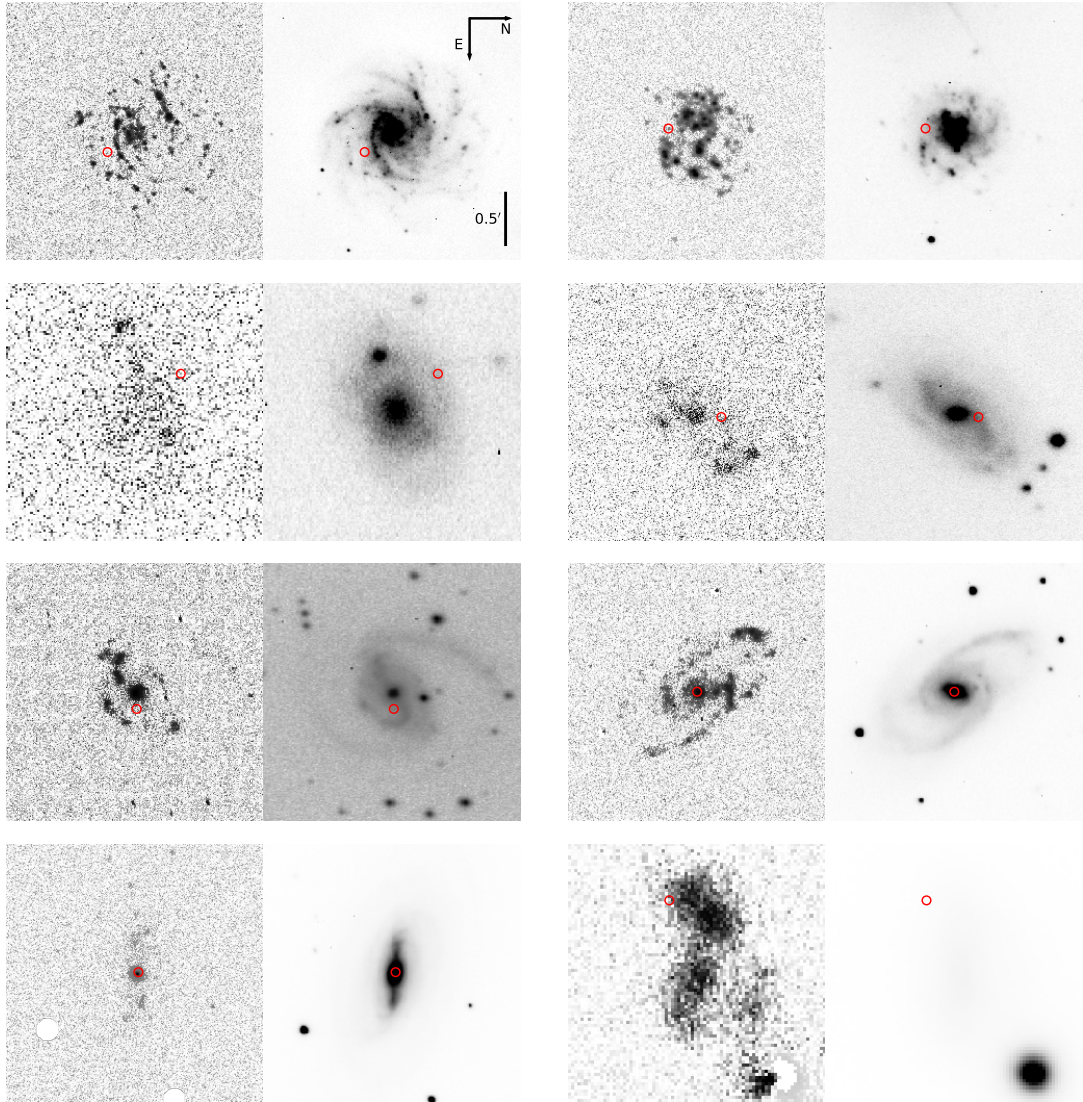


FIGURE A.6: Continuum-subtracted $H\alpha$ images (left panel of each sub-plot) and r' -band images (right panel of each sub-image). The SN positions are marked with a red circle. Reading left to right, the hosts of SN 2003lo, SN 2005aq, SN Gaia14ahl, SN 2005ma, SN 2016hgf, SN 2019rz, AT 2018lkg and AT 2014eu are shown.

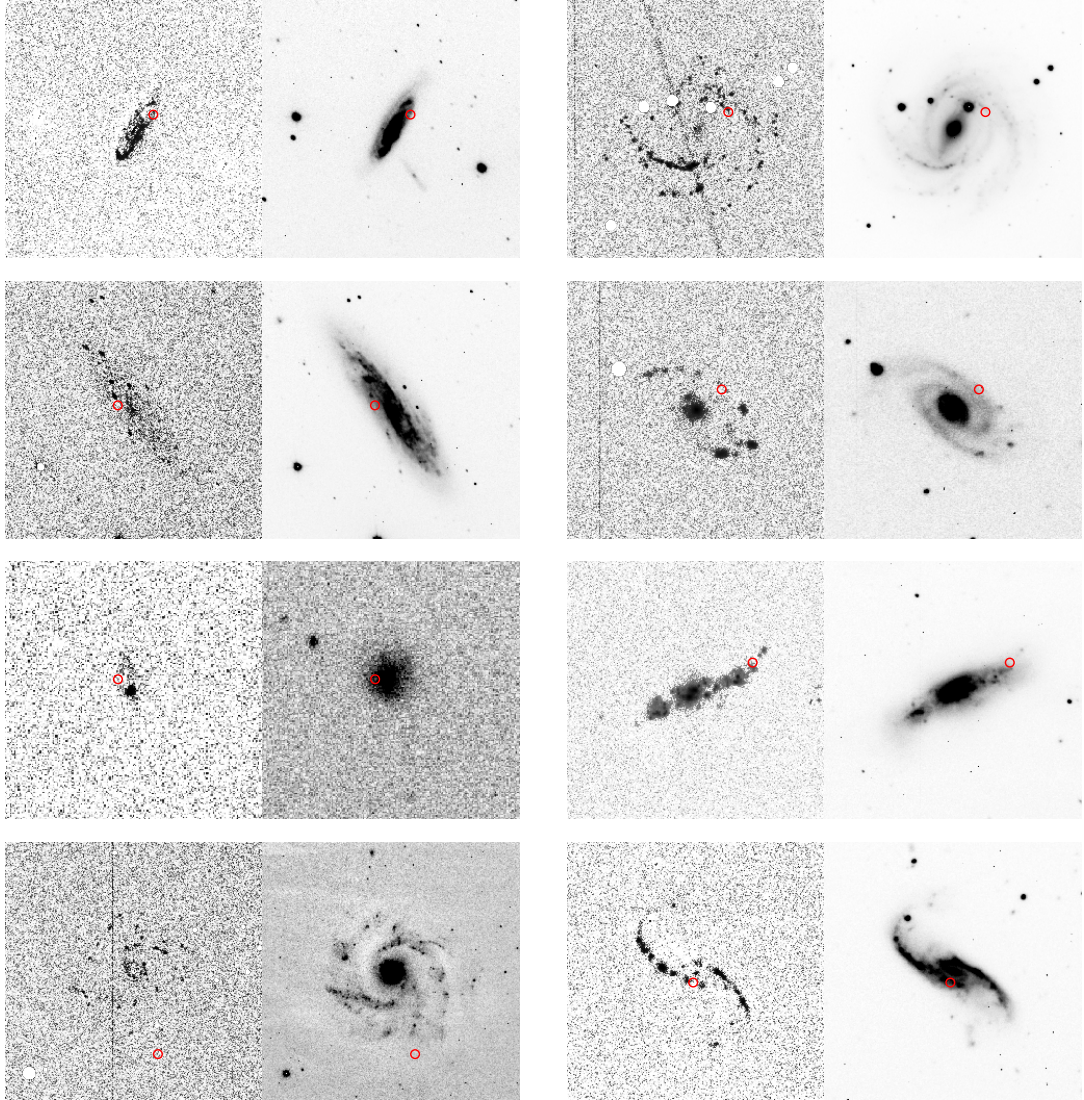


FIGURE A.7: Continuum-subtracted H α images (left panel of each sub-plot) and r' -band images (right panel of each sub-image). The SN positions are marked with a red circle. Reading left to right, the hosts of SN 2014ee, SN 2002fj, SN 2015bh, SN 2014es, SN 1997ab, SN 2014G, SN 1996bu and SN 1987F are shown.

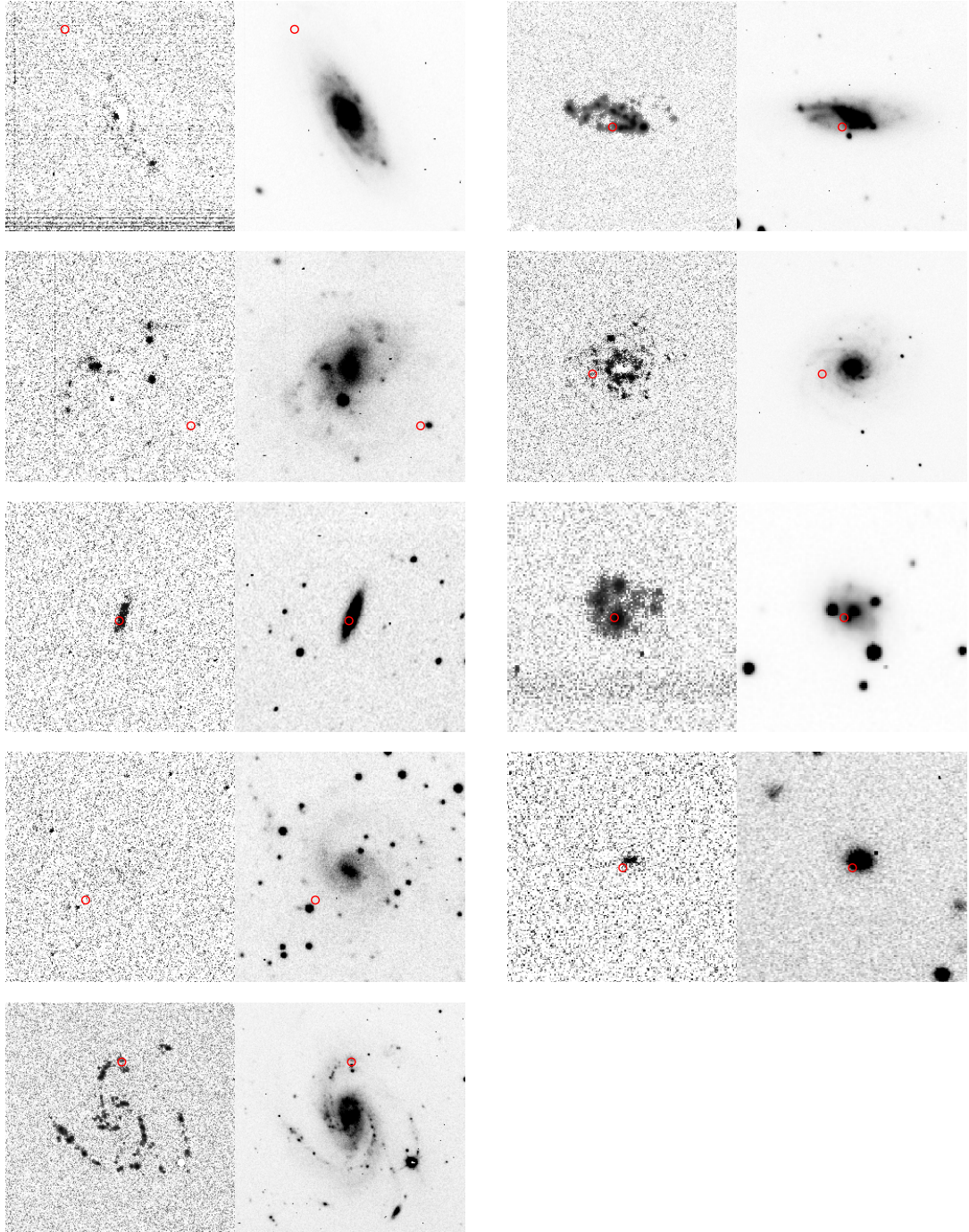


FIGURE A.8: Continuum-subtracted $H\alpha$ images (left panel of each sub-plot) and r' -band images (right panel of each sub-image). The SN positions are marked with a red circle. Reading left to right, the hosts of SN 2008ip, SN 2006am, SN 2003dv, SN 2015bf, SN 2016bly, SN 2017gas, SN 2006bo, SN 2018hpb and SN 2013fs are shown.

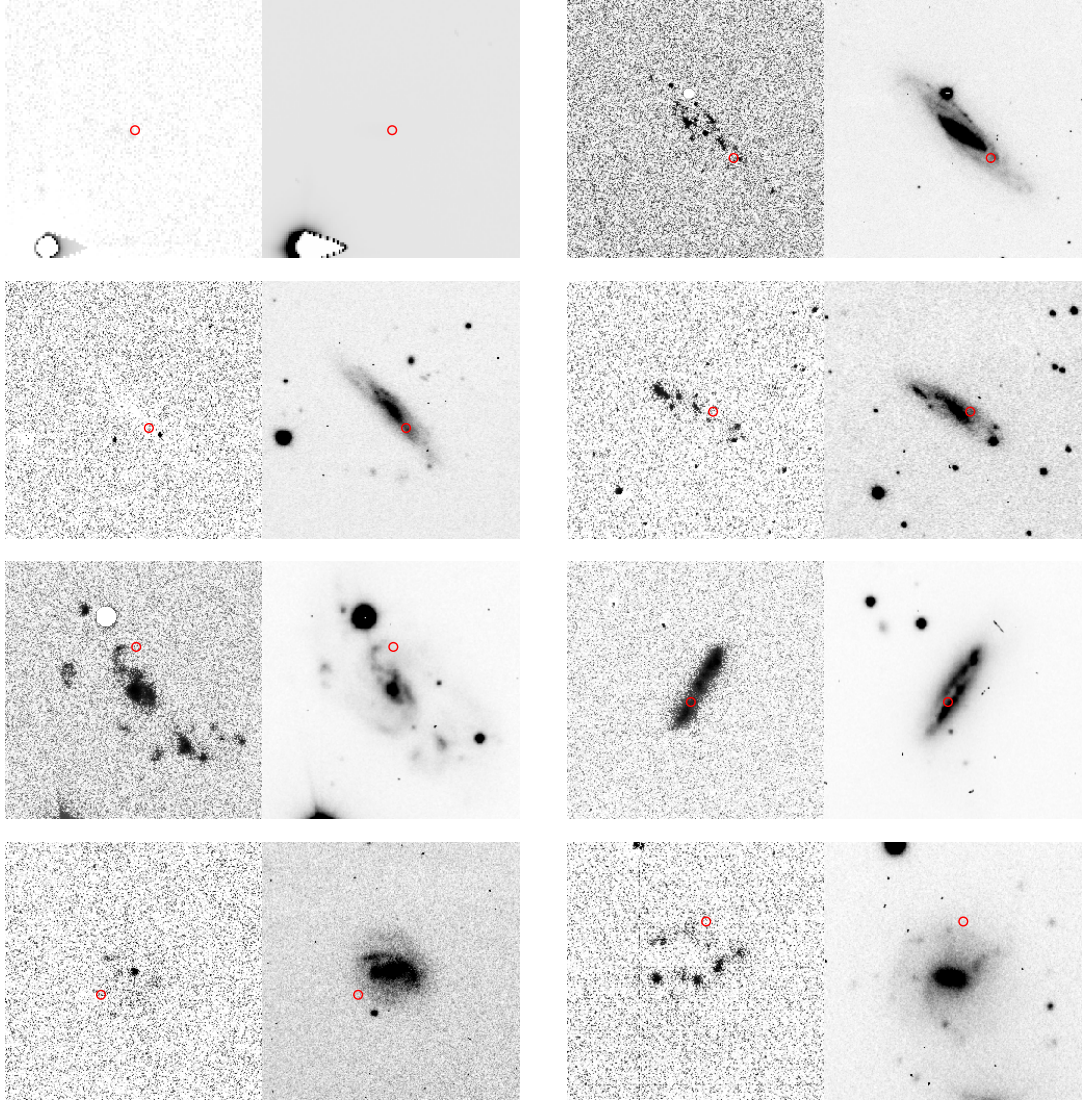


FIGURE A.9: Continuum-subtracted $H\alpha$ images (left panel of each sub-plot) and r' -band images (right panel of each sub-image). The SN positions are marked with a red circle. Reading left to right, the hosts of PS15cwt, SN 2011js, SN 2006qt, SN 2005kd, SN 2007ak, SN 2013ha, SN 1987C and SN 2016ehw are shown.

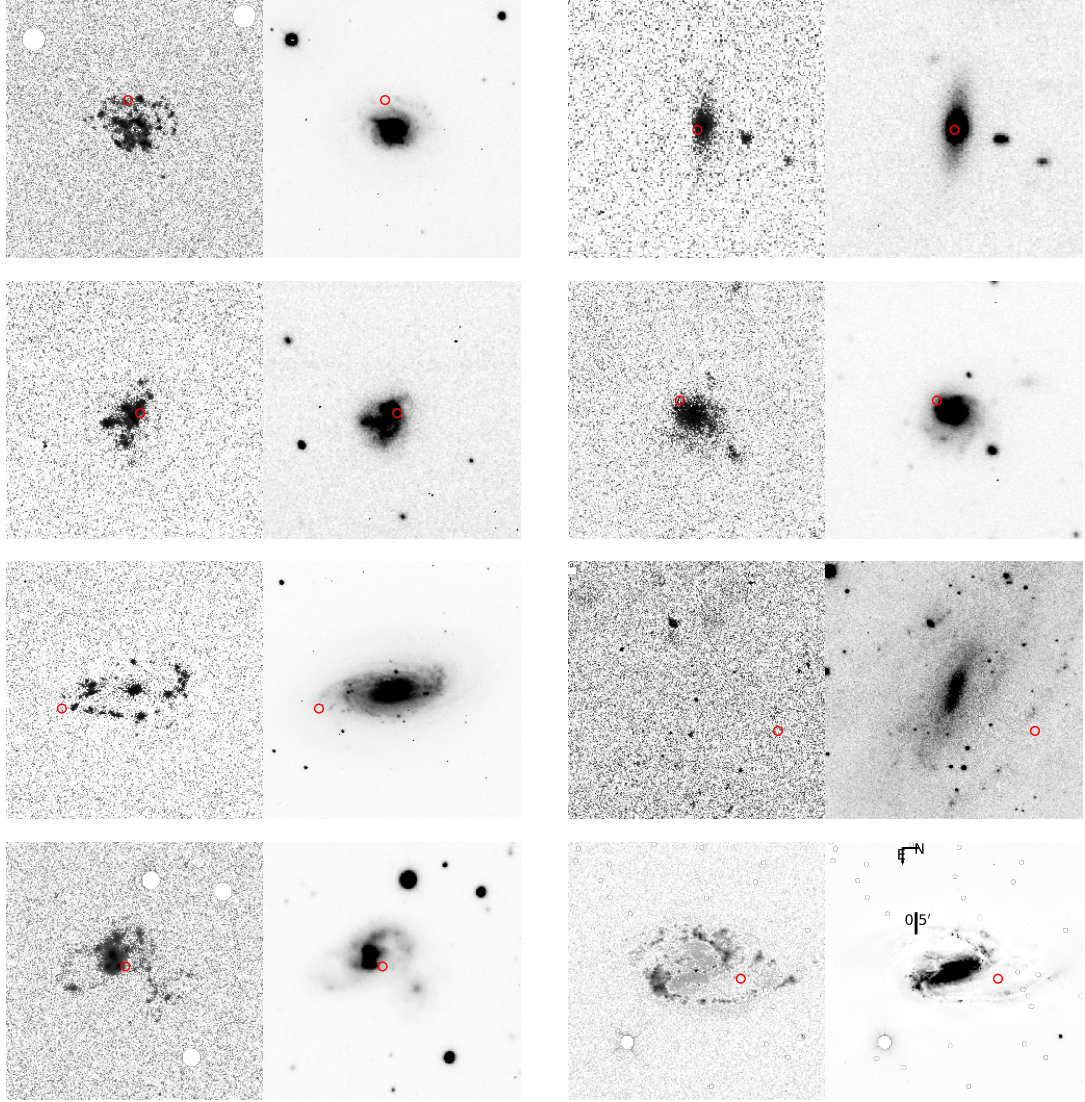


FIGURE A.10: Continuum-subtracted $H\alpha$ images (left panel of each sub-plot) and r' -band images (right panel of each sub-image). The SN positions are marked with a red circle. Reading left to right, the hosts of ASASSN-15lf, SN 2012ab, PS15aip, SN 2006M, SNhunt248, SN 1978G, SN 2006dn and SN 1997bs are shown.

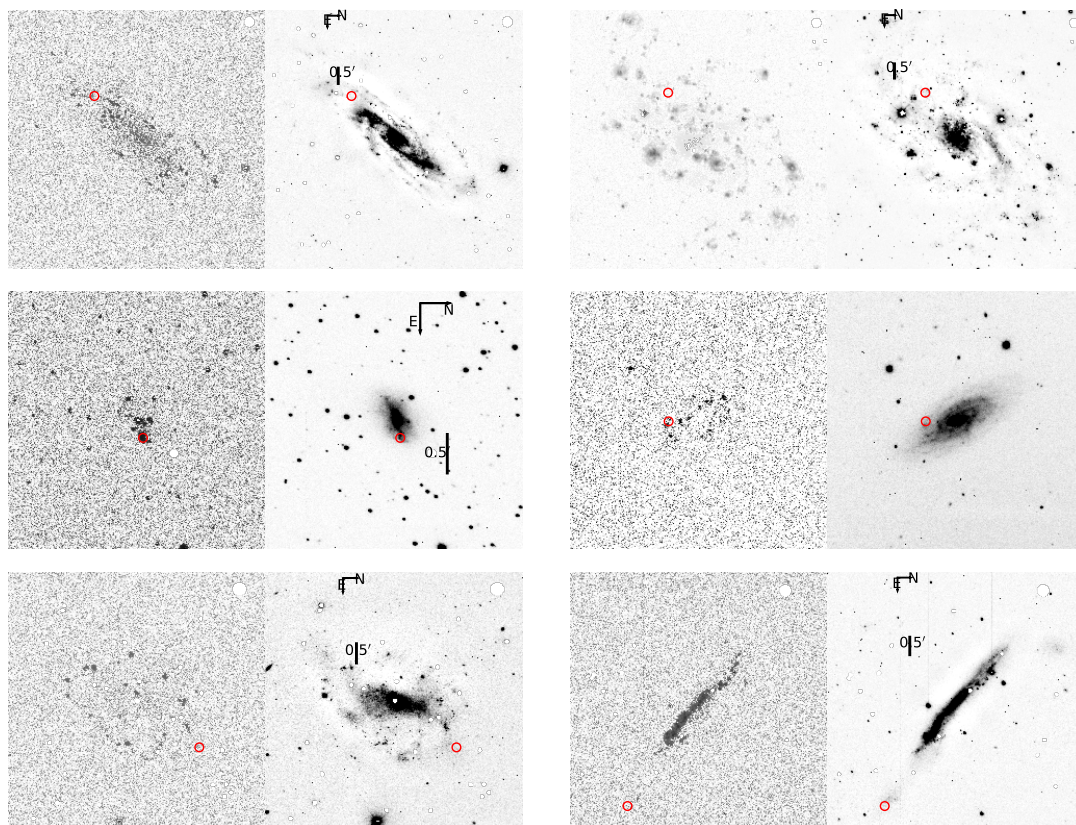


FIGURE A.11: Continuum-subtracted H α images (left panel of each sub-plot) and r' -band images (right panel of each sub-image). The SN positions are marked with a red circle. Reading left to right, the hosts of SN 1999bw, SN 2002kg, SN 2006fp, SN 2006bv, SN 2002bu and SN 2000ch are shown.

A.4 Classical nova spectra

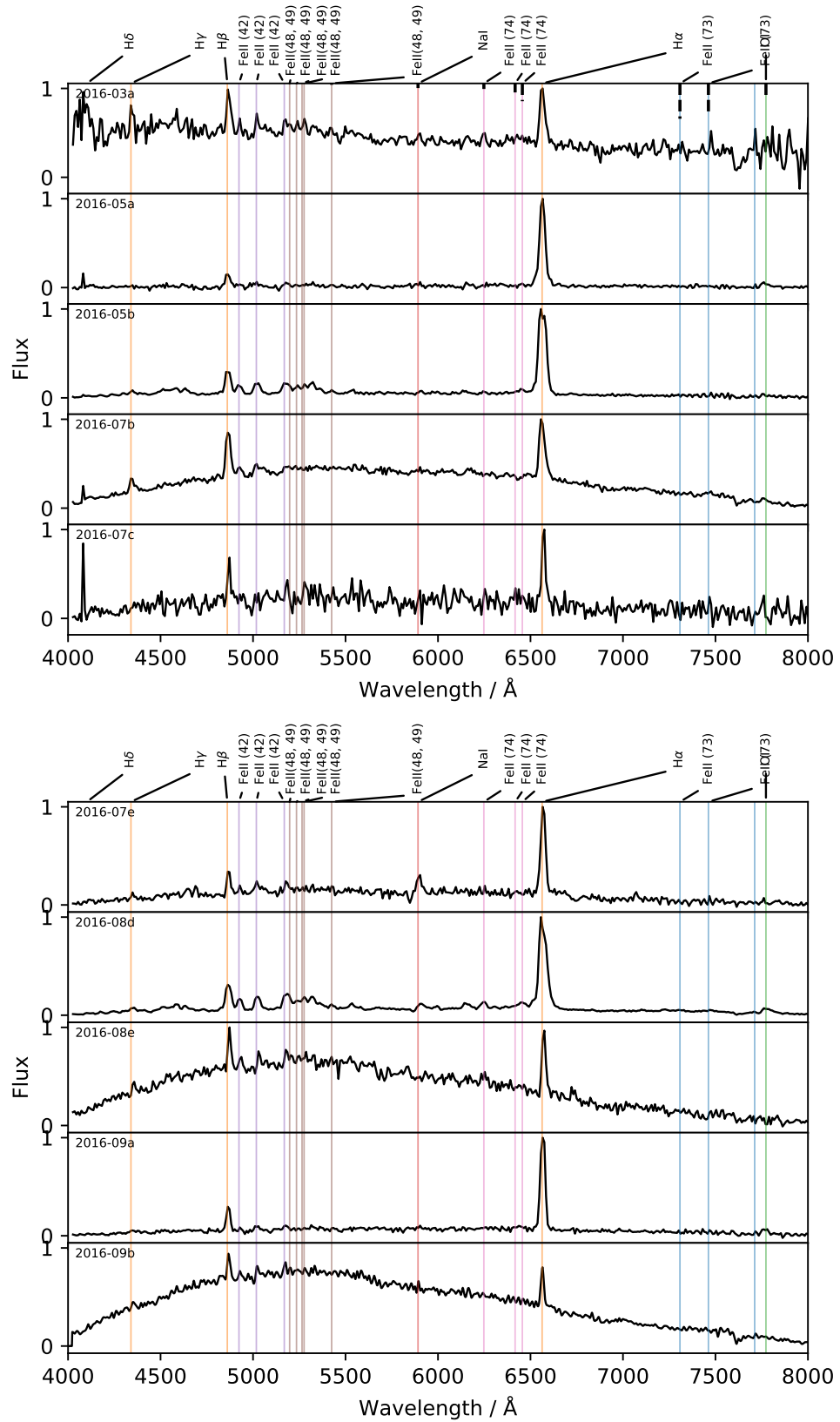


FIGURE A.13: Spectra of FeII CNe 11-20 with notable lines marked.

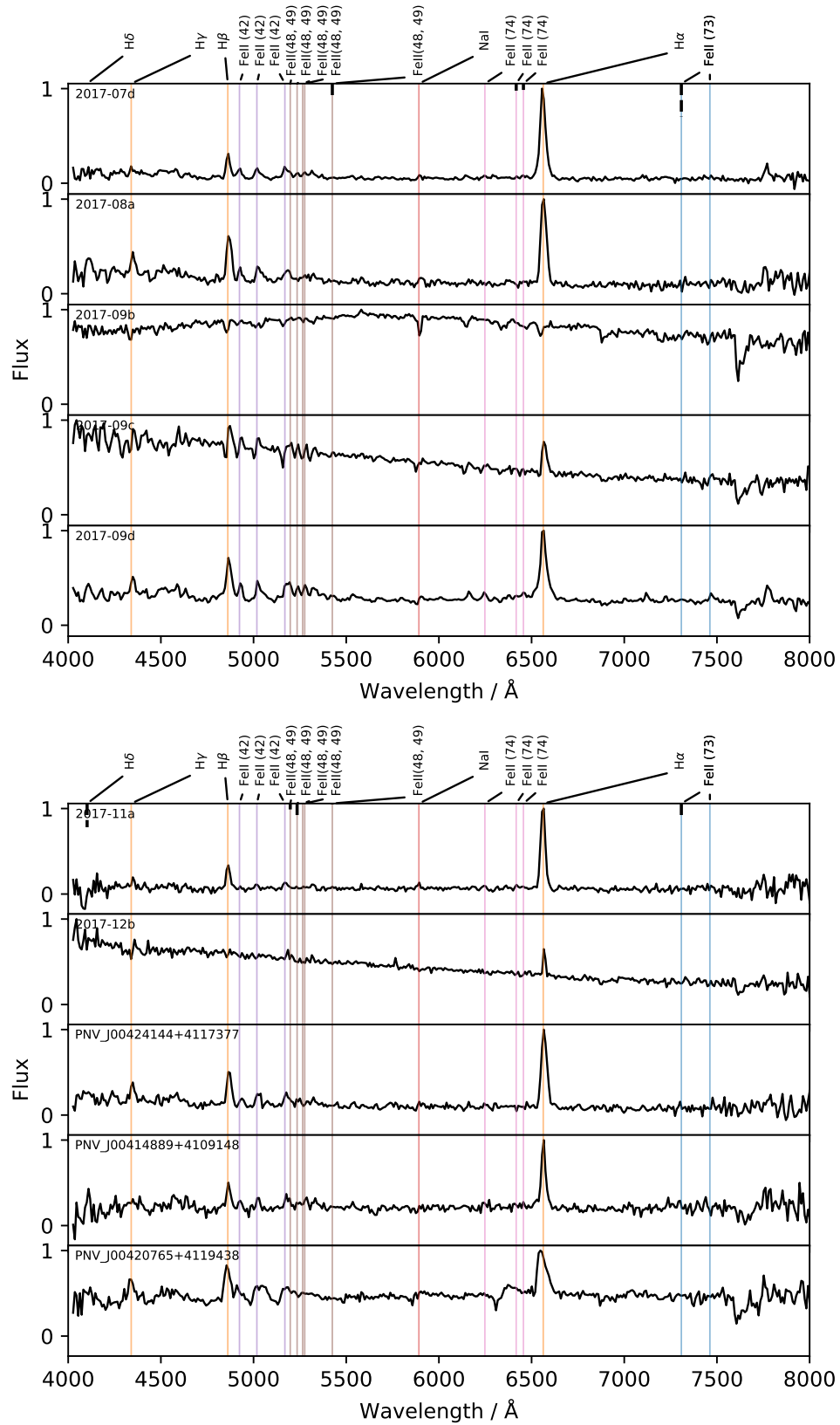


FIGURE A.15: Spectra of FeII CNe 31-40 with notable lines marked.

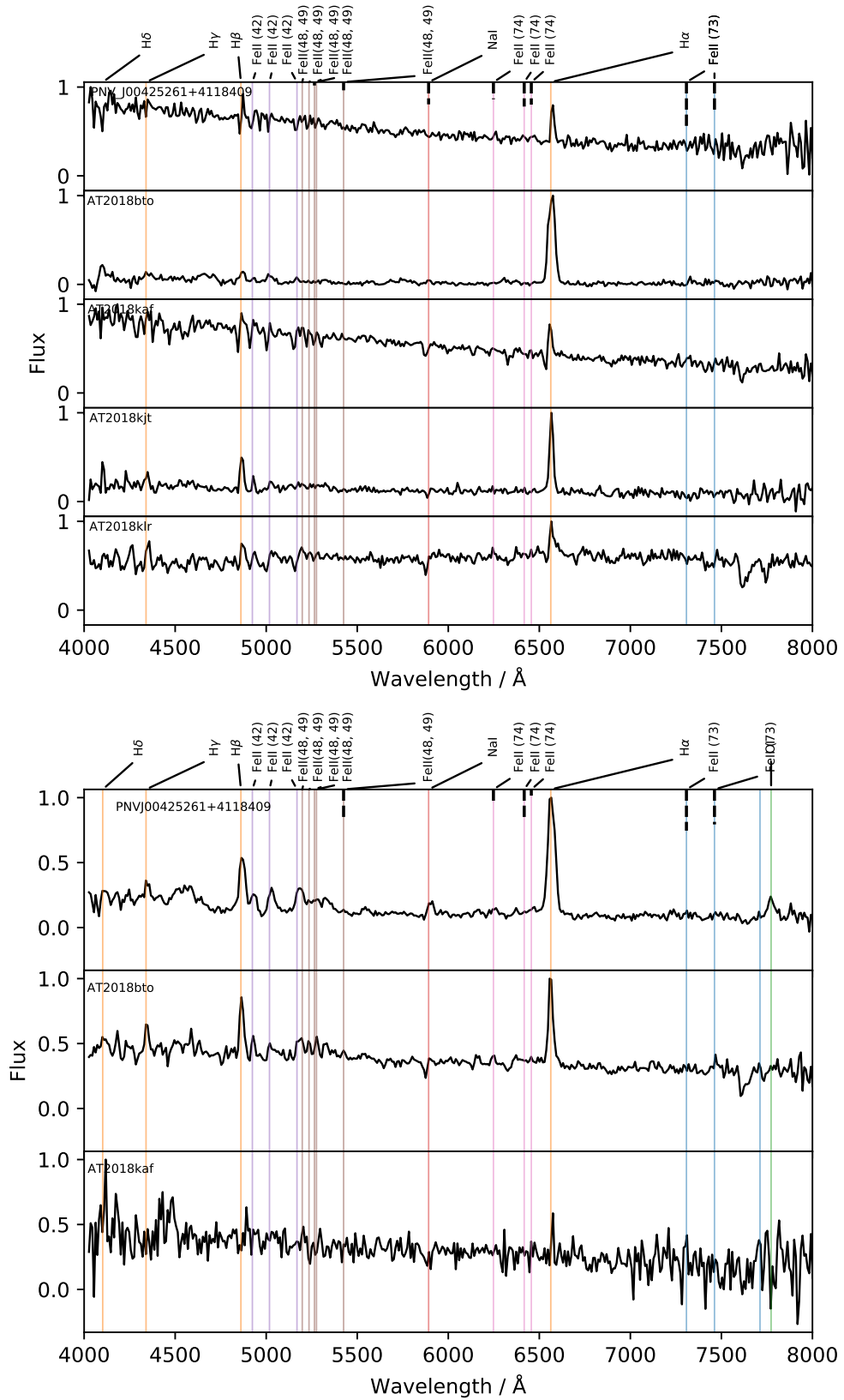


FIGURE A.16: Spectra of FeII CNe 41-49 with notable lines marked.

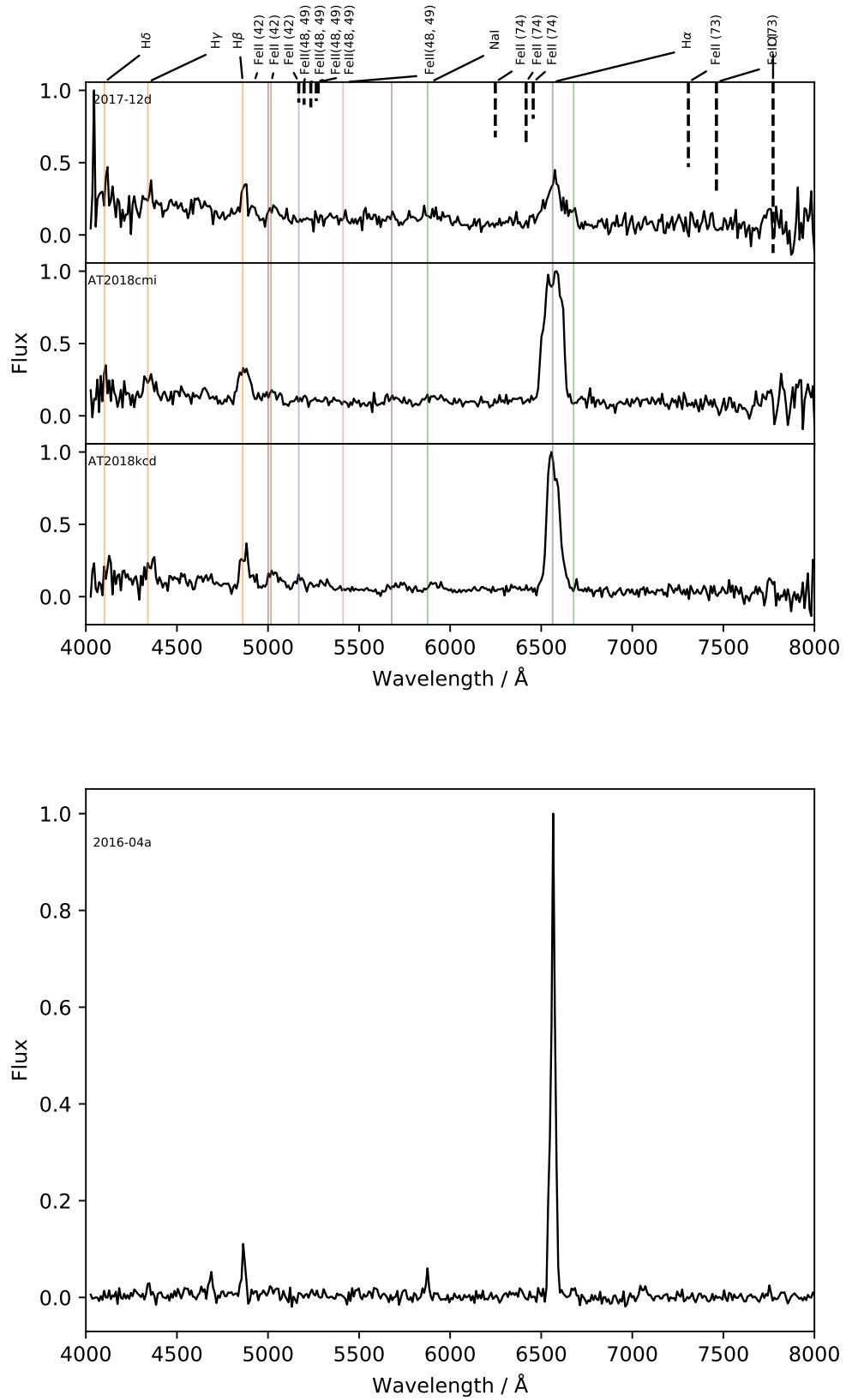


FIGURE A.18: Spectra of HeN CNe 4-6 with notable lines marked and the single HeNn CN.

Bibliography

- Abbott B. P., et al., 2017, [ApJL](#), **848**, L12
- Adams S. M., Kochanek C. S., Prieto J. L., Dai X., Shappee B. J., Stanek K. Z., 2016, [MNRAS](#), **460**, 1645
- Aghakhanloo M., Murphy J. W., Smith N., Hložek R., 2017, [MNRAS](#), **472**, 591
- Akashi M., Kashi A., 2020, [MNRAS](#), **494**, 3186
- Aldering G., Humphreys R. M., Richmond M., 1994, [AJ](#), **107**, 662
- Anderson T. W., Darling D. A., 1952, [The Annals of Mathematical Statistics](#), **23**, 193
- Anderson J. P., James P. A., 2008, [MNRAS](#), **390**, 1527
- Anderson J. P., James P. A., 2009, [MNRAS](#), **399**, 559
- Anderson J. P., Habergham S. M., James P. A., Hamuy M., 2012, [MNRAS](#), **424**, 1372
- Anderson J. P., et al., 2014, [ApJ](#), **786**, 67
- Andrews J. E., et al., 2021, [ApJ](#), **917**, 63
- Angus C. R., Levan A. J., Perley D. A., Tanvir N. R., Lyman J. D., Stanway E. R., Fruchter A. S., 2016, [MNRAS](#), **458**, 84
- Arbour R., 2008, Central Bureau Electronic Telegrams, **1235**, 2
- Aretxaga I., Benetti S., Terlevich R. J., Fabian A. C., Cappellaro E., Turatto M., Della Valle M., 1999, [MNRAS](#), **309**, 343
- Arnett W. D., 1980, [ApJ](#), **237**, 541
- Arnett W. D., Bahcall J. N., Kirshner R. P., Woosley S. E., 1989, [ARA&A](#), **27**, 629
- Arnould M., 1976, [A&A](#), **46**, 117

- Arp H. C., 1956a, [AJ](#), **61**, 15
- Arp H. C., 1956b, [AJ](#), **61**, 15
- Ayani K., Kawabata T., Yamaoka H., 2002, *IAU Circ.*, [7864](#), 4
- Aydi E., et al., 2017, [MNRAS](#), **474**, 2679
- Baade W., 1943, [ApJ](#), **97**, 119
- Baade W., Zwicky F., 1934, [Physical Review](#), **46**, 76
- Baily F., 1845, *The Catalogue of Stars of the British Association for the Advancement of Science*. London
- Banerjee D. P. K., et al., 2020, [ApJL](#), **904**, L23
- Barbon R., Ciatti F., Rosino L., 1979, *A&A*, **72**, 287
- Barnsley R. M., Jermak H. E., Steele I. A., Smith R. J., Bates S. D., Mottram C. J., 2016, [Journal of Astronomical Telescopes, Instruments, and Systems](#), **2**, 015002
- Barsukova E. A., Valeev A. F., Sholukhova O., Fabrika S., Hornoch K., Pietsch W., Goranskij V. P., 2010, *The Astronomer's Telegram*, [2789](#), 1
- Barsukova E. A., et al., 2014, *The Astronomer's Telegram*, [6498](#), 1
- Barsukova E. A., Valeev A. F., Goranskij V. P., Henze M., Shafter A. W., Hornoch K., 2017, *The Astronomer's Telegram*, [10596](#), 1
- Bartunov O. S., Tsvetkov D. Y., Filimonova I. V., 1994, [PASP](#), **106**, 1276
- Bellm E. C., et al., 2019, [PASP](#), **131**, 018002
- Benetti S., 2000, *Mem. Soc. Astron. Italiana*, **71**, 323
- Benetti S., Zwitter T., 1996, *IAU Circ.*, [6410](#), 1
- Benetti S., Cappellaro E., Danziger I. J., Turatto M., Patat F., Della Valle M., 1998, [MNRAS](#), **294**, 448
- Benetti S., et al., 2002, *IAU Circ.*, [7789](#), 2
- Benvenuti P., Maccheto F., Schreier E. J., 1996, *Science with the Hubble Space Telescope*—II
- Berger E., et al., 2009a, [ApJ](#), **699**, 1850

- Berger E., Foley R., Ivans I., 2009b, *The Astronomer's Telegram*, [2184](#), 1
- Bersier D., Smartt S., Yaron O., 2016, *Transient Name Server Classification Report*, [2016-650](#), 1
- Bianchini A., Friedjung M., Brinkmann W., 1992, *A&A*, [257](#), 599
- Bildsten L., Shen K. J., Weinberg N. N., Nelemans G., 2007, *ApJL*, [662](#), L95
- Blaña Díaz M., Wegg C., Gerhard O., Erwin P., Portail M., Opitsch M., Saglia R., Bender R., 2017, *MNRAS*, [466](#), 4279
- Blagorodnova N., et al., 2020, *MNRAS*, [496](#), 5503
- Blanc N., et al., 2005a, *The Astronomer's Telegram*, [570](#), 1
- Blanc N., et al., 2005b, *The Astronomer's Telegram*, [630](#), 1
- Blanc N., et al., 2005c, *The Astronomer's Telegram*, [630](#), 1
- Blondin S., Tonry J. L., 2007, *ApJ*, [666](#), 1024
- Blondin S., Modjaz M., Kirshner R., Challis P., Brown W., 2006a, *Central Bureau Electronic Telegrams*, [494](#), 1
- Blondin S., Masters K., Modjaz M., Kirshner R., Challis P., Matheson T., Berlind P., 2006b, *Central Bureau Electronic Telegrams*, [636](#), 1
- Blondin S., Modjaz M., Kirshner R., Challis P., Matheson T., Mamajek E., 2006c, *Central Bureau Electronic Telegrams*, [679](#), 1
- Blondin S., Modjaz M., Kirshner R., Challis P., Berlind P., 2006d, *IAU Circ.*, [8680](#), 2
- Blondin S., Calkins M., Ayani K., Yamaoka H., 2008, *Central Bureau Electronic Telegrams*, [1201](#), 1
- Blondin S., Dessart L., Hillier D. J., 2018, *MNRAS*, [474](#), 3931
- Bode M. F., Evans A., 2008, *Classical Novae*, 2nd Edition. Edited by M.F. Bode and A. Evans. Cambridge Astrophysics Series, No. 43, Cambridge: Cambridge University Press, 2008.
- Boian I., Groh J. H., 2018, *Astronomy & Astrophysics*, 617, A115
- Boian I., Groh J. H., 2020, *MNRAS*, [496](#), 1325

- Bond H. E., Bedin L. R., Bonanos A. Z., Humphreys R. M., Monard L. A. G. B., Prieto J. L., Walter F. M., 2009, *ApJL*, 695, L154
- Bonnaud C., et al., 2005, Central Bureau Electronic Telegrams, 296, 1
- Bose S., Dong S., Sun F., Prieto J. L., Stanek K. Z., 2017, The Astronomer's Telegram, 10669, 1
- Bose S., Dong S., Chen P., Rupert J., Stanek K. Z., Stritzinger M., 2018, Transient Name Server Classification Report, 2018-1770, 1
- Bostroem K. A., et al., 2019, *MNRAS*, 485, 5120–5141
- Botticella M. T., et al., 2009, *MNRAS*, 398, 1041
- Boyle W. S., Smith G. E., 1970, *The Bell System Technical Journal*, 49, 587
- Bradley L., et al., 2022, astropy/photutils:, doi:10.5281/zenodo.6385735, <https://doi.org/10.5281/zenodo.6385735>
- Branch D., Wheeler J. C., 2017, Supernova Explosions, doi:10.1007/978-3-662-55054-0.
- Branch D., et al., 2002, *ApJ*, 566, 1005
- Brennan S. J., et al., 2022a, *MNRAS*, 513, 5642
- Brennan S. J., et al., 2022b, *MNRAS*, 513, 5666
- Brown T. M., et al., 2013, *PASP*, 125, 1031
- Bruch R. J., et al., 2021, *ApJ*, 912, 46
- Bufano F., et al., 2018, The Astronomer's Telegram, 11135, 1
- Bullivant C., et al., 2018, *MNRAS*, 476, 1497
- Burrows A., 1990, *Annual Review of Nuclear and Particle Science*, 40, 181
- Burrows C. J., et al., 1995, *ApJ*, 452, 680
- Cai Y. Z., et al., 2021, *A&A*, 654, A157
- Cao Y., Kasliwal M. M., 2012, The Astronomer's Telegram, 4216, 1
- Cao Y., Kasliwal M. M., 2013, The Astronomer's Telegram, 5173, 1
- Cao Y., Miller A., 2014, The Astronomer's Telegram, 6411, 1

- Cao L., Qiu Y. L., Qiao Q. Y., Hu J. Y., Li W., Filippenko A., 1999, *IAU Circ.*, [7288](#), 1
- Cao Y., Ben-Ami S., Polishook D., Sternberg A., Arcavi I., Gal-Yam A., Kasliwal M. M., 2011a, *The Astronomer's Telegram*, [3497](#), 1
- Cao Y., Quimby R., Ben-Ami S., Sternberg A., Arcavi I., Gal-Yam A., Kasliwal M. M., 2011b, *The Astronomer's Telegram*, [3498](#), 1
- Cao Y., Levitan D., Xu D., Groot I. A. P., Kasliwal M. M., 2011c, *The Astronomer's Telegram*, [3533](#), 1
- Cao Y., Kasliwal M. M., Mooley K., Arcavi I., Polishook D., 2011d, *The Astronomer's Telegram*, [3649](#), 1
- Cao Y., Kasliwal M. M., Sesar B., Ben-Ami S., Xu D., 2011e, *The Astronomer's Telegram*, [3666](#), 1
- Cao Y., Kasliwal M. M., Yaron O., 2011f, *The Astronomer's Telegram*, [3701](#), 1
- Cao Y., et al., 2012a, *The Astrophysical Journal*, 752, 133
- Cao Y., Sesar B., Kasliwal M. M., 2012b, *The Astronomer's Telegram*, [4127](#), 1
- Cao Y., et al., 2012c, *The Astronomer's Telegram*, [4193](#), 1
- Cao Y., Kasliwal M. M., Maguire K., Sullivan M., Sesar B., Whi C. J., 2012d, *The Astronomer's Telegram*, [4270](#), 1
- Cao Y., Kasliwal M. M., Levitan D., Yaron O., 2012e, *The Astronomer's Telegram*, [4291](#), 1
- Cao Y., et al., 2013a, *The Astrophysical Journal*, 775, L7
- Cao Y., Mooley K., Vreeswijk P., De Cia A., Yaron O., Kasliwal M. M., 2013b, *The Astronomer's Telegram*, [4835](#), 1
- Cao Y., Kulkarni S. R., Yaron O., De Cia A., Arcavi I., Kasliwal M. M., 2013c, *The Astronomer's Telegram*, [5123](#), 1
- Cao Y., Tang S., Kasliwal M. M., Cenko S. B., Clubb K. I., 2013d, *The Astronomer's Telegram*, [5260](#), 1
- Capaccioli M., Della Valle M., D'Onofrio M., Rosino L., 1989, *AJ*, 97, 1622
- Carey G., 2019, *Transient Name Server Discovery Report*, [2019-151](#), 1

- Cartier R., Terreran G., Margutti R., Blanchard P., Espinoza J., Ugarte P., 2018, The Astronomer's Telegram, [12080](#), 1
- Challis P., Calkins M., 2009, Central Bureau Electronic Telegrams, [1649](#), 1
- Challis P., Kirshner R., Smith N., 2010, Central Bureau Electronic Telegrams, [2548](#), 1
- Chandrasekhar S., 1931, [The Astrophysical Journal](#), 74, 81
- Chapman J. M., Norris R. P., Reynolds J. E., te Lintel Hekkert P., 1992, IAU Circ., [5616](#), 2
- Chatzopoulos E., Wheeler J. C., Vinko J., 2012, [ApJ](#), 746, 121
- Chevalier R. A., Plait P. C., 1988, [ApJL](#), 331, L109
- Childress M., Scalzo R., Yuan F., Schmidt B., Tucker B., 2013, The Astronomer's Telegram, [5455](#), 1
- Childress M., Tucker B., Scalzo R., Yuan F., Zhang B., Ruiter A., Seitzzahl I., Schmidt B., 2015, The Astronomer's Telegram, [7458](#), 1
- Chinetti K., Darnley M. J., Williams S. C., 2016a, The Astronomer's Telegram, [9296](#), 1
- Chinetti K., Darnley M. J., Page K. L., Williams S. C., 2016b, The Astronomer's Telegram, [9329](#), 1
- Chugai N. N., 1991, [MNRAS](#), 250, 513
- Chugai N. N., 2001, [MNRAS](#), 326, 1448
- Chugai N. N., Danziger I. J., 1994, [MNRAS](#), 268, 173
- Chugai N. N., Danziger I. J., 2003, [Astronomy Letters](#), 29, 649
- Chugai N. N., Danziger I. J., Della Valle M., 1995, [MNRAS](#), 276, 530
- Chugai N. N., et al., 2004, [MNRAS](#), 352, 1213
- Ciardullo R., Ford H. C., Neill J. D., Jacoby G. H., Shafter A. W., 1987, [ApJ](#), 318, 520
- Clocchiatti A., et al., 1994, IAU Circ., [6065](#), 1
- Collins George W. I., Claspy W. P., Martin J. C., 1999, [PASP](#), 111, 871
- Conseil E., 2018, Transient Name Server Discovery Report, [2018-807](#), 1
- Crotts A. P. S., Kunkel W. E., McCarthy P. J., 1989, [ApJL](#), 347, L61

- Crowther P. A., 2007, [ARA&A](#), **45**, 177
- Crowther P. A., 2013, [MNRAS](#), **428**, 1927
- Cummings J. D., Kalirai J. S., Tremblay P. E., Ramirez-Ruiz E., Choi J., 2018, [ApJ](#), **866**, 21
- Darnley M. J., Henze M., 2020, [Advances in Space Research](#), **66**, 1147
- Darnley M. J., Williams S. C., 2016a, The Astronomer's Telegram, [8617](#), 1
- Darnley M. J., Williams S. C., 2016b, The Astronomer's Telegram, [8661](#), 1
- Darnley M. J., Williams S. C., 2016c, The Astronomer's Telegram, [8710](#), 1
- Darnley M. J., Williams S. C., 2016d, The Astronomer's Telegram, [9143](#), 1
- Darnley M. J., et al., 2004, [MNRAS](#), **353**, 571
- Darnley M. J., et al., 2006, [MNRAS](#), **369**, 257
- Darnley M. J., Ribeiro V. A. R. M., Bode M. F., Hounsell R. A., Williams R. P., 2012, [The Astrophysical Journal](#), **746**, 61
- Darnley M. J., Williams S. C., Bode M. F., Henze M., Ness J. U., Shafter A. W., Hornoch K., Votruba V., 2014a, [A&A](#), **563**, L9
- Darnley M. J., et al., 2014b, The Astronomer's Telegram, [6540](#), 1
- Darnley M. J., Shafter A. W., Williams S. C., Hornoch K., Henze M., Fabrika S., 2015, The Astronomer's Telegram, [8109](#), 1
- Darnley M. J., Rodriguez-Gil P., Prieto-Arranz J., et al. 2016, The Astronomer's Telegram, [9852](#), 1
- Darnley M. J., Healy M. W., Henze M., Williams S. C., 2017, The Astronomer's Telegram, [11117](#), 1
- Darnley M. J., Healy M. W., Williams S. C., 2018a, The Astronomer's Telegram, [11983](#), 1
- Darnley M. J., Healy M. W., Williams S. C., 2018b, The Astronomer's Telegram, [12017](#), 1
- Darnley M. J., Carey G., Healy M. W., Williams S. C., 2018c, The Astronomer's Telegram, [12245](#), 1

- Darnley M. J., et al., 2019, *Nature*, **565**, 460
- Davis K. W., et al., 2022, arXiv e-prints, p. [arXiv:2211.05134](https://arxiv.org/abs/2211.05134)
- De K., et al., 2020, *ApJ*, **905**, 58
- De K., Fremling U. C., Gal-Yam A., Yaron O., Kasliwal M. M., Kulkarni S. R., 2021, *ApJL*, **907**, L18
- Della Valle M., Izzo L., 2020, *A&A Rev.*, **28**, 3
- Della Valle M., Livio M., 1995, *ApJ*, **452**, 704
- Della Valle M., Livio M., 1998, *ApJ*, **506**, 818
- Della Valle M., Bianchini A., Livio M., Orio M., 1992, *A&A*, **266**, 232
- Dessart L., Hillier D. J., Gezari S., Basa S., Matheson T., 2009, *MNRAS*, **394**, 21
- Dessart L., Hillier D. J., Li C., Woosley S., 2012, *MNRAS*, **424**, 2139
- Dessart L., John Hillier D., Audit E., 2017, *A&A*, **605**, A83
- Di Carlo E., et al., 2002, *ApJ*, **573**, 144
- Doggett J. B., Branch D., 1985, *AJ*, **90**, 2303
- Dong X. Y., Qiu Y. L., Hu J. Y., Li W. D., 2001, *IAU Circ.*, **7596**, 2
- Dong Y., et al., 2022, *ApJ*, **934**, 102
- Dopita M. A., Ryder S. D., 1990a, *IAU Circ.*, **4950**, 3
- Dopita M. A., Ryder S. D., 1990b, *IAU Circ.*, **4950**, 3
- Downes R. A., Duerbeck H. W., 2000, *The Astronomical Journal*, **120**, 2007
- Drout M. R., et al., 2014, *ApJ*, **794**, 23
- Duerbeck H. W., 1990, in Cassatella A., Viotti R., eds, , Vol. 369, *IAU Colloq. 122: Physics of Classical Novae*. p. 34, [doi:10.1007/3-540-53500-4_90](https://doi.org/10.1007/3-540-53500-4_90)
- Duyvendak J. J. L., 1942, *PASP*, **54**, 91
- Dwarkadas V. V., 2011, *MNRAS*, **412**, 1639
- Dwek E., Sarangi A., Arendt R. G., Kallman T., Kazanas D., Fox O. D., 2021, *ApJ*, **917**, 84

- Earl N., et al., 2022, *astropy/specutils*: V1.6.0, [doi:10.5281/zenodo.5911360](https://doi.org/10.5281/zenodo.5911360), <https://doi.org/10.5281/zenodo.5911360>
- Ederoclite A., et al., 2016, *The Astronomer's Telegram*, [9281](#), 1
- Eldridge J. J., Fraser M., Maund J. R., Smartt S. J., 2014, *MNRAS*, 446, 2689
- Elias-Rosa N., et al., 2010, *ApJL*, [714](#), [L254](#)
- Elias-Rosa N., et al., 2016, *The Astronomer's Telegram*, [8727](#), 1
- Elias-Rosa N., et al., 2018, *MNRAS*, [475](#), [2614](#)
- Elmhamdi A., Danziger I. J., Branch D., Leibundgut B., Baron E., Kirshner R. P., 2006, *A&A*, [450](#), [305](#)
- Ergon M., et al., 2014, *The Astronomer's Telegram*, [5857](#), 1
- Evans A., van Loon J. T., Zijlstra A. A., Pollacco D., Smalley B., Tyne V. H., Eyres S. P. S., 2002, *MNRAS*, [332](#), [L35](#)
- Evans C. J., Lennon D. J., Smartt S. J., Trundle C., 2006, *A&A*, [456](#), [623](#)
- Eyres S. P. S., et al., 2018, *MNRAS*, 481, 4931
- Fabrika S., Barsukova E. A., Valeev A. F., Sholukhova O., Hornoch K., Goranskij V. P., Pietsch W., 2010, *The Astronomer's Telegram*, [3068](#), 1
- Fabrika S., Barsukova E. A., Valeev A. F., Sholukhova O., Henze M., Shafter A. W., Hornoch K., 2013a, *The Astronomer's Telegram*, [5543](#), 1
- Fabrika S., et al., 2013b, *The Astronomer's Telegram*, [5554](#), 1
- Fabrika S., Barsukova E. A., Valeev A. F., Sholukhova O., Hornoch K., Shafter A. W., Henze M., 2014a, *The Astronomer's Telegram*, [5745](#), 1
- Fabrika S., Barsukova E. A., Valeev A. F., Sholukhova O., Hornoch K., Shafter A. W., Henze M., 2014b, *The Astronomer's Telegram*, [5754](#), 1
- Fabrika S., et al., 2014c, *The Astronomer's Telegram*, [6473](#), 1
- Fabrika S., et al., 2015a, *The Astronomer's Telegram*, [6985](#), 1
- Fabrika S., Barsukova E. A., Valeev A. F., Vinokurov A., Sholukhova O., Hornoch K., Henze M., Shafter A. W., 2015b, *The Astronomer's Telegram*, [7158](#), 1
- Fabrika S., et al., 2015c, *The Astronomer's Telegram*, [8033](#), 1

- Fabrika S., Sholukhova O., Valeev A. F., Hornoch K., Henze M., Shafter A. W., 2015d, *The Astronomer's Telegram*, [8287](#), 1
- Fabrika S., et al., 2016a, *The Astronomer's Telegram*, [9443](#), 1
- Fabrika S., Sholukhova O., Valeev A. F., Sarkisyan A., Hornoch K., Henze M., Shafter A. W., 2016b, *The Astronomer's Telegram*, [9557](#), 1
- Fabrika S., Sholukhova O., Valeev A. F., Sarkisyan A., Vinokurov A., Hornoch K., Henze M., Shafter A. W., 2016c, *The Astronomer's Telegram*, [9563](#), 1
- Fabrika S., Sholukhova O., Vinokurov A., Valeev A. F., Sarkisyan A., Hornoch K., Henze M., Shafter A. W., 2017a, *The Astronomer's Telegram*, [9941](#), 1
- Fabrika S., Sholukhova O., Vinokurov A., Valeev A. F., Sarkisyan A., Hornoch K., Henze M., Shafter A. W., 2017b, *The Astronomer's Telegram*, [9942](#), 1
- Fabrika S., Sholukhova O., Vinokurov A., Valeev A. F., Sarkisyan A., Hornoch K., Henze M., Shafter A. W., 2017c, *The Astronomer's Telegram*, [10887](#), 1
- Fabrika S., Sholukhova O., Vinokurov A., Valeev A. F., Sarkisyan A., Hornoch K., Henze M., Shafter A. W., 2017d, *The Astronomer's Telegram*, [10986](#), 1
- Fabrika S., Sholukhova O., Vinokurov A., Valeev A. F., Solovyeva Y., Hornoch K., Henze M., Shafter A. W., 2017e, *The Astronomer's Telegram*, [10998](#), 1
- Fabrika S., et al., 2018, *The Astronomer's Telegram*, [11203](#), 1
- Faran T., et al., 2014, *MNRAS*, [445](#), 554
- Fassia A., et al., 2000, *MNRAS*, [318](#), 1093
- Feindt U., Nordin J., Rigault M., Brinnel V., Dhawan S., Goobar A., Kowalski M., 2019, *Journal of Cosmology and Astroparticle Physics*, 2019, 005–005
- Ferrarese L., Côté P., Jordán A., 2003, *ApJ*, [599](#), 1302
- Fields B. D., 2011, *Annual Review of Nuclear and Particle Science*, [61](#), 47
- Filipović M. D., et al., 2022, *MNRAS*, [512](#), 265
- Filippenko A. V., 1989, *AJ*, [97](#), 726
- Filippenko A. V., 1997, *ARA&A*, [35](#), 309
- Filippenko A. V., 2000, *IAU Circ.*, [7421](#), 3

- Filippenko A. V., Barth A. J., 1997, *IAU Circ.*, [6794](#), 1
- Filippenko A. V., Chornock R., 2001a, *IAU Circ.*, [7571](#), 2
- Filippenko A. V., Chornock R., 2001b, *IAU Circ.*, [7737](#), 2
- Filippenko A. V., Chornock R., 2003, *IAU Circ.*, [8051](#), 2
- Filippenko A. V., Garnavich P., 1999, *IAU Circ.*, [7328](#), 3
- Filippenko A. V., Schlegel D., 1995, *IAU Circ.*, [6139](#), 2
- Filippenko A. V., Matheson T., Ho L. C., 1993, *ApJL*, [415](#), L103
- Filippenko A. V., Barth A. J., Bower G. C., Ho L. C., Stringfellow G. S., Goodrich R. W., Porter A. C., 1995, *AJ*, [110](#), 2261
- Filippenko A. V., Li W. D., Modjaz M., 1999, *IAU Circ.*, [7152](#), 2
- Filippenko A. V., Li W. D., Treffers R. R., Modjaz M., 2001a, *International Astronomical Union Colloquium*, 183, 121–130
- Filippenko A. V., Li W. D., Treffers R. R., Modjaz M., 2001b, in Paczynski B., Chen W.-P., Lemme C., eds, *Astronomical Society of the Pacific Conference Series Vol. 246*, IAU Colloq. 183: Small Telescope Astronomy on Global Scales. p. 121
- Filippenko A. V., Silverman J. M., Foley R. J., 2007, *Central Bureau Electronic Telegrams*, [1129](#), 2
- Flewelling H. A., et al., 2020, *ApJS*, [251](#), 7
- Flores Velázquez J. A., et al., 2020, *MNRAS*, 501, 4812
- Foley R. J., Li W., Moore M., Wong D. S., Pooley D., Filippenko A. V., 2006, *Central Bureau Electronic Telegrams*, [695](#), 1
- Foley R. J., et al., 2009, *AJ*, [138](#), 376
- Foley R. J., Berger E., Fox O., Levesque E. M., Challis P. J., Ivans I. I., Rhoads J. E., Soderberg A. M., 2011, *The Astrophysical Journal*, 732, 32
- Foley R. J., et al., 2013, *ApJ*, [767](#), 57
- Fox O., et al., 2009, *ApJ*, 691, 650
- Fox O. D., Chevalier R. A., Skrutskie M. F., 2010, *The Astronomer's Telegram*, [2665](#), 1

- Fox O. D., et al., 2011, [ApJ](#), 741, 7
- Fox O. D., Filippenko A. V., Skrutskie M. F., Silverman J. M., Ganeshalingam M., Cenko S. B., Clubb K. I., 2013, [AJ](#), 146, 2
- Fox O. D., et al., 2017, [The Astrophysical Journal](#), 836, 222
- Fox O. D., et al., 2020, [MNRAS](#), 498, 517
- Fox O. D., et al., 2022, [ApJL](#), 929, L15
- Fraser M., et al., 2010, [ApJL](#), 714, L280
- Fraser M., et al., 2013a, [MNRAS](#), 433, 1312
- Fraser M., et al., 2013b, [Monthly Notices of the Royal Astronomical Society: Letters](#), 439, L56
- Fraser M., et al., 2015, [MNRAS](#), 453, 3886
- Fremming C., et al., 2020, [ApJ](#), 895, 32
- Friedjung M., 1992, [A&A](#), 262, 487
- Gaia Collaboration et al., 2018, [A&A](#), 616, A1
- Gajda G., Gerhard O., Blaña M., Zhu L., Shen J., Saglia R. P., Bender R., 2021, [A&A](#), 647, A131
- Gal-Yam A., Leonard D. C., 2009, [Nature](#), 458, 865
- Gal-Yam A., Shemmer O., Dann J., 2001, [IAU Circ.](#), 7676, 2
- Gal-Yam A., Shemmer O., Dann J., 2002, [IAU Circ.](#), 7818, 2
- Gal-Yam A., et al., 2007, [ApJ](#), 656, 372
- Gal-Yam A., Yaron O., Pastorello A., Taubenberger S., Fraser M., Perley D., 2021, [Transient Name Server AstroNote](#), 76, 1
- Galbany L., et al., 2016, [A&A](#), 591, A48
- Galbany L., et al., 2018, [ApJ](#), 855, 107
- Galbany L., et al., 2019, [A&A](#), 630, A76
- Gangopadhyay A., et al., 2020, [MNRAS](#), 499, 129

- García B., Mermilliod J. C., 2001, [A&A](#), **368**, 122
- Garnavich P., Challis P., Riess A., Kirshner R., Berlind P., 1995, *IAU Circ.*, **6124**, 3
- Gehrz R. D., 1988, [ARA&A](#), **26**, 377
- Georgy C., Meynet G., Walder R., Folini D., Maeder A., 2009, [A&A](#), **502**, 611
- Gerardy C. L., et al., 2002, [ApJ](#), **575**, 1007
- Gies D. R., 1987, [ApJS](#), **64**, 545
- Gilkis A., Arcavi I., 2022, [MNRAS](#), **511**, 691
- Ginsburg A., Mirocha J., 2011, PySpecKit: Python Spectroscopic Toolkit (ascl:1109.001)
- Gorbovskoy E., et al., 2019, *The Astronomer's Telegram*, **12399**, 1
- Graham M. L., et al., 2019, [The Astrophysical Journal](#), **871**, 62
- Green D. W. E., 2008, *Central Bureau Electronic Telegrams*, **1554**, 2
- Groh J. H., Meynet G., Ekström S., 2013a, [A&A](#), **550**, L7
- Groh J. H., Georgy C., Ekström S., 2013b, [A&A](#), **558**, L1
- Guillochon J., Parrent J., Kelley L. Z., Margutti R., 2017, [ApJ](#), **835**, 64
- Gutierrez J., Garcia-Berro E., Iben Icko J., Isern J., Labay J., Canal R., 1996, [ApJ](#), **459**, 701
- Gutierrez C. P., et al., 2017, *The Astronomer's Telegram*, **10318**, 1
- Habergham S. M., Anderson J. P., James P. A., 2010, [ApJ](#), **717**, 342
- Habergham S. M., James P. A., Anderson J. P., 2012, [MNRAS](#), **424**, 2841
- Habergham S. M., Anderson J. P., James P. A., Lyman J. D., 2014, [MNRAS](#), **441**, 2230
- Hachisu I., Kato M., 2004, [ApJL](#), **612**, L57
- Hachisu I., Kato M., Nomoto K., 1999, [ApJ](#), **522**, 487
- Hagen H. J., Engels D., Reimers D., 1997, [A&A](#), **324**, L29
- Hakobyan A. A., Barkhudaryan L. V., Karapetyan A. G., Gevorgyan M. H., Mamon G. A., Kunth D., Adibekyan V., Turatto M., 2020, [MNRAS](#), **499**, 1424
- Hamuy M., Maza J., 2003, *IAU Circ.*, **8045**, 2

- Hamuy M., Phillips M., Suntzeff N., Maza J., 2003, International Astronomical Union Circular, [8151](#), [2](#)
- Hansen C. J., Kawaler S. D., 1994, *Stellar Interiors. Physical Principles, Structure, and Evolution.*, [doi:10.1007/978-1-4419-9110-2](https://doi.org/10.1007/978-1-4419-9110-2).
- Hartigan J. A., Hartigan P. M., 1985, *The Annals of Statistics*, **13**, 70
- Hartwig E., 1885, *Astronomische Nachrichten*, **112**, 403
- Harvey E. J., et al., 2019, *A&A*
- Harvey E. J., et al., 2020, *MNRAS*, **499**, [2959](#)
- Haydon D. T., Kruijssen J. M. D., Chevance M., Hygate A. P. S., Krumholz M. R., Schrubba A., Longmore S. N., 2020, *MNRAS*, **498**, [235](#)
- Helou G., Madore B., 1988, in *European Southern Observatory Conference and Workshop Proceedings*. pp 335–340
- Hendry M. A., et al., 2005, *MNRAS*, **359**, [906](#)
- Henry R., Worthey G., 1999, *Publications of the Astronomical Society of the Pacific*, **111**, 919
- Henze M., Pietsch W., Burwitz V., Kaur A., Hartmann D. H., Milne P., Williams G., 2011a, *Central Bureau Electronic Telegrams*, [2631](#), [6](#)
- Henze M., Pietsch W., Greiner J., 2011b, *The Astronomer's Telegram*, [3712](#), [1](#)
- Hillebrandt W., Niemeyer J. C., Reinecke M., 2000, in Holt S. S., Zhang W. W., eds, *American Institute of Physics Conference Series Vol. 522*, American Institute of Physics Conference Series. pp 53–64 ([arXiv:astro-ph/0005584](https://arxiv.org/abs/astro-ph/0005584)), [doi:10.1063/1.1291695](https://doi.org/10.1063/1.1291695)
- Hillman Y., 2022, arXiv e-prints, p. [arXiv:2205.14708](https://arxiv.org/abs/2205.14708)
- Hillman Y., Prialnik D., Kovetz A., Shara M. M., Neill J. D., 2014, *MNRAS*, **437**, [1962](#)
- Hillman Y., Prialnik D., Kovetz A., Shara M. M., 2015, *MNRAS*, **446**, [1924](#)
- Hillman Y., Prialnik D., Kovetz A., Shara M. M., 2016, *ApJ*, **819**, [168](#)
- Hirai R., Sato T., Podsiadlowski P., Vigna-Gómez A., Mandel I., 2020, *MNRAS*, **499**, 1154
- Hiramatsu D., et al., 2021a, *Nature Astronomy*, **5**, [903](#)

- Hiramatsu D., et al., 2021b, *ApJ*, **913**, 55
- Ho A. Y. Q., et al., 2020, *ApJ*, **895**, 49
- Hornoch K. / Kucakova H., 2019, *The Astronomer's Telegram*, **12414**, 1
- Hornoch K., Prieto J., Khan R., Pejcha O., 2010a, *Central Bureau Electronic Telegrams*, **2136**, 1
- Hornoch K., et al., 2010b, *Central Bureau Electronic Telegrams*, **2341**, 2
- Hornoch K., Hornochova P., Zasche P., Wolf M., 2010c, *Central Bureau Electronic Telegrams*, **2391**, 3
- Hosseinzadeh G., McCully C., Zabludoff A. I., Arcavi I., French K. D., Howell D. A., Berger E., Hiramatsu D., 2019, *The Astrophysical Journal*, **871**, L9
- Hounsell R., et al., 2010, *ApJ*, **724**, 480
- Hounsell R., et al., 2016, *ApJ*, **820**, 104
- Huang C., Chevalier R. A., 2018, *MNRAS*, **475**, 1261
- Hubble E., 1926, *Contributions from the Mount Wilson Observatory / Carnegie Institution of Washington*, **324**, 1
- Hubble E. P., 1929, *ApJ*, **69**, 103
- Hughes D. W., 1980, *Nature*, **285**, 132
- Humphreys R. M., 2005, in Humphreys R., Stanek K., eds, *Astronomical Society of the Pacific Conference Series Vol. 332, The Fate of the Most Massive Stars*. p. 93
- Humphreys R. M., Davidson K., 1994, *PASP*, **106**, 1025
- Humphreys R. M., Davidson K., Jones T. J., Pogge R. W., Grammer S. H., Prieto J. L., Pritchard T. A., 2012, *ApJ*, **760**, 93
- Humphreys R. M., Davidson K., Gordon M. S., Weis K., Burggraf B., Bomans D. J., Martin J. C., 2014, *ApJL*, **782**, L21
- Humphreys R. M., Weis K., Davidson K., Gordon M. S., 2016, *ApJ*, **825**, 64
- Humphreys R. M., Davidson K., Van Dyk S. D., Gordon M. S., 2017, *ApJ*, **848**, 86
- Hunter J. D., 2007, *Computing in Science & Engineering*, **9**, 90

- Hurst G. M., et al., 2001, IAU Circ., [7662](#), 1
- Hyland A. R., Neugebauer G., 1970, [ApJL](#), [160](#), L177
- Inserra C., 2019, [Nature Astronomy](#), [3](#), 697
- Inserra C., et al., 2012, Central Bureau Electronic Telegrams, [3101](#), 2
- Izzo L., et al., 2015, [The Astrophysical Journal](#), 808, L14
- Izzo L., et al., 2018, [MNRAS](#), [478](#), 1601
- James P. A., Anderson J. P., 2006, [A&A](#), [453](#), 57
- Jerkstrand A., Maeda K., Kawabata K. S., 2020, [Science](#), [367](#), 415
- Jha S., Challis P., Kirshner R., Berlind P., 2000, IAU Circ., [7381](#), 2
- Joglekar H., Gangal K., Vahia M., Sule A., 2011, Puratattva-Bulletin of the Indian Archaeological Society, 41, 207
- Jones D. O., et al., 2021, [The Astrophysical Journal](#), 908, 143
- Justham S., Podsiadlowski P., Vink J. S., 2014, [The Astrophysical Journal](#), 796, 121
- Kahabka P. / van den Heuvel E. P. J., 1997, [ARA&A](#), [35](#), 69
- Kangas T., et al., 2017, [A&A](#), [597](#), A92
- Kangas T., et al., 2022, [MNRAS](#), [511](#), 2977
- Kankare E., et al., 2012, [MNRAS](#), [424](#), 855
- Kankare E., et al., 2013, The Astronomer's Telegram, [5338](#), 1
- Kankare E., et al., 2017, The Astronomer's Telegram, [10391](#), 1
- Kasliwal M. M., 2011, PhD thesis, California Institute of Technology
- Kasliwal M. M., Kulkarni S. R., Gal-Yam A., Yaron O., Quimby R. M., Ofek E. O., Nugent P., Poznanski D., 2010, [ApJL](#), [723](#), L98
- Kasliwal M. M., et al., 2011a, [ApJ](#), 730, 134
- Kasliwal M. M., Cenko S. B., Kulkarni S. R., Ofek E. O., Quimby R., Rau A., 2011b, [ApJ](#), [735](#), 94
- Kasliwal M. M., Kulkarni S. R., Gal-Yam A., Nugent P. E., Sullivan M., Bildsten L., Yaron O., Perets H. B., 2012a, [ApJ](#), [755](#), 161

- Kasliwal M. M., et al., 2012b, *ApJ*, 755, 161
- Kasliwal M. M., et al., 2017, *ApJ*, 839, 88
- Kato M., Saio H., Hachisu I., 2018, *ApJ*, 863, 125
- Kennicutt R. C., 1998, *Annual Review of Astronomy and Astrophysics*, 36, 189
- Kent S. M., 1983, *ApJ*, 266, 562
- Kent S. M., 1987, *AJ*, 94, 306
- Kent S. M., 1989, *AJ*, 97, 1614
- Kerins E., Darnley M. J., Duke J. P., Gould A., Han C., Newsam A., Park B. G., Street R., 2010, *MNRAS*, 409, 247
- Kewley L. J., Rupke D., Zahid H. J., Geller M. J., Barton E. J., 2010, *ApJL*, 721, L48
- Khazov D., et al., 2016, *ApJ*, 818, 3
- Kiewe M., et al., 2012, *ApJ*, 744, 10
- Kilpatrick C. D., et al., 2021, *MNRAS*, 504, 2073
- Kochanek C. S., 2011, *ApJ*, 741, 37
- Kochanek C. S., 2019, *MNRAS*, 483, 3762
- Kochanek C. S., Szczygiel D. M., Stanek K. Z., 2012, *ApJ*, 758, 142
- Kochanek C. S., et al., 2017, *PASP*, 129, 104502
- Kokubo M., et al., 2019, *The Astrophysical Journal*, 872, 135
- König O., et al., 2022, *Nature*, 605, 248
- Kotak R., Vink J. S., 2006, *A&A*, 460, L5
- Kotak R., Meikle W. P. S., European Supernova Collaboration Rodriguez-Gil P., 2003, *IAU Circ.*, 8124, 1
- Kumar V., et al., 2022, *MNRAS*, 510, 4265
- Kuncarayakti H., Maeda K., Anderson J. P., Hamuy M., Nomoto K., Galbany L., Doi M., 2016, *MNRAS*, 458, 2063
- Kurfürst P., Pejcha O., Krtićka J., 2020, *A&A*, 642, A214

- LSST Science Collaboration et al., 2009, arXiv e-prints, p. [arXiv:0912.0201](#)
- Law N. M., et al., 2009, [Publications of the Astronomical Society of the Pacific](#), **121**, 1395
- Leonard D. C., Filippenko A. V., Barth A. J., Matheson T., 2000, [ApJ](#), **536**, 239
- Leung K. N. . S.-C., 2018, [Space Science Reviews](#), 214
- Li W., Smith N., Miller A. A., Filippenko A. V., 2009a, The Astronomer's Telegram, [2212](#), 1
- Li W., Smith N., Miller A. A., Filippenko A. V., 2009b, The Astronomer's Telegram, [2212](#), 1
- Li W., Filippenko A. V., Miller A. A., Cuillandre J. C., Elias-Rosa N., van Dyk S. D., 2009c, The Astronomer's Telegram, [2312](#), 1
- Li W., et al., 2011, [MNRAS](#), **412**, 1441
- Li W., Wang X., Zhang T., 2014, The Astronomer's Telegram, [6734](#), 1
- Li S., Riess A. G., Busch M. P., Casertano S., Macri L. M., Yuan W., 2021, [The Astrophysical Journal](#), 920, 84
- Lin H., et al., 2021, [MNRAS](#), **505**, 4890
- Lundmark K., 1922, [PASP](#), **34**, 207
- Lundmark K., 1923, [PASP](#), **35**, 95
- Lunnan R., et al., 2014, [The Astrophysical Journal](#), 787, 138
- MacLeod M., Macias P., Ramirez-Ruiz E., Grindlay J., Batta A., Montes G., 2017, [ApJ](#), **835**, 282
- Madrid J. P., Sparks W. B., Ferguson H., Livio M., Macchetto D., 2006, in American Astronomical Society Meeting Abstracts. p. 182.05
- Margutti R., Soderberg A., Milisavljevic D., 2013, The Astronomer's Telegram, [5106](#), 1
- Margutti R., et al., 2014, [ApJ](#), **780**, 21
- Margutti R., et al., 2019, [ApJ](#), **872**, 18
- Marion G. H., Calkins M., 2011, Central Bureau Electronic Telegrams, [2668](#), 2

- Martin C., et al., 2003, in Blades J. C., Siegmund O. H. W., eds, Proc. SPIE Vol. 4854, Future EUV/UV and Visible Space Astrophysics Missions and Instrumentation.. pp 336–350, [doi:10.1117/12.460034](https://doi.org/10.1117/12.460034)
- Martin T. B., Drissen L., Melchior A.-L., 2018, *MNRAS*, **473**, 4130
- Massey P., Olsen K. A. G., Hodge P. W., Strong S. B., Jacoby G. H., Schlingman W., Smith R. C., 2006, *AJ*, **131**, 2478
- Matheson T., Jha S., Challis P., Kirshner R., Calkins M., 2001, IAU Circ., **7597**, 3
- Matheson T., Jha S., Challis P., Kirshner R., Calkins M., 2002a, IAU Circ., **7784**, 3
- Matheson T., Jha S., Challis P., Kirshner R., Berlind P., 2002b, IAU Circ., **7844**, 5
- Matheson T., Challis P., Kirshner R., Calkins M., 2003, IAU Circ., **8246**, 1
- Matheson T., Challis P., Kirshner R., Calkins M., 2004, IAU Circ., **8268**, 2
- Mauerhan J., Smith N., 2012, *MNRAS*, **424**, 2659
- Mauerhan J. C., et al., 2013, *MNRAS*, **430**, 1801
- Mauerhan J. C., et al., 2017a, *ApJ*, **834**, 118
- Mauerhan J. C., Filippenko A. V., Brink T. G., Zheng W., 2017b, The Astronomer's Telegram, **10911**, 1
- Maund J. R., Smartt S. J., Kudritzki R. P., Podsiadlowski P., Gilmore G. F., 2004, *Nature*, **427**, 129
- Maund J. R., et al., 2006, *MNRAS*, **369**, 390
- Maund J. R., Fraser M., Reilly E., Ergon M., Mattila S., 2015, *MNRAS*, **447**, 3207
- Mayall N. U., Oort J. H., 1942, *PASP*, **54**, 95
- Maza J., van den Bergh S., 1976, *ApJ*, **204**, 519
- Maza J., et al., 2009, Central Bureau Electronic Telegrams, **1928**, 1
- Mazzali P. A., Röpke F. K., Benetti S., Hillebrandt W., 2007, *Science*, **315**, 825
- McCray Richard / Fransson C., 2016, *ARA&A*, **54**, 19
- McLaughlin D. B., 1960, The Spectra of Novae. p. 585
- McLaughlin D. B., 1945, *PASP*, **57**, 69

- Meikle P., Fassia A., Geballe T. R., Lundqvist P., Chugai N., Farrah D., Sollerman J., 2003, in Hillebrandt W., Leibundgut B., eds, From Twilight to Highlight: The Physics of Supernovae. p. 229 ([arXiv:astro-ph/0211144](https://arxiv.org/abs/astro-ph/0211144)), [doi:10.1007/10828549_30](https://doi.org/10.1007/10828549_30)
- Milisavljevic D., et al., 2015, *ApJ*, **815**, 120
- Miller A. A., Li W., Nugent P. E., Bloom J. S., Filippenko A. V., Merritt A. T., 2009, The Astronomer's Telegram, **2183**, 1
- Millour F., et al., 2020, arXiv e-prints, p. [arXiv:2006.15660](https://arxiv.org/abs/2006.15660)
- Minkowski R., 1941, *PASP*, **53**, 224
- Miyaji S., Nomoto K., Yokoi K., Sugimoto D., 1980, *PASJ*, **32**, 303
- Modjaz M., Li W. D., Garnavich P., Jha S., Challis P., Kirshner R., Berlind P., 1999, *IAU Circ.*, **7268**, 1
- Modjaz M., Kirshner R., Challis P., Hao H., 2005a, *IAU Circ.*, **8492**, 3
- Modjaz M., Kirshner R., Challis P., Calkins M., 2005b, *IAU Circ.*, **8628**, 2
- Modjaz M., Gutiérrez C. P., Arcavi I., 2019, *Nature Astronomy*, **3**, 717
- Mokiem M. R., et al., 2007, *A&A*, **473**, 603
- Molaro P., Izzo L., Mason E., Bonifacio P., Della Valle M., 2016, *MNRAS*, **463**, L117
- Morales Garoffolo A., et al., 2013, The Astronomer's Telegram, **4767**, 1
- Moriya T. J., Maeda K., Taddia F., Sollerman J., Blinnikov S. I., Sorokina E. I., 2014, *MNRAS*, **439**, 2917–2926
- Morozova V., Piro A. L., Valenti S., 2017, *ApJ*, **838**, 28
- Morozova V., Piro A. L., Valenti S., 2018, *The Astrophysical Journal*, **858**, 15
- Munari U., et al., 2002, *A&A*, **389**, L51
- Murphey C. T., Hogan J. W., Fields B. D., Narayan G., 2021, *MNRAS*, **507**, 927
- Muthukrishna D., Parkinson D., Tucker B. E., 2019, *ApJ*, **885**, 85
- Nagao T., et al., 2021, *MNRAS*, **505**, 3664
- Nakano S., et al., 1996, *IAU Circ.*, **6505**, 1
- Nakano S., Yusa T., Kadota K., 2009, Central Bureau Electronic Telegrams, **2006**, 1

- Nakaoka T., et al., 2021, *ApJ*, **912**, 30
- Neric M., Wilber A., Wagner R. M., Starrfield S., Woodward C. E., 2015, *The Astronomer's Telegram*, **7606**, 1
- Neunteufel P., Yoon S. C., Langer N., 2019, *A&A*, **627**, A14
- Newville M., et al., 2021, *lmfit/lmfit-py*: 1.0.3, doi:10.5281/zenodo.5570790, <https://doi.org/10.5281/zenodo.5570790>
- Nomoto K., 1984, *ApJ*, **277**, 791
- Nomoto K., 1987, *ApJ*, **322**, 206
- Nomoto K., Sparks W. M., Fesen R. A., Gull T. R., Miyaji S., Sugimoto D., 1982, *Nature*, **299**, 803
- Nomoto K., Suzuki T., Shigeyama T., Kumagai S., Yamaoka H., Saio H., 1993, *Nature*, **364**, 507
- Nugent P., 2007, *The Astronomer's Telegram*, **1213**, 1
- Nyholm A., et al., 2020, *Astronomy & Astrophysics*, **637**, A73
- Ochner P., et al., 2014a, *The Astronomer's Telegram*, **5767**, 1
- Ochner P., Benetti S., Tomasella L., Terreran G., Pastorello A., Cappellaro E., Elias-Rosa N., Turatto M., 2014b, *The Astronomer's Telegram*, **6488**, 1
- Ochner P., et al., 2014c, *The Astronomer's Telegram*, **6750**, 1
- Ofek E. O., et al., 2014, *ApJ*, **789**, 104
- Ofek E. O., et al., 2019, *Publications of the Astronomical Society of the Pacific*, **131**, 054204
- Oppenheimer J. R., Volkoff G. M., 1939, *Physical Review*, **55**, 374
- Orio M., Shaviv G., 1993, *Ap&SS*, **202**, 273
- Osborne J. P., 2015, *Journal of High Energy Astrophysics*, **7**, 117
- Osterbrock D. E., Ferland G. J., 2006, *Astrophysics of gaseous nebulae and active galactic nuclei*. University Science Books; Sausalito, CA
- Pagnotta A., Schaefer B. E., 2014, *ApJ*, **788**, 164

- Papenkova M., Li W. D., 2001, *IAU Circ.*, [7737](#), 1
- Park H. S., Moon D.-S., Zaritsky D., Kim S. C., Lee Y., Cha S.-M., Lee Y., 2019, *The Astrophysical Journal*, [885](#), 88
- Parrent J., et al., 2011, *The Astronomer's Telegram*, [3510](#), 1
- Pastorello A., et al., 2002, *MNRAS*, [333](#), 27
- Pastorello A., et al., 2007, *Nature*, [447](#), 829
- Pastorello A., et al., 2010, *MNRAS*, [408](#), 181
- Pastorello A., Stanishev V., Smartt S. J., Fraser M., Lindborg M., 2011, *Central Bureau Electronic Telegrams*, [2851](#), 2
- Pastorello A., et al., 2013, *The Astrophysical Journal*, [767](#), 1
- Pastorello A., et al., 2017, *MNRAS*, [474](#), 197–218
- Pastorello A., et al., 2019a, *A&A*, [625](#), L8
- Pastorello A., et al., 2019b, *A&A*, [628](#), A93
- Patton R. A., Kochanek C. S., Adams S. M., 2019, *MNRAS*, [489](#), 1986
- Payne-Gaposchkin C., 1964, *The galactic novae*. New York: Dover Publication, 1964
- Pejcha O., 2009, *ApJL*, [701](#), L119
- Perets H. B., Gal-Yam A., Mazzali P. A., Arnett D., Kagan D., Filippenko A. V., 2010, *Nature*, [465](#), 322
- Perley D. A., et al., 2016, *The Astrophysical Journal*, [830](#), 13
- Perley D. A., et al., 2019, *MNRAS*, [484](#), 1031
- Perley D. A., et al., 2020, *ApJ*, [904](#), 35
- Perley D. A., et al., 2022, *ApJ*, [927](#), 180
- Pessi T., et al., 2022, *ApJ*, [928](#), 138
- Pettini M., Pagel B. E. J., 2004, *MNRAS*, [348](#), L59
- Phillips M. M., 1993, *ApJL*, [413](#), L105
- Piascik A. S., Steele I. A., Bates S. D., Mottram C. J., Smith R. J., Barnsley R. M., Bolton B., 2014, in *Proc. SPIE*. p. 91478H, [doi:10.1117/12.2055117](https://doi.org/10.1117/12.2055117)

- Pietrzyński G., et al., 2019, *Nature*, **567**, 200
- Pietsch W., 2010, *Astronomische Nachrichten*, **331**, 187
- Pietsch W., et al., 2007, *A&A*, **465**, 375
- Podsiadlowski P., Joss P. C., Hsu J. J. L., 1992, *ApJ*, **391**, 246
- Pollas C., Albanese D., Benetti S., Bouchet P., Schwarz H., 1995, *IAU Circ.*, **6170**, 1
- Popper D. M., 1937, *PASP*, **49**, 283
- Prentice S. J., et al., 2018, *ApJL*, **865**, L3
- Prieto J., Garnavich P., Depoy D., Marshall J., Eastman J., Frank S., 2005, *Central Bureau Electronic Telegrams*, **302**, 1
- Prieto J. L., et al., 2008, *ApJL*, **681**, L9
- Prieto J. L., Brimacombe J., Drake A. J., 2012, *The Astronomer's Telegram*, **4439**, 1
- Pskovskii I. P., 1977, *Soviet Ast.*, **21**, 675
- Puckett T., George D., Ceravolo P., Nakano S., Sano Y., Kushida Y., Kushida R., 2005a, *IAU Circ.*, **8615**, 1
- Puckett T., et al., 2005b, *IAU Circ.*, **8647**, 1
- Puls J., et al., 1996, *A&A*, **305**, 171
- Ransome C. L., Habergham-Mawson S. M., Darnley M. J., James P. A., Filippenko A. V., Schlegel E. M., 2021, *MNRAS*, **506**, 4715
- Ransome C. L., Habergham-Mawson S. M., Darnley M. J., James P. A., Percival S. M., 2022, *MNRAS*, **513**, 3564
- Reaves G., 1953, *PASP*, **65**, 242
- Reguitti A., et al., 2019, *MNRAS*, **482**, 2750
- Reynolds T., et al., 2016, *The Astronomer's Telegram*, **9357**, 1
- Riess A. G., et al., 2004, *ApJ*, **607**, 665
- Ripero J., et al., 1993, *IAU Circ.*, **5731**, 1
- Ritchey G. W., 1917, *Publications of the Astronomical Society of the Pacific*, **29**, 210

- Robertson J. W., Honeycutt R. K., Hillwig T., Jurcevic J. S., Henden A. A., 2000, *AJ*, **119**, 1365
- Roming P., Pritchard T., Brown P., 2011, *The Astronomer's Telegram*, **3690**, 1
- Rosenbush A. E., 1999, *Astrophysics*, **42**, 43
- Rosino L., 1964, *Annales d'Astrophysique*, **27**, 498
- Rosino L., 1973, *A&AS*, **9**, 347
- Rosino L., Capaccioli M., D'Onofrio M., Della Valle M., 1989, *AJ*, **97**, 83
- Rui L., Wang X., Zhang T., Jia J., Lu Y., 2016, *The Astronomer's Telegram*, **9667**, 1
- Rust B. W., 1974, PhD thesis, Oak Ridge National Laboratory, Tennessee
- Ryder S., Staveley-Smith L., Dopita M., Petre R., Colbert E., Malin D., Schlegel E., 1993, *ApJ*, **416**, 167
- SAS Institute 1989, SAS/STAT user's guide. SAS Institute Inc., Cary, NC, https://documentation.sas.com/doc/en/pgmsascdc/9.4_3.4/statug/statug_cluster_details17.htm
- Sala G., et al., 2014, *The Astronomer's Telegram*, **6616**, 1
- San Julian-Jacques D., Fernandez-Torreiro M., Perez-Fournon I., 2019, *Research Notes of the American Astronomical Society*, **3**, 144
- Sana H., et al., 2012, *Science*, **337**, 444
- Santander-García M., Rodríguez-Gil P., Corradi R. L. M., Jones D., Miszalski B., Boffin H. M. J., Rubio-Díez M. M., Kotze M. M., 2015, *Nature*, **519**, 63
- Schaefer B. E., 2013, *The Observatory*, **133**, 227
- Schaefer B. E., 2018a, *Journal of Astronomical History and Heritage*, **21**, 7
- Schaefer B. E., 2018b, *MNRAS*, **481**, 3033
- Schaefer B. E., 2021, in *American Astronomical Society Meeting Abstracts*. p. 306.02
- Schaefer B. E., Roscherr B., 1998, *IAU Circ.*, **7058**, 2
- Schlegel E. M., 1990, *MNRAS*, **244**, 269
- Schlegel E. M., Kirshner R. P., Huchra J. P., Schild R. E., 1996, *AJ*, **111**, 2038

- Schlegel E. M., Ryder S., Staveley-Smith L., Petre R., Colbert E., Dopita M., Campbell-Wilson D., 1999, *AJ*, **118**, 2689
- Scholz F. W., Stephens M. A., 1987, *Journal of the American Statistical Association*, **82**, 918
- Schulze S., et al., 2021, *ApJS*, **255**, 29
- Schwartz M., Li W., Filippenko A. V., Chornock R., 2003, *IAU Circ.*, **8051**, 1
- Sedgwick T. M., Baldry I. K., James P. A., Kelvin L. S., 2019, *MNRAS*, **484**, 5278
- Sell P. H., Maccarone T. J., Kotak R., Knigge C., Sand D. J., 2015, *MNRAS*, **450**, 4198
- Selvelli P., Gilmozzi R., 2019, *A&A*, **622**, A186
- Shafter A. W., 2007, in *American Astronomical Society Meeting Abstracts*. p. 51.15
- Shafter A. W., 2013, *The Astronomical Journal*, **145**, 117
- Shafter A. W., 2017, *ApJ*, **834**, 196
- Shafter A. W., 2019, *Extragalactic Novae; A historical perspective*, [doi:10.1088/2514-3433/ab2c63](https://doi.org/10.1088/2514-3433/ab2c63).
- Shafter A. W., Irby B. K., 2001a, *ApJ*, **563**, 749
- Shafter A. W., Irby B. K., 2001b, *ApJ*, **563**, 749
- Shafter A. W., Rau A., Quimby R. M., Kasliwal M. M., Bode M. F., Darnley M. J., Misselt K. A., 2008, *The Astrophysical Journal*, **690**, 1148
- Shafter A. W., Ciardullo R., Bode M. F., Darnley M. J., Misselt K. A., 2010a, *The Astronomer's Telegram*, **2834**, 1
- Shafter A. W., Ciardullo R., Bode M. F., Darnley M. J., Misselt K. A., 2010b, *The Astronomer's Telegram*, **2843**, 1
- Shafter A. W., Ciardullo R., Darnley M. J., Bode M. F., Misselt K. A., 2010c, *The Astronomer's Telegram*, **2898**, 1
- Shafter A. W., Ciardullo R., Darnley M. J., Bode M. F., Misselt K. A., 2010d, *The Astronomer's Telegram*, **2949**, 1
- Shafter A. W., Ciardullo R., Bode M. F., Darnley M. J., Misselt K. A., 2010e, *The Astronomer's Telegram*, **2987**, 1

- Shafter A. W., Bode M. F., Darnley M. J., Ciardullo R., Misselt K. A., 2010f, *The Astronomer's Telegram*, [3006](#), 1
- Shafter A. W., Hornoch K., Darnley M. J., Bode M. F., Ciardullo R., Misselt K. A., 2010g, *The Astronomer's Telegram*, [3039](#), 1
- Shafter A. W., Ciardullo R., Darnley M. J., Bode M. F., Misselt K. A., 2010h, *The Astronomer's Telegram*, [3074](#), 1
- Shafter A. W., et al., 2011a, [The Astrophysical Journal](#), 734, 12
- Shafter A. W., Ciardullo R., Bode M. F., Darnley M. J., 2011b, *The Astronomer's Telegram*, [3699](#), 1
- Shafter A. W., Ciardullo R., Darnley M. J., Bode M. F., 2011c, *The Astronomer's Telegram*, [3769](#), 1
- Shafter A. W., Darnley M. J., Bode M. F., Ciardullo R., 2011d, *The Astronomer's Telegram*, [3778](#), 1
- Shafter A. W., Bode M. F., Darnley M. J., Ciardullo R., Cao Y., Hornoch K., 2011e, *The Astronomer's Telegram*, [3825](#), 1
- Shafter A. W., Darnley M. J., Bode M. F., Ciardullo R., 2011f, *The Astronomer's Telegram*, [3833](#), 1
- Shafter A. W., Darnley M. J., Bode M. F., Ciardullo R., 2012a, [The Astrophysical Journal](#), 752, 156
- Shafter A. W., Darnley M. J., Bode M. F., Ciardullo R., Hornoch K., 2012b, *The Astronomer's Telegram*, [3850](#), 1
- Shafter A. W., Darnley M. J., Bode M. F., Ciardullo R., 2012c, *The Astronomer's Telegram*, [3877](#), 1
- Shafter A. W., Darnley M. J., Bode M. F., Ciardullo R., Hornoch K., Cao Y., Kasliwal M. M., 2012d, *The Astronomer's Telegram*, [3912](#), 1
- Shafter A. W., Darnley M. J., Bode M. F., Ciardullo R., 2012e, *The Astronomer's Telegram*, [4256](#), 1
- Shafter A. W., Hornoch K., Ciardullo R., Darnley M. J., Bode M. F., 2012f, *The Astronomer's Telegram*, [4368](#), 1

- Shafter A. W., Hornoch K., Ciardullo R., Darnley M. J., Bode M. F., 2012g, *The Astronomer's Telegram*, [4391](#), 1
- Shafter A. W., Hornoch K., Ciardullo J. V. R., Darnley M. J., Bode M. F., 2012h, *The Astronomer's Telegram*, [4503](#), 1
- Shafter A. W., Hornoch K., Ciardullo R., Darnley M. J., Bode M. F., 2012i, *The Astronomer's Telegram*, [4658](#), 1
- Shafter A. W., Hornoch K., Ciardullo R., Darnley M. J., Bode M. F., 2012j, *The Astronomer's Telegram*, [4683](#), 1
- Shafter A. W., Ciardullo R., Darnley M. J., Bode M. F., 2013a, *The Astronomer's Telegram*, [4720](#), 1
- Shafter A. W., Hornoch K., Ciardullo R., Darnley M. J., Bode M. F., 2013b, *The Astronomer's Telegram*, [4768](#), 1
- Shafter A. W., Curtin C., Pritchett C. J., Bode M. F., Darnley M. J., 2014, in Woudt P. A., Ribeiro V. A. R. M., eds, *Astronomical Society of the Pacific Conference Series Vol. 490, Stellar Novae: Past and Future Decades*. p. 77 ([arXiv:1307.2296](#))
- Shafter A. W., Henze M., Igarashi A. S., Horst J., Darnley M. J., Williams S. C., Rector T. A., 2017, *The Astronomer's Telegram*, [10981](#), 1
- Shara M. M., Drissen L., 1995, *ApJ*, [448](#), 203
- Shara M. M., Moffat A. F. J., 1982, *ApJL*, [258](#), L41
- Shara M. M., Moffat A. F. J., Webbink R. F., 1985, *ApJ*, [294](#), 271
- Shara M. M., Sandage A., Zurek D. R., 1999, *PASP*, [111](#), 1367
- Shara M. M., Yaron O., Prialnik D., Kovetz A., Zurek D., 2010, *The Astrophysical Journal*, [725](#), 831
- Shara M. M., et al., 2017a, *Nature*, [548](#), 558
- Shara M. M., Doyle T., Lauer T. R., Zurek D., Baltz E. A., 2017b, *ApJ*, [839](#), 109
- Shara M. M., et al., 2018, *MNRAS*, [474](#), 1746
- Shen K. J., Bildsten L., 2009, *ApJ*, [699](#), 1365
- Shivvers I., Groh J. H., Mauerhan J. C., Fox O. D., Leonard D. C., Filippenko A. V., 2015, *The Astrophysical Journal*, [806](#), 213

- Shore S. N., 2012, *Bulletin of the Astronomical Society of India*, **40**, 185
- Siebert M. R., Pan Y. C., Foley R. J., 2018, *Transient Name Server Classification Report*, **2018-1003**, 1
- Silverman J. M., Kleiser I. K. W., Morton A. J. L., Filippenko A. V., 2010, *Central Bureau Electronic Telegrams*, **2223**, 1
- Silverman J. M., et al., 2013, *ApJS*, **207**, 3
- Sitaram M., Darnley M. J., 2018a, *The Astronomer's Telegram*, **11866**, 1
- Sitaram M., Darnley M. J., 2018b, *The Astronomer's Telegram*, **11923**, 1
- Skrutskie M. F., et al., 2006, *AJ*, **131**, 1163
- Smartt S. J., Eldridge J. J., Crockett R. M., Maund J. R., 2009, *MNRAS*, **395**, 1409
- Smartt S. J., et al., 2017, *Nature*, **551**, 75
- Smith N., 2006, *ApJ*, **644**, 1151
- Smith N., 2013, *MNRAS*, **434**, 102
- Smith N., 2014, *Annual Review of Astronomy and Astrophysics*, **52**, 487
- Smith N., Hartigan P., 2006, *ApJ*, **638**, 1045
- Smith R., Steele I., 2017, *Liverpool Telescope Technical Note 1: Telescope and IO: O Throughput*. Liverpool John Moores University
- Smith N., Tombleson R., 2015, *MNRAS*, **447**, 598
- Smith N., Gehrz R. D., Hinz P. M., Hoffmann W. F., Hora J. L., Mamajek E. E., Meyer M. R., 2003, *AJ*, **125**, 1458
- Smith N., et al., 2007, *The Astrophysical Journal*, **666**, 1116
- Smith N., Hinkle K. H., Ryde N., 2009a, *AJ*, **137**, 3558
- Smith N., et al., 2009b, *ApJ*, **695**, 1334
- Smith N., et al., 2009c, *ApJL*, **697**, L49
- Smith N., et al., 2010, *AJ*, **139**, 1451
- Smith N., Li W., Silverman J. M., Ganeshalingam M., Filippenko A. V., 2011, *MNRAS*, **415**, 773

- Smith N., Mauerhan J. C., Kasliwal M. M., Burgasser A. J., 2013, *MNRAS*, **434**, 2721
- Smith N., Mauerhan J. C., Prieto J. L., 2014, *MNRAS*, **438**, 1191
- Smith N., et al., 2015, *MNRAS*, **449**, 1876–1896
- Smith N., et al., 2016, *MNRAS*, **458**, 950
- Smith N., et al., 2018, *MNRAS*, **480**, 1466
- Smith N., et al., 2020, *MNRAS*, **492**, 5897
- Somero A., et al., 2016, The Astronomer’s Telegram, **9744**, 1
- Stanek K. Z., 2017, Transient Name Server Discovery Report, **2017-862**, 1
- Starrfield S., 1971, *MNRAS*, **152**, 307
- Starrfield S., 1989, Starrfield, S. in Classical Novae. Cambridge Astrophysics Series, No. 43, Cambridge: Cambridge University Press, 1989.
- Starrfield S., Truran J. W., Sparks W. M., Kutter G. S., 1972, *ApJ*, **176**, 169
- Starrfield S., Sparks W. M., Truran J. W., 1976, in Eggleton P., Mitton S., Whelan J., eds, IAU Symposium Vol. 73, Structure and Evolution of Close Binary Systems. p. 155
- Starrfield S., Iliadis C., Hix W. R., 2016, *PASP*, **128**, 051001
- Stathakis R. A., Sadler E. M., 1991, *MNRAS*, **250**, 786
- Steele I. A., 2004, *Astronomische Nachrichten*, **325**, 519
- Steele T. N., Silverman J. M., Ganeshalingam M., Lee N., Li W., Filippenko A. V., 2008, Central Bureau Electronic Telegrams, **1275**, 1
- Steele T. N., Cobb B., Filippenko A. V., 2009a, Central Bureau Electronic Telegrams, **2011**, 1
- Steele T. N., Cobb B., Filippenko A. V., 2009b, Central Bureau Electronic Telegrams, **2011**, 1
- Stephens M. A., 1974, *Journal of the American Statistical Association*, **69**, 730
- Stephenson F. R., Yau K. K. K., 1986, Quarterly Journal of the Royal Astronomical Society

- Stritzinger M., Folatelli G., Morrell N., 2008, Central Bureau Electronic Telegrams, [1218](#), [1](#)
- Stritzinger M., Morrell N., Folatelli G., Covarrubias R., Phillips M. M., 2009, Central Bureau Electronic Telegrams, [1725](#), [1](#)
- Stritzinger M., Prieto J. L., Morrell N., Pignata G., 2011, Central Bureau Electronic Telegrams, [2623](#), [2](#)
- Stritzinger M., et al., 2012, [ApJ](#), [756](#), [173](#)
- Strolger L. G., Seguel J. C., Krick J., Block A., Candia P., Smith R. C., Suntzeff N. B., Phillips M. M., 2000, IAU Circ., [7524](#), [2](#)
- Strotjohann N. L., et al., 2021, [ApJ](#), [907](#), [99](#)
- Sun G., Gao X., 2018, Transient Name Server Discovery Report, [2018-1506](#), [1](#)
- Sun N.-C., Maund J. R., Crowther P. A., Hirai R., Kashapov A., Liu J.-F., Liu L.-D., Zapartas E., 2022, [MNRAS](#), [510](#), [3701](#)
- Taddia F., et al., 2012, [A&A](#), [545](#), [L7](#)
- Taddia F., et al., 2015, [A&A](#), [580](#), [A131](#)
- Taggart K., Perley D. A., 2021, [MNRAS](#), [503](#), [3931](#)
- Tajitsu A., Sadakane K., Naito H., Arai A., Aoki W., 2015, [Nature](#), [518](#), [381](#)
- Tamburro D., Rix H.-W., Walter F., Brinks E., de Blok W. J. G., Kennicutt R. C., Low M.-M. M., 2008, [The Astronomical Journal](#), [136](#), [2872](#)
- Tammann G. A., Sandage A., 1968, [ApJ](#), [151](#), [825](#)
- Tanaka J., Nogami D., Fujii M., Ayani K., Kato T., 2011, [Publications of the Astronomical Society of Japan](#), [63](#), [159](#)
- Tang S., Cao Y., Kasliwal M. M., Cenko S. B., Shivvers I., Tuck B. E., 2013a, The Astronomer's Telegram, [5180](#), [1](#)
- Tang S., Cao Y., Kasliwal M. M., Waszczak A., Johansson J., O'Sullivan D., Ben-Ami S., 2013b, The Astronomer's Telegram, [5367](#), [1](#)
- Tang S., Cao Y., Kasliwal M. M., 2013c, The Astronomer's Telegram, [5539](#), [1](#)
- Tang S., Cao Y., Kasliwal M. M., 2014, The Astronomer's Telegram, [5852](#), [1](#)

- Tanvir N. R., Levan A. J., Fruchter A. S., Hjorth J., Hounsell R. A., Wiersema K., Tunnicliffe R. L., 2013, *Nature*, **500**, 547
- Tartaglia L., et al., 2020, *A&A*, **635**, A39
- Taubenberger S., et al., 2008, *MNRAS*, **385**, 75
- Tendulkar S., Kasliwal M., Quimby R., Kulkarni S., 2009a, *The Astronomer's Telegram*, **2291**, 1
- Tendulkar S. P., Kasliwal M. M., Quimby R., Kulkarni S. R., 2009b, *The Astronomer's Telegram*, **2291**, 1
- Terreran G., et al., 2016, *MNRAS*, **462**, 137
- The Astropy Collaboration Robitaille, Thomas P. Tollerud, Erik J. Greenfield, Perry Droettboom, Michael Bray, Erik Aldcroft, Tom Davis, Matt 2013, *A&A*, **558**, A33
- Thilker D. A., et al., 2005, *The Astrophysical Journal*, **619**, L67
- Thoene C., de Ugarte Postigo A., Leloudas G., Cano Z., Maeda K., 2015, *The Astronomer's Telegram*, **8417**, 1
- Thompson T. A., Prieto J. L., Stanek K. Z., Kistler M. D., Beacom J. F., Kochanek C. S., 2009, *ApJ*, **705**, 1364
- Thöne C. C., et al., 2017, *A&A*, **599**, A129
- Thrasher P., Li W., Filippenko A. V., 2008, *Central Bureau Electronic Telegrams*, **1211**, 1
- Tody D., 1986, in Crawford D. L., ed., *Society of Photo-Optical Instrumentation Engineers (SPIE) Conference Series Vol. 627, Instrumentation in astronomy VI*. p. 733, [doi:10.1117/12.968154](https://doi.org/10.1117/12.968154)
- Tomasella L., Valenti S., Ochner P., Benetti S., Cappellaro E., Pastorello A., 2011, *Central Bureau Electronic Telegrams*, **2830**, 2
- Tomasella L., Benetti S., Cappellaro E., Turatto M., 2018, *The Astronomer's Telegram*, **11168**, 1
- Tomasella L., Cappellaro E., Benetti S., Turatto M., 2019, *The Astronomer's Telegram*, **12397**, 1
- Tonry J., et al., 2019, *Transient Name Server Discovery Report*, **2019-172**, 1

- Turatto M., Cappellaro E., Danziger I. J., Benetti S., Gouiffes C., Della Valle M., 1993, [MNRAS](#), **262**, 128
- Uomoto A., 1989, *IAU Circ.*, **4792**, 3
- Utrobin V. P., 1987, *Soviet Astronomy Letters*, **13**, 50
- Utrobin V. P., Chugai N. N., 2017, [MNRAS](#), **472**, 5004
- Valeev A. F., et al., 2013, *The Astronomer's Telegram*, **5461**, 1
- Van Dyk S. D., Matheson T., 2012, [ApJ](#), **746**, 179
- Van Dyk S. D., Peng C. Y., King J. Y., Filippenko A. V., Treffers R. R., Li W., Richmond M. W., 2000, [PASP](#), **112**, 1532
- Van Dyk S. D., Li W., Filippenko A. V., 2003, [PASP](#), **115**, 1289
- Van Dyk S. D., Li W., Filippenko A. V., Humphreys R. M., Chornock R., Foley R., Challis P. M., 2006, arXiv e-prints, pp [astro-ph/0603025](#)
- Van Dyk S. D., Cenko S. B., Clubb K. I., Fox O. D., Zheng W., Kelly P. L., Filippenko A. V., Smith N., 2013, *The Astronomer's Telegram*, **4891**, 1
- Villar V. A., Berger E., Metzger B. D., Guillochon J., 2017, [ApJ](#), **849**, 70
- Vink J. S., 2018, [A&A](#), **619**, A54
- Wagner R. M., et al., 2000, in *American Astronomical Society Meeting Abstracts*. p. 44.13
- Walborn N. R., Prevot M. L., Prevot L., Wamsteker W., Gonzalez R., Gilmozzi R., Fitzpatrick E. L., 1989, [A&A](#), **219**, 229
- Walker M. F., 1954, [Publications of the Astronomical Society of the Pacific](#), **66**, 230
- Wanajo S., Nomoto K., Janka H. T., Kitaura F. S., Müller B., 2009, [ApJ](#), **695**, 208
- Wang L., Höflich P., Wheeler J. C., 1997, [ApJL](#), **483**, L29
- Ward C., et al., 2021, [ApJ](#), **913**, 102
- Warner B., 2003, *Cataclysmic Variable Stars*. . Cambridge, UK: Cambridge University Press, September 2003., doi:[10.1017/CBO9780511586491](#)
- Warner B., 2006, [Astronomy & Geophysics](#), **47**, 1.29

- Wayland J. D., Zheng W., Filippenko A. V., 2018, Transient Name Server Discovery Report, [2018-1408](#), 1
- Weis K., Bomans D. J., 2005, [A&A](#), 429, L13
- Weis K., Bomans D. J., 2020, [Galaxies](#), 8, 20
- Wenger M., et al., 2000, [A&AS](#), 143, 9
- Wheeler J. C., Harkness R. P., 1990, [Reports on Progress in Physics](#), 53, 1467
- Wheeler J. C., et al., 1993, [ApJL](#), 417, L71
- Whelan J., Iben Icko J., 1973, [ApJ](#), 186, 1007
- White G. L., Malin D. F., 1987, [Nature](#), 327, 36
- Widrow L. M., Dubinski J., 2005, [ApJ](#), 631, 838
- Williams R. E., 1992, [AJ](#), 104, 725
- Williams R. E. e. a., 1993, *Frontiers of Astronomy in the 1990s*
- Williams R. E., 1995, [PASP](#), 107, 152
- Williams R., 2012, [The Astronomical Journal](#), 144, 98
- Williams S. C., Darnley M. J., 2015a, *The Astronomer's Telegram*, [8141](#), 1
- Williams S. C., Darnley M. J., 2015b, *The Astronomer's Telegram*, [8281](#), 1
- Williams S. C., Darnley M. J., 2015c, *The Astronomer's Telegram*, [8360](#), 1
- Williams S. C., Darnley M. J., 2015d, *The Astronomer's Telegram*, [8441](#), 1
- Williams S. C., Darnley M. J., 2016a, *The Astronomer's Telegram*, [8576](#), 1
- Williams S. C., Darnley M. J., 2016b, *The Astronomer's Telegram*, [8622](#), 1
- Williams S. C., Darnley M. J., 2016c, *The Astronomer's Telegram*, [9076](#), 1
- Williams S. C., Darnley M. J., 2016d, *The Astronomer's Telegram*, [9116](#), 1
- Williams S. C., Darnley M. J., 2016e, *The Astronomer's Telegram*, [9661](#), 1
- Williams S. C., Darnley M. J., 2017a, *The Astronomer's Telegram*, [10028](#), 1
- Williams S. C., Darnley M. J., 2017b, *The Astronomer's Telegram*, [10042](#), 1

- Williams S. C., Darnley M. J., 2017c, *The Astronomer's Telegram*, [10143](#), 1
- Williams S. C., Darnley M. J., 2017d, *The Astronomer's Telegram*, [10432](#), 1
- Williams S. C., Darnley M. J., 2017e, *The Astronomer's Telegram*, [10487](#), 1
- Williams S. C., Darnley M. J., 2017f, *The Astronomer's Telegram*, [10497](#), 1
- Williams S. C., Darnley M. J., 2017g, *The Astronomer's Telegram*, [10619](#), 1
- Williams S. C., Darnley M. J., 2017h, *The Astronomer's Telegram*, [10619](#), 1
- Williams S. C., Darnley M. J., 2017i, *The Astronomer's Telegram*, [10741](#), 1
- Williams S. C., Darnley M. J., 2017j, *The Astronomer's Telegram*, [10754](#), 1
- Williams S. C., Darnley M. J., 2017k, *The Astronomer's Telegram*, [10814](#), 1
- Williams S. C., Darnley M. J., 2017l, *The Astronomer's Telegram*, [10990](#), 1
- Williams S. C., Darnley M. J., 2017m, *The Astronomer's Telegram*, [11088](#), 1
- Williams R. E., Phillips M. M., Hamuy M., 1994, *ApJS*, [90](#), 297
- Williams S. C., Darnley M. J., Bode M. F., Shafter A. W., Zhang J. J., Mazzali P., Pian E., 2014a, *The Astronomer's Telegram*, [5723](#), 1
- Williams S. C., Darnley M. J., Steele I. A., Smith R. J., Bode M. F., Piascik A. S., Shafter A. W., 2014b, *The Astronomer's Telegram*, [6704](#), 1
- Williams S. C., Darnley M. J., Bode M. F., Steele I. A., 2015a, *ApJL*, [805](#), L18
- Williams S. C., Darnley M. J., Bode M. F., Shafter A. W., 2015b, *The Astronomer's Telegram*, [7580](#), 1
- Williams S. C., Darnley M. J., Bode M. F., Shafter A. W., 2015c, *The Astronomer's Telegram*, [7828](#), 1
- Williams S. C., Darnley M. J., Bode M. F., 2015d, *The Astronomer's Telegram*, [7958](#), 1
- Williams S. C., Darnley M. J., Henze M., Shafter A. W., Hornoch K., 2015e, *The Astronomer's Telegram*, [8242](#), 1
- Williams S. C., Darnley M. J., Bode M. F., Shafter A. W., 2016a, *The Astrophysical Journal*, [817](#), 143
- Williams S. C., Darnley M. J., Thorstensen J. R., Klusmeyer J. A., Shafter A. W., Henze M., Hornoch K., Chinetti K., 2016b, *The Astronomer's Telegram*, [9411](#), 1

- Williams S. C., Darnley M. J., Hornoch K., 2017a, *The Astronomer's Telegram*, [10451](#), 1
- Williams S. C., Darnley M. J., Hornoch K., Shafter A. W., 2017b, *The Astronomer's Telegram*, [10520](#), 1
- Williams S. C., Darnley M. J., Carey G., 2018, *The Astronomer's Telegram*, [11162](#), 1
- Williams S. C., Darnley M. J., Healy M. W., 2019, *The Astronomer's Telegram*, [12349](#), 1
- Woosley S. E., Smith N., 2022, *ApJ*, [938](#), 57
- Woosley S. E., Weaver T. A., 1995, *ApJS*, [101](#), 181
- Woosley S. E., Eastman R. G., Weaver T. A., Pinto P. A., 1994, *ApJ*, [429](#), 300
- Woosley S. E., Heger A., Weaver T. A., 2002, *Reviews of Modern Physics*, [74](#), 1015
- Xu Z., Gao X., 2018, *Transient Name Server Discovery Report*, [2018-1637](#), 1
- Yamanaka M., Okushima T., Arai A., Sasada M., Sato H., 2010, *Central Bureau Electronic Telegrams*, [2539](#), 1
- Yao Y., et al., 2019, *ApJ*, [886](#), 152
- Yaron O., Prialnik D., Shara M. M., Kovetz A., 2005, *ApJ*, [623](#), 398
- Yaron O., et al., 2017, *Nature Physics*, [13](#), 510–517
- Yaron O., Gal-Yam A., Ofek E., Sass A., Knezevic N., 2019, *Transient Name Server AstroNote*, [15](#), 1
- Yin Q., Gao X., 2018, *Transient Name Server Discovery Report*, [2018-1544](#), 1
- Yuan F., et al., 2016, *MNRAS*, [461](#), 2003
- Yusa T., 2010, *Central Bureau Electronic Telegrams*, [2483](#), 1
- Zhang M., 2019, *Transient Name Server Discovery Report*, [2019-197](#), 1
- Zhang M., Gao X., 2019a, *Transient Name Server Discovery Report*, [2019-130](#), 1
- Zhang M., Gao X., 2019b, *Transient Name Server Discovery Report*, [2019-130](#), 1
- Zhang J., Wang X., Li W., Dong X., Wu X., 2014, *The Astronomer's Telegram*, [6723](#), 1
- Zhang J., et al., 2016, *The Astronomer's Telegram*, [8933](#), 1
- Zhang J., Xu L., Wang X., 2018, *The Astronomer's Telegram*, [11379](#), 1

- Zhang J., Xin Y., Wang X., 2019, Transient Name Server Classification Report, [2019-70](#), [1](#)
- Zhang J., et al., 2020a, [MNRAS](#), [498](#), [84](#)
- Zhang X., Xiang D., Lin H., Wang X., Rui L., Zhang T., Zhang J., 2020b, Transient Name Server Classification Report, [2020-2552](#), [1](#)
- Zhao F.-Y., Strom R. G., Jiang S.-Y., 2006, , [6](#), [635](#)
- Zwicky F., 1936, [PASP](#), [48](#), [191](#)
- Zwicky F., 1964, [ApJ](#), [139](#), [514](#)
- de Jager C., 1998, [A&A Rev.](#), [8](#), [145](#)
- de Ugarte Postigo A., Thoene C. C., Leloudas G., Aceituno F., 2015, The Astronomer's Telegram, [7514](#), [1](#)
- de Vaucouleurs G., 1958, [ApJ](#), [127](#), [487](#)
- de Vaucouleurs G., 1978, [ApJ](#), [223](#), [351](#)
- de Vaucouleurs G., Corwin H. G. J., 1985, [ApJ](#), [295](#), [287](#)
- van Dyk S. D., 1992, [AJ](#), [103](#), [1788](#)
- van Dyk S. D., Hamuy M., Filippenko A. V., 1996, [AJ](#), [111](#), [2017](#)
- van den Bergh S., 1997, [AJ](#), [113](#), [197](#)
- van den Bergh S., Tammann G. A., 1991, [ARA&A](#), [29](#), [363](#)
- van den Heuvel E. P. J., Bhattacharya D., Nomoto K., Rappaport S. A., 1992, [A&A](#), [262](#), [97](#)
- Özdönmez A., Ege E., Güver T., Ak T., 2018, [MNRAS](#), [476](#), [4162](#)